

Stellar Population Models and Chemical Enrichment in Early-Type Galaxies

Adam Thomas Knowles

A THESIS SUBMITTED IN PARTIAL FULFILMENT
OF THE REQUIREMENTS FOR THE DEGREE OF
DOCTOR OF PHILOSOPHY

Jeremiah Horrocks Institute for Mathematics, Physics and Astronomy
University of Central Lancashire

October 2019

Declaration

Type of Award: Doctor of Philosophy

School: Physical Sciences and Computing

I declare that while registered as a candidate for the research degree, I have not been a registered candidate or enrolled student for another award of the University or other academic or professional institution.

I declare that no material contained in the thesis has been used in any other submission for an academic award and is solely my own work.

No proof-reading service was used in the compilation of this thesis.

Adam Thomas Knowles

October 2019

Abstract

The stellar populations within galaxies contain information about how those galaxies formed. Hidden in its integrated light, the abundances of different chemical elements in the atmospheres of its constituent stars give clues about a galaxy's past. Through modelling of stellar populations, these clues may be revealed.

This thesis is focused on developing such models, with particular interest given to abundance patterns, to address a well known limitation of SSPs built from purely empirical stellar spectra that reside in the local solar neighbourhood. Such stars have the imprint of the formation history of the Milky Way and would not fully represent a system that has formed differently. The work is focused on the generation of a new semi-empirical stellar spectra library. Using predictions of how atmospheric abundances affect theoretical stellar spectra, empirical spectra are differentially corrected to create semi-empirical spectra with different $[\alpha/\text{Fe}]$ ratios. I then used these semi-empirical star spectra in the computation of new semi-empirical single-age, single-metallicity stellar populations models (SSPs) with variable $[\alpha/\text{Fe}]$.

The empirical MILES stellar library is used to test three different, state-of-the-art libraries of theoretical stellar spectra that are commonly used in stellar population analysis. The aim is to find where models best represent real star spectra, in a differential way and hence identify good choices of models to use in the creation of semi-empirical stars. We find that most spectral line strengths are well reproduced by the models, particularly those indices that are sensitive to iron and sodium. Exceptions include the higher order Balmer lines ($\text{H}\delta$, $\text{H}\gamma$), in which the models predict

more variation than in data, particularly at low effective temperatures. We also investigate the impact of microturbulence on line-strengths, and find that although the absolute effect can be large (up to $\sim 1-2\text{\AA}$), the differential effect is minimal. Corruptions with C₂ line lists for the Coelho set of models are identified and corrected for, improving them for future applications. Using cool giant models, we show that using differential predictions of models produce less or similar agreements with observations than the models' absolute predictions. This result justifies using the theoretical models in a differential way only, when predicting the effect of abundance patterns on SSPs.

Next, I generate a new, high resolution, theoretical stellar spectral library using existing methodologies (ATLAS9 model atmospheres and ASS ϵ T radiative transfer). These models are fully consistent, in that the abundances have been varied the same way in both model atmosphere and spectral synthesis components. The final grid spans a large range of effective temperature, surface gravity, metallicity, α -element and carbon abundances. All theoretical spectra have a large wavelength coverage (1680-9000 \AA), with a fine linear sampling of $\delta\lambda=0.05\text{\AA}$. The choice of microturbulence for each model is based on a modification of a previously derived formula for effective temperatures below 6000K, which relates the effective temperature and surface gravity to the microturbulence. The library is tested in both high and low (MILES) resolution regimes, through index measurements and spectral plots. The new theoretical library can reproduce the effects caused by variations in parameters compared to observations of individual stars and other theoretical libraries.

Using interpolations within the theoretical library, I create families of theoretical MILES stars with different $[\alpha/\text{Fe}]$ abundances. Ratios of theoretical spectra are then used to predict how star spectra change with atmospheric abundances, referred to as differential corrections. The application of these corrections to empirical MILES

stars produces families of semi-empirical (sMILES) stars with different $[\alpha/\text{Fe}]$ abundances than found in the local solar neighbourhood. The final result is 5 families of 801 sMILES stars with $[\alpha/\text{Fe}]$ abundances ranging from -0.2 to 0.6 dex at MILES resolution (FWHM=2.5Å) and wavelength coverage (3540.5Å - 7409.6Å). I then use sMILES stars to create semi-empirical SSPs, with varying $[\alpha/\text{Fe}]$ abundances for a large range of ages and metallicities. The range and sampling of $[\alpha/\text{Fe}]$ abundance represent an improvement over previously calculated models (e.g. Vazdekis et al. 2015). The intention is to make the high resolution library and sMILES stars publicly available through the online UCLan database. As new isochrones become available, based on a wider range of abundance patterns, sMILES stars may be used to create SSPs with different abundance ratios.

sMILES SSP predictions are then compared to previously computed SSPs. I find reasonable agreements between model predictions for line-strength changes with age and metallicity. For intermediate and old ages, sMILES and Vazdekis et al. model predictions of $[\text{MgFe}]$ agree well, for a range of metallicities. I identify differences for total metallicity indicators between SSP models for young, metal-rich populations. Finally, I demonstrate a potential application of sMILES SSPs, focusing on abundance patterns in a set of stacked SDSS galaxy spectra (Ferreras et al. 2019). Based on a comparison between sMILES model predictions and observations of Mg_b and $\text{Fe}5270$ line-strengths, I demonstrate that sMILES SSPs can identify $[\alpha/\text{Fe}]$ variations of stellar populations in these satellite galaxy spectra for different velocity dispersions and satellite-to-primary mass ratios. Using Lick indices, I find that satellite galaxies are $[\alpha/\text{Fe}]$ -enhanced to varying degrees. Future fitting of indices and full spectra, of satellites compared to primary galaxies will allow us to measure underlying stellar population parameters to investigate galactic conformity.

Contents

Declaration	ii
Abstract	iii
Acknowledgements	xviii
1 Introduction and Motivation	1
1.1 Stellar Population Modelling	1
1.2 Abundance Ratios and Patterns	6
1.2.1 Galaxy Formation Scenarios	10
1.3 Stellar Spectral Libraries	12
1.4 Stellar Population Models in Early-Type Galaxies and Spiral Bulges .	17
1.5 Milky Way Abundances	19
1.6 Bulges in External Systems	20
1.7 Initial Mass Functions in Early-Type Galaxies	24
1.8 Composite Populations and Galactic Chemical Evolution	26
2 Testing Theoretical Stellar Spectra	30
2.1 Introduction	30
2.2 Models of Stellar Spectra	31
2.2.1 Conroy	36
2.2.2 Coelho	37

2.2.3	Allende Prieto	38
2.3	Empirical Stellar Spectra	39
2.4	Direct Comparisons	40
2.4.1	Microturbulent Velocity	41
2.4.2	Abundances in CAP models	48
2.4.3	Absolute Comparisons	49
2.5	Response Functions and their application	50
2.6	Discussion	65
2.6.1	Indices	65
2.6.2	Synthetic Spectra	68
2.6.3	Coelho Latest Revisions	71
2.6.4	$H\beta$ and $H\beta_0$	73
2.6.5	Model Strengths and Weaknesses	79
2.7	Conclusions	80
3	Generating a New High Resolution Theoretical Stellar Library	83
3.1	Introduction	83
3.2	Generating Theoretical Stellar Spectra	84
3.2.1	Microturbulence	87
3.2.2	Element Variation in Grids	93
3.2.3	Computation	103
3.3	Processing	104
3.4	Testing Theoretical Grid	108
3.4.1	Effective Temperature	108
3.4.2	Surface Gravity	109
3.4.3	$[M/H]$	114
3.4.4	$[\alpha/M]$	119
3.4.5	$[C/M]$	124

3.5	Summary	133
4	Semi-Empirical Stellar Library	134
4.1	Introduction	134
4.2	MILES Star Parameters	137
4.2.1	Cenarro	137
4.2.2	Prugniel & Sharma	138
4.2.3	Final Parameter Choice	140
4.3	Interpolation of Theoretical Stellar Spectra	143
4.4	Differential Correction to MILES Spectra	147
4.5	SSP Generation	156
4.5.1	SSP calculation	156
5	Semi-Empirical SSPs : Testing and Application	167
5.1	Testing SSPs	167
5.1.1	Age	169
5.1.2	Metallicity	170
5.1.3	$[\alpha/\text{Fe}]$	174
5.1.4	$[\text{MgFe}]$ and $[\text{MgFe}]'$	178
5.2	Application	188
5.3	Summary	194
6	Conclusions & Future Work	200
6.1	Conclusions	200
6.2	Future Work	205
A	Response Function Tables	225
B	Models vs MILES Lick Indices	235

List of Tables

2.1	Codes and parameters used in the computation of models tested in Chapter 2	34
2.2	Effective temperature, surface gravity, element and metallicity enhancements of the models tested in Chapter 2	35
2.3	Effect of microturbulence on Lick line-strengths for Cool Dwarf, Cool Giant and Turn-off stars	47
2.4	Extract from the CAP Cool Giant response function	53
2.5	Reduced χ^2_{ν} values for comparisons of normalized observations (from MILES) versus normalized models (using response functions)	62
2.6	Gradient and intercept values calculated from a linear regression for comparisons of normalized observations (from MILES) versus normalized models (using the response functions)	63
2.7	RMS scatter about the model=observation line for three applications of CAP Cool Giant models	69
2.8	Comparison between $H\beta$ and $H\beta_0$ response functions	78
3.1	1930 and BL1853 (Fanelli et al. 1990) spectral indices definitions, presented in Figure 3.20.	119
4.1	Age steps of computed sMILES SSPs	160

5.1	Differences between sMILES and Vazdekis et al. SSP predictions for changes in Mg_b , Fe5270 and Fe5330 indices with variations in α abundances	185
5.2	MIUSCAT SSP-equivalent ages and metallicities of stacked satellite galaxy spectra for various velocity dispersion and satellite-to-primary mass ratio bins (Ferreras et al. 2019)	194
A.1	Conroy Cool Dwarf Response Function	226
A.2	Conroy Cool Giant Response Function	227
A.3	Conroy Turn-off Response Function	228
A.4	Coelho Cool Dwarf Response Function	229
A.5	Coelho Cool Giant Response Function	230
A.6	Coelho Turn-off Response Function	231
A.7	CAP Cool Dwarf Response Function	232
A.8	CAP Cool Giant Response Function	233
A.9	CAP Turn-off Response Function	234
C.1	MILES star parameters from Sharma et al. (2016) and the overlap region between Prugniel et al. (2011) and Sharma et al. (2016)	240

List of Figures

1.1	Example SSP fit from Vazdekis & Arimoto (1999)	3
1.2	Comparison of abundance pattern as a function of metallicity from Şen et al. (2018)	13
1.3	Illustration of SSP differential correction method from (Vazdekis et al. (2015)	16
2.1	MILES Lick indices versus Model Lick indices, for hydrogen-sensitive features	42
2.2	MILES Lick indices versus Model Lick indices, for iron-sensitive features	43
2.3	MILES Lick indices versus Model Lick indices, for magnesium-sensitive features	44
2.4	MILES Lick indices versus Model Lick indices, for carbon-sensitive features	45
2.5	MILES Lick indices versus Model Lick indices, for calcium and sodium- sensitive features	46
2.6	Normalised MILES Lick indices versus Normalised Model Lick in- dices, for hydrogen-sensitive features	55
2.7	Normalised MILES Lick indices versus Normalised Model Lick in- dices, for iron-sensitive features	56
2.8	Normalised MILES Lick indices versus Normalised Model Lick in- dices, for magnesium-sensitive features	57

2.9	Normalised MILES Lick indices versus Normalised Model Lick indices, for carbon and nitrogen-sensitive features	58
2.10	Normalised MILES Lick indices versus Normalised Model Lick indices, for calcium and sodium-sensitive features	59
2.11	Comparison between differential and absolute model predictions of line-strengths	70
2.12	Model spectral ratios in C ₂ 4668 region	72
2.13	Model spectral ratios in H δ_A region	72
2.14	Normalised MILES Lick indices versus the Normalised Lick indices of corrupted and corrected Coelho (2014) models	74
2.15	Corrupted and corrected Coelho (2014) model spectral ratios in the C ₂ 4668 region	75
2.16	Normalised MILES Lick indices versus Normalised Model Lick indices for H β and H β_0 indices	77
3.1	Example ATLAS9 Model Atmosphere output	86
3.2	Comparison between the original Dutra-Ferreira et al. (2016) and the modified microturbulence relation used in this work (DF16Mod) . . .	91
3.3	Comparison between DF16Mod, Thygesen et al. (2012) and APOGEE microturbulence relations	92
3.4	Comparison of DF16Mod and APOGEE microturbulence relations in the Cenarro et al. (2007) MILES parameter range	94
3.5	Abundance pattern and stellar parameter coverage of the 3500-6000K theoretical library	98
3.6	Effect of removing TiO lines at different effective temperatures in the high resolution theoretical stellar library	99
3.7	Comparison of a solar abundance calcium spectrum and a calcium-enhanced spectrum from the theoretical library	102

3.8	Largest linear wavelength sampling in ASSeT as a function of effective temperature	106
3.9	Extract from a FERRE model data file	107
3.10	Spectral sequence of effective temperature from the MILES resolution and wavelength range theoretical library	110
3.11	Spectral sequence of effective temperature from the MILES resolution theoretical library in the $H\delta_F$ Lick index region	111
3.12	Spectral sequence of effective temperature from the MILES resolution theoretical library in the TiO_2 Lick index region	112
3.13	Spectral sequence of surface gravity from the MILES resolution and wavelength range theoretical library	114
3.14	Spectral sequence of surface gravity from the theoretical library in Na_D Lick index region	115
3.15	Spectral sequence of surface gravity from the MILES resolution theoretical library in TiO_2 Lick index region	116
3.16	Spectral sequence of surface gravity from the high resolution theoretical library in CaT index region	117
3.17	Spectral sequence of metallicity from the MILES resolution and wavelength range theoretical library	120
3.18	Spectral sequence of metallicity from the MILES resolution theoretical library in the $Fe5270$ Lick index region	121
3.19	Spectral sequence of metallicity from the MILES resolution theoretical library in part of the UV regime	122
3.20	Spectral sequence of metallicity from the MILES resolution theoretical library in another part of the UV regime	123
3.21	Spectral sequence of α -element variations from the MILES resolution and wavelength range theoretical library	125

3.22	Spectral sequence of α -element variations from the MILES resolution theoretical library in the Mg_b Lick index region	126
3.23	Spectral sequence of α -element variations from the high resolution theoretical library in the CaT index region	127
3.24	Spectral sequence of carbon variations from the MILES resolution and wavelength theoretical library	129
3.25	Spectral sequence of carbon variations from the MILES resolution theoretical library in the C_24668 Lick index region	130
3.26	Spectral sequence of carbon variations from the MILES resolution theoretical library in the UV wavelength regime	131
3.27	Spectral sequence of carbon variations from the MILES resolution theoretical library in another part of the UV wavelength regime . . .	132
4.1	Illustration of the semi-empirical MILES (sMILES) stellar library aimed for in this work, in comparison to the empirical MILES library	136
4.2	Comparison of MILES star T_{eff} values between Prugniel & Sharma and Cenarro parameter sets	141
4.3	Comparison of MILES T_{eff} , $\log g$ and metallicity values between Prug- niel & Sharma and Cenarro parameter sets, in the range of the theo- retical library	142
4.4	Comparison between spectra produced via linear and quadratic Bézier interpolations in FERRE, near the edges of the theoretical grid . . .	146
4.5	Differential corrections for MILES star m0067	148
4.6	Differential corrections for MILES star m0923	149
4.7	Spectral sequence of sMILES stars, with the empirical MILES star, around Mg_b Lick index	151
4.8	Spectral sequence of sMILES stars, with the empirical MILES star, around $Ca4227$ Lick index	152

4.9	α -deficient (-0.2) sMILES library, for the MILES wavelength range . . .	153
4.10	Solar α abundance (0.0) sMILES library, for the MILES wavelength range	154
4.11	α -enhanced (0.2) sMILES library, for the MILES wavelength range . . .	154
4.12	α -enhanced (0.4) sMILES library, for the MILES wavelength range . . .	155
4.13	α -enhanced (0.6) sMILES library, for the MILES wavelength range . . .	155
4.14	Final semi-empirical MILES (sMILES) stellar library produced in this work in α abundance and metallicity, in comparison to the empirical MILES library	157
4.15	Total SSP metallicity as a function of α abundance and metallicity of theoretical stellar spectra from this work	163
5.1	Spectral sequence of age from sMILES SSPs, in the $H\beta$ and $H\beta_o$ Lick index regions	171
5.2	sMILES and Vazdekis et al. SSP predictions of $H\beta$ and $H\beta_o$ index variations with age, for α -enhanced populations.	172
5.3	Spectral sequence of metallicity from sMILES SSPs, in the Fe5270 and Fe5335 Lick index regions	175
5.4	sMILES and Vazdekis et al. SSP predictions of Fe5270 and Fe5335 index variations with total metallicity, for α -enhanced populations. . .	176
5.5	Demonstration of SSP age and metallicity degeneracy in sMILES SSPs, for the MILES wavelength range	177
5.6	Spectral sequence of α -abundance from sMILES SSPs, in the Ca4227 and Mg_b Lick index regions	179
5.7	Difference in total metallicity indicator (González, 1993) between sMILES and Vazdekis et al. SSPs	183
5.8	Difference in total metallicity indicator (Thomas et al., 2003b) between sMILES and Vazdekis et al. SSPs	184

5.9	Difference in total metallicity indicators between sMILES models with $\alpha=0.2$ models computed with scaled-solar or α -enhanced isochrones	187
5.10	Comparison of Stacked SDSS satellite galaxy and sMILES SSP spectra, for μ_1 satellite-to-primary mass ratio and three velocity dispersions, in the Mg_b and Fe5270 Lick index regions	195
5.11	Comparison of Stacked SDSS satellite galaxy and sMILES SSP spectra, for μ_3 satellite-to-primary mass ratio and three velocity dispersions, in the Mg_b and Fe5270 Lick index regions	196
B.1	Difference in MILES Lick Indices versus equivalent model predictions as a function of effective temperature, surface gravity, $[Fe/H]$ and $[Mg/Fe]$	237
B.2	Difference in MILES Lick Indices versus equivalent model predictions as a function of effective temperature, surface gravity, $[Fe/H]$ and $[Mg/Fe]$	238
B.3	Difference in MILES Lick Indices versus equivalent model predictions as a function of effective temperature, surface gravity, $[Fe/H]$ and $[Mg/Fe]$	239

Acknowledgements

I would like to thank my supervisor, Anne Sansom, without whom this thesis would not be possible. Her patience, expertise and attention to detail has vastly improved the quality of my work. Her guidance and advice over the last few years have helped develop me as a researcher but more importantly, as a person. I also thank my second supervisor Don Kurtz, for his support during my years as UCLan. His knowledge and experience have been extremely helpful and insightful. Roger Clowes also played an important part in the writing of his thesis and I would like to express my gratitude towards both him and Don for taking the time to read a draft version of this thesis and provide thorough feedback.

The JHI staff members and students, past and present, have provided a warm and welcoming environment in which to learn. I'd like to thank all the PhD and MSc students that have been here during my PhD, for providing a fun and productive environment to work in every day.

I also thank the IAC for providing funding for 2 separate visits to Tenerife. Alex, Carlos, Ana, Jesús at the IAC gave constant support to complete the work of this thesis and I enjoyed working with them all very much. I would particularly like to mention Miguel, Angel and Yolanda for providing a place to stay during my visits to Tenerife. Their kind and welcoming nature made both visits extremely comfortable and enjoyable. I thank the STFC for the studentship that covered tuition and maintenance fees throughout my PhD.

I wish to also thank my Ph.D panel, Mark Norris and Ricardo Schiavon, for

taking the time to read and examine this work and for providing useful feedback that significantly improved the quality of this thesis.

My family, particularly my Mum and Dad, have provided constant love and support throughout my life and I will always be grateful to be born into such a caring environment.

Last, but by no means least, I thank my partner Ashleigh for always being there. Her love made the tough times easier and I feel lucky to have such a person in my life.

Chapter 1

Introduction and Motivation

Stellar population analysis is used to measure the properties of stellar systems (e.g. galaxies and globular clusters), using the assumed knowledge of how their constituent stars evolve. The chemical composition of these stars gives information about the history of their formation. Stellar population analysis connects the fields of stellar and galactic astrophysics, providing an insight as to when and how the stars formed in a galaxy's past.

For galaxies at a higher redshift than the Local Group, it is currently not possible to resolve their constituent stellar populations star-by-star. Instead, it is only possible to measure integrated light produced by the contributions of all the stars. This thesis aims to improve the models used to extract the information regarding the formation of these unresolved populations, with a particular focus on abundance patterns.

1.1 Stellar Population Modelling

Stellar Population Synthesis is a method used to interpret a galaxy's integrated light and extract its stellar properties. To do this, models that describe the evolution of stellar populations and produce their resulting spectra are required. The idea of

CHAPTER 1

an evolutionary population model that could be used to make predictions for stellar populations in galaxies started with Tinsley (Tinsley 1968; Tinsley 1980). She developed models that predicted how the colours and chemical abundances of populations would change with time based on the chemical evolution of the gas, based on a ‘birth-rate’ function, describing the number of stars formed in 10^9 yr intervals. This methodology, which requires inputs from nucleosynthesis models and stellar evolution models, still provides the basis of the most up-to-date models. An important advance to Tinsley’s work came with additional parameters, describing the star formation history of the population, incorporated into models (Faber 1972; Searle et al. 1973). The modern framework to produce such models that match both the Galactic Chemical Evolution (GCE) of the gas and resulting populations is given by Composite Populations, discussed in Section 1.8.

A simpler approach to extract information from a galaxy’s integrated light is to match the spectrum to spectra of Simple Stellar Populations (SSPs) - coeval, single metallicity and abundance pattern (chemical composition) stellar populations. SSP fitting avoids complexities of the gas evolution but can still be used as a powerful tool for investigation of galaxy formation and evolution, discussed in Section 1.4. Figure 1.1 shows an example of the fit of an SSP spectrum to that of a galaxy. It is also possible to produce composite stellar populations by combining SSPs. Although this thesis is focused on SSP building, in particular the information that abundance patterns contain, consideration of star formation histories and galactic chemical evolution is discussed in 1.8 to provide context of galaxy formation and evolution.

An SSP requires 4 basic ingredients to build (see e.g. Tinsley & Gunn 1976; Tinsley 1978; Bruzual 1983):

- Two components of stellar evolution theory in the form of isochrones and

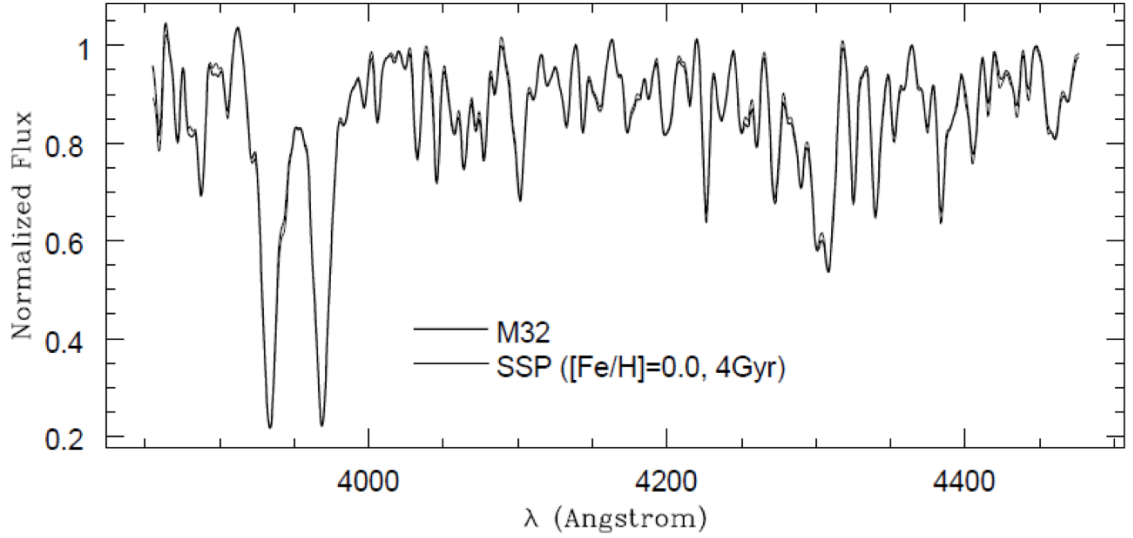


Figure 1.1: Example of an SSP fit to M32 (a dwarf elliptical) from Vazdekis & Arimoto (1999).

evolutionary tracks - theoretical curves on a Hertzsprung-Russell diagram that represent the evolutionary positions of stars having the same age but differing masses or having the same mass but differing ages respectively.

- Stellar spectral libraries, defined as a set of individual star spectra that cover a range in stellar properties such as effective temperature (T_{eff}), surface gravity ($\log g$), metallicity ($[\text{Fe}/\text{H}]$).
- Initial Mass Function (IMF), which describes the distribution of initial masses for a stellar population.

With these ingredients defined, equation 1.1 can be used to describe the evolution of the SSP (Conroy 2013).

$$f_{\text{SSP}}(t, Z) = \int_{m_{\text{lo}}}^{m_{\text{up}}(t)} f_{\text{star}}[T_{\text{eff}}(M), \log g(M)|t, Z] \Phi(M) dM, \quad (1.1)$$

where f_{SSP} is the resulting (metallicity and time-dependent) SSP spectrum (in units

CHAPTER 1

of flux/ \AA , for example) from all the star contributions, f_{star} is a star spectrum (also in units of flux/ \AA), M is defined as the initial stellar mass and $\Phi(M)$ is the initial mass function. SSP model spectra are built by adding-up the spectral contributions from all the stars on an isochrone and weighting them by the relative light contributions at each point, determined by the IMF and stellar evolution. The evolution of the SSP spectrum is then described using the evolutionary tracks of the individual stars within the SSP.

Some of the commonly used scaled-solar¹ stellar population models are those by Bruzual & Charlot (2003), Schiavon (2007)², Vazdekis et al. (2010) and Leitherer et al. (2010) (Starburst99). Despite the fact that the framework and methodology of producing stellar population models is well established, problems still exist that mean it is not an easy task to produce SSPs. Three of the most important issues are discussed below.

Firstly, a problem when studying the integrated light of stellar populations is the age-metallicity degeneracy. This arises from a galaxy getting redder as it ages - due to stars moving away from the upper main sequence to later stages of stellar evolution, including the giant branch phase of evolution - and also reddening for increasing metal abundance because of the effective temperature decrease due to increases in line opacity, dominating in the blue more than the red. This led to the estimation (Worthey, 1994) that a factor 3 increase in metallicity is the same as a factor 2 increase in age in optical colours. The age-metallicity degeneracy can be broken using a combination of a Balmer-line index with a metal-line index, provided these indices can be measured and interpreted accurately. Alternatively colour-colour diagrams may be used to disentangle metallicity and age effects. For example, in populations with ages $\lesssim 300$ Myr, (B-K) appears to be mainly sensitive

¹Scaled-solar refers to models with $[X/\text{Fe}]=0$ for all elements X, except for Fe

²Schiavon (2007) also produce SSPs for different abundance patterns, using predictions from Korn et al. (2005).

CHAPTER 1

to age whereas (J-K) is very sensitive to metal content (e.g. Figures 11.6 and 11.7 from Salaris & Cassisi 2005). The main contributions to J and K fluxes in an SSP comes from the AGB evolutionary phase for ages $\lesssim 1$ Gyr and upper RGB for later ages, whereas the B fluxes are always dominated by the turn-off and upper main sequence phases. Therefore, J-K is determined by the colour of the AGB and upper RGB, which is mainly sensitive to the initial metallicity, although there is some sensitivity to age below a few Gyr. B-K however, is dominated by the turn-off brightness and color, which is dominated by age, although there is some sensitivity to metallicity.

Secondly, there is a relatively poor understanding of some of the later phases of stellar evolution, particularly the asymptotic-giant branch phase (AGB). These stars are bright and therefore do have a significant effect on the population spectrum at $10^8 - 10^9$ yrs. Figure 11.1 of Salaris & Cassisi (2005) shows the fractional contribution of different evolutionary phases to the total SSP light as a function of SSP age. The main source of the uncertainty lies in the difficulty of modelling the effect of mass loss, which will have a considerable impact on their evolution.

Thirdly lies the problems involving abundance patterns. Until very recently, most stellar population models were limited by the fact that they lacked chemical abundances that differed from that of the solar neighbourhood. The information encoded in the abundance patterns of galaxies is found to be extremely useful in the context of stellar population analysis. The stellar library and isochrone components of the SSP models are both abundance pattern dependent. The abundance pattern limitation is the area that this project will be aimed towards - expanding the range of abundance patterns that can be specified by the Medium-resolution Isaac Newton Telescope Library of Empirical Spectra (MILES) (Sánchez-Blázquez et al., 2006)³. Although this thesis is focused on addressing the limitations in abundance patterns

³<http://www.iac.es/proyecto/miles/pages/stellar-libraries/miles-library.php>

CHAPTER 1

when building SSPs from stars in the Milky Way, it is also worth noting there are also issues with the metallicity and age coverage of empirical stellar libraries. For example, there are no young, metal-poor stars present in the Milky Way now, which limits the age and metallicity of SSPs that could be built. Below I discuss the information that abundance patterns hold as well as the current state of the field in terms of stellar spectral libraries.

1.2 Abundance Ratios and Patterns

The elemental abundance patterns of galaxies can tell us about the timescales in which their constituent stellar populations are formed, with even moderate resolution (e.g. $R \sim 2000$ in Parikh et al. 2019, using MaNGA Blanton et al. 2017) spectra containing details that allow for measurements of abundances. In resolved stellar populations it is possible to study the star formation history using Hertzsprung-Russell diagrams, focusing on Turn-Off points and other aspects of this diagnostic diagram. When investigating the star formation time-scales of an integrated population, the main abundance ratio of interest is $[\alpha/\text{Fe}]^4$. This is because it is known that the sources and time-scales of interstellar medium (ISM) enrichment for the α -capture and iron-peak elements are different. The dominant sources of ISM enrichment are Type II and Type Ia supernovae, as well as AGB stars. Supernovae (Type II) from massive star progenitors enrich the ISM with a range of heavy elements over time-scales of less than 10^8 yr. Type Ia supernovae, from white dwarf progenitors, enrich the ISM with mainly iron-peak elements over longer time-scales, ranging from prompt explosions of $\sim 10^8$ yr to more delayed enrichment over 10^{10} yr (Pagel 2009; Sullivan et al. 2006; Mannucci 2008; Maoz et al. 2010). Because the

⁴ α here is defined as the elements that make up, and are a product of, the α -capture process - a process of nuclear fusion that converts carbon and other element to heavier elements. Typically, the α -elements considered are O, Ne, Mg, Si, S, Ca and Ti.

CHAPTER 1

time-scales of element production in the two types of supernovae are different, it is possible to use the ratio of α -capture and iron-peak elements (e.g. from observations of $[\text{Mg}/\text{Fe}]^5$) as a clock to constrain the time-scale over which the stars were produced. For example, if a population was formed in a fast process, one would expect it to contain a high $[\alpha/\text{Fe}]$. If the population was formed over a larger time-scale, this would allow time for Type Ia supernovae enrichment, resulting in a population with a lower $[\alpha/\text{Fe}]$. The first of these scenarios assumes that there is a short burst of star formation. It is also worth noting that in a scenario in which there is continuous star formation, like that of a galactic disk, there will be a steady state of Type II supernovae.

Traditionally, one way in which abundance ratios are measured when observing integrated populations is to measure spectral indices. Commonly, such indices are defined by three bandpasses, a feature band and two sidebands (pseudocontinua), and are then measured as a pseudo-equivalent width. The most popular system of indices is the LICK/IDS system (Worthey 1994; Worthey & Ottaviani 1997) that defines 25 spectral indices between 4000-6500 Å, although other systems have been designed for use with specific spectral libraries and spectral resolutions, such as the Line Index System (LIS) MILES system Vazdekis et al. (2010), which was flux and wavelength calibrated unlike the older LICK system. There are other ways to define indices, such as flux ratio indices defined by Rose (1984) or the indices based on the D4000 feature Poggianti & Barbaro (1997). The main purpose of defining line indices is to address the age-metallicity degeneracy. Hydrogen line bands attempt to maximise the age dependence and minimise metallicity dependence, whereas iron line bands attempt exactly the opposite. The abundance patterns of galaxies are not always the same as that of the solar neighbourhood. This can be seen in our own Galaxy from relations like that shown in the work of Edvardsson et al. (1993),

⁵ $[\text{A}/\text{B}] = \log[n(\text{A})/n(\text{B})]_* - \log[n(\text{A})/n(\text{B})]_{\odot}$, where $n(X)/n(Y)$ is the number abundance ratio of element A, relative to element B.

CHAPTER 1

who show how abundance patterns vary as function of $[\text{Fe}/\text{H}]$ in nearby field F and G disk dwarf stars. For example, in Figure 15 (panel b) of Edvardsson et al. (1993), they show how $[\text{Mg}/\text{Fe}]$ is enhanced (~ 0.3) at low values (~ -0.7) of $[\text{Fe}/\text{H}]$. Similar trends have been found in more recent and large scale surveys, such as Hayden et al. (2015) who show how $[\alpha/\text{Fe}]$ varies as a function of $[\text{Fe}/\text{H}]$ in red giant stars.

With an index system defined, it is possible to use the indices to investigate the properties of stellar populations in galaxies. Moreover, it is possible to study how the indices are sensitive to elemental abundance changes using theoretically produced stellar spectra. This investigation is usually presented in the form of response functions, which are tables that show how spectral features are affected by abundance changes. This type of study was first performed in the work of Tripicco & Bell (1995) with the assessment of how Lick indices vary with abundance changes in 10 elements using synthetic spectra. A refined version of this study was then carried out (Korn et al., 2005) that used updated linelists and atomic transition probabilities with more accurate atmospheric models and also incorporated a range of metallicities. The derived response functions of Korn et al. (2005) are some of the most popular and have been widely used to date. More modern and larger numbers of theoretical spectra have been used in more recent studies (e.g. Lee et al. 2009; Zamora et al. 2015). With measures of how spectral indices are sensitive to elemental abundances, one can use the derived response functions to differentially correct indices to account for changes in abundance patterns. There are many applications of such work throughout the literature in both Milky Way and extragalactic studies (e.g. Trager et al. 2000b; Proctor & Sansom 2002, Schiavon 2007, Maraston & Strömbäck 2011; Thomas et al. 2011; Onodera et al. 2015; Concas et al. 2017; Sesto et al. 2018; Parikh et al. 2018).

Another approach to account for different abundance patterns is full spectrum fitting. One of the first works to take a differential abundance pattern approach in

CHAPTER 1

full spectrum fitting was that of Prugniel et al. (2007) followed by that of Walcher et al. (2009). This work was then expanded by Conroy & van Dokkum (2012), who varied 11 elements separately and focused on the response of the full spectrum for elemental abundances, at \approx fixed metallicity ($[\text{Fe}/\text{H}]$) near the solar value. A method of differentially correcting the star or SSP spectra can then be used to account for variations in abundance patterns. If accurate measures are made that quantify how full spectra are sensitive to elemental abundances, it is possible to begin to build stellar spectral libraries that contain abundance patterns different from our own solar neighborhood. Such a library would allow one to produce stellar population synthesis models that include stars with abundance patterns that differ from that of the solar neighbourhood. This is motivated by the different abundance patterns seen in external systems such as Early-Type and Dwarf Spheroidals galaxies (e.g. Letarte et al. 2007; Conroy et al. 2014). An illustration of these abundance pattern differences is shown in Figure 1.2, where I show Figure 4 of Şen et al. (2018), which plots the $[\text{Mg}/\text{Fe}]$ vs $[\text{Fe}/\text{H}]$ for Milky Way stars from Venn et al. (2004), stars from the Fornax dwarf galaxy in Letarte et al. (2010) and Shetrone et al. (2003), red giants from the LMC (Pompéia et al., 2008), giant ellipticals from Conroy et al. (2014), stars from NGC1396 (Mentz et al. (2016)) and Virgo cluster dwarf ellipticals. I also plot a sample of early-type galaxy measurements from McDermid et al. (2015) on the same figure. Despite the observed variation, most of the stellar population models and stellar library components to date rarely contain different abundance ratios and patterns because the stars used to build the SSPs are taken from the solar neighbourhood (e.g. Bruzual & Charlot 2003; Maraston 2005; Vazdekis et al. 2010). The differential correction process can be made on the star or SSP level. Vazdekis et al. (2015) did a differential correction on the SSP level, shown in Figure 1.3. Mathematically, the differential correction on the SSP and star level should be equivalent. They generated SSPs at $[\alpha/\text{Fe}]=0.0$ and 0.4 . Conroy et al. (2018) also

CHAPTER 1

perform differential corrections on an SSP level, computing responses for changes in 18 individual elements at different metallicities. The details of this work are discussed, in the context of this thesis project, in Chapter 5.

This thesis project will be focusing on the star level. Chapter 3 will describe the generation of theoretical stellar spectra that cover a wider range of abundance ratios and Chapter 4 describes the semi-empirical library that was produced using a differential correction to empirical spectra. The differential approach reduces the reliance of absolute predictions of theoretical stellar spectra, which are known to have issues (see Chapter 2).

The process of differentially correcting empirical stellar spectra is reliant on the accuracy of theoretical stellar spectra used. With large numbers of models currently available, each with their own set of advantages, assumptions and limitations, deciding which synthetic spectra to use is not a straightforward task. Chapter 2 of this thesis tests the predictions of three stellar spectral model libraries against empirical star data in the context of abundance patterns, with the aim of highlighting current strengths and weaknesses of the models. These models represent theoretical spectral libraries of some of the most recent works in stellar population analysis, covering a broad range of parameter space, suitable for modelling integrated stellar population spectra. This work will assist in the identification of the best model to use when building a new semi-empirical variable abundance pattern stellar spectral library.

1.2.1 Galaxy Formation Scenarios

Another interesting property that abundance patterns in stellar populations probe is the formation and evolution of galaxies. Abundance patterns not only act as a clock, revealing the time-scales of star formation, but also can act as tracers of formation scenario. For example, the combination of information regarding the age, metallicity and abundance pattern of populations should allow for the distinction

CHAPTER 1

between classical bulge and pseudobulge formation (Sánchez-Blázquez 2016; Fisher & Drory 2016). Formation of Classical bulges is expected to be a fast process (Eggen et al. 1962; Scannapieco & Tissera 2003) whereas pseudobulges are expected to form more slowly from disc material (e.g. Martínez-Valpuesta & Gerhard 2013). Measurements of radial gradients in abundances can shed light on a galaxy’s past, particularly how it formed. Studies of our own Galaxy have shown evidence for the composite nature of the bulge, with multiple populations present in $[\alpha/\text{Fe}]$ (e.g. from Recio-Blanco et al. (2017), using the Gaia-ESO survey Gilmore et al. (2012)).

In addition, abundance patterns should help identify if a galaxy has formed independently or if mergers have played a part (Choi et al. 2014). Figure 12 of Choi et al. (2014) shows an example of how abundance pattern and metallicity of stellar populations would change as a function of mass, if a galaxy evolved independently or was involved in some form of merger. The stellar populations are assumed to be measured via a spectroscopic fibre that has an extent of one effective radius. In that work, four scenarios were considered: an isolated evolving galaxy, a dry (no star formation) major merger (mass ratio $\sim 1:1$) of two galaxies or mass growth outside of one effective radius that results in a doubling of total mass, a dry minor merger (1:10) within one effective radius and finally, the introduction of low mass galaxies with scaled-solar abundance ratios. In the first scenario (passive evolution), the galaxy ages as expected and the abundance pattern trends are unchanged. The second scenario (major merger or mass growth outside of one effective radius that results in a double total mass) results in a galaxy that has increased in mass but has abundance pattern trends that are unchanged. This is true for both the major merger and for the case in which the inner galaxy evolves normally but with mass growth in the outskirts because the spectroscopic data is insensitive to regions beyond one effective radius. The third scenario (a dry minor merger within an effective radius) has an effect on both the stellar population age and abundance pattern trends,

CHAPTER 1

as the introduction of a lower mass galaxy will add stars with different ages and $[\text{Mg}/\text{Fe}]$ values, compared to the higher mass galaxy, to the integrated light. The final scenario considered (an introduction of low mass galaxies with scaled-solar abundance ratios) results in the most massive galaxies evolving as in scenario one, but the low-mass end ages are affected by the introduction of young (recently formed) stellar populations. A key point of this work was to highlight that age effects are far more subtle and difficult to measure, due to difficulties in measurements of stellar ages, than changes in abundance pattern. The study of abundance patterns will more likely lead to clearer distinctions in formation scenarios because the changes in abundance ratios with formation scenario are larger and more obvious than changes in stellar population age.

1.3 Stellar Spectral Libraries

Spectral libraries are needed to convert the outputs of calculations made in stellar evolution theory, whose predictions result in values of surface gravities and effective temperature at different metallicities, into spectra. An important aspect of the libraries is the types of stars they contain, including dwarfs, giants and evolved stars of different types. Ideally, the library would contain a large range of effective temperature, surface gravity and metallicity (e.g. characterised by $[\text{Fe}/\text{H}]$). More recent work has also allowed for $[\text{Mg}/\text{Fe}]$ (a proxy for $[\alpha/\text{Fe}]$) to be included (Milone et al. 2011).

Stellar spectral libraries can consist of theoretical spectra (e.g. Coelho 2014) or observed spectra (e.g. Sánchez-Blázquez et al. 2006). However, there is no single library that covers the range of possibilities, particularly in elemental abundance patterns, needed for constructing SSP models that can be applied to environments different from our own Galaxy.

Theoretical spectra have the advantage of covering a wide parameter space and

CHAPTER 1

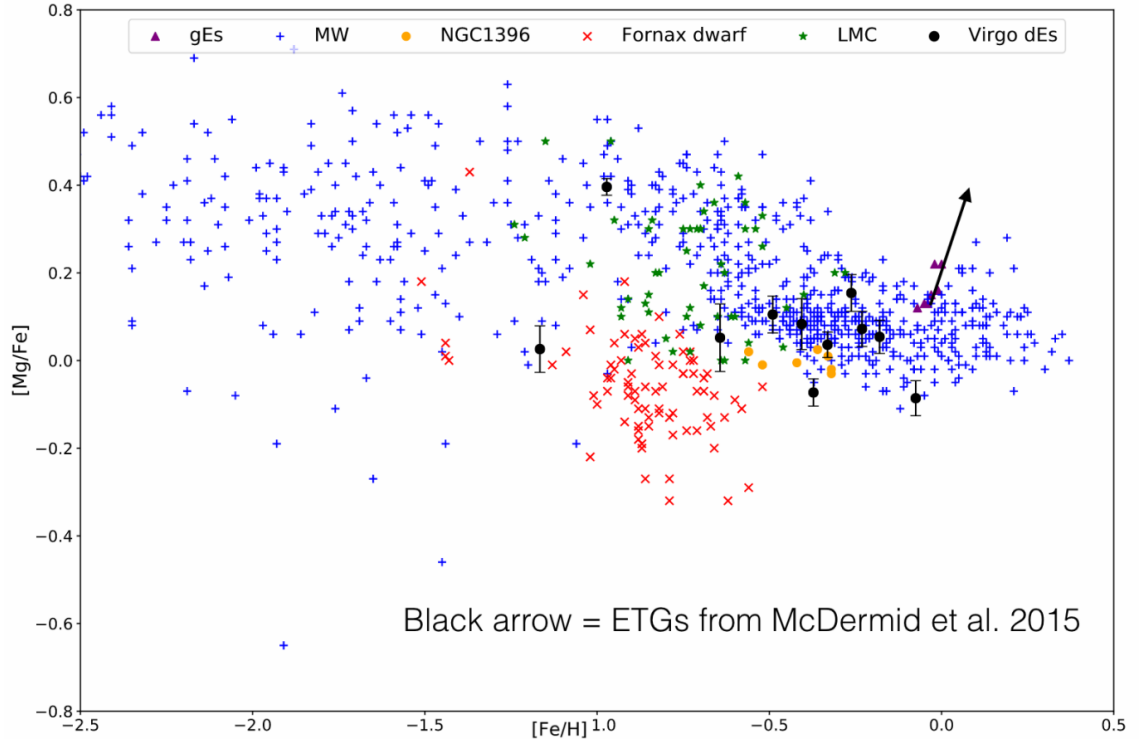


Figure 1.2: Comparison of $[Mg/Fe]$ values as a function of $[Fe/H]$ for various systems from Şen et al. (2018). Blue plus signs are Milky Way stars (Venn et al. 2004), red crosses are stars from the Fornax dwarf in Letarte et al. (2010) and Shetrone et al. (2003). Green stars are red giants from the LMC (Pompéia et al. 2008) and purple triangles are giant ellipticals from Conroy et al. (2014). Orange circles are radial bins in NGC1396 (Mentz et al. 2016) and black circles are the dwarf ellipticals from Şen et al. (2018). I also show measurements from a sample of early-type galaxies in McDermid et al. (2015), which I have shown via a black arrow.

CHAPTER 1

also do not have observational issues. However, they are limited by the models used to reproduce the vast number of spectral lines in a stellar spectrum, which make simplifying physical assumptions. The treatment of convection, microturbulence, geometry, LTE are all choices that have to be made and will in some way limit the accuracy of the models. Historically, theoretical libraries would focus on one particular limit in effective temperature, such as the very highest temperature (O and Wolf Rayet - Smith et al. 2002) or very coolest temperature (Husser et al. 2013). However, there have been theoretical libraries created with much wider parameter coverage (e.g. Kurucz 1979a). More recently, large theoretical libraries have been computed for specific applications, such as spectroscopic surveys or SSP modelling (e.g. Coelho et al. 2005; Coelho 2014; Bohlin et al. 2017; Allende Prieto et al. 2018).

Although the observational spectra correctly represent all of the physics and spectral lines present in the observed stars, they suffer from standard observational constraints such as limited wavelength coverage, spectral resolution, atmospheric absorption and noise. A major issue currently plaguing empirical libraries is the limited parameter space covered, which is unavoidable as the spectra can mostly only be drawn from samples of stars in the solar neighbourhood and so will be representative of the Milky Way's chemical history and abundance, as is shown in Figure 1.2. It is possible to obtain spectra of stars from further distances, but because of the long exposure times needed only small samples can be collected.

One of the first widely used empirical stellar libraries was that of the LICK-IDS Library (Faber et al. 1985). This library was low resolution and also had a set of defined line-strengths consisting of low resolution line indices defined as pseudo-equivalent widths of strong absorption lines in the spectrum between 4200-6400 Å. More recently, three very popular empirical libraries are the INDO-US Library of Coudé Feed Stellar Spectra (Valdes et al. 2004) that consists of ~ 1300 stars with spectral coverage between 3460 and 9464 Å, the Medium-resolution Isaac Newton

CHAPTER 1

Telescope Library of Empirical Spectra (MILES) (Sánchez-Blázquez et al. 2006) that has ~ 1000 stars with spectral coverage between 3500 and 7500Å and ELODIE (Prugniel et al. 2007) that is made up of ~ 1400 stars with spectral coverage between 3900 and 6800Å. A major advantage of the MILES library over that of the LICK-IDS library, is that MILES spectra are flux calibrated. Coverage of these two libraries in effective temperature and surface gravity is good around solar $[\text{Fe}/\text{H}]$. Problems arise outside the solar metallicity and abundance ratio regions, and thus the range of stellar population ages and star formation histories that can be modelled is limited. These libraries (and therefore the SSP models that can be built with them) are limited by the fact that they contain only Milky Way stars, meaning that the abundance patterns of these stars reflect formation of the local solar neighbourhood, including the Galactic disk and halo.

To account for abundance patterns that differ from the solar neighbourhood, a combination of predictions from theoretical spectra and accuracy of empirical spectra is made. Usually, a quantification of how abundances affect spectral lines is applied to empirical spectra to account for non-solar abundance patterns. This is at the heart of the aims of this project, to allow for a spectral library to be built with stars that contain abundances that better match with external galaxies. I will be using some state-of-the-art theoretical spectra and applying their abundance predictions to existing MILES spectra. I will thus produce a library of semi-empirical star spectra that are built with SSP modelling in mind, covering a broad range of stellar parameter space. See Figure 3.5 for an illustration of the semi-empirical grid and the theoretical grid in the dimensions of T_{eff} , $\log g$, $[\text{M}/\text{H}]$, $[\text{C}/\text{M}]$ and $[\alpha/\text{M}]$.

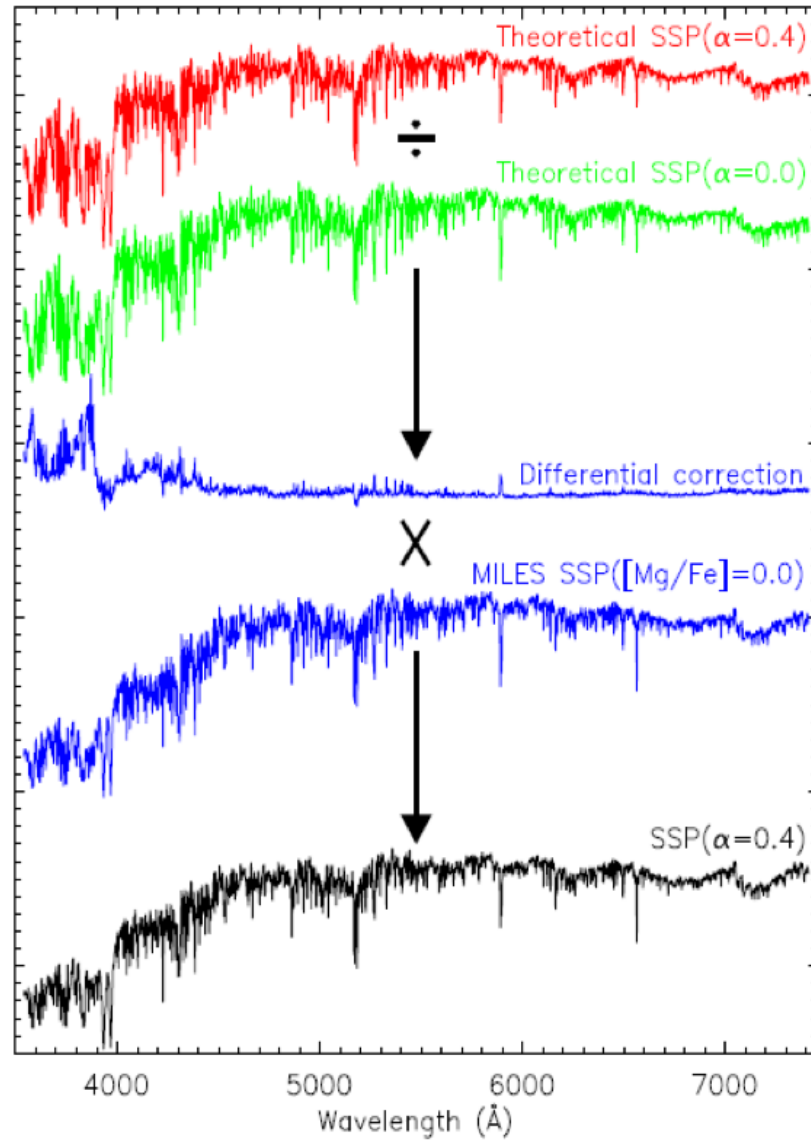


Figure 1.3: Illustration of differential correction method applied to SSPs (Vazdekis et al. (2015), their Figure 4). The red and green spectra show SSPs calculated using theoretical α -enhanced stars and solar abundance stars respectively. These are divided to leave the differential correction - the prediction of how an α enhancement affects the resulting SSP spectrum. This prediction is then applied to an empirical SSP, built using existing MILES stars at $[\text{Mg}/\text{Fe}]=0$, resulting in a semi-empirical SSP with an α enhancement. Note here that their work only considered $[\alpha/\text{Fe}]=0$ and 0.4 dex, while this thesis increases this range and to go below as well as above $[\text{X}/\text{Fe}]=0$.

1.4 Stellar Population Models in Early-Type Galaxies and Spiral Bulges

When evidence that non-solar abundance patterns were present within the Milky Way galaxy, curiosities about external systems were sparked. Early observational studies of elliptical galaxies (Peletier 1989) suggested a deviation of magnesium to iron ratio ($[\text{Mg}/\text{Fe}]$) from solar value. Focus has been made on $[\text{Mg}/\text{Fe}]$ due to the strong Fe I and Mg_b features present in modest resolution optical spectra. With the development of spectral synthesis models came the discovery that $[\text{Mg}/\text{Fe}]$ varied in early-type galaxies (Worthey et al. 1992). One of the first large investigations of abundance patterns came with Trager et al. (2000b); Trager et al. (2000a), with early-type galaxies. By fitting $\text{H}\beta$, Mg_b and two iron features, positive enhancements were found in $[\text{Mg}/\text{Fe}]$ that correlated with velocity dispersion. This initial discovery has since been confirmed by other, more recent studies that all showed a positive correlation between $[\text{Mg}/\text{Fe}]$ -enhancement and velocity dispersion (e.g. Proctor & Sansom 2002; Thomas et al. 2005; Graves et al. 2009; Vazdekis et al. 2015). Studies with larger numbers of indices were also developed, which increased the efficiency of breaking the age-metallicity degeneracy and also studies the variation of abundance patterns with Hubble type and spheroidal component (Proctor & Sansom 2002; Sansom & Northeast 2008; Greene et al. 2015).

As population models have developed to allow for variation in other elements, further studies have been able to investigate correlations with total α , rather than just Mg, as well as carbon and nitrogen. An interesting, but troublesome element investigated in early-type galaxies has been calcium. Commonly measured from the strong absorption feature present at 4227\AA , calcium abundances were found not to track magnesium despite also being an α element. This was highlighted in the early works of Vazdekis et al. (1997) and then further noted with the variable abundance

CHAPTER 1

models of Thomas et al. (2003b). Further works of Schiavon (2007) and Johansson et al. (2012) reported $[\text{Ca}/\text{Fe}]$ values of close to zero from early-type galaxies in the SDSS data. Even more recent studies with the most up-to-date population models also notice this phenomenon (Conroy et al. 2014). However, there are some caveats to the results of the under-abundance of calcium in early-type galaxies. Prochaska et al. (2005) defined a different Ca4227 index, in order to avoid a contamination of the CN4216 molecular band that is present in the blue pseudocontinuum band of the original Lick index. The result of the new index was calcium measurements that were more consistent with known magnesium over-abundances found in early-type galaxies. The carbon sensitivity of the Ca4227 Lick index can be seen in the models of Schiavon (2007) (their Figure 14).

Carbon and Nitrogen abundances can also be probed, due to the presence of molecular features in optical spectra (such as CN and C_2). Lick index studies of these elements in early-type galaxies was performed by Schiavon (2007). It was found that $[\text{C}/\text{Fe}]$ and $[\text{N}/\text{Fe}]$ abundances increase as a function of increasing luminosity. Work has started on creating consistent stellar spectral models with enhancements in both Carbon and Nitrogen (e.g. like those presented in Zamora et al. (2015)), which will allow for population models to be built with more accuracy in the optical and infrared.

Spiral bulges are typically classified according to observational properties, such as surface brightness profiles and bulge to total light ratios (B/T). They are commonly split into two groups - the classical bulges and pseudobulges. Classical bulges tend to have Sérsic indices $n > 2$ and pseudobulges tend to have $n < 2$ (e.g. closer to an exponential profile (Fisher & Drory 2008; Gadotti 2009)). The Sérsic index describes how the surface brightness of a galaxy varies as a function of radius, usually expressed in terms of the half light radius (R_e) and surface brightness at that radius (I_e), such that $I(R) \propto I_e \exp(-b_n(R/R_e)^{1/n})$. b_n here is a constant, usually

CHAPTER 1

defined in terms of n , to describe the shape of the light profile. From studies like those of Erwin et al. (2015) it has been found that pseudobulges appear over all types of spiral galaxy, while classical bulges tend to be found in early-type spirals but are absent in later-types than Sc. As mentioned in Section 1.6, investigation of the stellar populations present in the bulges of spiral galaxies, particularly the information regarding abundance patterns, may shed light on the difference in formation scenarios between the two classes.

1.5 Milky Way Abundances

Studies of abundances and abundance patterns ($[\text{Fe}/\text{H}]$ and $[\alpha/\text{Fe}]$) have been possible on large scales, thanks to studies like the APO Galactic Evolution Experiment (APOGEE; Majewski 2012). This survey investigates ~ 100000 giant stars in a small wavelength region of 1.51-1.70 μm and measures T_{eff} , $\log g$, $[\text{Fe}/\text{H}]$, $[\alpha/\text{Fe}]$ and abundances of 15 other chemical elements in our own Galaxy. The infrared wavelength range of APOGEE, and therefore reduced extinction effects, allows for the assessment of the star formation rate and chemical evolution of the bulge.

Bulge star oxygen abundances measured by Zoccali et al. (2006), Lecureur et al. (2007) and Fulbright et al. (2007) all found $[\text{O}/\text{Fe}]$ values higher than stars in the thick disk (Bensby et al. 2004). This result suggests that the bulge and thick disk components do not have the same chemical evolution or IMF. In contrast to this result, Meléndez et al. (2008) and Alves-Brito et al. (2010) found no difference between $[\text{O}/\text{Fe}]$ for bulge and thick disk giant stars. In general terms, bulge star oxygen abundances as a function of metallicity (from large studies such as García Pérez et al. 2018 and da Silveira et al. 2018) match with the chemical evolution models, by Friaça & Barbuy (2017), with a specific $\text{SFR} = 0.5 \text{ Gyr}^{-1}$. The star formation rate in Friaça & Barbuy (2017) is defined as the inverse of the system formation timescale, defined as the star formation rate (in units of $M_{\odot} \text{ Gyr}^{-1}$)

CHAPTER 1

divided by the mass of gas (in units of M_{\odot}) available for star formation. Magnesium abundances as a function of $[\text{Fe}/\text{H}]$ from McWilliam (2016), Johnson et al. (2014) and Gonzalez et al. (2015) show a clear downward trend past $[\text{Fe}/\text{H}]=0$. This was in disagreement with previous studies (Lecureur et al. 2007 and Bensby et al. 2013) that showed increasing $[\text{Mg}/\text{Fe}]$ with increasing $[\text{Fe}/\text{H}]$. The chemical evolution models of Friaça & Barbuy (2017) also fit the $[\text{Mg}/\text{Fe}]$ plateau at sub-solar $[\text{Fe}/\text{H}]$ trend well, with a specific SFR of 3 Gyr^{-1} . The location of the knee in $[\text{Mg}/\text{Fe}]$ vs $[\text{Fe}/\text{H}]$ however, is better modelled by a specific SFR = 0.5 Gyr^{-1} , consistent with the $[\text{O}/\text{Fe}]$ trends. The knee described here is referring to the location at which the $[\text{Mg}/\text{Fe}]$ vs $[\text{Fe}/\text{H}]$ trends turns over from approximately constant to lower values (e.g. at $[\text{Fe}/\text{H}] \sim -0.75$ in Figure 1.2). This knee is typically interpreted as a tracer of star formation timescale, through the sensitivity of its location to the metal-enrichment achieved by a system before Type Ia supernovae begin contributing to chemical enrichment of the ISM at $\sim 10^8$ - 10^{10} yr (see Section 1.2), compared to the enrichment timescales of Type II supernovae. Systems that have either a poor efficiency of metal production and retention, or not a high star formation rate (SFR) will have a knee at a lower metallicity than a system with a higher SFR or higher production of metals. For example, from resolved star studies of the Sculptor Dwarf Spheroidal, the knee occurs at $[\text{Fe}/\text{H}] \sim -1.8$ (McWilliam & Smecker-Hane 2005; Sbordone et al. 2007)

1.6 Bulges in External Systems

Other than the Milky Way and M31, in which individual stars can be resolved, studies of spiral bulges are limited to integrated stellar population studies. Some of the first works in bulge stellar population analysis (e.g. Balcells & Peletier (1994)) highlighted connections between bulge colour and galaxy luminosity and local surface

CHAPTER 1

brightness. It was found that the more massive, luminous bulges and the higher surface brightness regions, the redder the constituent population. Another interesting discovery was that early-type bulges were as red as elliptical galaxies with little differences between the colours of bulges (Peletier & Balcells 1996), which suggested a connection between the two morphologies. This was interpreted as early-type bulges being the same age as ellipticals and less massive, late-type bulges being younger and possibly more metal poor. The similarities in properties between early-type spiral bulges and elliptical galaxies may imply a similarity of formation process of these types. Spiral bulges have been suggested to be former ellipticals which accrete a disk later on (Classical Bulges, e.g. Barnes & White 1984). Another possibility is a more secular evolution, in which bulges are gradually built from the already existing disk (Disky Bulges, e.g. Sheth et al. 2005). In principle, these two formation scenarios can be distinguished by their star formation histories. Classical bulges form in rapid and efficient bursts of star formation, whereas Disky Bulges (also known as pseudobulges) form in a slower process from the infall of disk material.

A problem with the initial studies, using colours, in constraining the SFH was the age-metallicity degeneracy (see Section 1.1). Redder bulges could be either old and/or metal rich, which makes any interpretation of the formation mechanism from the colour difficult. Typically, the first spectroscopic studies focused on the relation between line-strengths and central velocity dispersion (σ) (e.g. Bender et al. 1993). It was shown that the properties of bulges were similar to that of ellipticals. Studies of Jablonka et al. (1996) found metallicity-luminosity relations and α element over-abundances that were similar to early-type galaxies. Biases of these studies were highlighted (Kormendy & Kennicutt 2004), with the early work investigating mainly early-type spirals. Later studies, that included an age range of bulges, studied the relationship between magnesium sensitive indices and σ and found differences between elliptical galaxies and bulges. Studies found a steepening

CHAPTER 1

of the Mg- σ relation at lower mass bulges (Falc3n-Barroso et al. 2002; Trager et al. 1999; Proctor & Sansom 2002). Figure 18 of Ganda et al. (2007) highlights that the Mg_b- σ relations between late-type bulges and early type galaxies lie parallel to each other. Any differences between late-type bulges and early type galaxies disappear at low σ (Sansom & Northeast 2008).

Complexities in the interpretation of the results explained above are introduced when consideration of the age-metallicity degeneracy is made. This degeneracy may mean that the similarities between index- σ relations of bulges and early-type galaxies do not show a true similarity between the constituent populations. This is because indices like Mg₂ and Mg_b can be higher in older or more metal rich populations. Therefore, there could be large differences between the ages or metallicities of bulges and ellipticals that would not be present in the index measurements if there was such an age-metallicity degeneracy. A typical technique to attempt to break this degeneracy is to combine indices that are sensitive to abundance variations or metallicity with indices that are sensitive to age variations. A typical example of this is a index-index plot of the Mg_b index versus the H β index, which are sensitive to magnesium abundances and age respectively. These measured indices are then compared to predictions of SSP models to obtain properties, such as $[\alpha/\text{Fe}]$ or SSP-equivalent age, of the stellar populations. Studies using this technique showed that bulges spanned a large range in SSP ages of $\approx 2 - 13$ Gyr as well as a trend with SSP age and metallicity and σ (Proctor & Sansom 2002 for E, S0 and Spiral bulges, Peletier et al. 2007). It was found that the more massive bulges were more metal rich, older and have a higher $[\alpha/\text{Fe}]$, all of which agree with relations found in ellipticals. This higher $[\alpha/\text{Fe}]$ is usually interpreted as shorter timescales of star formation. Interestingly, Proctor & Sansom (2002) found a correlation between magnesium and iron with σ , which meant there was no strong correlation with $[\text{Mg}/\text{Fe}]$ and σ in bulges (see their Figure 13). This result is in disagreement

CHAPTER 1

with elliptical galaxy trends.

A limitation of the studies discussed above was that the majority of them investigated only the very centres of the bulges. Studies of the variation in stellar population with radius would allow for more information about the formation of the bulge to be obtained. This would shed light on the dominant processes involved in the formation. Strong gradients in both metallicity and $[\alpha/\text{Fe}]$ would be expected for processes of monolithic collapse (e.g. Eggen et al. 1962; Ferreras & Silk 2002), which would then be flattened by subsequent merger events (White 1980; Mihos & Hernquist 1994). Pseudobulges are more complicated, due to the complex process involved in the redistribution of disk material, but are expected to have lower metallicity gradients than the classical bulge scenario (Moorthy & Holtzman 2006). In more recent years, the study of the radial variation of spectral features and comparison to SSP-equivalent parameters has started. These studies have found that a large majority of the bulges have almost no gradient in age (or slightly positive), slightly positive or zero gradient in $[\alpha/\text{Fe}]$ and negative metallicity gradients (e.g. Jablonka et al. 2007; MacArthur et al. 2009; Sánchez-Blázquez et al. 2011), although the work of Morelli et al. (2016) did find some negative gradients in $[\alpha/\text{Fe}]$, in the bulges of isolated galaxies. The metallicity gradients found in bulges are generally steeper than in the disk region (Moorthy & Holtzman 2006). These results are in agreement with elliptical galaxy findings, in that the gradients in bulges and elliptical galaxies are similar in value (Jablonka et al. 2007; Morelli et al. 2008). Another interesting investigation is the effect of bars on the stellar population gradients. The differences were explored in several studies, all of which found no significant effect (e.g. Moorthy & Holtzman 2006; Pérez & Sánchez-Blázquez 2011). Moorthy & Holtzman 2006 did find that if a slight positive age gradient was found, it was always in barred galaxies. The interpretation of this result was that barred galaxies have extended star formation in the centre, due to the inflow of gas driven by the bar. An

important issue with the interpretation of gradients in bulges is contamination of light from the disk stellar population, which would be most important in the outer regions of the bulge. This can be avoided if edge-on systems are studied (e.g. like that of Jablonka et al. 2007). Another interesting possibility would be the study of the vertical variation in the stellar populations of bulges.

1.7 Initial Mass Functions in Early-Type Galaxies

As mentioned in Section 1.1, a key component of SSP models is the IMF. The first full description of an IMF came with the single power law of Salpeter (1955), which was then developed to the lowest stellar masses through multicomponent power laws (Kroupa et al. 1993) or a combination of a lognormal distribution at the lowest masses and a power law at higher masses (Chabrier 2003). These initial works were based on resolved star studies, where it is possible to directly count and measure masses of individual stars. This type of work has led to the interesting discovery of an almost universal IMF within the Milky Way (Bastian et al. 2010). For external systems that are too distant to resolve on a star-by-star basis, techniques that can be used via unresolved stellar population analysis (e.g. SSP analysis) are required. The low-mass end of the IMF of nearby galaxies can be constrained via gravity-sensitive spectral features that can indicate the ratio of dwarf to giant stars in a population. One of the first types of this work was by Spinrad & Taylor (1971) for the nuclei of M31, M32 and M81. Interestingly, the best-fitting models of this work suggested a deviation from the Salpeter (1955) IMF in the centre of M31, with a dwarf-enriched main sequence. This result was confirmed by the work of Faber & French (1980), who also found a bottom-heavy IMF using the gravity-sensitive Na 8190 line. Investigation of the near-IR also suggested concentrations of metal-rich dwarf stars in the centre of massive galaxies (e.g. Carter et al. 1986). There are gravity-sensitive indices in many wavelength regimes, that can be used

CHAPTER 1

to probe the IMF. Two of the most commonly used gravity-sensitive features in the optical wavelength range are the sodium doublet (NaD) and TiO_2 ⁶ (Trager et al. 1998). In longer wavelengths, there are also IMF sensitive features, such as Na8190 (e.g. used in the previously mentioned work as well as in La Barbera et al. 2013), Na1.14 and Na2.21 (Conroy & van Dokkum 2012). Another useful indicator is the Wing-Ford band at $\approx 9800\text{-}10250\text{\AA}$, originally proposed as a mass-function probe in old stellar populations by Whitford (1977). Some of the first works in the comparison of models to observations of the strength of the Wing-Ford band in the bulges of ellipticals also suggested a bottom-heavy IMF in those systems (Hardy 1990). Some recent examples of using gravity-sensitive spectral features can be found in Cenarro et al. (2003), van Dokkum & Conroy (2010) and La Barbera et al. (2013). Another method to constrain the IMF is through measures of the stellar mass-light (M/L) ratio through dynamical analyses (e.g. Treu et al. 2010; Cappellari et al. 2012). The first method mentioned, using spectral features, is the one of interest to this thesis, but in an ideal scenario both methods would be used together to probe the IMF (e.g. Lyubenova et al. 2016) and should produce results in agreement with one another. Interestingly, when comparing dynamical and spectroscopic constraints, Smith (2014) showed that on average both methods are in agreement in the conclusion of the presence of bottom-heavy IMFs in early-type galaxies. However, on a galaxy-by-galaxy basis there is no correlation between the two methods. More recently, a study of two elliptical galaxies found that both the dynamical and spectroscopic approaches suggest a Milky-Way IMF and also rule out a very bottom-heavy IMF (Smith et al. 2015).

A major problem that affects the spectral analysis of IMF variations comes with the sensitivity of indices to other factors, particularly abundance pattern - not only are these indices affected by the dwarf to giant ratio, but also the $[\alpha/\text{Fe}]$ and

⁶It is worthwhile noting here that strictly speaking TiO_2 is not a direct gravity-sensitive index, but is indirectly sensitive to the IMF via a strong sensitivity to effective temperature.

CHAPTER 1

[Na/Fe] abundances of the underlying stellar populations. This means that non-solar abundance pattern SSPs are required for a full analysis, which can not be done in a fully empirical way, as explained in Section 1.3. This problem has started to be addressed through variable abundance pattern and IMF SSP calculations such as those in Conroy & van Dokkum (2012). This thesis builds upon the work and methodology of La Barbera et al. (2017), which focused on SSP analysis with variable sodium abundances and IMFs. I generate a library of semi-empirical stellar spectra that has variable $[\alpha/\text{Fe}]$ abundances, with the method described in La Barbera et al. (2017), that can then be used to generate SSPs. The variation of $[\alpha/\text{Fe}]$ is known to be difficult to model in certain star types, discussed in Chapter 2. Sodium is easier to model because its impact on atmospheric structure is expected to be small due to Na producing limited opacity and due to it contributing electrons in the outermost layers of the coolest stars only (as shown in the models of Mészáros et al. 2012), meaning that it can be varied in the spectral synthesis component only (see Chapter 3). However, Conroy & van Dokkum (2012) show that sodium is an important electron contributor in their late-type giant and dwarf models. This results in sodium indirectly affecting the strength of many spectral features through its effect on the ionization balance of other species, as well as having significant impact on the temperature structure of the atmosphere through contributions to the H^- opacity. The work of this thesis will be an intermediate stage in a final stellar spectral library that varies $[\alpha/\text{Fe}]$ and $[\text{Na}/\text{Fe}]$ for use in SSP modelling.

1.8 Composite Populations and Galactic Chemical Evolution

Whilst this thesis is focused on building and improving SSPs, it is worth to note that this concept is limited by the assumption that SSPs are a population of stars

CHAPTER 1

with the same chemical composition and age, assumed to be born in a single instantaneous burst of star formation, which would not be fully representative of a galaxy's evolution.

More realistic models of stellar populations in galaxies would include some description of the system's chemical evolution caused by the enrichment of the interstellar medium, as well as stars with differing ages represented by a star formation history (SFHs). Composite Stellar Populations (CSPs) allow for the possibility of SFHs, with star formation occurring over non-instantaneous time scales, through combinations of SSPs that have different ages and initial chemical compositions. Such populations can be found within the Milky Way, with the presence of both young and old populations evident in the thin disc and halo respectively.

Galactic Chemical Evolution (GCE) takes the modelling a step further, through tracing how the gas in a system chemically changes with time due to stellar evolution and external sources of gas inflow. GCE requires the use of multiple SSPs and a description of the gas evolution. Below I briefly discuss some simple cases of GCE models.

A key parameter needed for a description of a consistent GCE and CSP model is the Star Formation Rate (SFR). If the model is that of a closed-box, the SFR gives the time evolution of the amount of stars formed and the resulting chemical evolution will lead to an Age-Metallicity Relation (AMR). An AMR is a direct result of a closed-boxed GCE model, and will provide a description of how the chemical composition of the SSPs representing different stellar populations in a galaxy will change with their age. The combination of these two parameters is the definition of the Star Formation History (SFH) of the system, where SFH is a function of both the SFR and AMR (e.g. Salaris & Cassisi 2005). It is worth noting that the SFR and AMR are intimately connected - each generation of stars will add chemically enriched gas to the ISM, through processes mentioned in Section 1.2.

CHAPTER 1

In a more realistic GCE model, that may not necessarily be a closed-box, the SFR and the IMF are ideally known. If the accretion and loss of the gas in the system are also known, consideration of stellar evolution calculations then provide the chemical evolution of the gas for each generation of stars and the chemistry of the inflow and outflow gas. The time-dependent quantities that need to be calculated are the gas mass, $g(t)$, the mass locked in stars, $s(t)$, and the mass fraction of the element i , $X_i(t)$. The chemical evolution of the gas is then tracked from the following equations. The total mass of the entire system is the summation of the gas and star mass:

$$M(t) = g(t) + s(t). \quad (1.2)$$

The change of total mass with time will be dependent on the rate of gas injected into the system from outside, $F(t)$, and the rate of gas leaving the system, $E(t)$.

$$dM(t)/dt = F(t) - E(t). \quad (1.3)$$

The evolution of $g(t)$ will depend on $F(t)$ and $E(t)$, but also the amount of gas leaving stars into the ISM, $e(t)$, and the SFR (which locks up mass):

$$dg(t)/dt = F(t) - E(t) + e(t) - \text{SFR}. \quad (1.4)$$

The mass locked in stars will be dependent on the SFR as well as the mass leaving stars:

$$ds(t)/dt = \text{SFR} - e(t) \quad (1.5)$$

With these defined, the time evolution of the mass fraction of element i can be found by the balance of the mass of element i ejected from stars, $e_i(t)$, the mass of element locked into stars, $X_i(t)\text{SFR}$, the mass of element i coming from material entering the system, $X_f(t)F(t)$, and the mass of element i leaving the system $X_i(t)E(t)$ (Salaris & Cassisi 2005) :

$$d(g(t)X_i(t))/dt = e_i(t) - X_i(t)\text{SFR} + X_f(t)F(t) - X_i(t)E(t) \quad (1.6)$$

CHAPTER 1

The complications with this problem arise due to the lack of prior knowledge of the SFR (and also the IMF). A typical approach to this issue is to assume an SFR, and several functional forms of this assumption have been taken throughout the literature. One of the oldest and most popular forms is the exponential model ($\text{SFR} \propto e^{-t/\tau}$), originating from closed-box models (Schmidt 1959), in which no gas leaves or enters the system. Exponential SFRs have been shown to be invalid in many cases, such as elliptical galaxies (e.g. Proctor & Sansom 2002). More recently, from studies of high-redshift galaxies, models in which the SFR increases with time have been used to explain galaxy evolution in the early universe (Maraston et al. 2010; Lee et al. 2010). A more complex model that could be used to explain all phases of galactic evolution may consist of some rising SFR component at early times with a decay component dominating at later times. A fully GCE model requires combinations of SSPs and gas evolution calculations. The ideas described here and in Section 1.2 aid the interpretation of SSP-fitting, which does not require the fully consistent approach described in this section.

This thesis is split as follows. Chapter 2 presents the testing of theoretical stellar spectra. Chapter 3 presents the generation and testing of a new high-resolution theoretical stellar library. Chapter 4 presents the generation of the semi-empirical stellar library and computation of new SSP spectra. Chapter 5 presents the initial testing of the SSPs and a demonstration of an application for them to stacked SDSS spectra of satellite galaxies. Chapter 6 presents the final summary and conclusions, including future possibilities.

Chapter 2

Testing Theoretical Stellar Spectra

2.1 Introduction

Differentially correcting empirical stellar spectra relies on the accuracy of the theoretical stellar spectra used. With a large number of models currently available, each with their own set of advantages, assumptions and limitations, deciding which synthetic spectra to use is difficult. In this chapter, we test the predictions of three stellar spectral model libraries against empirical star data in the context of abundance patterns, with the aim of highlighting current strengths and weaknesses of the models. These models represent some of the most recent works in stellar population analysis, covering a broad range of parameter space, suitable for modelling integrated stellar populations. This work expands on Sansom et al. (2013), testing more state-of-the-art theoretical stellar spectral models.

This chapter is a reduced version of an accepted publication in MNRAS (Knowles et al. 2019) and the structure is as follows. Section 2.2 describes the three models of stellar spectra that are tested in this study. Section 2.3 outlines the MILES empirical spectra used in the comparison. In Section 2.4 we directly compare Lick indices of MILES stars to those predicted from theoretical stellar spectra. Section 2.5 presents a differential approach, using response functions, in which we compare

normalised Lick indices¹ from empirical MILES stars to those predicted from theoretical response functions. Section 2.6 discusses the findings and possible physical reasons for model disagreements, through analysis of both indices and full spectra. Section 2.7 presents our conclusions.

2.2 Models of Stellar Spectra

Throughout this chapter we will be using three model libraries of stellar spectra, produced by three independent authors, to test responses of the models to changes in abundance pattern, relative to solar. The models we have chosen are state-of-the-art in the context of stellar population analyses from integrated light. They have been created for use in stellar population modelling, covering a wide range of stellar parameters and abundance patterns. Some recent works applying these models can be found in Conroy et al. (2014), Vazdekis et al. (2015), and Holtzman et al. (2015). These models built on the first predictions of SSP spectra with abundance variations from the works of Coelho et al. (2007), Prugniel et al. (2007), Percival et al. (2009), Lee et al. (2009). All of these works predict the spectra of stellar populations with abundance variations, rather than the classical approach of predicting indices. This section describes and outlines the various codes and parameters used in the production of the theoretical stellar spectra from each of three modellers.

Generation of synthetic spectra requires two main steps. Firstly, calculation of the model atmosphere provides a mathematical model describing the variation of physical parameters such as density, temperature and pressure as a function of radial depth, for an assumed star type and composition. The second step is to pass photons through the generated atmosphere to compute an emergent spectrum. This requires

¹In this work the indices we test are not technically Lick indices, because they are not measured at the resolution of Lick spectra ($\sim 9\text{\AA}$ in Burstein et al. 1984; Faber et al. 1985). We use the term ‘Lick’ to refer to the 25 optical absorption-line indices defined in that system.

CHAPTER 2

the use of a synthetic spectrum code together with a list of line and molecular absorption transitions and a specification of element abundances. The self-consistent approach to generate a theoretical stellar spectrum would be to exactly match the abundances in both steps of the production. To reduce computational time, a simplification is made in which only the dominant sources of opacity are varied in the model atmosphere whilst more elements are varied in the synthetic spectrum. However if one uses ATLAS12 (Kurucz 1996) or OMARCS (Gustafsson et al. 2008) model atmosphere codes, it is possible to have the same abundance pattern in both components of the spectrum generation.

One of the most commonly used codes to generate model atmospheres is ATLAS (Kurucz 1979b and updates), a one dimensional, local thermodynamic equilibrium and plane-parallel code. The original code provides a base on which developments have been made, e.g. ATLAS9 (Kurucz 1993) and ATLAS12 (Kurucz 2005; Castelli 2005a). An important effect in the generation of stellar photospheres is the line opacity due to atomic (and molecular) line absorption. Line opacity depends on temperature, pressure, chemical composition and microturbulence (v_{turb}). Statistical methods were developed to deal with the vast number of lines present in stellar atmospheres. The method implemented provides one of the biggest differences between the versions of the ATLAS code. ATLAS9 uses Opacity Distribution Functions (ODFs) as an approach to this problem. ODFs treat the line opacities in a given frequency interval by a smoothly varying function. The ODFs have to be computed for a particular abundance pattern prior to generating the model atmospheres. ATLAS12 uses the Opacity Sampling method (OS) to compute the line opacity at a number of frequency points.

Another important parameter in the computation of stellar spectra is v_{turb} . This microturbulence has a large impact on strong or saturated lines, and therefore the choice of this parameter when calculating a synthetic spectrum will affect the

CHAPTER 2

resulting line-strengths. In order to gain an understanding of line-strength uncertainties involved with the v_{turb} parameter, we produced several models changing v_{turb} (see Section 2.4).

In this chapter we test three star types with varying element abundances, that represent Cool Dwarf (CD) ($T_{\text{eff}}=4575\text{K}$, $\log g=4.60$ dex), Cool Giant (CG) ($T_{\text{eff}}=4255\text{K}$, $\log g=1.90$ dex) and Turn-off (TO) ($T_{\text{eff}}=6200\text{K}$, $\log g=4.10$ dex) stars with the same parameters as in Korn et al. (2005) and the analysis of Sansom et al. (2013). These star types are chosen as they are representative of stars present in older stellar populations that future work will focus on, using results from this study.

Below we specify the codes used by the three modellers to produce spectra, the wavelength range, sampling, elements varied and stellar parameters used. Table 2.1 summarises this information. All models assume that the α -capture group elements are O, Ne, Mg, Si, Ca and Ti, unless otherwise stated. Spectra with abundance patterns of Solar and those in Table 2.2 were provided. Table 2.2 summarises the T_{eff} , $\log g$ and element enhancements provided by each modeller, for use in Section 5. The $[M/H]$ value in Table 2.2 is defined as a scaled metallicity.

Table 2.1: Codes and parameters used by the three modellers when generating their theoretical spectra. These parameters are for spectra used in the derivation of response functions in Section 2.5. In the final column we specify the consistency of abundance specification between the model atmosphere (MA) generation and radiative transfer (RT) process.

Model	Atmosphere Code	Synthetic Spectrum Code	Wavelength Range (Å)	Sampling ($\Delta \log \lambda(\text{Å})$)	vturb (kms ⁻¹)	Solar Abundance Reference	MA + RT Compatible
Couroy	ATLAS12	SYNTHE	3700-10000	2.17×10^{-5}	2	Asplund 2009	Yes
Coelho	ATLAS12	SYNTHE	2995-8005	1.4×10^{-6}	2	Grevesse & Sauval 1998	Yes
Allende Prieto (CAP)	ATLAS9	ASScT	1200-30000	6×10^{-7}	1.5	Asplund 2005	Yes (C, M, α)

Table 2.2: T_{eff} , $\log g$ and element enhancements above solar (0.3 dex unless stated otherwise) for the three star types, provided by the modellers for the response function analysis in Section 2.5. The $[M/H]$ column in this table is for the specific case of all metals increased by 0.3 dex.

Model	T_{eff} (CD,CG,TO) (K)	$\log g$ (CD,CG,TO) (dex)	C	N	O	Mg	Fe	Ca	Na	Si	Cr	Ti	$[M/H]$
Conroy	4500,4250,6150	4.60,1.94,4.06	✓(0.15 dex)	✓	x	✓	✓	✓	✓	✓	✓	✓	✓
Coelho	4575,4255,6200	4.60,1.90,4.10	✓	✓	✓	✓	x	✓	x	x	x	x	✓
CAP	4575,4255,6200	4.60,1.90,4.10	✓	✓	✓	✓	✓	✓	✓	✓	✓	✓	✓

2.2.1 Conroy

Theoretical star spectra from Conroy were calculated using the ATLAS12 atmosphere code and SYNTHE (Kurucz & Avrett 1981) spectral synthesis package. Groups of Cool Dwarf, Cool Giant and Turn-off star spectra were calculated with a wavelength range of 3700-10000 Å and sampling of $\Delta \log \lambda(\text{Å}) = 2.17 \times 10^{-5}$. It is worth highlighting here that only spectra with a C+0.15 dex variation (compared with C+0.3 dex of the other two authors) were provided, which will impact on the derived responses for indices that are particularly sensitive to carbon abundances. The reason for this was to avoid the generation of Carbon stars. The solar abundances adopted in the model atmosphere and synthetic spectrum code were from Asplund et al. (2009). Note that the stellar parameters used in producing the model atmospheres were slightly different than the parameters of the other two modellers. This was because these models already existed prior to the current work, rather than being created specifically for this project (as in the other two cases). Further description of the stellar spectral models can be found in Conroy & van Dokkum (2012). Please note that the native resolution and wavelength range of the models presented in Conroy & van Dokkum (2012) is higher than given in Table 2.1, but the spectra were down-sampled and cut at 10000 Å. The line lists used in the production of Conroy’s models are described in Conroy & van Dokkum (2012) and are based on lists compiled by Kurucz ². Some of the differences between the three models seen in Sections 4 and 5 may be explained by the inclusion of predicted lines (PLs) in Conroy models that are not present in the other two model libraries. The PLs were included in the Conroy models provided because they were generated for other applications, particularly to compute broad band colours, which are known to be underestimated if PLs are missing (e.g. Section 3 of Coelho 2014 and Section 3.2 of Coelho et al. 2007). Most of the PLs are weak, and therefore contribute to the

²<http://kurucz.harvard.edu>

CHAPTER 2

overall continuum shape. However, there are cases of strong PLs that produce lines that disagree with observations, particularly in the bluer parts of the spectrum (see bottom panel of Figure 2.2 and Figure 3 of Munari et al. 2005 as well as Figures 7-18 of Bell et al. 1994). The PLs affect the absolute comparisons more than the differential comparisons.

2.2.2 Coelho

Theoretical star spectra provided by Coelho used both the ATLAS12 model atmosphere code and SYNTHE (Kurucz & Avrett 1981; Sbordone et al. 2004) spectral synthesis code to generate groups of spectra for a Cool Dwarf, Cool Giant and Turn-off star. The original wavelength range of the spectra was 3000-8005 Å with a sampling of $\Delta \log \lambda(\text{Å}) = 1.4 \times 10^{-6}$. The solar abundances used in the model atmosphere and synthetic spectrum code were those of Grevesse & Sauval (1998). These models are different from those previously published by Coelho, which were based on ATLAS9 (Coelho 2014). The atomic line lists used in Coelho's models are a combination of lists from Coelho et al. (2005), Castelli (2005a) and Castelli (2005b). In the present work we adopt the same molecular opacities as in Coelho (2014), with the following updates³: C₂ D-A (from Brooke et al. 2013, CH (from Jorgensen et al. 1996, with energy levels substituted from Zachwieja 1995, Zachwieja 1997, Colin & Bernath 2010, Bembenek et al. 1997, Kepa et al. 1996), and CN A-X and B-X (from Brooke et al. 2014). During the progress of the present work, we identified that the file regarding the transition D-A of the molecule C₂ used in Coelho (2014) was corrupted. We therefore warn that the predictions of that library around the main C₂ features should be taken with care. This is illustrated in Section 2.6.3, where we compare the corrupted and corrected models. This corruption is likely to be the

³As made available by R. Kurucz; downloaded on Dec 2016 from <http://kurucz.harvard.edu/molecules.html>

CHAPTER 2

origin of the strong missing opacity around 4000 Å in the second panel of Figure 10 in Coelho (2014), which can be attributed to Swan Bands. Note that this problem did not affect earlier models, including Coelho et al. (2005), Coelho et al. (2007) nor Vazdekis et al. (2015).

2.2.3 Allende Prieto

The spectra provided by Allende Prieto (hereafter referred to as CAP) were made using the ATLAS9 model atmosphere code along with the ASS ϵ T (Koesterke 2009) spectral synthesis software, used in 1-D. The wavelength range of the spectra was 1200-30000 Å with a sampling of $\Delta \log \lambda(\text{Å}) = 6.5 \times 10^{-7}$. The solar abundances used in both the model atmosphere and synthetic spectrum code was that of Asplund et al. (2005). Further details of the models can be found in Allende Prieto et al. (2014). The line lists used in the CAP models are detailed in Mészáros et al. (2012) and are based on Kurucz lists.

For the CAP models that we generate for Section 2.4, we use ATLAS9. We direct interested readers to Mészáros et al. (2012) and webpages for the ATLAS-APOGEE survey analysis ⁴ for further information on the ODFs and models used in this analysis. Currently for ATLAS9, the ODFs publicly available from the ATLAS-APOGEE website provide a range of abundances in $[M/H]$, $[\alpha/M]$ and $[C/M]$. $[M/H]$ here is defined as a scaled metallicity. This definition means elements with $Z > 2$ are all scaled together e.g. $[M/H]=0.2$ means $[Fe/H]=0.2=[X/H]$, where $X=3,4,\dots,99$. Note that with these definitions, $[M/H]$ represents all elements other than the α -capture elements if there is an α enhancement or deficiency (e.g. if $[M/H]=0.2$ and $[\alpha/M]=0.1$, this means that $[\alpha/H]=0.3$ and $[Fe/H]=0.2$).

⁴<http://www.iac.es/proyecto/ATLAS-APOGEE/>

2.3 Empirical Stellar Spectra

The empirical data are from the Medium resolution Isaac Newton Library of Empirical Spectra (MILES) (Sánchez-Blázquez et al. 2006). Whilst stars from our Galaxy do not cover the full parameter range of stars in other galaxies, they do cover a broad range in stellar parameters. These empirical spectra have a wavelength range of 3500-7500Å, resolution (FWHM) of 2.5Å and sampling of 0.9Å (Falcón-Barroso et al. 2011). They have a typical signal-to-noise of over 100 Å⁻¹, apart from stars which are members of globular clusters. Of the 985 stars in MILES, Milone et al. (2011) measured the [Mg/Fe] abundances for 752 stars. We use their [Mg/Fe] measurement as a proxy for all [α /Fe] abundances in these stars. Therefore MILES is a stellar library for which we know attributes of effective temperature (T_{eff}), surface gravity ($\log g$), metallicity ([Fe/H]) and abundance ratios ([α /Fe]) for a large proportion of the whole library. This, with the MILES spectra, allows us a uniformly calibrated dataset of stars to test theoretical spectra. We initially use a sub-sample of 51 of the 752 stars that matched the T_{eff} and $\log g$ parameters of the three theoretical stars described in Section 2.2, within the observational errors. Stars were chosen that were within $\Delta T_{\text{eff}} \leq \pm 100\text{K}$, $\Delta \log g \leq \pm 0.2$ of the Cenarro et al. (2007) atmospheric parameters, for three specific star types. These limits led to a sample of 7 Cool Dwarfs, 13 Cool Giants and 31 Turn-off stars with a variety of [Mg/Fe] values (see Sansom et al. 2013, Table A1 for details of these individual star parameters and Lick indices). Therefore we have both MILES spectra and their Lick indices available for testing. Whilst full spectrum fitting has become increasingly popular for stellar population analysis in recent years, Lick indices are useful for testing properties of theoretical spectra against observations because they focus on the strongest spectral features. We use the T_{eff} , $\log g$, [Fe/H] and [Mg/Fe] values of the MILES stars presented in Table A1 of Sansom et al. (2013), based on parameters in Cenarro et al. (2007), unless stated otherwise. The errors on the measured MILES

Lick indices were computed by Sánchez-Blázquez (priv comm.), from the error spectra obtained by propagating uncertainties throughout the reductions, including flux and wavelength calibration, as well as the errors in the velocity calculations, for each star.

2.4 Direct Comparisons

The first test we perform directly compares MILES and theoretical star Lick indices. New models are generated that match the MILES stars exactly in T_{eff} , $\log g$, $[\text{Fe}/\text{H}]$ and $[\alpha/\text{Fe}]$ for Coelho and CAP models. The theoretical spectra were degraded to the MILES resolution of $\text{FWHM}=2.5\text{\AA}$ (Falcón-Barroso et al. 2011) using a convolution code produced in python and then resampled to match existing MILES sampling of 0.9\AA . The line spread function adopted in the convolution code was a Gaussian kernel, that extended to 3σ , of decreasing FWHM with wavelength in order to convert the theoretical spectra from fixed resolving power to fixed FWHM. Indices are then measured for both the MILES stars and corresponding theoretical star using LECTOR software (Vazdekis 2011). This approach of directly producing models was made for both the Coelho and CAP models, to compare to the subsample of 51 MILES stars, described in Section 2.3. Rather than generating models directly for this comparison, spectra were created for Conroy models using an interpolation within a pre-existing grid presented in Conroy & van Dokkum (2012). 4 of the 51 MILES stars fell outside of the parameter range in the grid and were therefore not modelled for Conroy in this comparison. The missing stars were 3 Turn-off stars (HD084937, HD338529, BD+092190) and 1 cool giant star (HD131430). Although this direct comparison will assess the absolute behaviour of models, the main purpose of this test is to look for trends between models rather than absolute agreement between models and empirical data. The absolute test we perform here will aid the assessment of the differential test performed in Section 5.

CHAPTER 2

The available measured MILES star parameters are T_{eff} , $\log g$, $[\text{Fe}/\text{H}]$ and $[\text{Mg}/\text{Fe}]$. CAP models, are generated by specifying T_{eff} , $\log g$, $[\text{M}/\text{H}]$, $[\alpha/\text{M}]$ and $[\text{C}/\text{M}]$ and v_{turb} . Therefore, conversions from MILES parameters to the model parameters are required, in addition to assumptions of $[\text{C}/\text{M}]$ and v_{turb} for the empirical stars. The choice of v_{turb} to use in the models is explained in Section 4.1 and the conversion process is described in Section 4.2.

2.4.1 Microturbulent Velocity

To investigate the effects of microturbulent velocity on the differential application of theoretical line-strengths, 3 different star models were produced using the codes of Allende Prieto et al. (2014). For each base star type (Cool Dwarf, Cool Giant and Turn-off), we produced an $[\alpha/\text{M}] = 0.25$ dex and a $[\alpha/\text{M}] = 0$ dex spectrum at $v_{\text{turb}} = 1$ km/s (v_1) and 2 km/s (v_2). All the models were produced with the same initial sampling of $\Delta \log \lambda (\text{\AA}) = 0.025$ (at 3000 \AA) to isolate the effects of v_{turb} . The models were blurred to MILES FWHM of 2.5 \AA and resampled to MILES linear sampling of 0.9 \AA using the same procedure as described previously. LECTOR was then used to compute the line-strengths. To assess the differential effect, we took a difference of line-strengths through:

$$\left(v_2 \left(\left[\frac{\alpha}{M} \right] = 0.25 \right) - v_2(\odot) \right) - \left(v_1 \left(\left[\frac{\alpha}{M} \right] = 0.25 \right) - v_1(\odot) \right), \quad (2.1)$$

where v_i represents the spectrum with $v_{\text{turb}} = i$ km/s. Indices measured in the model spectra as well as index differences are shown in Table 2.3.

CHAPTER 2

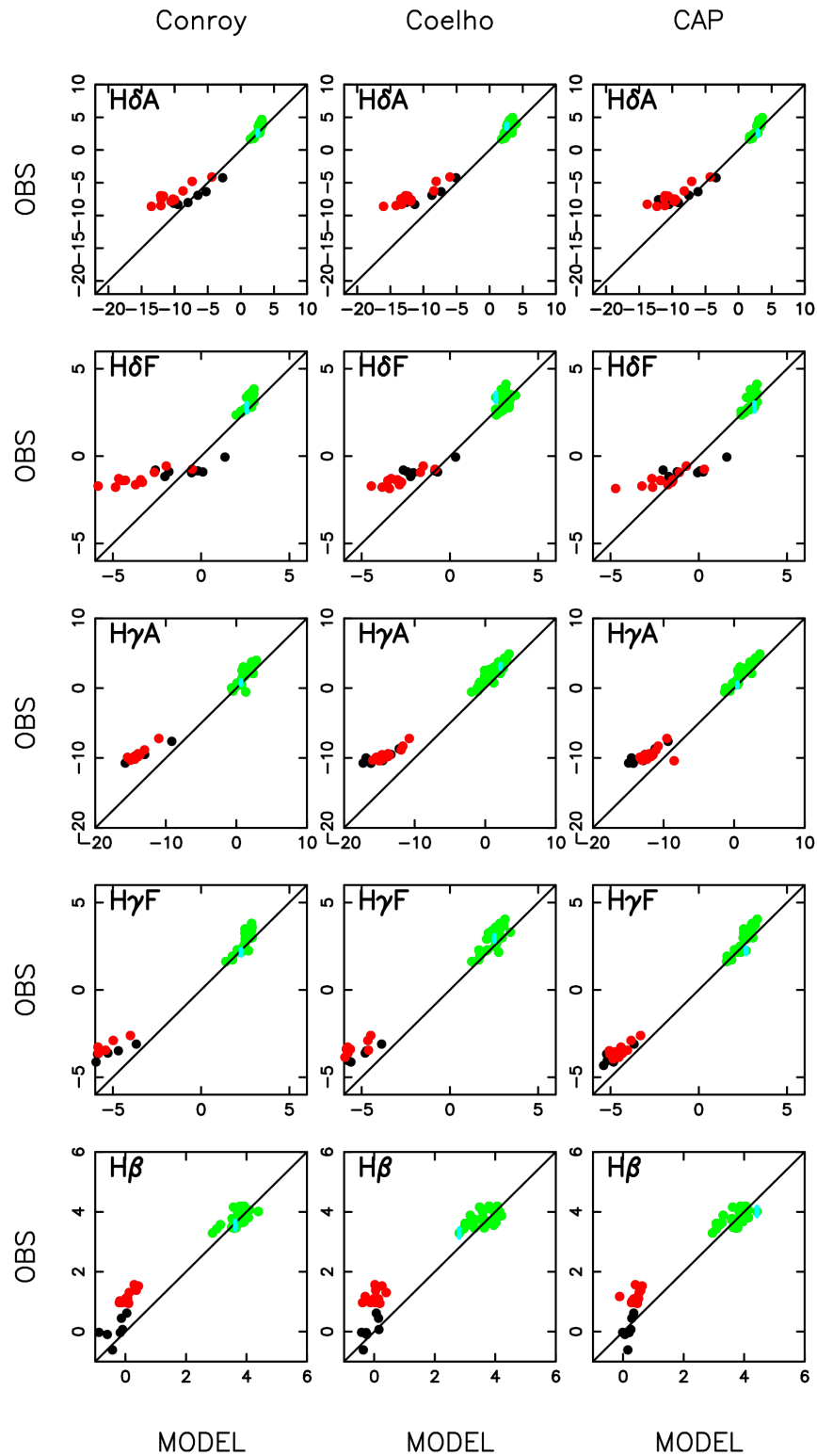


Figure 2.1: MILES Lick Indices versus Model Lick Indices, for Conroy, Coelho and Allende Prieto (CAP) theoretical spectra that match the MILES atmospheric parameters given in Cenarro et al. (2007), for hydrogen-sensitive features. The three star types are shown in each case, with green, black and red circles representing Turn-off, Cool Dwarf and Cool Giant stars respectively.

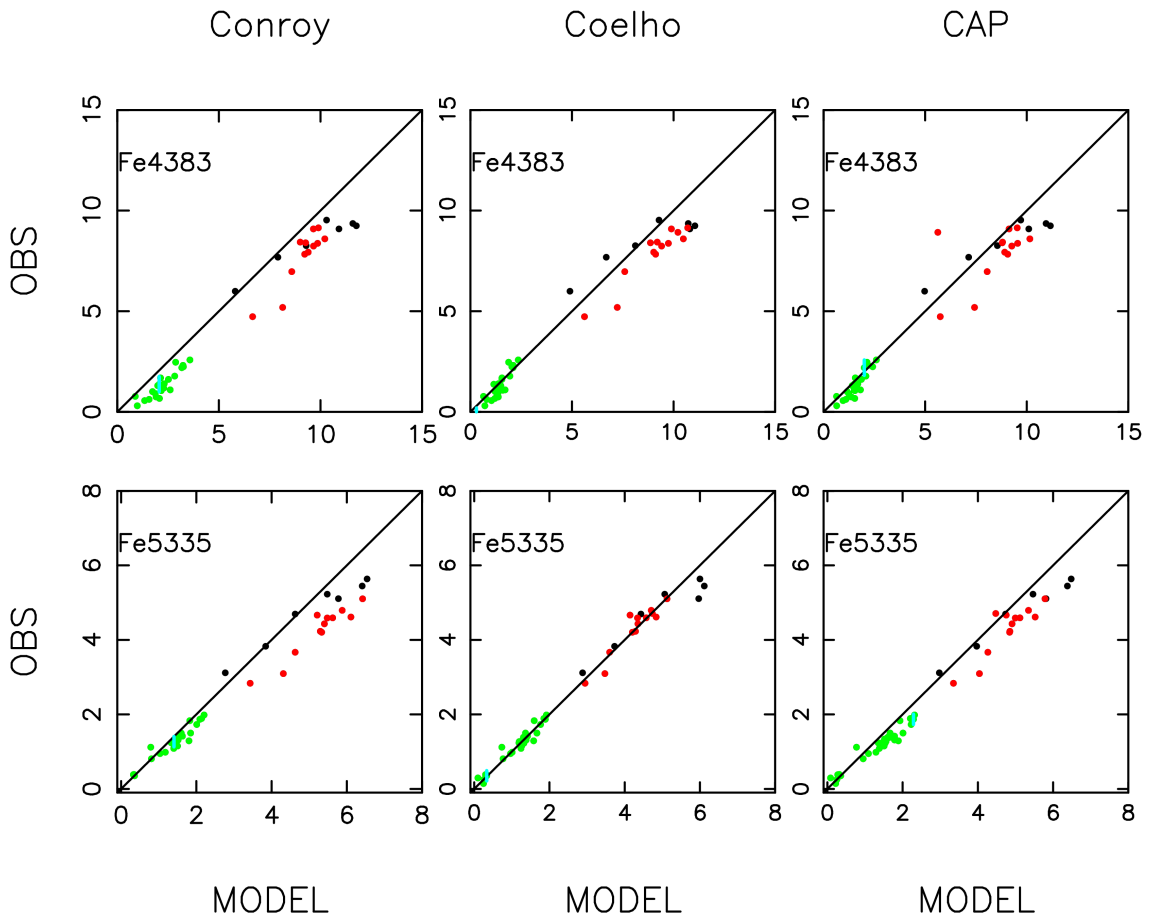


Figure 2.2: MILES Lick Indices versus Model Lick Indices, for Conroy, Coelho and Allende Prieto (CAP) theoretical spectra respectively, for iron-sensitive features. Same parameters and labelling procedure as Figure 2.1.

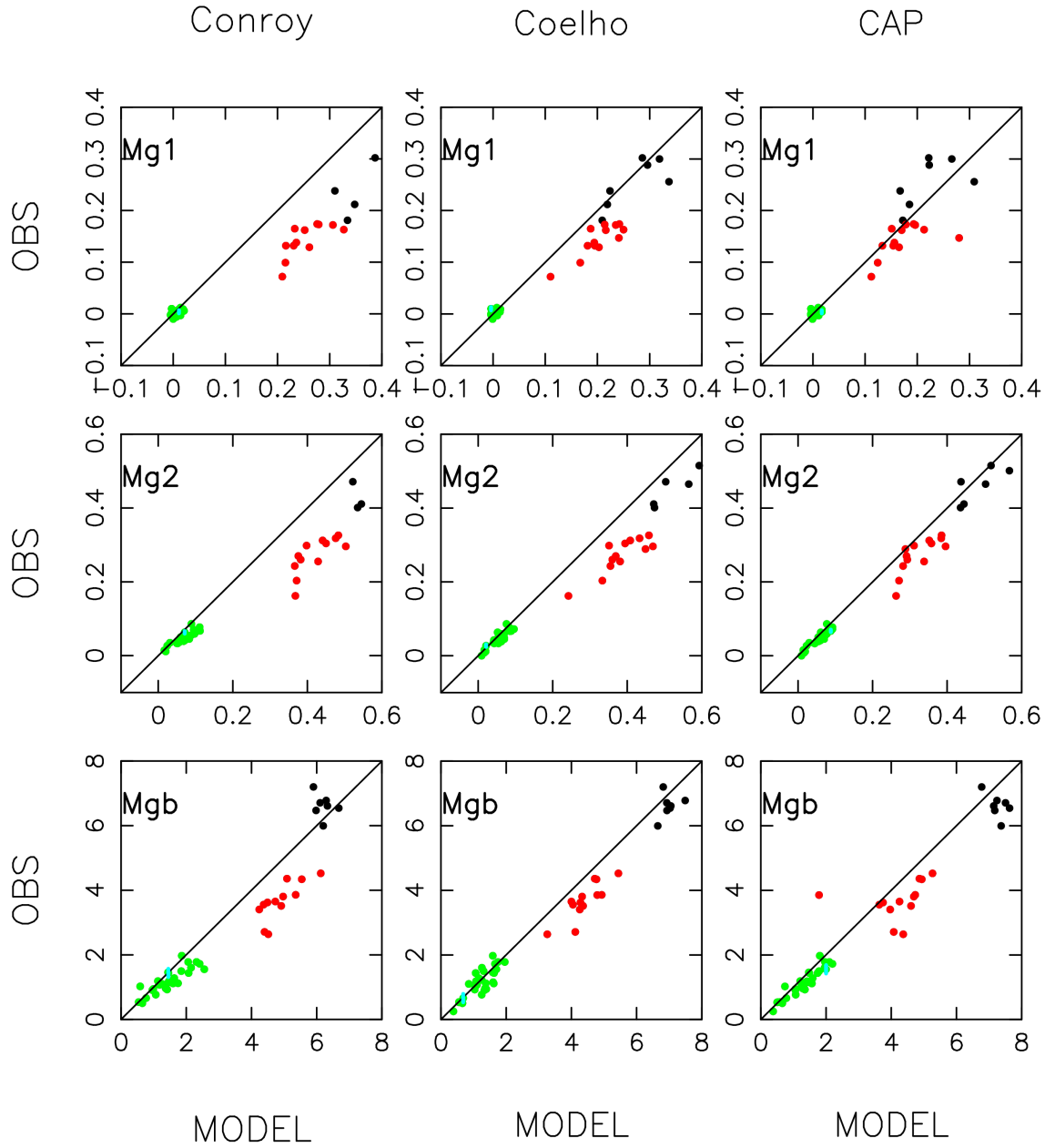


Figure 2.3: MILES Lick Indices versus Model Lick Indices, for Conroy, Coelho and Allende Prieto (CAP) theoretical spectra respectively, for magnesium-sensitive features. Same parameters and labelling procedure as Figure 2.1.

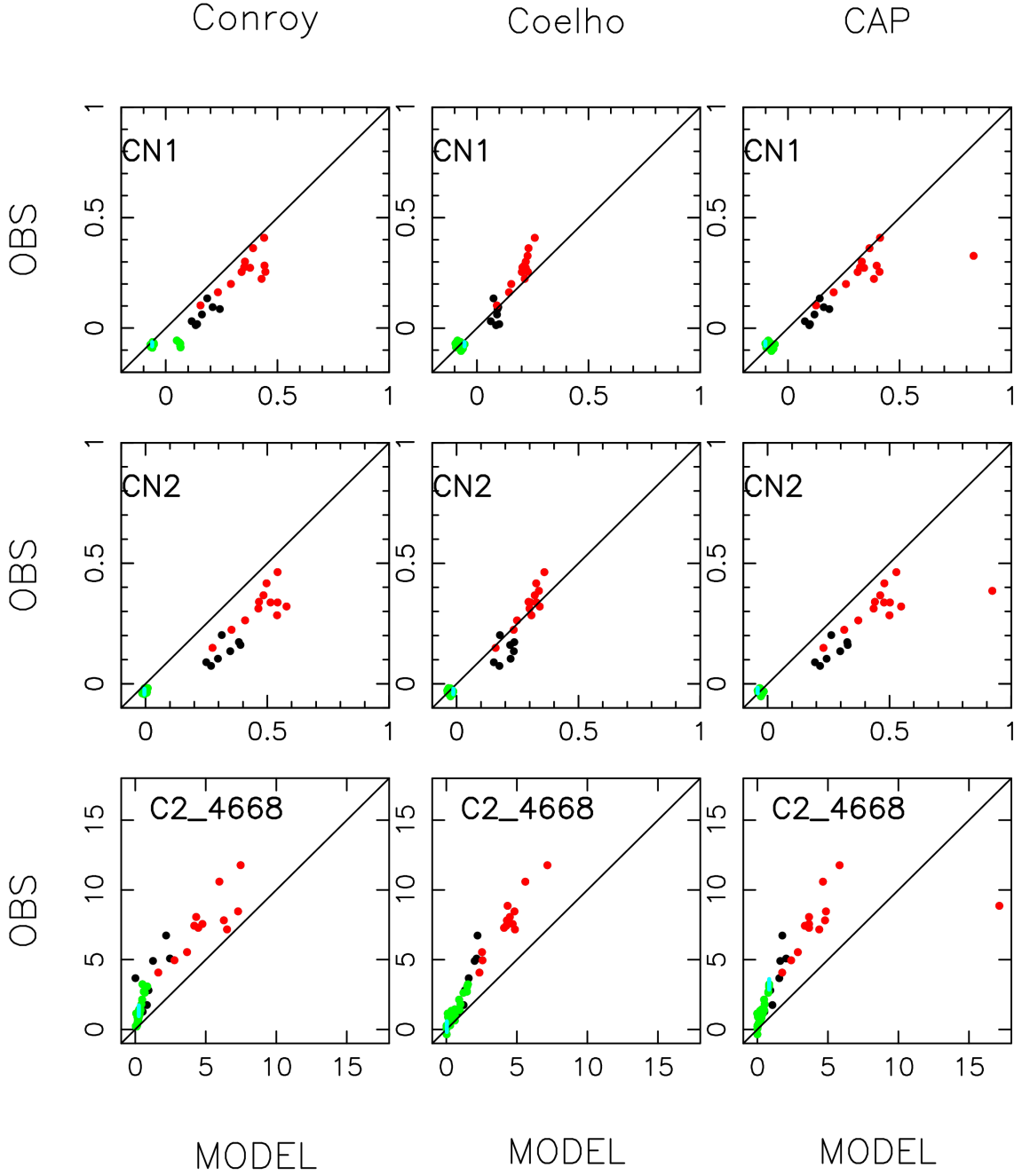


Figure 2.4: MILES Lick Indices versus Model Lick Indices, for Conroy, Coelho and Allende Prieto (CAP) theoretical spectra respectively, for carbon-sensitive features. Same parameters and labelling procedure as Figure 2.1. The outlier point in the CAP model plots is HD131430, with parameters $T_{\text{eff}}=4190\text{K}$, $\log g = 1.95$, $[\text{Fe}/\text{H}]=0.1$ and $[\text{Mg}/\text{Fe}]=-0.398$.

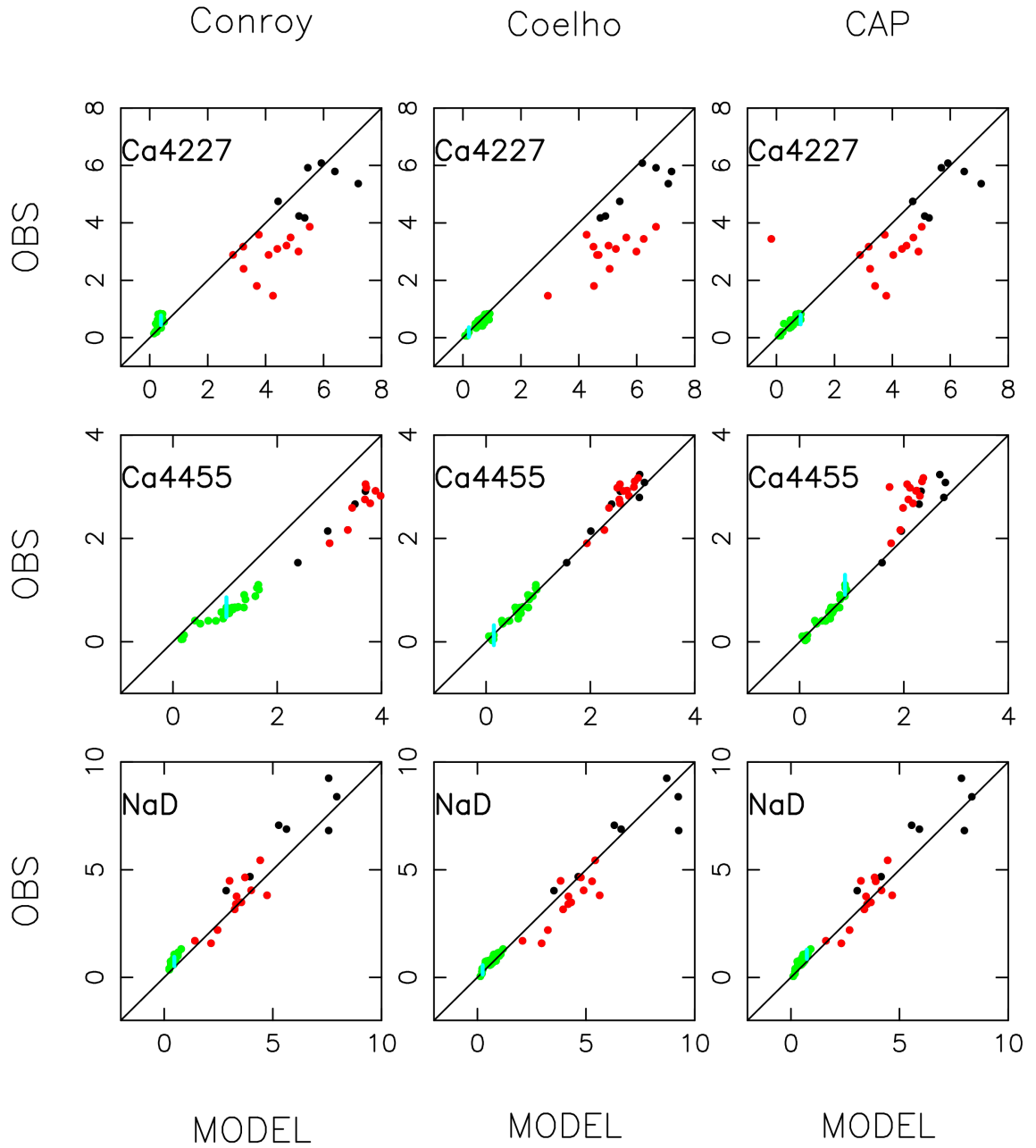


Figure 2.5: MILES Lick Indices versus Model Lick Indices, for Conroy, Coelho and Allende Prieto (CAP) theoretical spectra respectively, for calcium and sodium sensitive features. Same parameters and labelling procedure as Figure 2.1.

Table 2.3: Effects of vturb on line-strength indices. Each row shows different generated spectra and columns show the measured Lick index strengths. The important comparison is between the red rows in each sub box. The three sub boxes (from top to bottom) show results for a Cool Giant, Turn-off and Cool Dwarf star respectively. The row $v_2([\alpha/M]=0.25)-v_1([\alpha/M]=0.25)$ shows the absolute difference between two α -enhanced spectra with vturb=2 and 1 kms^{-1} respectively. The $v_2(\delta)-v_1(\delta)$ row shows differences between two normalised spectra (α -enhanced - solar) with vturb=2 kms^{-1} and 1 kms^{-1} . $v_2(\delta)-v_1(\delta)$ in red shows the differential effect of vturb choice on line-strength. It is shown that the differential effect is small.

Spectrum Units	H α	H δ	CN1	CN2	Cs1227	Cs1300	H γ A	Fe431	C2468	H β	Fe5015	Mg $_1$	Mg $_2$	Mg $_3$	Fe5270	Fe5335	Fe5406	Fe5709	Fe5782	Nad	TO1	TO2			
	A	A	A	A	A	A	A	A	A	A	A	A	A	A	A	A	A	A	A	A	A	A	mag		
T _{eff} = 4200 K, Log g = 2.09																									
$v_1([\frac{\alpha}{M}] = 0.25)$	-7.49	-0.38	0.235	0.367	6.31	7.80	-12.41	-4.70	8.59	2.22	5.15	3.37	0.66	7.80	0.193	0.456	6.86	4.07	4.36	2.91	1.67	1.01	3.79	0.067	0.136
$v_1(\odot)$	-9.09	-1.13	0.314	0.441	5.03	8.36	-12.33	-4.87	9.39	2.14	5.01	3.35	0.33	7.23	0.184	0.387	5.26	4.27	4.69	3.09	1.61	1.14	4.15	0.032	0.083
$v_2([\frac{\alpha}{M}] = 0.25)$	-8.27	-0.89	0.256	0.411	6.16	8.76	-13.30	-4.38	8.86	2.67	5.76	3.86	0.68	9.67	0.221	0.477	6.58	4.67	5.22	3.31	2.06	1.34	3.79	0.07	0.146
$v_2(\odot)$	-10.06	-1.66	0.338	0.487	4.88	9.36	-13.15	-4.51	9.54	2.57	5.63	3.83	0.34	9.18	0.212	0.407	4.97	4.83	5.54	3.47	1.99	1.49	4.5	0.035	0.094
$v_1(\delta)=v_1([\frac{\alpha}{M}] = 0.25)-v_1(\odot)$	1.59	0.746	-0.079	-0.074	1.28	-0.55	-0.08	0.17	-0.80	0.08	0.15	0.02	0.33	0.57	0.009	0.069	1.60	-0.20	-0.33	-0.18	0.06	-0.13	-0.35	0.035	0.053
$v_2(\delta)=v_2([\frac{\alpha}{M}] = 0.25)-v_2(\odot)$	1.79	0.77	-0.082	-0.076	1.28	-0.60	-0.15	0.13	-0.68	0.11	0.134	0.03	0.35	0.48	0.009	0.070	1.61	-0.16	-0.31	-0.16	0.07	-0.16	-0.36	0.035	0.052
$v_2([\frac{\delta}{M}] = 0.25)-v_1([\frac{\delta}{M}] = 0.25)$	-0.77	-0.50	0.021	0.044	-0.15	0.96	-0.89	0.32	0.275	0.45	0.61	0.491	0.02	1.88	0.028	0.021	-0.28	0.59	0.86	0.39	0.33	-0.00	0.003	0.01	
$v_2(\delta)-v_1(\delta)$	0.20	0.03	-0.003	-0.002	0.00	-0.04	-0.07	-0.03	0.12	0.03	-0.01	0.01	0.02	-0.08	0.000	0.001	0.01	0.03	0.02	0.01	-0.02	0.00	0	-0.001	
T _{eff} = 6253 K, Log g = 4.28																									
$v_1([\frac{\alpha}{M}] = 0.25)$	2.81	3.10	-0.100	-0.042	0.88	3.90	0.62	2.50	1.72	0.69	2.30	0.52	4.07	3.94	0.008	0.088	2.37	1.82	1.87	0.80	0.52	0.25	0.67	0.002	0.007
$v_1(\odot)$	2.59	2.96	-0.097	-0.042	0.66	4.15	0.28	2.28	1.91	0.68	2.15	0.43	3.96	3.77	0.008	0.073	1.85	1.67	1.77	0.79	0.48	0.23	0.73	0.002	0.006
$v_2([\frac{\alpha}{M}] = 0.25)$	2.63	2.88	-0.092	-0.034	0.88	4.53	0.04	2.38	1.91	0.83	2.83	0.51	4.08	4.826	0.011	0.092	2.25	2.07	2.20	0.93	0.61	0.27	0.68	0.002	0.008
$v_2(\odot)$	2.41	2.73	-0.092	-0.035	0.67	4.75	-0.28	2.17	2.10	0.82	2.67	0.42	3.96	4.58	0.011	0.077	1.73	1.89	2.07	0.93	0.57	0.26	0.75	0.002	0.008
$v_1(\delta)=v_1([\frac{\alpha}{M}] = 0.25)-v_1(\odot)$	0.22	0.14	-0.001	0.000	0.22	-0.24	0.33	0.22	-0.19	0.01	0.11	0.09	0.11	0.18	0.000	0.015	0.52	0.16	0.11	0.01	0.04	0.01	-0.1	0.000	0.001
$v_2(\delta)=v_2([\frac{\alpha}{M}] = 0.25)-v_2(\odot)$	0.22	0.15	0.000	0.001	0.21	-0.21	0.31	0.22	-0.19	0.00	0.16	0.09	0.12	0.24	0.000	0.015	0.52	0.19	0.13	0.00	0.05	0.02	-0.07	0.000	0.000
$v_2([\frac{\delta}{M}] = 0.25)-v_1([\frac{\delta}{M}] = 0.25)$	-0.18	-0.22	0.006	0.008	0.00	0.63	-0.58	-0.12	0.18	0.14	0.57	-0.012	0.007	0.87	0.00	0.00	-0.12	0.25	0.32	0.14	0.09	0.02	0.00	0.000	0.001
$v_2(\delta)-v_1(\delta)$	0.0	0.01	0.001	0.001	-0.01	0.03	-0.02	0.00	0.00	0.00	0.10	0.01	0.01	0.06	0.000	0.000	0.00	0.03	0.02	-0.01	0.01	0.00	-0.00	0.000	-0.001
T _{eff} = 4658 K, Log g = 4.47																									
$v_1([\frac{\alpha}{M}] = 0.25)$	-7.51	-0.32	0.092	0.215	6.09	7.23	-11.90	-4.32	8.21	12.28	4.87	1.35	0.46	7.04	0.197	0.506	8.21	4.70	4.86	3.01	1.22	0.77	5.29	0.009	0.026
$v_1(\odot)$	-9.78	-1.37	0.122	0.237	5.01	8.03	-12.55	-4.76	9.42	2.23	4.79	1.47	0.40	7.00	0.165	0.444	7.11	4.86	5.20	3.25	1.18	0.85	5.77	0.003	0.019
$v_2([\frac{\alpha}{M}] = 0.25)$	-7.63	-0.39	0.100	0.237	6.01	7.76	-12.40	-4.26	8.26	2.54	5.35	1.66	0.40	7.97	0.214	0.517	7.98	4.50	5.22	3.19	1.42	0.92	5.27	0.011	0.031
$v_2(\odot)$	-9.92	-1.46	0.128	0.255	4.94	8.54	-12.97	-4.69	9.40	2.47	5.28	1.771	0.327	7.98	0.18	0.45	6.90	5.13	5.54	3.4	1.37	1.01	5.75	0.004	0.024
$v_1(\delta)=v_1([\frac{\alpha}{M}] = 0.25)-v_1(\odot)$	2.27	1.05	-0.030	-0.022	1.08	-0.80	0.65	0.44	-1.21	0.05	0.08	-0.12	0.06	0.03	0.032	0.062	1.10	-0.16	-0.34	-0.25	0.04	-0.07	-0.48	0.006	0.007
$v_2(\delta)=v_2([\frac{\alpha}{M}] = 0.25)-v_2(\odot)$	2.29	1.07	-0.028	-0.018	1.07	-0.79	0.58	0.43	-1.14	0.07	0.07	-0.11	0.07	-0.004	0.035	0.063	1.08	-0.13	-0.32	-0.23	0.05	-0.08	-0.48	0.007	0.007
$v_2([\frac{\delta}{M}] = 0.25)-v_1([\frac{\delta}{M}] = 0.25)$	-0.12	-0.08	0.008	0.022	-0.08	0.52	-0.50	0.06	0.05	0.27	0.48	0.31	-0.06	0.94	0.017	0.011	-0.23	0.30	0.36	0.18	0.20	0.15	-0.02	0.002	0.005
$v_2(\delta)-v_1(\delta)$	0.02	0.02	0.002	0.004	-0.01	0.01	-0.07	-0.01	0.07	0.02	-0.01	0.01	0.02	-0.04	0.003	0.001	-0.06	0.03	0.02	0.02	0.01	-0.01	0.00	0.001	0.000

CHAPTER 2

In general, the absolute effect of v_{turb} on the Cool Dwarf line-strengths is smallest, with typical differences of 0.2\AA between 1kms^{-1} and 2kms^{-1} respectively. The microturbulent velocity has a far greater effect on the Cool Giant spectra with several features differing by order ~ 1 to 2\AA , particularly $\text{H}\gamma_A$, G4300 and Fe5015, with a change in v_{turb} from 1 km/s to 2 km/s. The Turn-off stars are also significantly affected by v_{turb} . For all star types the differential v_{turb} effect is small; as can be seen in the $v_2(\delta)-v_1(\delta)$ of Table 2.3. Our findings show these differences are generally much smaller (~ 0.02 dex - see Table 2.3.) than the observational errors on line-strengths (~ 0.1 dex - e.g. see Table 2 of Sansom et al. 2013)

For simplicity, we have chosen to use a constant value of $v_{\text{turb}}=1.5\text{kms}^{-1}$ for all our models used in this chapter, unless otherwise stated. This choice is motivated by larger studies of stars in our Galaxy, where v_{turb} is measured between the 1 and 2kms^{-1} (e.g. Holtzman et al. 2015).

2.4.2 Abundances in CAP models

Two approximations are made for the element abundances of the CAP models. Firstly, it is assumed that $[\text{Mg}/\text{Fe}]$ is a proxy for $[\alpha/\text{Fe}]$. This is a reasonable assumption for solar neighbourhood stars, like the 51 MILES stars used in this study, as is shown by the work of Delgado Mena et al. (2010) and Holtzman et al. (2015). A second approximation of $[\text{C}/\text{Fe}] = 0$ for the MILES stars was made based on results from (da Silva et al. 2011; Holtzman et al. 2015) for stars in our Galaxy.

The $[\text{Mg}/\text{Fe}]$ and $[\text{Fe}/\text{H}]$ abundances of the MILES stars are matched in the generated CAP model through $[\alpha/\text{M}]$ and $[\text{M}/\text{H}]$ respectively. Therefore we use the assumption that $[\text{Fe}/\text{H}]\approx[\text{M}/\text{H}]$ and $[\text{Mg}/\text{Fe}]\approx[\alpha/\text{M}]$. $[\text{C}/\text{Fe}]$ values of the MILES stars are assumed to be 0 throughout, meaning that $[\text{C}/\text{M}]=0$ in the generated models. For these CAP models, solar abundances are defined on the Asplund et al. (2005) scale. Using these conversions, spectra are generated in a self-consistent way,

CHAPTER 2

with the abundances of α and C varied in the same way for both model atmosphere and spectral synthesis calculations.

2.4.3 Absolute Comparisons

Figures 2.1 - 2.5 show direct comparisons between the measured MILES Lick indices and corresponding model Lick indices for these MILES matched spectra.

Figure 2.1 shows the absolute line strengths of the higher order Balmer lines and $H\beta$ for Conroy, Coelho and CAP models deviate from observations and this effect increases towards more negative line strengths and cooler temperatures. Figure 2.2 shows that Conroy, Coelho and CAP models predict iron-sensitive features qualitatively well in the absolute comparison, with no strong systematic deviations from the 1:1 agreement lines. Figure 2.3 shows a good agreement, over a broad range in index strengths, particularly for CAP models compared with observations for magnesium-sensitive features. There are slight overpredictions of line strengths for Coelho and CAP Cool Giant models, whilst the Conroy cool star models overpredict these magnesium features the most, with clear systematic offsets. Figure 2.4 shows that Conroy, Coelho and CAP all underpredict the line strength indices in C_24668 and show less variation than is present in MILES stars. Moreover, Conroy and CAP models overpredict the line strength indices of CN_1 and CN_2 for the cool stars. Figure 2.5 shows the absolute predictions of the Conroy, Coelho and CAP models for calcium and sodium sensitive indices agree well with the observations. However, differences between models can be seen in the $Ca4455$ index, with Coelho Cool Giant models having a tighter relation to the 1:1 line and Conroy models showing systematic overpredictions of this line strength. For $Ca4227$, the scatter is larger for the cool stars, with all three models behaving similarly. Despite the differences seen between models in Figures 1-5, it is interesting to note how similar the three sets of models behave in general, given the different approaches, inputs and codes

of the three models. This tells us that the models are producing similar predictions of the physical processes, although there are still large differences between models and observations in absolute terms. This overall similarity of behaviour between models indicates that the absolute discrepancies between theory and observations is not dominated by choices indicated in Table 2.1, such as which software was used.

2.5 Response Functions and their application

The results of Section 2.4 highlight the disagreements between the models and MILES stars in absolute terms. Other studies have also shown wavelength-dependent disagreements between theoretical models and observed spectra (e.g. Martins & Coelho 2007; Bertone et al. 2008; Coelho 2014; Villaume et al. 2017a; Allende Prieto et al. 2018). One method to incorporate both the abundance pattern predictions provided by theoretical models, and the reliability of empirical libraries, is to use theoretical spectra to differentially correct empirical spectra. Variations to Lick indices, due to changes in stellar atmospheric abundances, can be quantified in terms of response functions (Tripicco & Bell 1995). These can be applied to change empirical or theoretical line-strengths due to variations in abundance patterns, particularly differences from solar neighbourhood abundances. We produce response function tables for the models of three star types: a Cool Dwarf, Cool Giant and a Turn-off star, described in Section 2. To test the responses of different theoretical models to abundance pattern changes, we compare their normalised Lick indices predictions to measured Lick indices of existing MILES stars (described in Section 2.3). The models we test in this section are described in Sections 2.2.1, 2.2.2 and 2.2.3.

We test the response functions, derived from theoretical spectra of the three star types, by applying them to a theoretical solar abundance pattern (base) star to account for changes in abundance patterns, namely $[\alpha/\text{Fe}]$ changes. The base model star has the same atmospheric parameters of T_{eff} and $\log g$ as a chosen MILES base

CHAPTER 2

star, within observational errors. The response functions will be used to modify Lick indices of the base model star to account for an abundance pattern of an existing MILES star with same T_{eff} and $\log g$ as the base star, referred to as an enhanced star. This approach attempts to isolate the effects of abundance and abundance pattern only. The base model parameters are shown in Section 2. The MILES Cool Dwarf, Turn-off and Cool Giant base stars are HD 032147, HD 016673 and HD 154733 respectively. The parameters of these stars are shown in Sansom et al. (2013), Table 2.3.

For example, we have 7 Cool Dwarf stars. 1 is the base star (\approx solar abundance pattern) and 6 are the same T_{eff} and $\log g$ as the base star (within errors) but with different $[\text{Fe}/\text{H}]$ and $[\alpha/\text{Fe}]$ values. We use the response functions to correct the indices of the base star to match the $[\text{Fe}/\text{H}]$ and $[\alpha/\text{Fe}]$ of the other 6 stars. We then compare the normalised indices of those 7 stars (derived from the application of the response functions) to the observations.

To derive the theoretical response functions, the model spectra were matched to MILES resolution and sampling. They were resampled from a log scale to linear scale, taking the largest wavelength interval of the raw theoretical spectrum as the linear sampling. The theoretical spectra were then degraded and resampled to match the MILES observations, as described in Section 2.4. The 25 Lick line-strength indices were then measured using LECTOR. Individual response functions for the three star types were derived by finding the differences of indices, relative to solar abundance pattern, for the element enhanced spectra of each star type. For example, to calculate the magnesium response function for a Cool Dwarf spectrum we take the difference in indices between the Mg+0.3 enhanced spectrum and solar abundance pattern spectrum. This is then repeated for all the element enhanced spectra provided, in order to derive the response functions for individual element changes and for overall metallicity changes. We then apply the response functions

CHAPTER 2

to account for changes in abundances as described below.

In the application of response functions, we make the typical assumption that absorption-line strengths are linearly proportional to the number of absorbers. We follow the methodology presented in Sansom et al. (2013), which is based on the works of Thomas et al. (2003b) and Korn et al. (2005). We account for indices that go negative by conserving flux, as described in equation 3 of Korn et al. (2005). We tested the reliability of interpolating response functions by computing a Cool Giant star for CAP models at intermediate $[\alpha/\text{Fe}]$ values (e.g. $[\alpha/\text{Fe}]=0.2$) and comparing the model Lick indices to those produced by applying response functions from each of the α elements individually. Apart from three outlier indices (Ca4227, C₂4668 and TiO₁) we find good agreement between the two methods, with an RMS scatter of 0.07 and 0.01 for indices that are measured in Å and mag, respectively. This is within typical index measurement errors. Investigation into the outlier indices found that the problem is due to both side and feature bands of the Lick index being affected by a total $[\alpha/\text{Fe}]$ enhancement, which does not match the effects caused by changing the α elements separately. However, because the majority of the MILES stars used in this study have an $[\text{Mg}/\text{Fe}]$ value much less than 0.3, the application of response functions in this range is reliable.

Due to the lack of MILES stars with combinations of T_{eff} , $\log g$ and $[\text{Fe}/\text{H}]$ to match the theoretical stars provided at solar $[\text{Fe}/\text{H}]$, the derived response functions are applied twice to the base model star indices. First, a correction is made to match the model to the equivalent MILES star in $[\text{Fe}/\text{H}]$ using the $[\text{M}/\text{H}]$ column of the response function (see Table 2.4). Second, a correction is made to reach the correct $[\alpha/\text{Fe}]$ using the α element columns. The α elements used in each case are specified in Section 2.

Table 2.4: Extract from Response Functions. CAP Cool Giant stars. Column 1 is the Lick index name, Column 2 is the units of the index, Column 3 is the model base star index strength and Columns 4-13 are the variation of the index strength (in units of mag or Å) when the element at the top of the column is increased by 0.3 dex above solar. The last column shows the variation of the index strength when there is an overall metallicity increase of 0.3 dex. Full versions of this and all the derived response functions can be found in Appendix A and online on the UCLan database at <http://uclan.ac.uk/175/>.

Index	Units	I ₀	C	N	O	Mg	Fe	Ca	Na	Si	Cr	Ti	[M/H]
Hδ _A	Å	-10.125	-2.337	0.007	0.865	0.966	-2.010	-0.085	-0.003	1.768	0.151	-0.321	-1.433
Hδ _F	Å	-1.922	-1.071	-0.156	0.225	0.074	-1.025	0.031	-0.017	1.267	-0.014	-0.254	-0.794
CN ₁	mag	0.341	0.510	0.089	-0.108	-0.053	-0.057	-0.010	-0.005	0.022	-0.016	0.002	0.040
CN ₂	mag	0.461	0.517	0.089	-0.110	-0.059	-0.064	-0.012	-0.004	0.049	-0.014	0.002	0.046
Ca4227	Å	4.111	-0.866	-0.172	0.386	0.439	0.266	1.897	0.091	-0.010	-0.040	-0.023	1.430
...

CHAPTER 2

The $[\alpha/\text{Fe}]$ -enhanced, or deficient, star indices are normalised by the corresponding solar abundance pattern base model (TI_{\odot}) or base MILES star (OI_{\odot}) indices through divisions given in equations (2) and (3). Non-solar $[\alpha/\text{Fe}]$ MILES or Model indices are referred to as OI_{α} and TI_{α} respectively. We refer to a MILES or Model normalised index as OBS/BASE or MODEL/BASE_MODEL respectively:

$$\text{OBS/BASE} = \frac{\text{OI}_{\alpha}}{\text{OI}_{\odot}} \quad (2.2)$$

$$\text{MODEL/BASE_MODEL} = \frac{\text{TI}_{\alpha}}{\text{TI}_{\odot}} \quad (2.3)$$

For molecular bands and weak-line features that tend to zero or are negative, the normalisation process is performed via a difference rather than a ratio.

$$\text{OBS} - \text{BASE} = \text{OI}_{\alpha} - \text{OI}_{\odot}, \quad (2.4)$$

$$\text{MODEL} - \text{BASE_MODEL} = \text{TI}_{\alpha} - \text{TI}_{\odot}. \quad (2.5)$$

Complete agreement between the observations and predictions from theoretical response functions would lead to a ratio of MILES Normalised Index = Model Normalised Index.

Figures 2.6 to 2.10 show the comparison of normalised Lick indices derived from MILES stars to those derived from predictions of the theoretical response functions, for selected Lick indices. These figures highlight the main effects that we found. Observational errors on indices were estimated per star type, considering twice the random errors. Selecting a larger sample of MILES cool stars to calculate the random errors, we find that the errors increase by a factor of ~ 40 percent compared to the error calculated from just the 13 Cool Giant stars. There is at least a factor of $\sqrt{2}$ because both the enhanced and the base star are affected in the normalised indices. That is why we have used a conservative value of twice the random errors. Systematic errors due to atmospheric parameter uncertainties were estimated for

CHAPTER 2

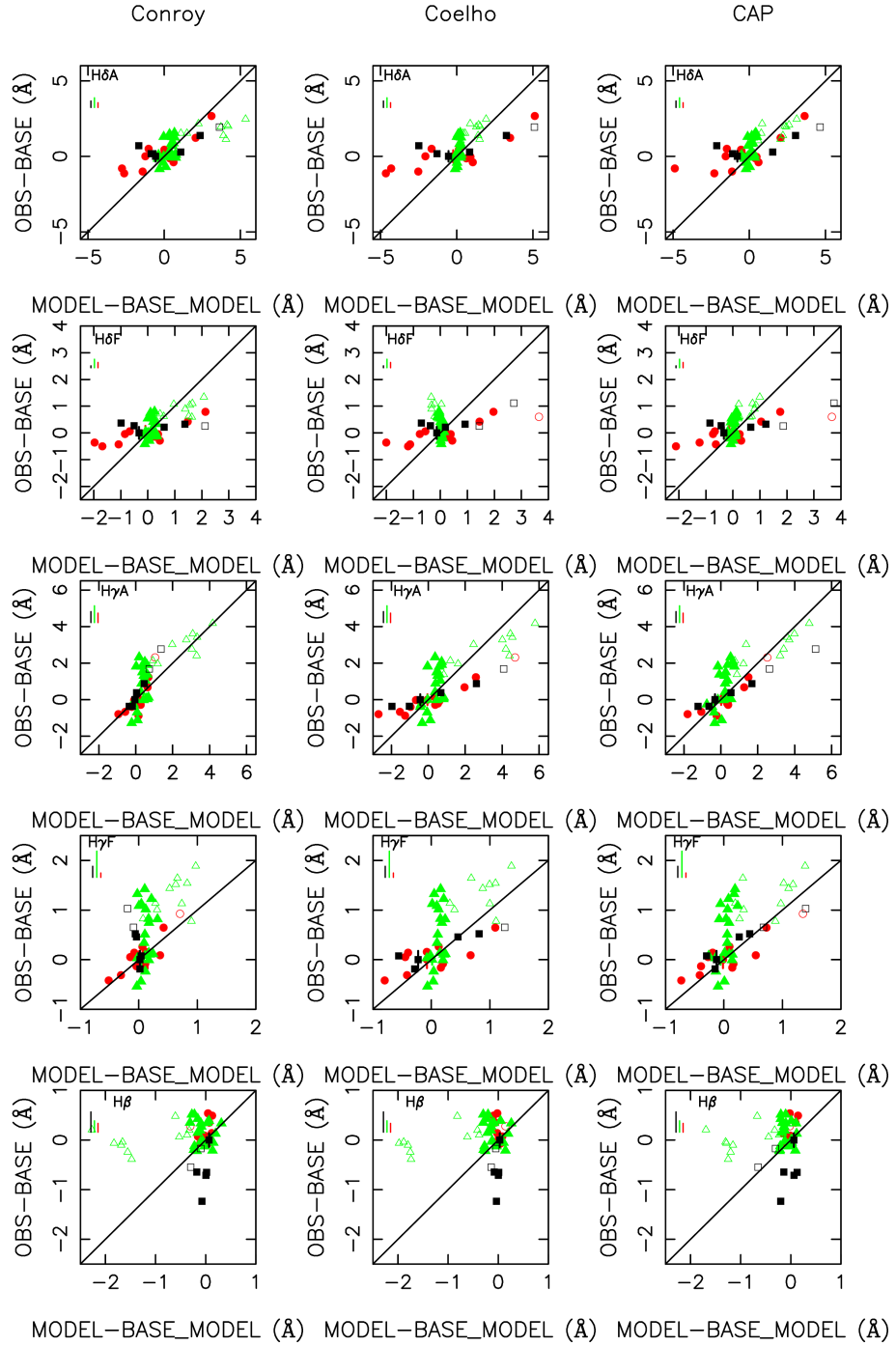


Figure 2.6: MILES Normalised Lick indices versus Conroy, Coelho and Allende Prieto (CAP) Model Normalised Lick indices derived from response functions, for Hydrogen indices. The three star types are shown in each case, with green triangles, black squares and red circles representing Turn-off, Cool Dwarf and Cool Giant stars respectively. Open symbols represent stars with $[\text{Fe}/\text{H}] < -0.4$. The observational error bar is shown on the corresponding base star point in each plot and $+1\sigma$ error bars due to star parameter uncertainties are shown top left in each plot.

CHAPTER 2

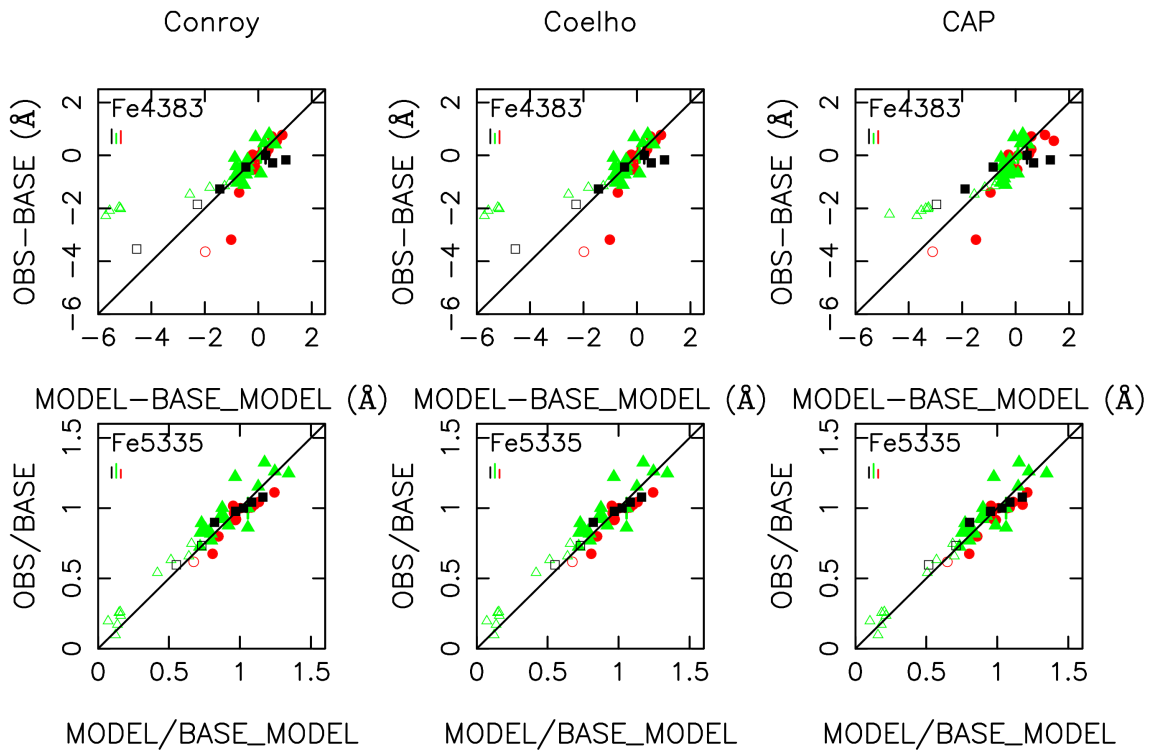


Figure 2.7: MILES Normalised Lick indices versus Conroy, Coelho and Allende Prieto (CAP) Model Normalised Lick indices, for Iron sensitive features. Symbols and colours as in Figure 2.6.

CHAPTER 2

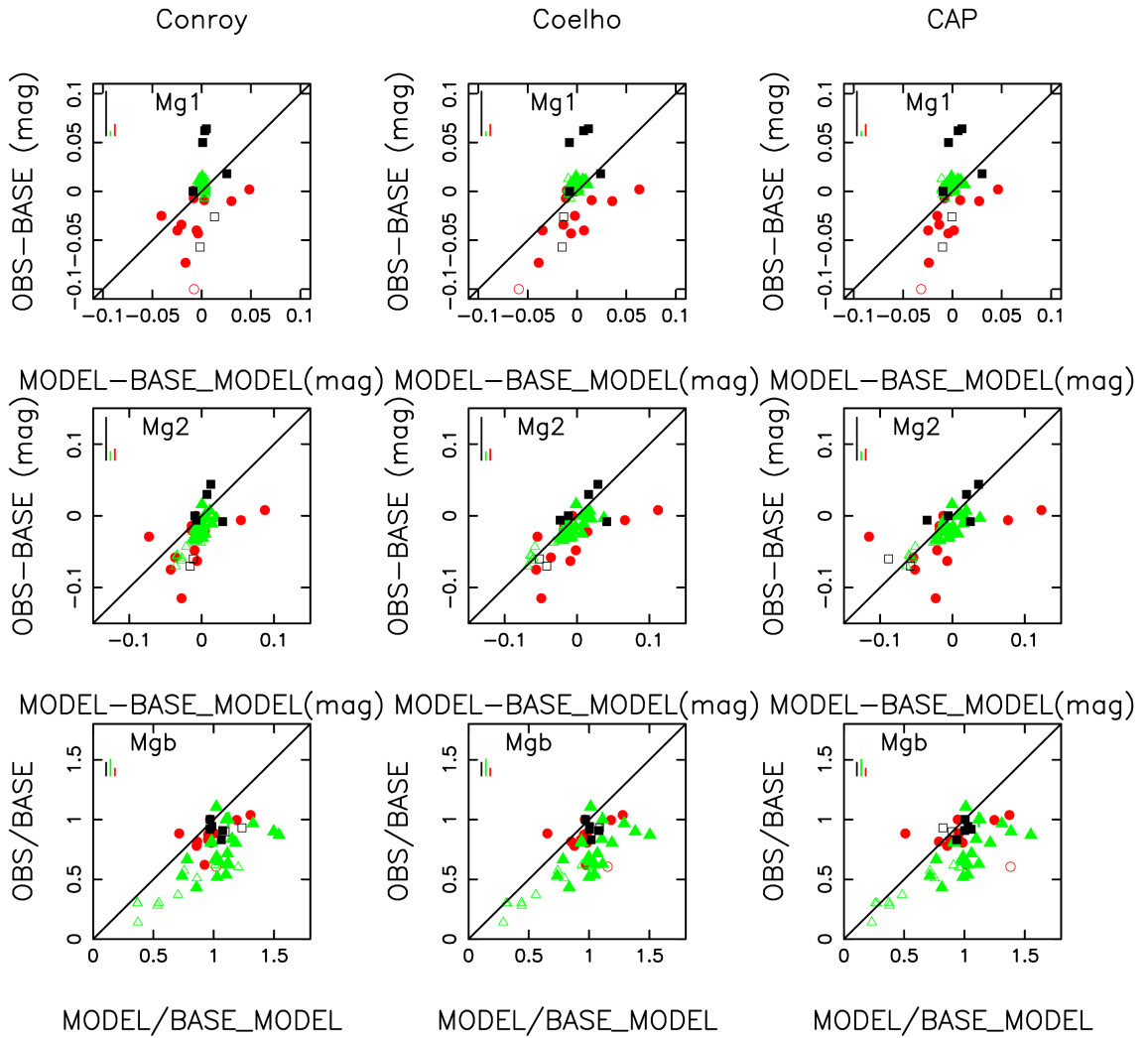


Figure 2.8: MILES Normalised Lick indices versus Conroy, Coelho and Allende Prieto (CAP) Model Normalised Lick indices, for Magnesium (Mg_1 , Mg_2 and Mg_b) sensitive features. Symbols and colours as in Figure 2.6.

CHAPTER 2

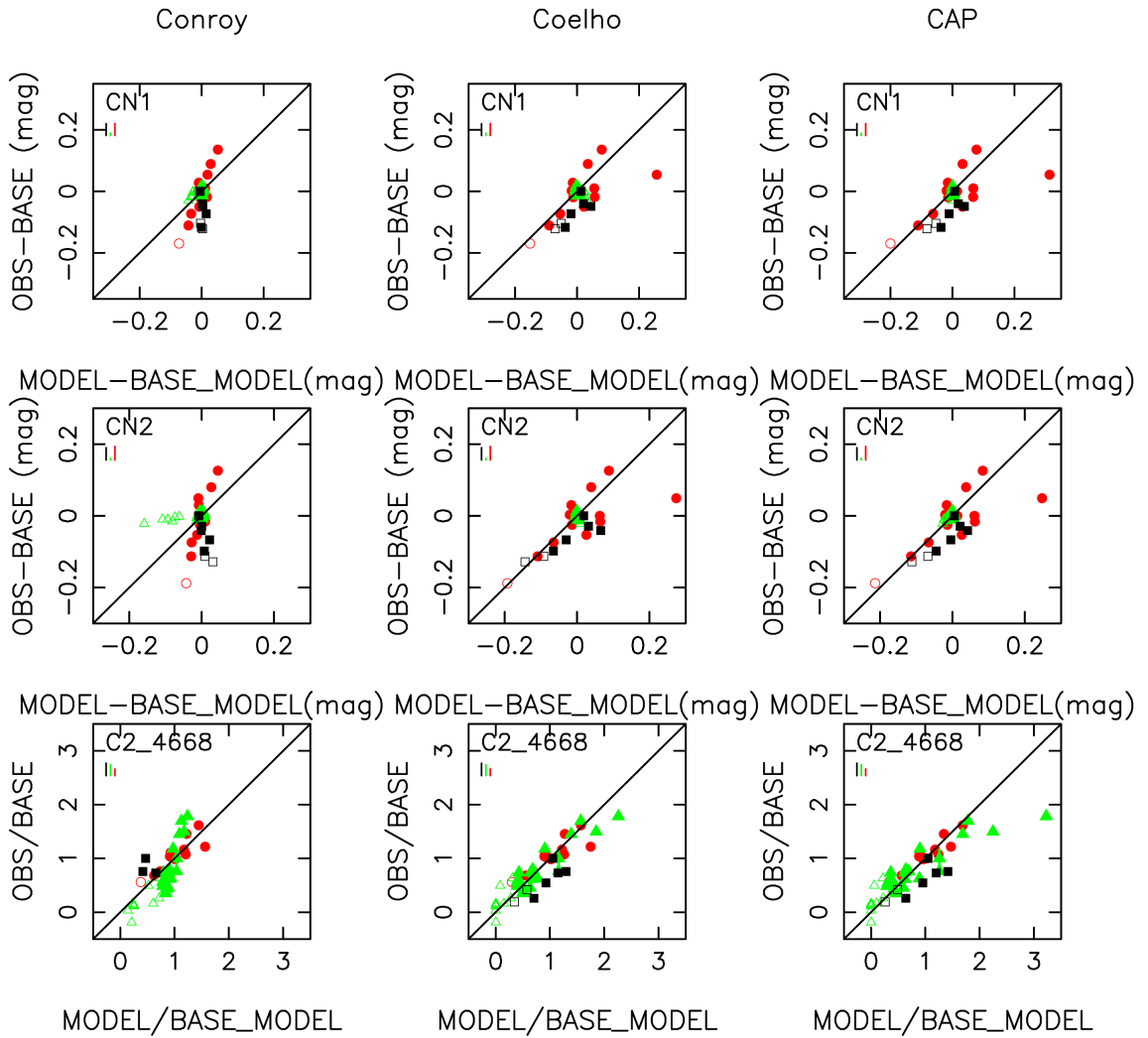


Figure 2.9: MILES Normalised Lick indices versus Conroy, Coelho and Allende Prieto (CAP) Model Normalised Lick indices, for Carbon and Nitrogen sensitive features. Symbols and colours as in Figure 2.6.

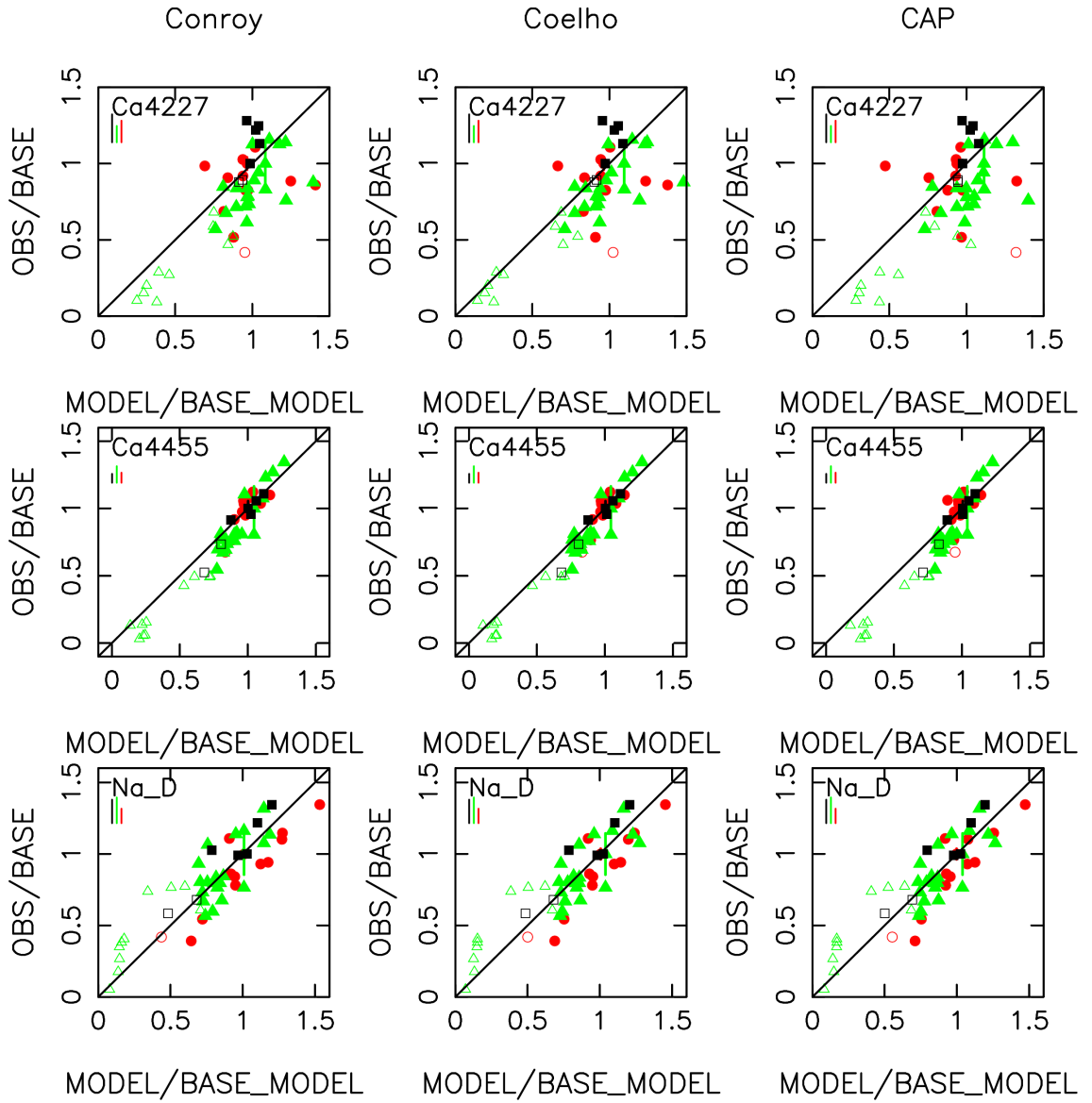


Figure 2.10: MILES Normalised Lick indices versus Conroy, Coelho and Allende Prieto (CAP) Model Normalised Lick indices, for Calcium and Sodium sensitive features. Symbols and colours as in Figure 2.6.

CHAPTER 2

each star type using the online MILES interpolator⁵. Note that errors in the atmospheric parameters of the base star would lead to systematic offsets in differences and systematic deviations in the slope in ratios. In Figures 2.6-2.10, stars with $[\text{Fe}/\text{H}] < -0.4$ (represented by open symbols) sometimes fall outside of the ranges of the plots, particularly for indices in the blue end of the spectrum, with two Cool Dwarfs, one Cool Giant and one Turn-off star affected. Another outlier is a Cool Giant with $[\text{Mg}/\text{Fe}] = -0.398$ (HD131430). This is likely to be uncertain because the calibration used in Milone et al. (2011) (their Figure 4) did not extend to such low values in $[\text{Mg}/\text{Fe}]$. This star is an outlier in CN_1 and CN_2 of the CAP and Coelho models.

Figure 2.6 shows the response function comparison of models versus empirical stars respectively for Hydrogen Lick indices. We find a disagreement in Turn-off stars for all models, with empirical stars showing a larger range of variation than predicted in the models, particularly for $\text{H}\gamma_{\text{A}}$. There is the opposite behaviour in models for the cool stars in Figure 2.6. All three models appear to overpredict the variation in the $\text{H}\delta_{\text{A}}$ and $\text{H}\delta_{\text{F}}$ indices in both Cool Dwarf and Cool Giant stars. This is the same trend in cool stars as found for Korn et al. (2005), Sansom et al. (2013) - see their Figure 1b. The models perform better for the $\text{H}\gamma_{\text{A}}$ and $\text{H}\gamma_{\text{F}}$ indices, lying closer to the 1:1 line for Conroy, and furthest for Coelho. Conroy's Cool Dwarf models predict almost no variation in $\text{H}\gamma_{\text{F}}$ for changes in abundance pattern, highlighted by the almost vertical pattern seen in the plot. Variation in the $\text{H}\beta$ index shows no clear trends. We investigate a different definition of the $\text{H}\beta$ index, $\text{H}\beta_0$, in section 2.6.4. For $\text{H}\beta_0$, we find a stronger correlation with abundance pattern and metallicity in $\text{H}\beta_0$ for all models, which is in agreement with the theoretical SSPs of Cervantes & Vazdekis (2009). In summary, for all indices, there is a general lack of agreement for cool stars in all three models, with some improvements seen

⁵www.iac.es/proyecto/mile/page/webpages.php

CHAPTER 2

in Conroy and CAP models.

Figure 2.7 shows the comparison between model predictions and MILES stars for two iron sensitive features. Other iron sensitive features show similar agreement. This highlights that all iron model response function predictions for all star types agree well with the MILES stars.

Figure 2.8 shows predictions of the models for Mg-sensitive indices. The scatter is quite large. All models show generally the same behaviour - the Cool Giant and Turn-off models all systematically overpredict the strength in Figure 2.8, lying below the 1:1 line. The Cool Dwarf models show a good agreement with the 1:1 line in these Mg-sensitive features.

Figure 2.9 shows predictions of the models for Carbon sensitive indices. There are systematic deviations from the 1:1 line in the CN features of Conroy's models, with a smaller range of differential behaviour in cool stars with a larger range of differential behaviour of CN_2 in metal poor Turn-off stars, compared to MILES stars. The differential predictions for the CN features of both Coelho and CAP models are similar, with a good agreement with the 1:1 lines.

For the C_24668 feature shown in Figure 2.9, the differential predictions of the Turn-off stars show good agreement between observations and models for the Coelho and CAP cases, but less so for the Conroy case. The cool star models of Coelho and CAP are in good agreement with the 1:1 lines. In the Conroy models, there are four outlier Cool Dwarf stars that fall outside of the plot. This is caused by a problem with the base model, which has a different index to the ones found in real stars. Conroy's base model index was -0.105, compared to 1.453 and 1.406 of Coelho and CAP models, respectively.

Figure 2.10 shows the response function predictions for Calcium and Sodium sensitive indices. This shows that all models predict the differential behaviour of Ca4455 , Ca4227 and NaD features well, with the models lying close to, the 1:1 line.

CHAPTER 2

Table 2.5: Reduced χ^2_ν values for comparisons of normalized observations (from MILES) versus normalized models (using the response functions for [M/H] and [α /Fe] changes in stars). The results are shown for Cool Giant stars and for star response functions from Conroy, Coelho and CAP. These values were calculated for stars with [Fe/H]>-0.4 and with HD131430 removed (see Section 2.5 for details).

	Conroy	Coelho	CAP
Index	χ^2_ν	χ^2_ν	χ^2_ν
H δ_A	1.44	6.21	1.92
H δ_F	3.24	3.01	1.51
CN ₁	0.32	0.33	0.40
CN ₂	0.36	0.35	0.35
Ca4227	7.12	6.94	10.13
H γ_A	0.07	0.80	0.21
H γ_F	0.56	2.26	1.09
Fe4383	0.55	0.36	0.39
Ca4455	0.75	0.69	1.06
C ₂ 4668	5.06	5.12	4.56
H β	0.35	0.56	0.36
Mg _b	19.13	19.90	26.26
Fe5335	5.05	4.87	4.61

Table 2.6: Gradient and intercept values calculated from a linear regression for comparisons of normalized observations (from MILES) versus normalized models (using the response functions for $[M/H]$ and $[\alpha/Fe]$ changes in stars). The results are shown for Cool Giant stars and for star response functions from Conroy, Coelho and CAP. These values were calculated for stars with $[Fe/H] > -0.4$ and with HD131430 removed.

Index	Conroy		Coelho		CAP	
	Gradient	Intercept	Gradient	Intercept	Gradient	Intercept
H δ_A	0.55 \pm 0.12	0.19 \pm 0.18 Å	0.32 \pm 0.07	0.19 \pm 0.18 Å	0.50 \pm 0.12	0.20 \pm 0.20 Å
H δ_F	0.25 \pm 0.06	-0.01 \pm 0.06 Å	0.25 \pm 0.06	-0.01 \pm 0.07 Å	0.33 \pm 0.08	0.00 \pm 0.07 Å
CN $_1$	2.33 \pm 0.37	0.00 \pm 0.01 mag	1.02 \pm 0.31	-0.01 \pm 0.01 mag	0.83 \pm 0.28	0.00 \pm 0.02 mag
CN $_2$	2.84 \pm 0.40	0.00 \pm 0.01 mag	0.84 \pm 0.26	-0.01 \pm 0.01 mag	0.83 \pm 0.26	0.00 \pm 0.01 mag
Ca4227	0.19 \pm 0.30	0.68 \pm 0.30	0.17 \pm 0.32	0.70 \pm 0.33	0.03 \pm 0.24	0.84 \pm 0.25
H γ_A	1.03 \pm 0.20	-0.07 \pm 0.09 Å	0.35 \pm 0.05	-0.01 \pm 0.08 Å	0.54 \pm 0.09	-0.06 \pm 0.08 Å
H γ_F	0.82 \pm 0.22	0.02 \pm 0.06 Å	0.39 \pm 0.12	0.03 \pm 0.06 Å	0.53 \pm 0.15	0.03 \pm 0.06 Å
Fe4383	1.85 \pm 0.29	-0.32 \pm 0.15 Å	0.84 \pm 0.13	-0.31 \pm 0.15 Å	1.39 \pm 0.20	-0.33 \pm 0.14 Å
Ca4455	0.94 \pm 0.29	0.07 \pm 0.29	1.07 \pm 0.31	-0.10 \pm 0.31	0.92 \pm 0.42	0.10 \pm 0.42
C $_2$ 4668	1.05 \pm 0.16	0.01 \pm 0.17	0.85 \pm 0.13	0.20 \pm 0.13	0.80 \pm 0.09	0.26 \pm 0.10
H β	1.73 \pm 0.76	0.13 \pm 0.06 Å	-2.87 \pm 1.14	0.13 \pm 0.06 Å	2.13 \pm 0.86	0.14 \pm 0.06 Å
Mg $_b$	0.63 \pm 0.20	0.23 \pm 0.20	0.60 \pm 0.24	0.27 \pm 0.24	0.39 \pm 0.19	0.47 \pm 0.19
Fe5335	0.87 \pm 0.15	0.07 \pm 0.15	0.91 \pm 0.15	0.04 \pm 0.16	0.95 \pm 0.15	0.00 \pm 0.15

CHAPTER 2

Models are assessed via reduced chi-squared (χ^2_ν) analysis. Table 2.5 shows χ^2_ν values, about the 1:1 agreement line, for the normalised Cool Giant models versus normalised MILES observations. The values calculated took into account the errors associated with the observations and systematic offsets caused by atmospheric parameter uncertainties added in quadrature. The calculations were performed using all stars with $[\text{Fe}/\text{H}] > -0.4$, apart from a Cool Giant star outlier (HD131430). With the $[\text{Fe}/\text{H}]$ cut and removal of HD131430, this left 11 Cool Giant stars for the calculation. We also assess the performance of models via linear regression between normalised index observations and model predictions. Table 2.6 shows the results for Cool Giant models, indicating the derived gradient and intercept for the best fitting linear trends. The results from this regression highlight the differences between the model trends and 1:1 agreement. With such a fit, if the model is agreeing fully with the observations we expect to find a gradient of 1 and intercept of 0. The combination of χ^2_ν , gradient and intercept gives information about any scatter or offsets of the models from the 1:1 agreement line.

We find there is a lack of agreement between cool star models and observations for Balmer features, with the χ^2_ν showing that for $\text{H}\delta_{\text{A}}$, $\text{H}\gamma_{\text{A}}$ and $\text{H}\gamma_{\text{F}}$ Coelho models are performing the worst, improvements are seen in CAP and Conroy is performing the best. Coelho models show the shallowest gradients for these $\text{H}\delta_{\text{A}}$ and $\text{H}\gamma_{\text{A}}$ features. The C_24668 results show that all the Cool Giant models have very similar differential predictions for this index. From the Mg_b results, there is a much larger scatter found than expected. This behaviour is also true for $\text{Ca}4227$, with large χ^2_ν values found. Reflecting the results shown in Figure 2.7, the χ^2_ν , gradient and intercept values highlight that iron features are fit well by the models. Considering the poorer fits, where $\chi^2_\nu > 1$ ($\text{H}\delta_{\text{A}}$, $\text{H}\delta_{\text{F}}$, $\text{Ca}4227$, $\text{H}\gamma_{\text{F}}$, $\text{Ca}4455$, C_24668 , Mg_b , $\text{Fe}5335$), we summarise that regarding the Cool Giant models: Conroy models perform best in 3 out of those 8 indices, and perform worst in 2 of them; Coelho models perform

CHAPTER 2

best in 2, and worst in 3 indices; CAP models perform best in 3 and worst in 3 indices. For the other 5 indices (CN_1 , CN_2 , $\text{H}\gamma_{\text{A}}$, $\text{Fe}4383$, $\text{H}\beta$) all the models fit the data ($\chi_{\nu}^2 < 1$). Cool Dwarf models show similar behaviour to the Cool Giant models whereas Turn-off models all have $\chi_{\nu}^2 < 1$ except for C_24668 and Mg_b . Regarding the gradients shown in Table 2.6 for red giant stars, Conroy models have 7 indices, Coelho models have 7 indices and CAP models have 9 indices, with a gradient in the range 0.5 to 1.5 of the 1:1 line.

2.6 Discussion

There are two main caveats to our analysis. Firstly, we have used MILES atmospheric parameters presented in Cenarro et al. (2007) throughout this chapter. Therefore, the effects of alternative stellar parameters have not been studied (e.g. Sharma et al. 2016). Secondly, we have not attempted to address other departures from solar-scaled patterns (such as C and N), which might affect the empirical stars but are not accounted for in the models. These departures may affect the absolute predictions more than differential predictions, compared later in this section. The effect of C, N and O abundances are beyond the current study due to the lack of abundance information currently available for MILES stars.

We will now discuss the main deviations found from the index analysis performed in Sections 2.4 and 2.5. We then discuss a correction found for Coelho models during this work and a different definition of $\text{H}\beta$. We finally summarise the main strengths and weaknesses of each model, individually.

2.6.1 Indices

We discuss the largest disagreements found between models in more detail, focusing on hydrogen-sensitive features. We also show the differences between using the

CHAPTER 2

models differentially and absolutely.

Hydrogen Indices

The cause of deviations between observed and absolute model predictions (Figure 2.1) for H_γ and H_δ features appears to be related to temperature, with increasing disagreement at lower star temperature. Low temperature stars are known to be difficult to model accurately, due to the complexity of absorption features in their atmospheres. The models tested here are generated using versions of ATLAS therefore, spherical geometry and non-LTE effects have been ignored. This will impact the lowest temperatures and may explain the lack of agreement between models and observations for the cool star models. The absolute effect of spherical geometry on Balmer lines can be large, resulting in differences between 3D LTE and 1D LTE temperature estimates of late-type stars of up to $\approx 200\text{K}$ (Table 4 of Amarsi et al. 2018). Balmer lines modelled under LTE conditions are known to match the line wings, but cannot reproduce the core of the lines (e.g. Figures 5 and 6 in Amarsi et al. 2018 and Section 4.2 in Martins & Coelho 2007). However, the effect of non-LTE in the temperature regimes tested in this Chapter are smaller than the 3D effects, particularly for the higher order Balmer features (Table 4 of Amarsi et al. 2018). The disagreement between model and observed hydrogen lines may also be explained by limitations in the atomic data in the region. In cool stars in particular, the Balmer lines can be weak and the region could instead be dominated by uncalibrated metal lines. Appendix B shows that this applies to both dwarf and giant stars, where I show a sample of 801 MILES star versus corresponding model Lick indices generated through interpolations of the theoretical grid presented in Chapter 3. The models overpredict variations in H_γ and H_δ features compared to observations. Where these features are used for age indicators in stellar populations, age estimates will be affected. In the absolute comparisons, where the models underpredict the strength of

CHAPTER 2

Hydrogen lines (Figure 2.1: Top four rows), the ages of stellar populations would be over-estimated. In the differential comparisons, where the models both under and overpredict the Hydrogen lines (Figure 2.6: Top four rows), the ages of stellar populations could be over or underpredicted. These differences are driven by temperature effects that are discussed in Appendix B.

Differential vs Absolute Indices

In this section we present quantitative results that highlight the differences in reliability between using theoretical models in a differential way and using their absolute predictions. In Figure 2.11 we show an alternative way to present this difference for the 11 CAP Cool Giant models versus the MILES giant stars in our 51 star sub-sample.

In Figure 2.11 we show the difference in theoretical and observational Lick indices versus wavelength for the 19 indices that are in units of \AA . For the red points (open circles), $\text{Theory} = (\text{Theoretical Enhanced Index} - \text{Theoretical Base Index})$ and $\text{Obs} = (\text{Observational Enhanced Index} - \text{Observational Base Index})$. For the blue points (stars), $\text{Theory} = \text{Theoretical Enhanced Index}$ and $\text{Obs} = \text{Observational Enhanced Index}$. The difference in location between the red points and blue points highlights the effect of normalising the enhanced indices by corresponding solar abundance pattern indices. In general, the differential predictions (red points) are far less scattered about the $\text{Theory} = \text{Obs}$ line than the absolute predictions (blue points), particularly in the blue part of the spectrum (below Mg_b). The differential approach generally appears to produce more reliable predictions than the absolute predictions, which is highlighted in Table 2.7, where we show the RMS scatter for the blue and red points in the case of $\text{Theory} - \text{Obs}$. For the differential approach, almost all of the indices are scattered less or the same as the absolute predictions about the $\text{Theory} = \text{Obs}$ line. The results in Table 2.7 show that the differential application of theoretical stellar

CHAPTER 2

spectra produces generally a better prediction of abundance pattern effects than the absolute. This is highlighted with the large (\sim factors of 2 or more) improvements in RMS scatter of the $H\delta_A$, G4300, $H\gamma$, Fe4383, Ca4455, C₂4668 and $H\beta$ indices. For the two carbon sensitive features, G4300 and C₂4668, the lack of carbon information in MILES stars may explain the poor absolute predictions of models in Table 2.7.

In Table 2.7 we also show the RMS scatter when assuming a zero α response (e.g. we only apply the response functions to match the MILES $[\text{Fe}/\text{H}]$ values, not the $[\alpha/\text{Fe}]$ as well). Interestingly, it can be seen that almost all the indices are as good or better than the differential approach that matched both $[\text{Fe}/\text{H}]$ and $[\alpha/\text{Fe}]$ values. This highlights the large metallicity dependence of these indices, with the α response being a secondary effect. Therefore, we conclude that this assessment, using response functions, does not test abundance patterns as well as expected, because of the small range of $[\text{Mg}/\text{Fe}]$ in the Cool Giant MILES stars used in this study. We also note that the lack of abundance consistency between the model atmosphere and radiative transfer parts of the code may also have an adverse effect when individual elements are varied via the response function tables.

2.6.2 Synthetic Spectra

To highlight comparisons between models we plot examples of spectral ratios in regions of Lick indices. Using the spectra generated for the direct comparison in Section 2.4, we investigate the differences between normalised (Non-solar abundance pattern star/Base star) cool giant empirical and model spectra. The stars we chose were HD113092 ($[\text{Fe}/\text{H}]=-0.370$, $[\text{Mg}/\text{Fe}]=0.182$) and HD154733 ($[\text{Fe}/\text{H}]=-0.080$, $[\text{Mg}/\text{Fe}]=0.009$). HD154733 was the Cool Giant base star used in the analysis in Section 5. The ratio of these two spectra shows the differential effect of both metallicity and α abundance changes. We focus on indices showing the largest disagreements between model and observations.

CHAPTER 2

Table 2.7: RMS scatter about the Theory=Obs line of the three different applications of CAP Cool Giant model predictions. The columns represent the index name, the differential predictions, absolute predictions and differential predictions fixing the α response to zero respectively. In general the differential scatter is smaller or performing the same as the absolute behaviour.

Index	Absolute Å	Differential Å	Differential (α -fixed) Å
H δ_A	2.86	1.02	0.59
H δ_F	0.75	0.60	0.36
Ca4227	1.14	1.23	1.10
G4300	2.39	0.86	0.51
H γ_A	2.54	0.49	0.51
H γ_F	1.00	0.26	0.23
Fe4383	1.13	0.56	0.73
Ca4455	0.69	0.22	0.18
Fe4531	0.53	0.28	0.29
C ₂ 4668	4.03	1.00	1.01
H β	0.74	0.22	0.22
Fe5015	0.53	0.30	0.27
Mg _b	0.77	1.03	0.86
Fe5270	1.08	1.02	1.07
Fe5335	0.69	0.38	0.43
Fe5406	0.36	0.36	0.34
Fe5709	0.50	0.54	0.54
Fe5782	0.34	0.27	0.24
Na _D	0.59	0.73	0.72

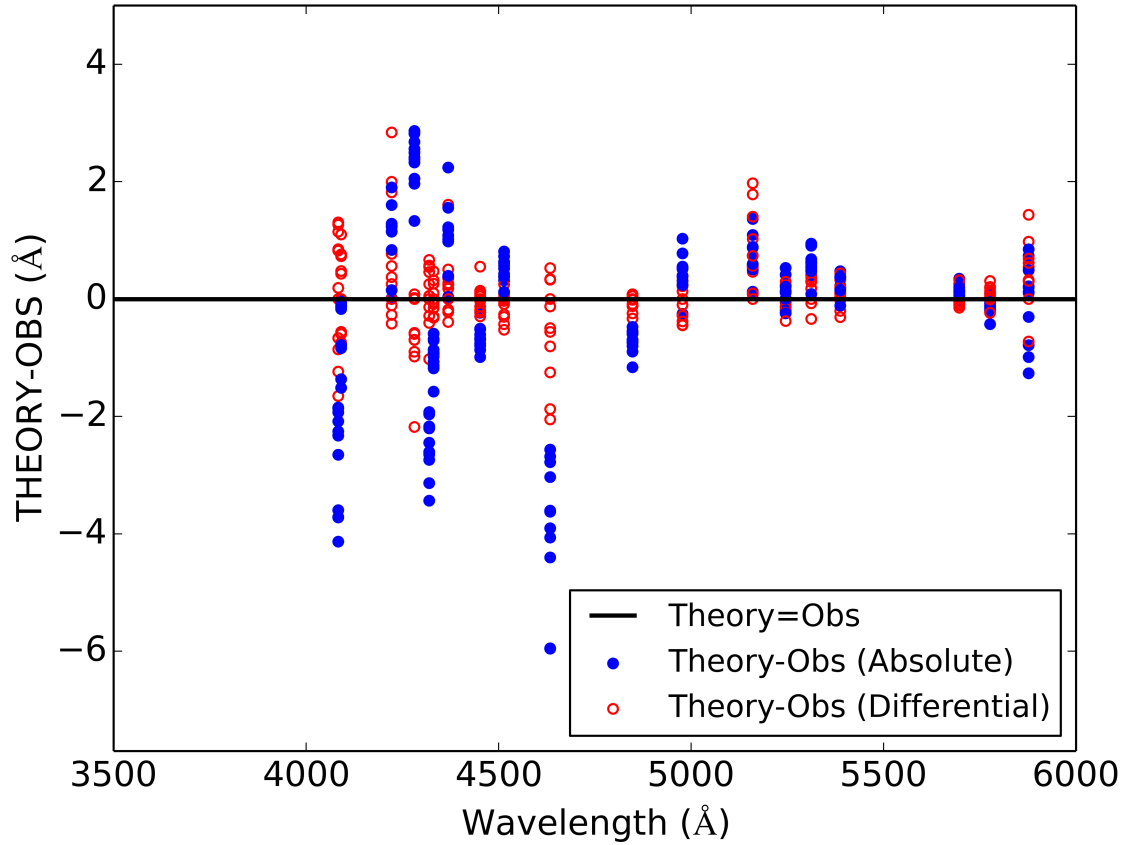


Figure 2.11: Comparison between the differential and absolute predictions of line-strengths for the 19 indices, with units of \AA , as a function of wavelength. This is illustrated for the CAP Cool Giant models, with the same parameter cuts as Table 2.5, leaving 11 stars. The vertical axis shows differences between theoretical and observed index values. Red and blue points represent the differential and absolute application of the models respectively. The absolute models have been produced with parameters that match those of Cenarro et al. (2007) MILES parameters.

CHAPTER 2

Figure 2.12 highlights spectral differences in the C_24668 region between the CAP and Coelho models. Normalised CAP models are offset from the normalised observations, which is not seen in the differential index analysis. On the other hand, normalised Coelho models lie closer to the normalised observations. These offsets of spectra appear to have little effect on the differential Lick indices. This is seen in Figure 2.9, where both Cool Giant models show good agreement with the observations in the C_24668 index.

Figure 2.13 highlights some of the problems with the higher order Balmer features seen in Figure 2.6. Both Coelho and CAP models are overpredicting features in $H\delta_A$, in pseudocontinua and feature bands. This overprediction may contribute to trends seen in Figure 2.6, with cool star models showing more variation in the index than in observed stars. These type of plots allowed us to identify that the file regarding the transition D-A of the molecule C_2 in Coelho (2014) models was corrupted. This corruption does not affect any of this work, but is discussed and illustrated in section 2.6.3.

2.6.3 Coelho Latest Revisions

During the work for this chapter, we identified a problem in the C_24668 region in the Coelho models. The origin of this problem was found to be in the C_2 line list of these models. Specifically there was a corruption with the file containing the D-A transition. This is the likely origin of the missing opacity which can be seen around 4000\AA in the second panel in Figure 10 of Coelho (2014). This corruption led to the problems shown in Figures 2.14 and 2.15. It can be seen in the left panel of Figure 2.14 that there was an issue regarding a lack of variation in the normalised C_24668 index for the corrupted (old) Coelho cool star models. This is clarified in the left panel of Figure 2.15, which shows that the corrupted Coelho models had almost no variation in the C_24668 spectral region with an increase of

CHAPTER 2

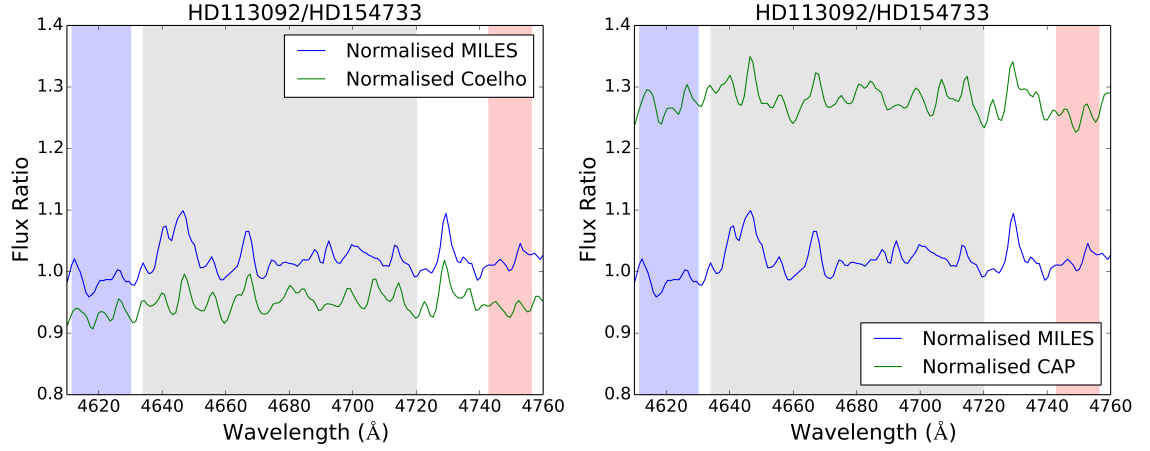


Figure 2.12: Spectral ratios in $C_2 4668$ region. The green and blue lines show a normalised (HD113092/HD154733) spectrum for the Cool Giant models and equivalent MILES stars respectively. The left and right panels show the Coelho and CAP models respectively. The blue, red and grey areas represent the blue continuum, red continuum and index band of the $C_2 4668$ Lick index definition respectively.

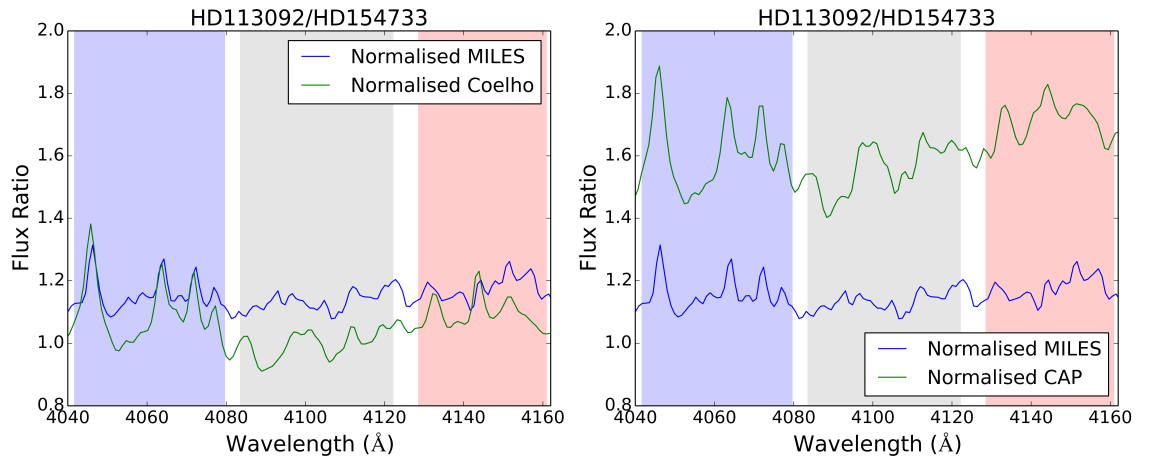


Figure 2.13: Spectral ratios in $H\delta_A$ region. The green and blue lines show a normalised (HD113092/HD154733) spectrum for the Cool Giant models and equivalent MILES stars respectively. The left and right panels show the Coelho and CAP models respectively. The blue, red and grey areas represent the blue continuum, red continuum and index band of the $H\delta_A$ Lick index definition respectively.

CHAPTER 2

0.3 dex in carbon. The models were recomputed with a corrected C₂ D-A transition for the current work and we plot the corrected models in the right panel of Figure 2.14 and in both panels of Figure 2.15 (green lines). It can be seen in the right panel of Figure 2.14 that the corruption is amended and the models now lie in closer agreement with MILES observations. This improvement is reflected in the spectral plots in Figure 2.15, with Coelho’s new models showing strong absorption features of the Swan bands (Swan (1875); Gonneau et al. (2016)). Typical features, originating from the (1,0) vibrational plus rotational transitions, in the Swan bands exist at 4684, 4697, 4715 and 4737 Å and these locations are shown in Figure 2.15. Numerically, this correction results in an increase in C₂4668 carbon response from 0.014 to 10.266 Å and an increase in C₂4668 overall metal response from -0.042 to 1.552 Å between the old and corrected Coelho models respectively. The response functions presented in the online data incorporate these corrections for Coelho’s models. These corrections will be present in future works involving Coelho models. This correction has negligible effect on the other indices.

2.6.4 H β and H β_0

We explore how well models agree with observations for a variation of the standard Lick index for H β . Cervantes & Vazdekis (2009) defined H β_0 with slightly different band limits than for H β , in a search for better age representation. Figure 2.16 shows the normalised index comparison for H β on the top row and H β_0 on the bottom row, zoomed in to exclude 6 low [Fe/H] Turn-off stars. In Table 2.8 we show the numerical differences in response functions of H β and H β_0 indices for the three models tested in this study. Figure 2.16 reveals a stronger correlation of H β_0 with abundance pattern than found for H β . This is highlighted in the larger H β_0 responses to magnesium variations, seen in Table 2.8 (Column 8). Table 2.8 also shows that for all the models, H β_0 has a stronger sensitivity to overall metallicity (Columns 9

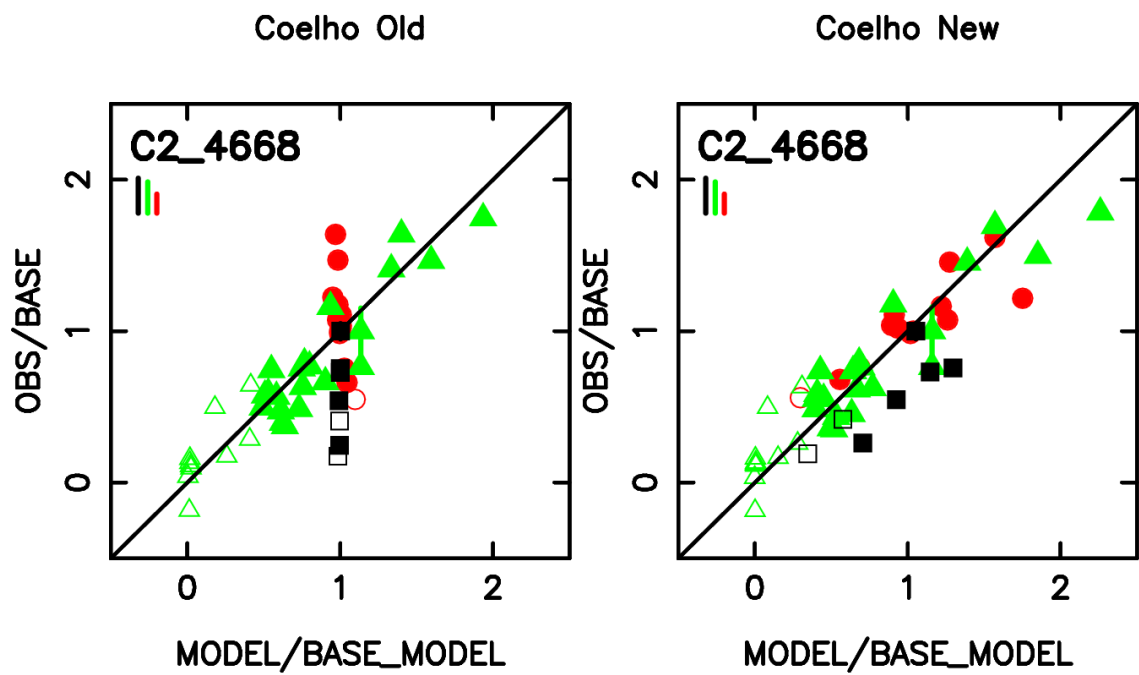


Figure 2.14: MILES Normalised Lick indices versus the Coelho (2014) models initially found in this study (Coelho Old) and the revised Coelho (Coelho New) models for C₂4668. Symbols and colours as in Figure 2.6.

CHAPTER 2

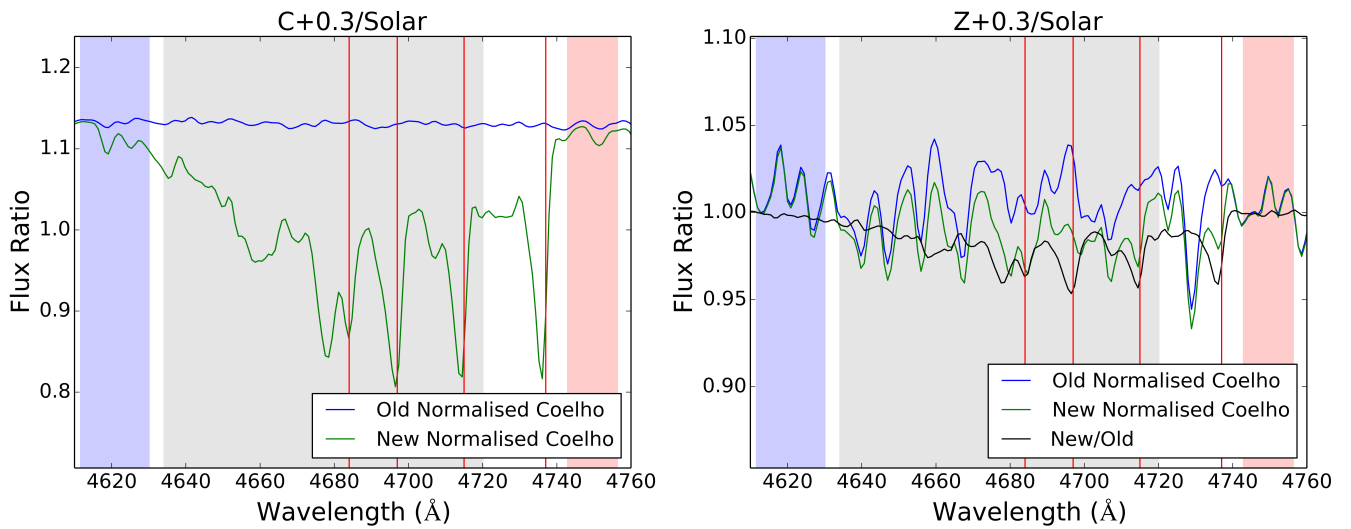


Figure 2.15: Spectral ratios in the C_{24668} region. The left plot shows a comparison between normalised spectra ($C+0.3/\text{Solar}$) for the Coelho old and revised Cool Giant models. The right plot shows a comparison between normalised spectra ($Z+0.3 \text{ Solar}$) for the Coelho old and revised Cool Giant models. In both plots the red vertical lines show positions of a few Swan Band (1,0) features and the blue, red and grey areas represent the blue continuum, red continuum and index band of the C_{24668} Lick index definition respectively.

CHAPTER 2

and 15), compared to $H\beta$, which is in agreement with the purely theoretical SSP models in Cervantes & Vazdekis (2009). However, Cervantes & Vazdekis (2009) (their Figure 2) also found that in SSP models computed entirely from empirical MILES stars, $H\beta_0$ is less sensitive to overall metallicity than $H\beta$. In summary, to make a conclusion about the true sensitivity of $H\beta_0$ to abundance pattern and overall metallicity in SSP models, would require a better understanding at the star level. A further investigation of the correlation of $H\beta_0$ with $[\alpha/\text{Fe}]$ and $[\text{Fe}/\text{H}]$ in a larger number of empirical stars, as well as an understanding of features present in the index bands of the models should shed light on the current problem of contradicting results between empirical and theoretical SSPs. Semi-empirical SSPs produced later in this thesis, for a large range of age, metallicity and $[\alpha/\text{Fe}]$ abundances may also help this issue, because SSPs will be computed for a larger range of $[\alpha/\text{Fe}]$ compared to the models tested in Cervantes & Vazdekis (2009). Visual differences between the two definitions and further discussion can be found in Vazdekis et al. (2015).

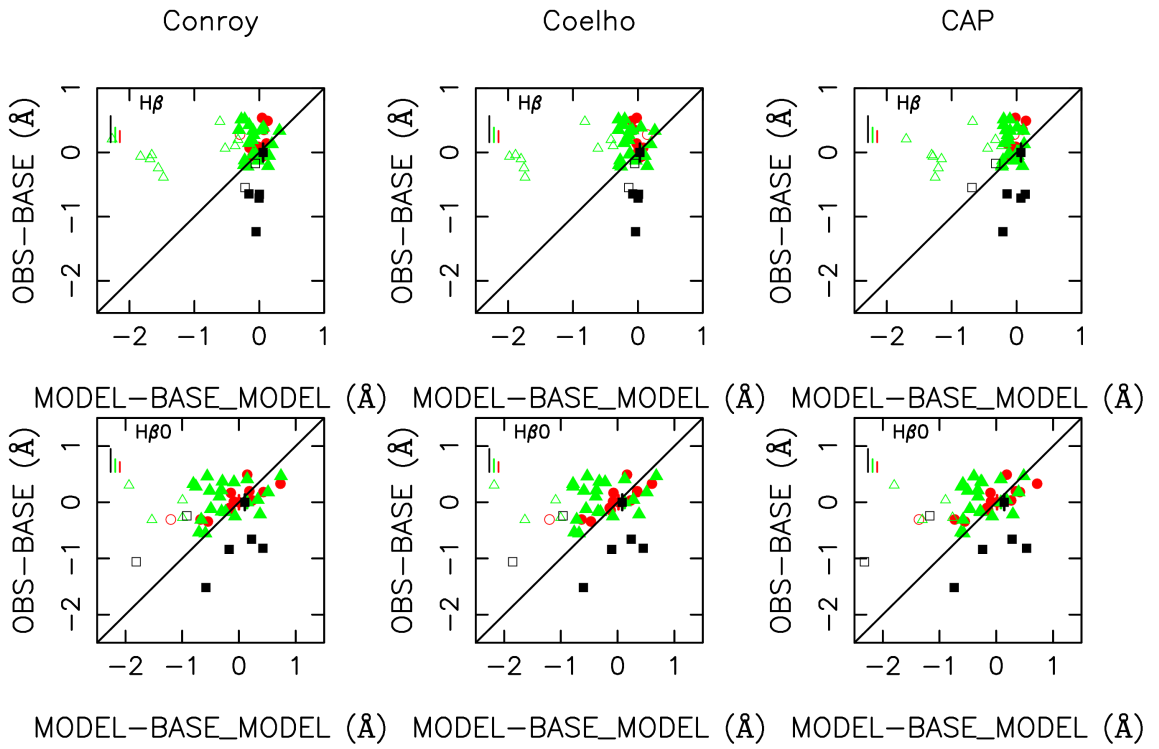


Figure 2.16: MILES Normalised Lick indices versus Conroy, Coelho and CAP Model Normalised Lick indices derived from response functions, for $H\beta$ and $H\beta_0$ indices. The three star types are shown in each case, with green triangles, black squares and red circles representing Turn-off, Cool Dwarf and Cool Giant stars respectively, as in Figure 2.1.

Table 2.8: Comparison between $H\beta$ and $H\beta_0$ response functions. Column 1 is the model, Column 2 is index, Column 3 is the units of the index, Column 4 is the model base star index strength and Columns 5-14 are the variation of the index strength when the element at the top of the column is increased by 0.3 dex (0.15 dex for C in Conroy models). The last column shows the variation of index strength when there is an overall metallicity increase of 0.3 dex. Blank columns show that the element was not varied by the modeller.

Model	Index	Units	I_0	C	N	O	Mg	Fe	Ca	Na	Si	Cr	Ti	[M/H]
Coelho Cool Dwarf	$H\beta$	Å	-0.21	-0.135	0.004	0.024	-0.176		-0.03					-0.048
Coelho Cool Dwarf	$H\beta_0$	Å	2.242	0.019	0.011	-0.001	-0.359		0.050					0.356
Coelho Cool Giant	$H\beta$	Å	-0.018	-0.187	0.014	0.083	-0.074		-0.012					-0.07
Coelho Cool Giant	$H\beta_0$	Å	2.801	-0.060	0.025	0.021	-0.190		0.016					0.438
Coelho Turn-off	$H\beta$	Å	3.768	-0.001	0.005	0.003	0.025		0.003					0.258
Coelho Turn-off	$H\beta_0$	Å	5.054	0.007	0.002	0.003	0.050		0.030					0.676
Conroy Cool Dwarf	$H\beta$	Å	-0.781	-0.100	0.007		-0.494	0.304	-0.021	0.046	0.046	-0.080	0.057	-0.116
Conroy Cool Dwarf	$H\beta_0$	Å	1.435	-0.101	0.013		-0.805	0.783	0.098	0.040	0.018	0.028	0.189	0.276
Conroy Cool Giant	$H\beta$	Å	0.218	-0.136	0.012		-0.171	0.313	0.007	0.007	0.052	-0.056	0.043	0.091
Conroy Cool Giant	$H\beta_0$	Å	3.222	-0.128	0.032		-0.286	0.539	0.040	0.006	0.030	0.022	0.207	0.544
Conroy Turn-off	$H\beta$	Å	3.547	-0.020	0.003		0.032	0.098	0.007	0.001	0.040	-0.030	0.081	0.253
Conroy Turn-off	$H\beta_0$	Å	4.853	-0.030	0.001		0.063	0.409	0.034	0.003	0.053	0.023	0.077	0.671
CAP Cool Dwarf	$H\beta$	Å	0.147	-0.427	0.000	0.170	-0.508	-0.111	-0.057	-0.021	-0.049	-0.114	0.108	0.019
CAP Cool Dwarf	$H\beta_0$	Å	2.127	-0.530	0.001	0.140	-0.799	0.315	-0.024	-0.033	-0.103	-0.001	0.186	0.332
CAP Cool Giant	$H\beta$	Å	0.449	-0.457	-0.001	0.336	-0.290	-0.071	-0.024	-0.009	-0.060	-0.093	0.187	0.117
CAP Cool Giant	$H\beta_0$	Å	2.710	-0.470	0.006	0.211	-0.452	0.166	-0.004	-0.013	-0.102	-0.015	0.229	0.526
CAP Turn-off	$H\beta$	Å	3.864	-0.034	0.001	0.013	-0.099	-0.182	-0.014	-0.004	-0.070	-0.044	0.072	0.157
CAP Turn-off	$H\beta_0$	Å	5.040	-0.083	0.001	0.016	-0.078	0.097	-0.002	-0.003	-0.042	-0.008	0.080	0.520

2.6.5 Model Strengths and Weaknesses

Comparisons between models were discussed in Sections 2.4 and 2.5. Here, we summarise the main strengths and weaknesses of each individual model compared to observations, in terms of absolute and differential behaviours.

We find that all three models do not fit the Balmer features well, in an absolute and differential analysis, with the greatest problems seen in cool stars models in an absolute sense (Figure 2.1) and in all star-types in a differential sense (Figure 2.6). All three models do quite well at predicting iron-sensitive features (Figures 2.2 and 2.7). All models tend to underpredict C_24668 line strengths in an absolute comparison (Figure 2.4). Calcium and sodium (Figures 2.5 and 2.10) sensitive features also show fairly good agreement with the data, with no clear systematics in both an absolute and differential sense, other than those noted below.

Conroy

Recall that in the absolute comparisons (Section 2.4), Conroy models were produced via interpolation in a pre-existing grid. Some systematic offsets between Conroy models and observations are seen in the absolute comparisons of magnesium-sensitive features, with the cool star models overpredicting feature strengths (Figure 2.3). Conroy Cool Giant and Turn-off models tend to overpredict magnesium-sensitive line strengths but show a good fit for Cool Dwarf stars, in the differential analysis (Figure 2.8). For CN_1 and CN_2 indices, Conroy cool star models overpredict line strengths in an absolute sense (Figure 2.4). In the differential case, Conroy cool star models show a smaller range than the data (Figure 2.9). Metal-poor Turn-off stars are underpredicted in CN_2 for Conroy models, in a differential analysis (Figure 2.9). Problems with Cool Dwarf models are found for C_24668 in the differential analysis, with problems found in the base star that results in some outliers (Figure 2.9). $Ca4455$ is overpredicted for all star types in an absolute sense (Figure 2.5)

CHAPTER 2

Coelho

Coelho models slightly overpredict cool star line strengths in magnesium-sensitive features for the absolute comparison (Figure 2.3) with overpredictions seen in the Cool Giant and Turn-off stars for the differential analysis (Figure 2.8). Coelho Cool Dwarf line strengths are fit well for the magnesium-sensitive indices in the differential analysis. CN and C₂4668 indices are fit well in the differential analysis for all star types (Figure 2.9). Coelho models also do well at fitting the CN indices in the absolute comparisons (Figure 2.4).

CAP

CAP models generally show good agreement in magnesium-sensitive features, for the absolute comparison (Figure 2.3), with very slight overpredictions seen in the Cool Giant stars. Overpredictions are seen for the Cool Giant and Turn-off stars for the differential analysis (Figure 2.8). CAP Cool Dwarf line strengths are fit well for the magnesium-sensitive indices in the differential analysis. CN and C₂4668 indices are fit well in the differential analysis for all star types (Figure 2.9). However, they overpredict cool star CN line strengths in the absolute comparisons (Figure 2.4).

2.7 Conclusions

In this Chapter, we have tested both the differential and absolute line-strength predictions of three state-of-the-art theoretical stellar model libraries, using empirical MILES stellar spectra. First, we directly tested three stellar model libraries, matching the parameters of T_{eff} , $\log g$, $[\text{Fe}/\text{H}]$ and $[\alpha/\text{Fe}]$ of MILES stars to study trends and aid the differential tests. We then used response functions to account for changes in $[\text{Fe}/\text{H}]$ and $[\alpha/\text{Fe}]$ abundances. The latest response functions calculated here are made publicly available in supplementary data online.

CHAPTER 2

In summary, we find that:

- Differences between models are generally less significant than the ways in which models vary from the data.
- All three models libraries do well at predicting abundance pattern effects in certain features, particularly those sensitive to iron and sodium.
- Problems exist in the Balmer features of all models, with overprediction of the variation in $H\delta$ and $H\gamma$ indices present in cool star models. There is no clear abundance pattern correlations shown in $H\beta$, however there is a weak abundance effect with $H\beta_0$ (See section 2.6.4).
- Using diagnostic index and spectral plots (like those shown in Figures 9 and 12) we identified a corrupted file of the transition D-A of C_2 , describing the Swan bands in Coelho (2014) models. This corrupted file was corrected for the present work. Section 2.6.3 (Figures 2.14 and 2.15) shows the effects of that corruption and its correction.
- As expected, the absolute differences between models and observations are generally worse than using the differential behaviour. This was investigated using the CAP Cool Giant models. In the application of these models, the differential approach produces less or similar scatter about the agreements with observations than the absolute predictions. In particular, the differential predictions of some hydrogen features are scattered by a factor of ~ 2 less than the absolute predictions. A large reduction in scatter between the two approaches is also seen in G4300 and $C_2 4668$ indices.
- In general, the largest differences between the observations and absolute model predictions are seen at lower temperatures, which may be explained by the

CHAPTER 2

omission of non-LTE and 3D geometry effects in all the models. The features that are largely affected in this temperature regime are the higher order Balmer features, with models overpredicting variations of line-strength index with abundance pattern in both differential and absolute predictions.

This chapter highlights the benefits of a differential approach to modelling abundance patterns. However it still has its limitations and errors that we have attempted to show in this chapter. Two caveats of this analysis have been highlighted in Section 2.6. We have not investigated if different stellar parameters for the MILES stars would affect our conclusions. We have also not attempted to study any abundances differences other than $[\alpha/\text{Fe}]$, such as C and N, which might affect the empirical stars but are not changed from scaled-solar in the models. As shown in the response tables in Appendix A, C and N have quite a large effect on the spectral indices, particularly in the blue. If more abundances are measured for MILES stars, these effects can be studied in future. However, it can be seen that different models produce slightly different predictions of abundance pattern effects, and awareness of this will be important in the application of these models. We have shown that using the models' differential predictions of abundance pattern effects produces a better agreement with observations than using the absolute predictions, particularly at bluer wavelengths. This finding will be used in the generation of a new semi-empirical model library of stars, that will make use of both observed spectra and differential predictions of theoretical spectra.

These results inform the choices in Chapter 3, where a new library of theoretical stellar spectra is produced.

Chapter 3

Generating a New High Resolution Theoretical Stellar Library

3.1 Introduction

This chapter describes the choices made and methods used in the generation of a new theoretical stellar library, that will be used to perform differential corrections to MILES stars. The choice to produce a new theoretical library, rather than using an existing one, was made to ensure the parameter coverage in both the fundamental parameters (T_{eff} , $\log g$ and $[M/H]$) and abundance pattern was sufficient to cover a large range of the existing empirical MILES library. The generation of new semi-empirical MILES stars will allow for SSPs to be built with abundance patterns that better match the observations of early-type galaxies. The final, high resolution theoretical model library, as well as a MILES resolution and sampling library, are presented. The codes and methods of generation are discussed first, followed by the pipeline of raw spectra processing and qualitative testing of the final grids.

3.2 Generating Theoretical Stellar Spectra

As described in Chapter 2 (section 2.2), the generation of theoretical stellar spectra requires two main processes : the model atmosphere calculation, followed by the radiative transfer of photons through the atmosphere to produce the emergent spectrum. Therefore, consideration for these two components was required. Based on the results obtained from testing of some of the most current and commonly used existing libraries, and the close collaboration with the modeller, the choice was made to follow the calculation method of Allende Prieto (described in detail in Mészáros et al. 2012 and Allende Prieto et al. 2018).

The model atmospheres used in this thesis were generated using ATLAS9. An example model atmosphere output of ATLAS9 is shown in Figure 3.1. Although in the future further abundance measurements for the MILES stars will be available, if we want to vary the abundances consistently in our synthetic spectra (i.e. in both processes of the computation), calculations of new ODFs with variable abundance patterns would be needed, which is a difficult and time consuming computationally. Instead, we compromise by computing stellar spectra with variable metallicity, carbon and α abundances for which recently computed ODFs already existed. The ODFs and model atmospheres used in this thesis are described in Mészáros et al. (2012) that are publicly available and were used for the APOGEE survey. The α elements we included are: O, Ne, Mg, Si, S, Ca and Ti. The ODFs and model atmospheres used in this work have Asplund et al. (2005) solar abundances with microturbulence of 2kms^{-1} .

Atmospheres used in this work have metallicity ranging from -2.5 to 0.5 in steps of 0.5 dex, for a range of carbon and α abundances presented later in this chapter. This covers a subsection of the MILES library. It is this region that is deemed reliable to interpolate in, given the distribution of MILES stars (see Figure 10 of Milone et al. 2011) and also see Quality Number (Q_n) in Figure 6 of Vazdekis et al.

CHAPTER 3

2015, originally defined in Vazdekis et al. 2010). Q_n gives a quantifiable measure of SSP spectra reliability, based on the density of stars around isochrone locations used in SSP calculations, with higher densities resulting in larger Q_n values. For the radiative transfer component of this work, we use ASS ϵ T (Advanced Spectrum SynthEsis Tool) (Koesterke 2009). ASS ϵ T is a package, consisting of a number of Fortran programs, which provide fast and accurate calculations of LTE and non-LTE spectra from 1D or 3D models. We use the 1D and LTE mode, with the input ATLAS9 atmospheres, to produce synthetic spectra (in the base, element-enhanced and element-deficient models). Important aspects of the models are summarised below.

- **Solar Abundances** - To maintain abundance consistency in the computation of spectra, we define abundances relative to Asplund et al. (2005) solar abundances in both ATLAS9 and ASS ϵ T.
- **Definitions of Abundances** - The models were computed with variable metallicity ($[M/H]$, $[\alpha/M]$ and carbon ($[C/M]$) abundances. $[M/H]$ here, like in Chapter 2, is defined as:

$$[M/H] = \log[n(M)/n(H)]_* - \log[n(M)/n(H)]_{\odot}, \quad (3.1)$$

where $n(M)$ is the number of nuclei of any particular element with Z greater than two, but not the summation of all, i.e. it applies to iron, lithium, potassium, and any one. $[M/H]$ here is defined as a scaled-metallicity in which all metals, apart from the α elements and carbon, are scaled by the same factor from the solar mixture (e.g. $[M/H]=0.2=[Fe/H]=[Li/H]$). This definition means $[\alpha/M]=[\alpha/Fe]$ and $[C/M]=[C/Fe]$.

- **ODFs** - To avoid complex computation of new ODFs with variable abundances, we generate models on a grid for which ODFs existed. Therefore, we were constrained to generate model atmospheres and synthetic spectra on the

CHAPTER 3



Figure 3.1: Example ATLAS9 Model Atmosphere output. Key sections and columns are labelled.

CHAPTER 3

existing grid points from the APOGEE survey. These grid points dictate the abundance pattern coverage presented later in this chapter.

3.2.1 Microturbulence

An important parameter in the computation of 1D stellar spectra is v_{turb} . Due to a limitation in the classical 1D models to fully treat the velocity fields present in stellar photospheres correctly, microturbulence is included to match the observed broadening of spectral lines (Struve & Elvey 1934; van Paradijs 1972). Treated as motions of mass below the mean free path of photons, microturbulence is usually modelled as a Gaussian distribution of velocity dispersion, which in turn produces Doppler shifts that mimic the effect of thermal motions. For weak lines that have typically Gaussian profiles, the effect of microturbulence is to increase the width and reduce the depth of the absorption line, producing no change in equivalent width. However, for strong and saturated lines for which absorption can occur in the damping wings of line profiles, microturbulence expands the wavelength range of possible absorption and results in the reduction of saturation and therefore increases the total absorption. Therefore, the choice of parameter is important because it can affect the resulting line-strengths when calculating synthetic spectra. Although the available ODFs, and therefore model atmospheres, were computed at 2kms^{-1} , v_{turb} can be varied in ASS ϵ T and therefore we considered the effect of this parameter on our grid. To investigate the effects of microturbulence on the absolute and differential application of theoretical line-strengths, we generated 3 sets of different star models with different v_{turb} values of 1kms^{-1} and 2kms^{-1} . The models represented Cool Dwarfs, Cool Giants and Turn-off stars. The full investigation is presented in Chapter 2 of this thesis. I summarise the results below.

In general, we found that Cool Dwarf line-strength indices were affected the least with typical absolute differences of 0.2\AA between 1kms^{-1} and 2kms^{-1} respectively.

CHAPTER 3

The effect was much greater on Cool Giant spectra with features differing by order 1-2Å with a change of v_{turb} from 1kms^{-1} to 2kms^{-1} . The effect is greater in Cool Giants, due to their lower surface gravity and therefore lower pressure broadening of spectral lines, resulting in narrower, less Gaussian-like line profiles, which are more affected by microturbulence (see above). The Turn-off stars were also significantly affected by v_{turb} changes. Despite the large absolute differences in line-strengths between v_{turb} of 1 and 2kms^{-1} , in all cases the effect of v_{turb} on the differential application of models was small ($\approx 0.02\text{\AA}$) compared to the observational errors on line-strengths ($\approx 0.1\text{\AA}$), shown in Chapter 2 (Table 2.3). Therefore, for work involving the semi-empirical library, which uses the models in a differential sense, the choice of v_{turb} is not as important as in the case of the models' absolute predictions.

We have shown, as well as other authors, that in absolute terms, v_{turb} can have a large effect on spectra (Conroy & van Dokkum (2012)). For any absolute application of our model grid, it will be important to make a careful consideration of this parameter. Two options for this parameter, common in previous libraries, would be to compute spectra at fixed v_{turb} (e.g. Conroy & van Dokkum 2012) or have a varying v_{turb} grid dimension (e.g. Allende Prieto et al. 2018). To reduce computation time, but to also incorporate v_{turb} values observed in real stars, we computed spectra with a varying microturbulence, depending on fundamental stellar parameters. As well as the study of line-strength effects, we investigated previous literature calibration equations.

We considered three equations present in the literature. These are:

$$v_{\text{turb}} \text{ (km/s)} = 2.478 - 0.325 \log g \quad (3.2)$$

$$v_{\text{turb}} \text{ (km/s)} = 0.871 - 2.42 \times 10^{-4}(\text{T}_{\text{eff}} - 5700) - 2.77 \times 10^{-7}(\text{T}_{\text{eff}} - 5700)^2 - 0.356(\log g - 4) \quad (3.3)$$

CHAPTER 3

$$\begin{aligned}
 v_{\text{turb}} \text{ (km/s)} &= 0.998 + 3.16 \times 10^{-4}(T_{\text{eff}} - 5500) - 0.253(\log g - 4) \\
 &\quad - 2.86 \times 10^{-4}(T_{\text{eff}} - 5500)(\log g - 4) + 0.165(\log g - 4)^2 \quad (3.4)
 \end{aligned}$$

Relation 3.2 was used by APOGEE (Holtzman et al. 2015) and was derived using a calibration subsample of red giants, but did not account for any relationship between effective temperature and v_{turb} . Relation 3.3 is from Thygesen et al. (2012) using a sample of 82 Red Giants in the Kepler field. This was a modified version of a previous calibration from Bruntt et al. (2012). Although this took into account both effective temperature and surface gravity effects, it was limited in that only Red Giants in a small T_{eff} range ($\approx 4000\text{-}5000\text{K}$) were used. In the figures below we refer to this equation as T12. Relation 2.4, from Dutra-Ferreira et al. (2016), was derived using a sample of Cool Dwarfs and Giants in the Hyades cluster and predictions of 3D models. Although in principle 3D models fully treat the velocity fields in a physically consistent way without the need of a microturbulence parameter, the calculated equivalent widths of lines from 3D models can be compared to 1D model predictions to obtain values for microturbulence. In the figures below we refer to this equation as DF16.

In general, based on the studies and observations mentioned above, the behaviour of v_{turb} with T_{eff} and $\log g$ follows the following criteria:

- v_{turb} is large ($\approx 4\text{kms}^{-1}$) for high T_{eff} ($\approx 6000\text{K}$) and low $\log g$ (≈ 2) (Figures 7 and 9 in Gray et al. 2001; Figure 1 in Montalbán et al. 2007). This value is larger than is reached by the APOGEE relation and therefore it would be unwise to use this calibration for our large parameter space grid.
- v_{turb} is smaller ($\ll 4\text{kms}^{-1}$) and can be as small as $< 1\text{kms}^{-1}$ at lower T_{eff} ($\approx 5000\text{K}$) and high $\log g$ (≈ 4.5) (Figure 5 in Ramírez et al. 2013)
- $v_{\text{turb}} \approx 2\text{-}3\text{kms}^{-1}$ at high T_{eff} ($\approx 7500\text{K}$) and high $\log g$ (≈ 4.0) (Figures 7 and

CHAPTER 3

9 in Gray et al. 2001; Figure 5 in Niemczura et al. 2015; Figure 5 in Ramírez et al. 2013). Generally this value is lower than present at high T_{eff} ($\approx 7000\text{K}$) and low $\log g$ (≈ 2.5) (Figure 1 in Montalbán et al. 2007).

- As seen in the observations from all studies considered, Giants have higher v_{turb} than Dwarfs.

Because our model grid spans a wide range of stellar parameter space, it was important to include (at least similar to the sense observed) the trends found in all three of the literature relations (3.2, 3.3 and 3.4) considered. The DF16 equation was calibrated using a sample of both Giant and Dwarf stars and included both T_{eff} and $\log g$ parameters. Therefore we used this form of relation 4, but with a slight modification of the cross term, such that:

$$v_{\text{turb}} \text{ (km/s)} = 0.998 + 3.16 \times 10^{-4}(T_{\text{eff}} - 5500) - 0.253(\log g - 4) - 2 \times 10^{-4}(T_{\text{eff}} - 5500)(\log g - 4) + 0.165(\log g - 4)^2 \quad (3.5)$$

We modified the cross term coefficient from 2.86×10^{-4} to 2×10^{-4} to better follow the trends of the relation 3.2 in the parameter range of APOGEE and satisfy the criteria above.

Figure 3.2 shows the difference between the original DF16 (red lines) and our DF16Mod (black lines) equations, for different values of T_{eff} . For $T_{\text{eff}}=5500\text{K}$, the equations are the same, so those two lines overlap.

Figure 3.3 plots our modified equation (black lines) and T12 equation (blue lines) for different values of T_{eff} along with the APOGEE calibration (green line). We conclude that it is important to include both effective temperature and surface gravity in the calibration, because observations and analyses (e.g. references given above) suggest that trends are present in both. Our modified relation (3.5) follows

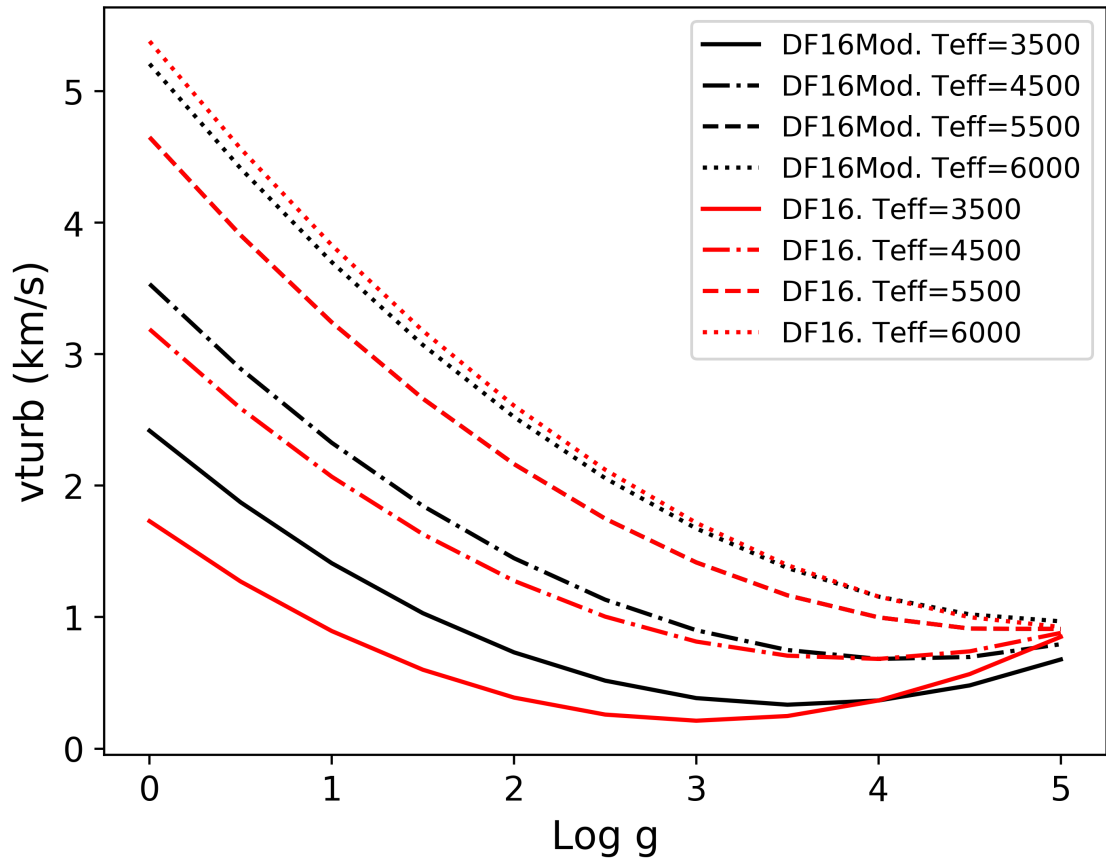


Figure 3.2: Microturbulence as a function of $\log g$ for the original Dutra-Ferreira et al. (2016) equation (DF16 Red lines) and the modified version of the equation (DF16Mod black lines) for values of T_{eff} . For $T_{\text{eff}}=5500\text{K}$, DF16=DF16Mod. The main difference can be seen at lower temperatures, where DF16Mod avoids dropping to unrealistically low values of v_{turb} . This modification better represents the trends found by observations.

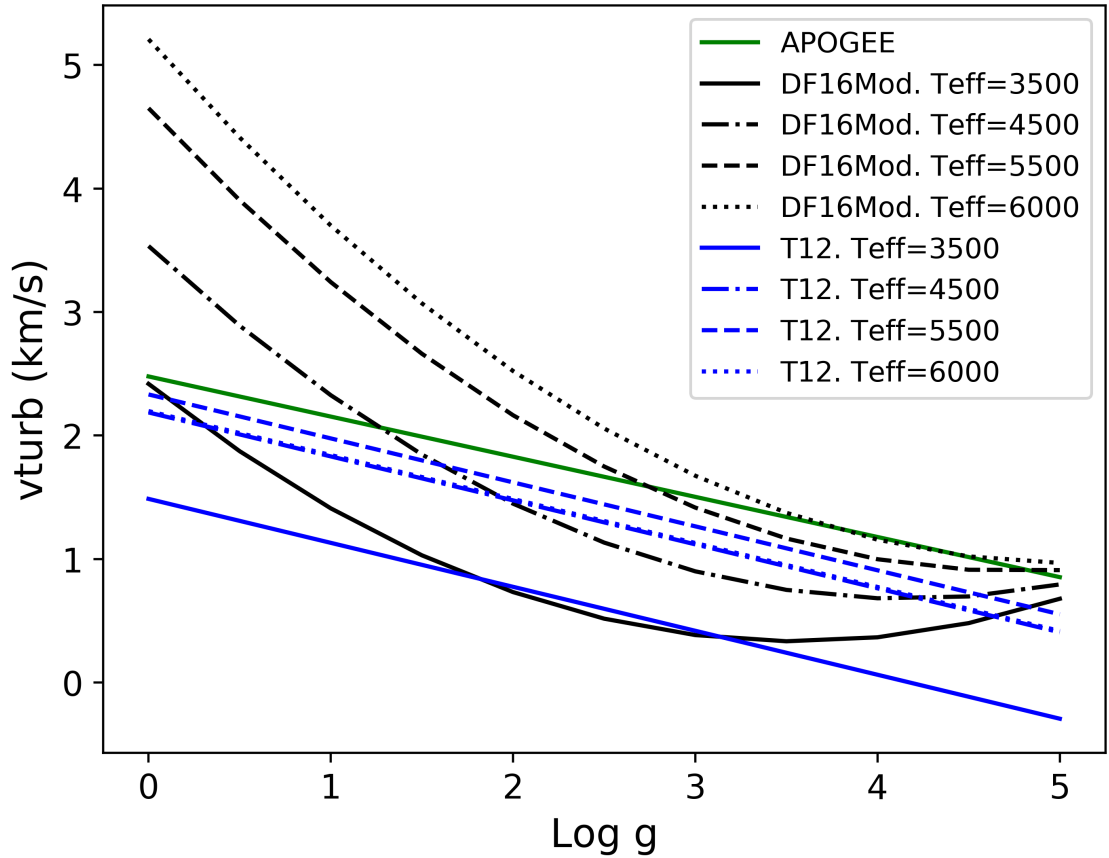


Figure 3.3: Microturbulence as a function of $\log g$ for the modified DF16 equation (DF16Mod. Black lines), the Thygesen et al. (2012) equation (T12. Blue lines) and the APOGEE equation (APOGEE. Green lines). Although the T12 equation appears to follow the linear behaviour of the APOGEE calibration well, problems arise at higher T_{eff} where the equation does not reach the higher values of v_{turb} observed at low $\log g$.

CHAPTER 3

the trends found in these studies as well as the APOGEE relation (3.2). We used our modified equation (3.5) for T_{eff} from 3500 to 6000K and for temperatures higher than this we lock the microturbulence to our relation (3.5) with a fixed $T_{\text{eff}}= 6000\text{K}$. We show the difference and RMS scatter between the APOGEE calibration and the our relation for the MILES parameters in Figure 3.4. This RMS scatter is small compared to the typical values of 1-2km/s found for v_{turb} in APOGEE (García Pérez et al. 2016).

3.2.2 Element Variation in Grids

The variation of element abundances in our grids of theoretical spectra are now discussed. The number of models needed was based on the number of varied elements, the range of variation and the grid steps we wished to take. This section discusses the grid chosen. It is important to be as consistent as possible in both the model atmosphere and synthetic spectrum codes. I specify what can be varied in each component.

- **Model Atmosphere (ATLAS9)** - $[M/H]$, $[\alpha/M]$ and $[C/M]$
- **Radiative Transfer (ASS ϵ T)** - $[X/H]$, where X can be any element from $Z=2$ to 99

To avoid computation of new ODFs, we were constrained to the existing ODF abundances of the ATLAS-APOGEE project. Therefore, variation of elements in the theoretical grid is driven by the ODFs and by the observations of abundance patterns in external systems (e.g. Şen et al. 2017, see Figure 1.2 in Chapter 1).

- $[\alpha/M]$ (from -0.25 to +0.75 in steps of 0.25 dex) - where $\alpha = \text{O, Ne, Mg, Ca, Si, S and Ti}$ to be consistent with the model atmosphere variations
- $[C/M]$ (from -0.25 to +0.25 in steps of 0.25 dex) - carbon abundance has a large impact on stellar spectra. Its atmospheric composition, relative to

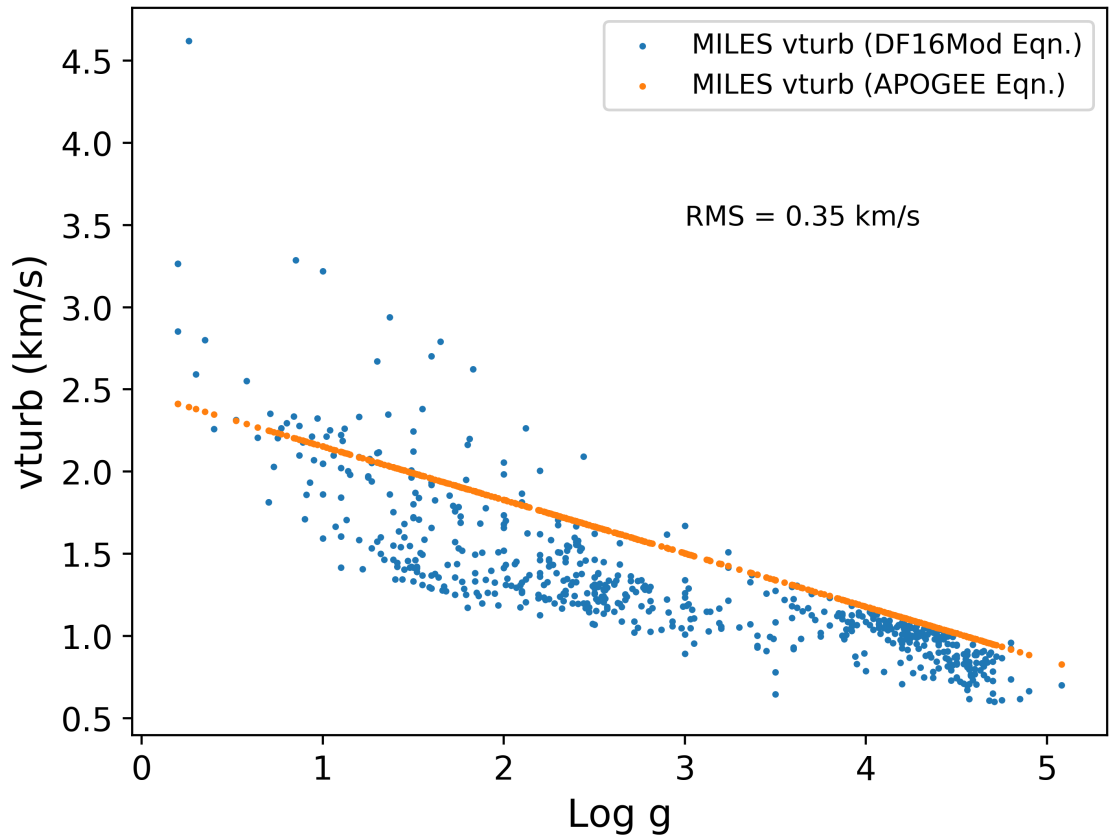


Figure 3.4: Microturbulence as a function of $\log g$ using the modified DF16 equation (DF16Mod blue points), and the APOGEE equation (APOGEE orange points) for the MILES stars with parameters of Cenarro et al. (2007). We also present the RMS scatter between the two estimates. For Dwarf stars, the DF16Mod agrees well with APOGEE, with deviations seen in Giant stars.

CHAPTER 3

oxygen, can lead to carbon stars. The balance of C and O is important in the molecular equilibrium of cool stars and the entire atmospheric structure changes significantly when C/O approaches one, producing carbon stars (Mészáros et al. 2012). Because carbon is separated and varied in the ODFs, it is possible to consistently vary carbon in the spectrum synthesis software, which may be used in future work that involves any carbon measurements of MILES stars.

The input line lists used in the computations are described in detail in Allende Prieto et al. (2018). I will summarise the information. Metal and molecular transitions are obtained from Kurucz¹. Molecules included in the calculation include H₂, CH, C₂, CN, CO, NH, OH, MgH, SiH, and SiO. TiO transitions are only included for stars below 6000K, as explained below.

For reasons explained below, we split the model grid into three smaller grids, based on the models' T_{eff} .

3500-6000K Grid

For our main grid, models were computed with the following parameter steps, such that:

- T_{eff} =3500K to 6000K in steps of 250K
- $\log g$ =0 to 5 in steps of 0.5 dex
- $[M/H]$ =-2.5 to +0.5 in steps of 0.5 dex
- $[\alpha/M]$ =-0.25 to +0.75 in steps of 0.25 dex
- $[C/M]$ =-0.25 to 0.25 in steps of 0.25 dex

¹<http://kurucz.harvard.edu/>

CHAPTER 3

Therefore, the number of models is

$$\begin{aligned}\text{Number of Models} &= T_{\text{eff}} \text{ steps} \times \log g \text{ steps} \times \text{Element Variations} \\ &= T_{\text{eff}} \times \log g \times [\text{M}/\text{H}] \times [\alpha/\text{M}] \times [\text{C}/\text{M}] \\ &= 11 \times 11 \times 7 \times 5 \times 3 = 12705 \text{ models}\end{aligned}$$

For these 12705 models, seven models were missing ODFs or did not converge. In order to maintain regularity of the grid, the missing models were computed using a linear interpolation of the nearest available grid points. The seven models generated via this interpolation were all at the lowest T_{eff} and highest $[\alpha/\text{M}]$ points:

- $T_{\text{eff}}=3500\text{K}$, $\log g=4.0$, $[\text{M}/\text{H}]=-2.0$, $[\alpha/\text{M}]=0.75$, $[\text{C}/\text{M}]=0.0$
- $T_{\text{eff}}=3500\text{K}$, $\log g=4.0$, $[\text{M}/\text{H}]=-2.0$, $[\alpha/\text{M}]=0.75$, $[\text{C}/\text{M}]=-0.25$
- $T_{\text{eff}}=3500\text{K}$, $\log g=4.5$, $[\text{M}/\text{H}]=-1.5$, $[\alpha/\text{M}]=0.50$, $[\text{C}/\text{M}]=-0.25$
- $T_{\text{eff}}=3500\text{K}$, $\log g=4.5$, $[\text{M}/\text{H}]=-1.5$, $[\alpha/\text{M}]=0.75$, $[\text{C}/\text{M}]=0.0$
- $T_{\text{eff}}=3500\text{K}$, $\log g=4.5$, $[\text{M}/\text{H}]=-2.0$, $[\alpha/\text{M}]=0.75$, $[\text{C}/\text{M}]=-0.25$
- $T_{\text{eff}}=3500\text{K}$, $\log g=5.0$, $[\text{M}/\text{H}]=-1.5$, $[\alpha/\text{M}]=0.50$, $[\text{C}/\text{M}]=0.0$
- $T_{\text{eff}}=3500\text{K}$, $\log g=5.0$, $[\text{M}/\text{H}]=-1.5$, $[\alpha/\text{M}]=0.75$, $[\text{C}/\text{M}]=0.25$

The main grid can be visualised in Figure 3.5, where the parameter coverage is presented.

For each spectrum in this main grid, using local machines at UCLan, the real time for computation on a single cpu was ≈ 1 hour, although particularly at the lowest temperatures this can increase to a few hours. Therefore, careful consideration of the number of spectra, the wavelength coverage, linelists used and number of abundance steps was necessary. A method to decrease computation time is to reduce the number of input atomic and molecular transitions. We did this for models above the upper T_{eff} of our main grid. For T_{eff} above 6000K, we removed a

CHAPTER 3

significant molecular contributor to the input linelists. TiO is prevalent in spectra at low temperatures, however at higher temperatures absorption features become weak. Figure 3.6 shows an example of the effect of removing TiO transitions from our models at various temperatures in the grid. As shown, the differences in the high resolution grid between the models at the highest temperatures is very small. We split our highest temperature models into two grids. We have a grid of models from 6250-8000K and a grid from 8250-10000K. The upper limit of these temperatures was chosen to cover a large proportion of the existing MILES library, in regions where stars that contain the most information regarding abundance patterns exist. The ODFs and model atmospheres available also make cuts to $\log g$ at the higher temperatures, that have increasing radiation pressure and therefore the lowest surface gravity models become unstable (e.g. see Figure 2 of Mészáros et al. 2012). Therefore, the number of models for our higher T_{eff} grids are as follows:

6250-8000K Grid

- T_{eff} =6250K to 8000K, in steps of 250K
- $\log g$ =1 to 5, in steps of 0.5 dex
- $[M/H]$ =-2.5 to +0.5, in steps of 0.5 dex
- $[\alpha/M]$ = -0.25 to +0.75, in steps of 0.25 dex
- $[C/M]$ =-0.25 to +0.25, in steps of 0.25 dex

Therefore the number of models in 6250-8000K grid

$$\begin{aligned} \text{Number of Models} &= T_{\text{eff}} \times \log g \times \text{Element Variations} \\ &= T_{\text{eff}} \times \log g \times [M/H] \times [\alpha/M] \times [C/M] \\ &= 8 \times 9 \times 7 \times 5 \times 3 = 7560 \text{ models} \end{aligned}$$

8250-10000K Grid

CHAPTER 3

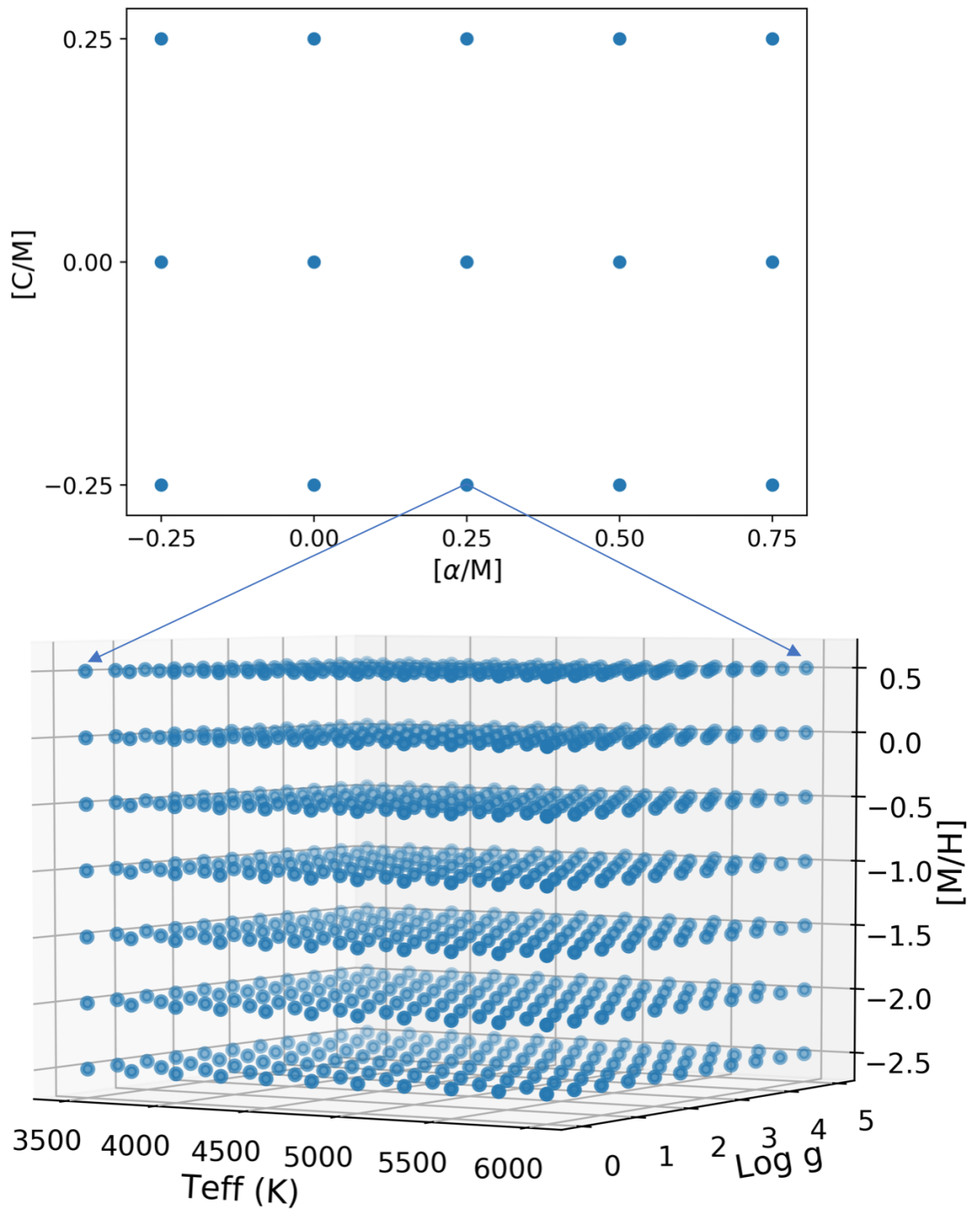


Figure 3.5: Top: Abundance pattern coverage in the $[C/M]$ vs $[\alpha/M]$ plane. Bottom: 3D stellar parameter coverage of 3500-6000K grid. Each point in the $[C/M]$ vs $[\alpha/M]$ plane represents $11 \times 11 \times 7 = 847$ models in the lowest T_{eff} grid.

CHAPTER 3

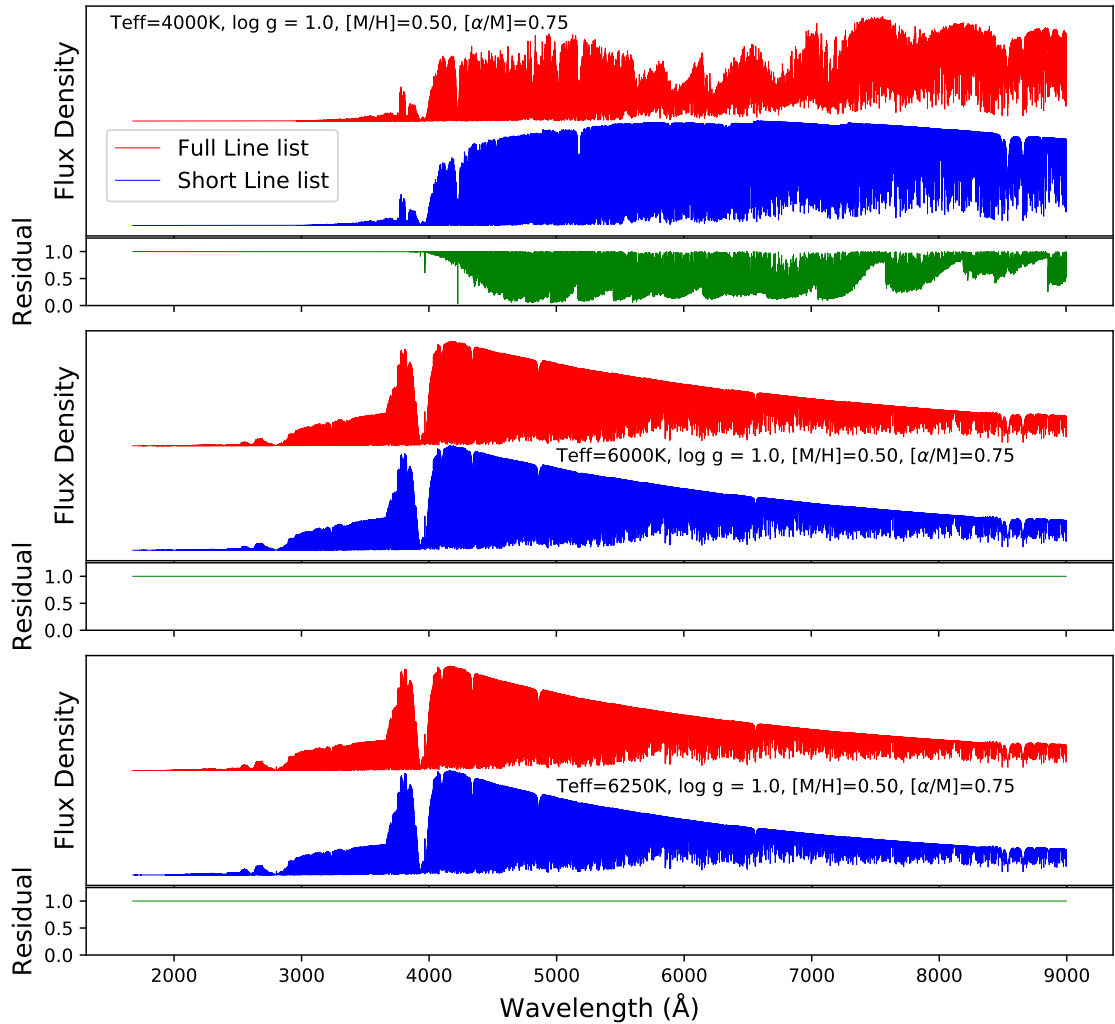


Figure 3.6: Effect of removing TiO lines from molecular line list at the different temperatures, for the high resolution grid. The red and blue spectra represent stars with the TiO line list included and removed for each temperature, respectively. The green line represents the residual obtained from a division of Full line list and Short line list spectra. Differences in the top panel ($T_{\text{eff}}=4000\text{K}$) are seen in locations known to be affected by TiO absorption (see Figure 5a of Kirkpatrick et al. 1991; Figure 1 of Plez 1998; Figure 1 of Allard et al. 2000).

CHAPTER 3

- $T_{\text{eff}}=8250\text{K}-10000\text{K}$ in steps of 250K
- $\log g=2$ to 5, in steps of 0.5 dex
- $[M/H]=-2.5$ to $+0.5$, in steps of 0.5 dex
- $[\alpha/M]=-0.25$ to $+0.75$, in steps of 0.25 dex
- $[C/M]=-0.25$ to 0.25 , in steps of 0.25 dex

Therefore the number of models in 8250-10000K grid is

$$\begin{aligned}\text{Number of Models} &= T_{\text{eff}} \times \log g \times \text{Element Variations} \\ &= T_{\text{eff}} \times \log g \times [M/H] \times [\alpha/M] \times [C/M] \\ &= 8 \times 7 \times 7 \times 5 \times 3 = 5880 \text{ models}\end{aligned}$$

No models in the two higher T_{eff} grids had missing ODFs or convergence issues.

[Ca/Fe]=0 Grid

We also compute a small model grid with $[Ca/Fe]=0.0$ to match results of integrated light studies of early-type galaxies in which calcium was found to track iron-peak elements (O'Connell (1976); Worthey (1994); Vazdekis et al. (1997); Trager et al. (1998); Thomas et al. (2003a); Schiavon (2007); Johansson et al. (2012); Conroy et al. (2014)).

- $T_{\text{eff}}=3500\text{K}$ to 6000K , in steps of 250K
- $\log g=0$ to 5, in steps of 0.5 dex
- $[M/H]=-2.5$ to $+0.5$, in steps of 0.5 dex
- $[\alpha/M]=0.25$, where α is O, Ne, Mg, Si, S and Ti
- $[C/M]=0.25$ - as was found by Conroy et al. (2014)

CHAPTER 3

We test the $[\text{Ca}/\text{Fe}]=0.0$ grid in Figure 3.7, where we plot the difference in the calcium-sensitive Ca4227 Lick index for $[\text{Ca}/\text{Fe}]=0.0$ compared to $[\text{Ca}/\text{Fe}]=0.25$, for a $T_{\text{eff}}=4500\text{K}$, $\log g = 2.0$, $[\text{M}/\text{H}]=0.0$ and $[\text{C}/\text{M}]=0.25$ spectrum. Both spectra were computed with $[\alpha/\text{M}]=0.25$, but with calcium removed from the α -capture group in the $[\text{Ca}/\text{Fe}]=0.0$ spectrum. Spectra in this plot are blurred to an illustrative resolution of 1.36\AA , like that of the INDO-US library. As expected the $[\text{Ca}/\text{Fe}]=0.25$ spectrum has a stronger Ca4227 index with a difference of $\approx 1.27\text{\AA}$. We present an example of part of our final, high resolution theoretical grid as follows: We show the 2D abundance variation grid in $[\alpha/\text{M}]$ vs $[\text{C}/\text{M}]$ space in the top of Figure 3.5. Each point in this 2D plot can be split into points of the 3D plot in T_{eff} , $\log g$ and $[\text{M}/\text{H}]$ at the bottom of the Figure 3.5, for the 3500-6000K grid. For the higher T_{eff} grids, each point in the $[\text{C}/\text{M}]$ vs $[\alpha/\text{M}]$ represents $8 \times 9 \times 7 = 504$ models and $8 \times 7 \times 7 = 392$ models in the 6250-8000K and 8250-10000K grid respectively.

In summary, four libraries of theoretical stellar spectra were computed. The first grid, named the 3500-6000K grid, was computed with 11 steps in effective temperature (from 3500 to 6000K in steps of 250K, 11 steps in surface gravity (from 0-5 in steps of 0.5 dex), 7 steps in metallicity $[\text{M}/\text{H}]$ in a range that covered a large proportion of the MILES empirical library, 7 steps in $[\alpha/\text{M}]$ in a range that covered a range of α abundance variation observed in external systems such as early-type galaxies and dwarf spheroidals (see Figure 1.2) and 3 steps in $[\text{C}/\text{M}]$ in a range that covered observations in previous integrated light studies (Conroy et al. 2014). The second grid, named the 6250-8000K grid, was computed with the same coverage in metallicity, $[\alpha/\text{M}]$ and $[\text{C}/\text{M}]$ as the 3500-6000K grid, but with 8 steps in effective temperature (6250 to 8000K in steps of 250K), 9 steps in surface gravity (1 to 5 in steps of 0.5 dex) to avoid unstable model atmospheres caused by radiation pressure instabilities and a reduced linelist in which TiO was removed. The third library, named the 8250-10000K, was computed with the same coverage in metallicity, $[\alpha/\text{M}]$

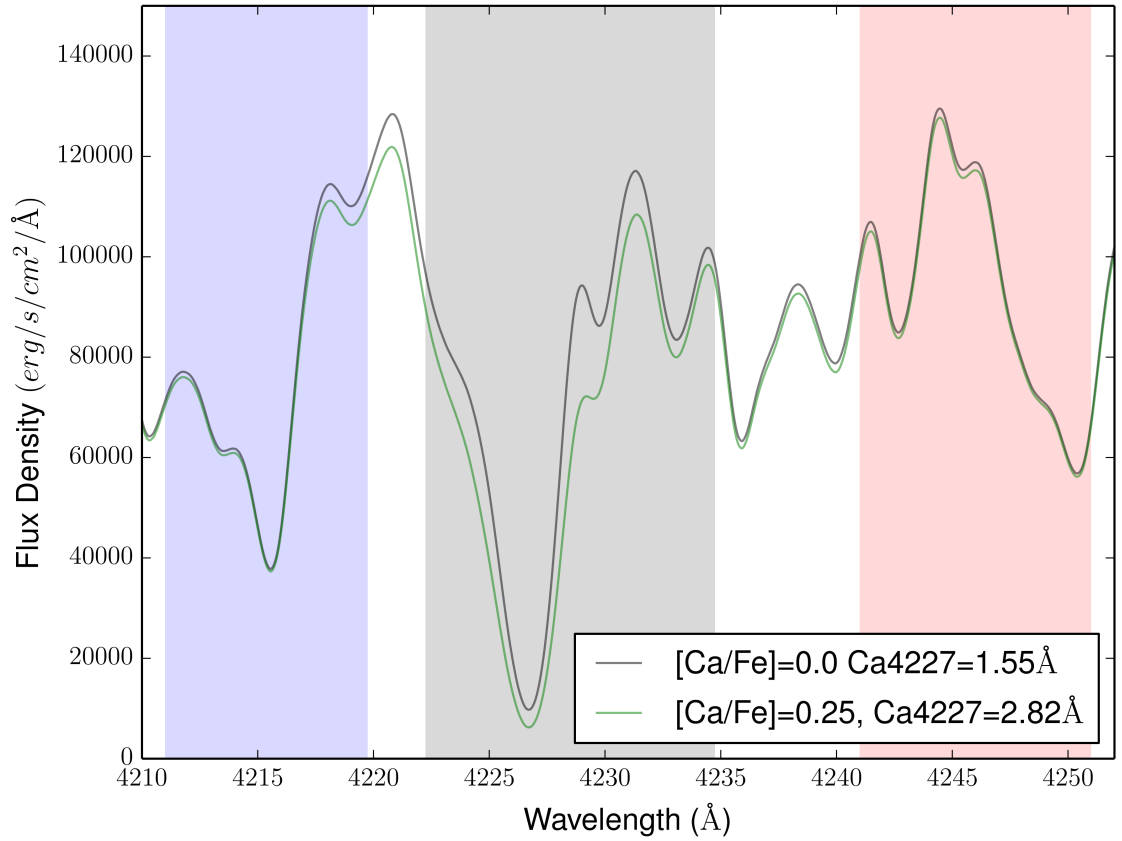


Figure 3.7: Comparison of $[\text{Ca}/\text{Fe}]=0$ and $[\text{Ca}/\text{Fe}]=0.25$ spectra in the Ca4227 Lick index region for the library, blurred to FWHM of 1.36\AA . The blue, red and grey areas represent the blue continuum, red continuum and index band of the Lick definition, respectively. The stars have parameters $T_{\text{eff}}=4500\text{K}$, $\log g=2.0$, $[\text{M}/\text{H}]=0.0$ and $[\text{C}/\text{M}]=0.25$ and $[\alpha/\text{M}]=0.25$, but the $[\text{Ca}/\text{Fe}]=0.0$ spectrum has calcium removed from the α group.

CHAPTER 3

and $[C/M]$ as the 3500-6000K grid, but with 8 steps in effective temperature (8250 to 10000K in steps of 250K), 7 steps in surface gravity (2 to 5 in steps of 0.5 dex) to avoid unstable model atmospheres caused by radiation pressure instabilities and a reduced linelist in which TiO was removed. The final grid, named the $[Ca/Fe]=0.0$ grid to investigate studies of early-type galaxies, in which calcium was found to track iron-peak elements, was computed with the same effective temperature, surface gravity, metallicity, $[\alpha/M]$ and $[C/M]$ coverage as the 3500-6000K grid, but with calcium removed from the α -capture group and put into the Fe-peak group, in the spectral synthesis stage.

3.2.3 Computation

Stellar spectral models were computed at the grid points described above. The wavelength range of the models was guided by the starting value of the extended MILES library ($\approx 1680\text{\AA}$) (Vazdekis et al. 2016) and the inclusion of the calcium triplet (CaT) features (at 8498, 8542 and 8662 \AA), to allow for investigation of IMF variations in early-type galaxies. This means that I generate a high resolution ($\delta\lambda = 0.05\text{\AA}$) theoretical library that spans the wavelength range of 1680-9000 \AA . However, for the semi-empirical library, we will be limited to producing semi-empirical stellar spectra with the current MILES wavelength range of 3500-7500 \AA . The model input files, consisting of a master file and a file specifying the abundances, and directory structure were set up using bash scripts and python codes, producing a single spectrum in a single directory that was numbered according to the looping structure in T_{eff} , $\log g$ and $[M/H]$ per $[C/M]$ and $[\alpha/M]$ step. Computations were made on Linux machines based at UCLan, with both individual local and higher performance machines used.

3.3 Processing

I now describe methods and procedures of processing raw spectra from ASS ϵ T into our final high resolution theoretical grid, as well as the MILES FWHM theoretical grid.

ASS ϵ T generates an \approx 20-30 mb .dat file in a directory structure. This file contains information regarding the input components, sampling used and also presents the resulting spectrum in a row format of wavelength (in units of \AA) and flux density measured at the stellar surface (in units of $\text{erg/s/cm}^2/\text{\AA}$). Python programs were made to extract wavelength and flux values and create columned format .txt files for each spectrum, needed for the next step. For reduction of file size, spectra were converted to .fits format using IRAF task ‘rspectext’, taking the log of the starting wavelength and sampling per spectrum of

$$d(\log_{10} \lambda) = \frac{\log_{10}(\lambda_{end}) - \log_{10}(\lambda_{start})}{n_{\lambda} - 1}, \quad (3.6)$$

where λ_{end} , λ_{start} and n_{λ} are the end wavelength, starting wavelength and number of wavelength points respectively. The log sampling is constant for each individual spectrum, as spectra are computed at constant resolving power. This results in constant $d(\log_{10} \lambda)$ but $d\lambda$ increases for increasing λ .

The next step involves rebinning raw spectra to a common $d\lambda$. ASS ϵ T samples the spectrum based on the formula:

$$0.3\sqrt{(v_{DOP}^2 + v_{TM}^2)}, \quad (3.7)$$

where v_{DOP} is the microturbulence and v_{TM} is the thermal Doppler width. This formula ensures the sampling of at least three wavelength points for the expected line width of the spectrum, but means that every spectrum was computed at slightly different sampling. I show in Figure 3.8 how the largest linear sampling (at the largest wavelength) varies as a function of T_{eff} for the grid. I used the IRAF task

CHAPTER 3

‘dispcor’ to rebin the raw spectra to a common starting and end wavelength as well as number of wavelength points. The common sampling was taken as the largest sampling value in the raw spectra. This resulted in spectra with $\lambda_{start} = 1677.10\text{\AA}$, $d\lambda=0.05\text{\AA}$ and $n_\lambda=146497$.

To create synthetic spectra that replicate existing MILES stars, on which differential corrections will be performed, I use the interpolation mode of the software package FERRE (Allende Prieto et al. 2006). Designed to match spectral models to observed data in order to obtain best fitting parameters of stars, FERRE contains routines that allows interpolation within model grids. FERRE was used to interpolate in our theoretical grid to the MILES stars in T_{eff} , $\log g$, $[\text{Fe}/\text{H}]$ and $[\alpha/\text{Fe}]$ as well as enhanced MILES stars, that had the same fundamental parameters as the original MILES stars but different abundances in α -capture elements (O, Ne, Mg, Ca Si, S and Ti). Ratios between enhanced and original MILES star models provide the differential response that is applied to create a library of semi-empirical stars, described in Chapter 4. In order to use FERRE, grid files must be generated containing all theoretical spectra in a line-by-line format. Python codes were used to generate the files, with an example structure of the 3500-6000K grid file shown in Figure 3.9. This file contains the spectra for the final high resolution theoretical library, with spectra binned to the same fine sampling. Three files are generated for the 3500-6000K, 6250-8000K and 8250-10000K grids. To assist with the interpolations, performed within grids later in this thesis, higher T_{eff} grid files were structured so that they overlapped. I took slices of the lower grids so that the publicly available, final high resolution grid files are for temperatures of 3500-6000K (with 12705 models), 6000-8000K (with 8505 models) and 8000-10000K (with 6615 models). Figure 3.9 shows the looping structure of the file as well as grid properties such as the number of dimensions, number of wavelength points, starting wavelength and sampling. The structure of this grid allows one to know the order of

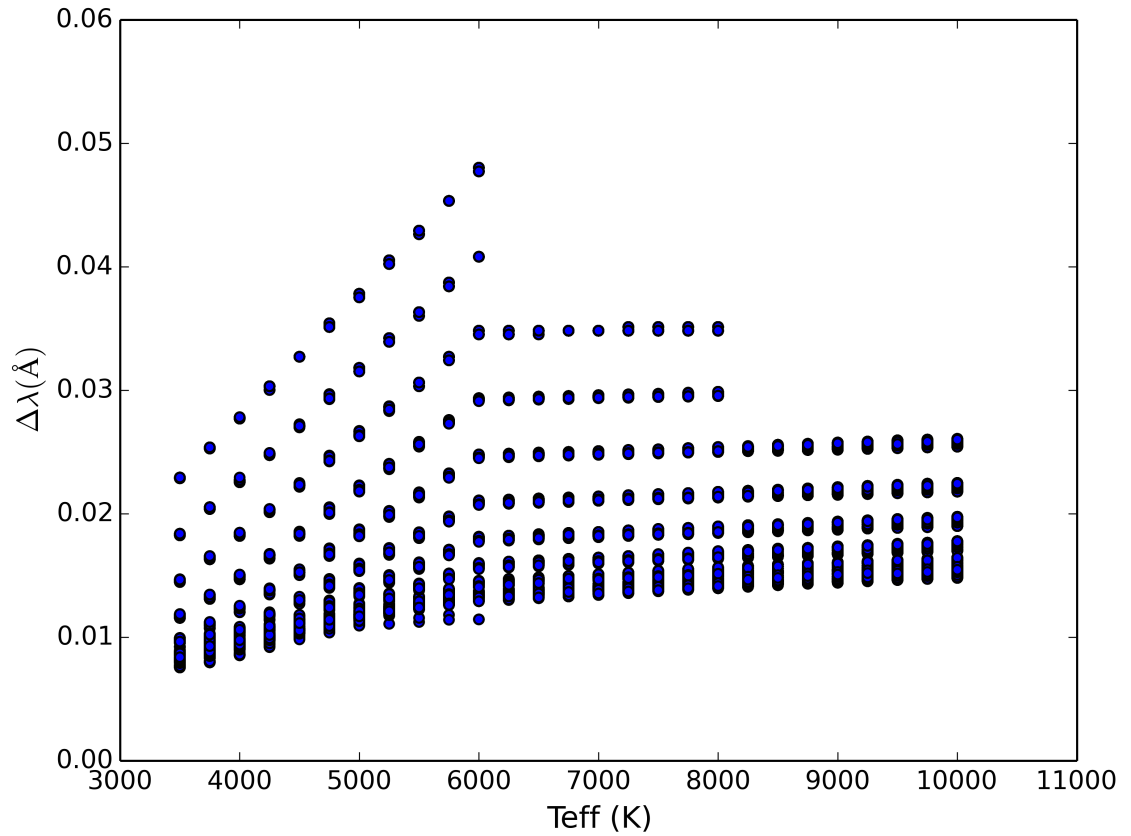


Figure 3.8: Largest wavelength ASS ϵ T sampling (in linear λ space) as a function of T_{eff} . Discontinuities at 6000K and above are caused by locking vturb for spectra above 6000K to the value produced from relation (3.5) with $T_{\text{eff}}=6000\text{K}$.

CHAPTER 3

```
&SYNTH
SYNTHFILE_INTERNAL = '3500RawGrid.dat'
ID = '3500Grid'
N_OF_DIM = 5
N_P = 7 5 3 11 11
LABEL(1) = 'METALS'
LABEL(2) = 'O Ne Mg Si S Ca Ti'
LABEL(3) = 'C'
LABEL(4) = 'TEFF'
LABEL(5) = 'LOGG'
LLIMITS = -2.5 -0.25 -0.25 3500 0.0
STEPS = 0.5 0.25 0.25 250 0.5
NPIX = 146497
WAVE = 1677.1 0.05
LOGW = 0
/
2.90652877766e-07 1.64888803056e-07 2.78591272718e-07 1.95505364786e-07 2.44667717197e-07 2.9
```

This is the input FERRE data file name.

This is the ID assigned to the input FERRE data file.

Figure 3.9: Extract of 3500-6000K FERRE model data files. The 4th, 5th, 11th and 12th lines give the number of grid dimensions, number of steps of each dimension in order of the subsequent LABEL lines, lower limits of the dimensions and the step size of each dimension respectively. NPIX gives the number of wavelength points and WAVE gives both starting wavelength and sampling respectively, both in Å. Therefore, the first flux values that appear on line 17 will be for a spectrum with parameters $[M/H]=-2.5$, $[\alpha/M]=-0.25$, $[C/M]=-0.25$, $T_{\text{eff}}=3500\text{K}$ and $\log g=0$ and the second spectrum on line 18 will have parameters $[M/H]=-2.5$, $[\alpha/M]=-0.25$, $[C/M]=-0.25$, $T_{\text{eff}}=3500\text{K}$ and $\log g=0.5$.

CHAPTER 3

spectra in the file. With FERRE used to match high resolution theoretical spectra to lower resolution observations, routines to blur large numbers of spectra are also available. IDL routines, provided by Carlos Allende Prieto, that work with FERRE data files were used to blur the high resolution theoretical library to MILES FWHM of 2.5\AA . The final step of processing is to match the grids to MILES wavelength range and sampling of $3540.5\text{-}7409.6\text{\AA}$ and 0.9\AA , respectively. This was performed with a routine that we added into the existing IDL code. The result is three model grid files at MILES wavelength scale and resolution. Models of existing MILES stars and MILES stars with different abundance patterns are created via interpolation in these MILES specific grids (Chapter 4).

3.4 Testing Theoretical Grid

I now test several components of the grid to check the computations. I investigate sequences of spectra in both high and MILES resolution libraries, in the wavelength range of MILES and extremes of our computed models. These sequences focus on variations in one parameter to check that trends of our library match expected behaviours of previous libraries and observations. Through spectral plots and index measurements I check that the grid correctly predicts qualitative changes to spectra due to changes of both stellar parameters and element abundances.

3.4.1 Effective Temperature

I plot sequences of T_{eff} from our grid that range from 3500K to 9500K . The figures are for solar $[\text{M}/\text{H}]$, $[\text{C}/\text{M}]$ and $[\alpha/\text{M}]$ abundances and giant ($\log g=2.0$) stars. In Figure 3.10 we plot the full MILES wavelength range of our models. The sequence shows that larger T_{eff} models have larger continuum contributions and therefore

CHAPTER 3

higher overall flux densities. Also shown in Figure 3.10, albeit less clearly, is a reduction in the wavelength of peak flux with increasing temperature, which can be to first order approximated as a correct estimation of Wien’s law. Also correctly estimated in the spectra in Figure 3.10 is the location of the Balmer jump in the spectra at 3647\AA , with the largest jumps seen in the hottest stars. In Figure 3.11, I focus on a particular T_{eff} -sensitive feature, namely the Lick index $H\delta_F$. The highest temperature spectra here correspond to spectral type A. Spectra in Figure 3.11 are normalised to the flux at 4065.2\AA , which is a wavelength in the blue side band in the Lick index definition, away from any strong features. In Figure 3.12, I show an effective temperature sequence for the theoretical library for a known IMF probe, TiO_2 . This index strength increases as effective temperature decreases and therefore the IMF sensitivity arises from the ratio of low mass (low effective temperature) to high mass stars on the main sequence (Fontanot et al. 2018). As expected, TiO bands are extremely prevalent in the lowest T_{eff} spectrum. Figure 3.12 also shows that the strongest Lick absorption index is present in the lowest effective temperature spectrum plotted, with decreasing index strength for increasing temperature. Although TiO lines have been removed for spectra $>6000\text{K}$, this trend is expected anyway, because the effect of TiO is small at the highest temperatures.

3.4.2 Surface Gravity

I check surface gravity dependence on our model grid by plotting sequences of $\log g$ for a 4500K , $[\text{M}/\text{H}]=[\text{C}/\text{M}]=[\alpha/\text{M}]=0$ spectrum in Figure 3.13. Although more difficult to see the effect of surface gravity, the sequence plotted is as expected with gravity-sensitive features appearing stronger in the higher $\log g$ stars. This increase can be explained by increased pressure broadening due to increased surface gravity. Pressure broadening can be described as a collisional broadening process, in which interactions between atoms shortens the lifetime of emission and thus increases the

CHAPTER 3

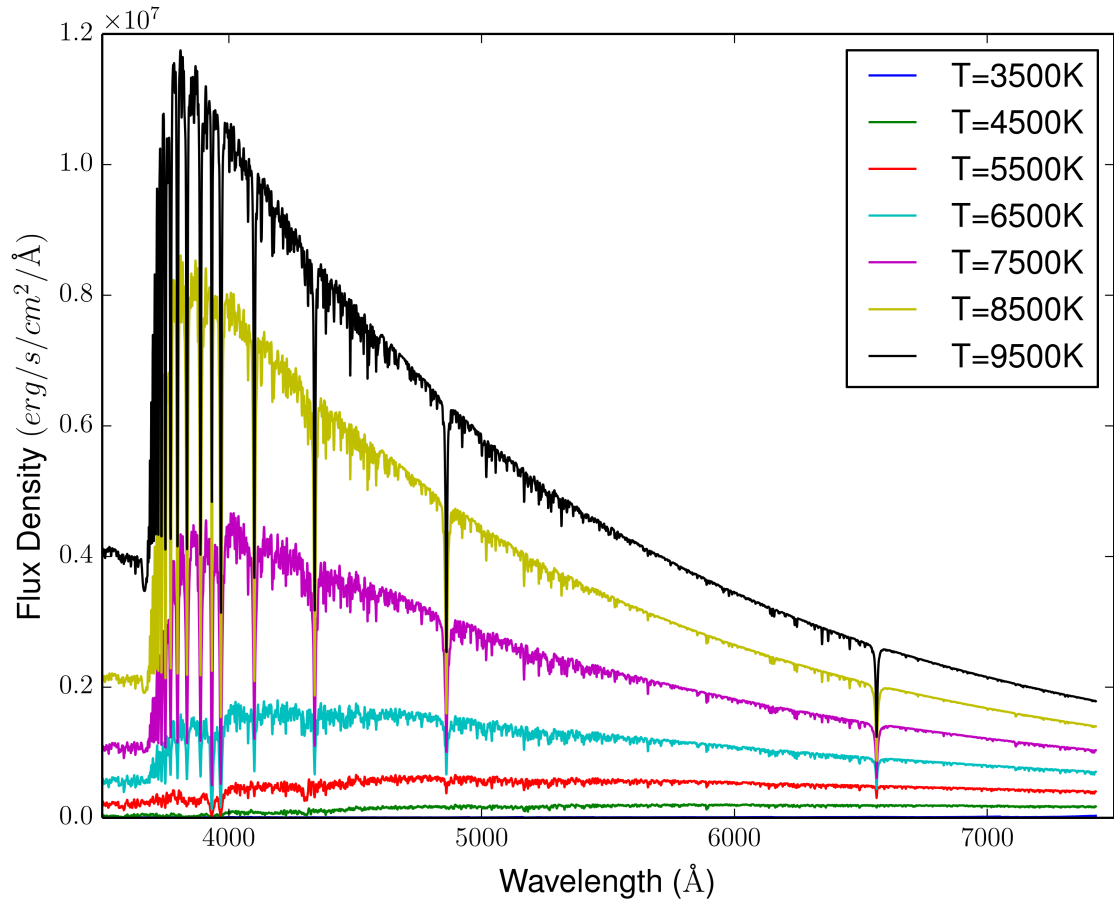


Figure 3.10: Spectral sequence of effective temperature from the theoretical library, blurred to MILES resolution and showing the MILES wavelength range. In this figure, the lowest T_{eff} spectrum lies close to zero and is therefore not visible. The behaviour is as expected, with highest T_{eff} models showing the highest continuum contribution. The stars have parameters $\log g=2.0$ and $[M/H]=[C/M]=[\alpha/M]=0$.

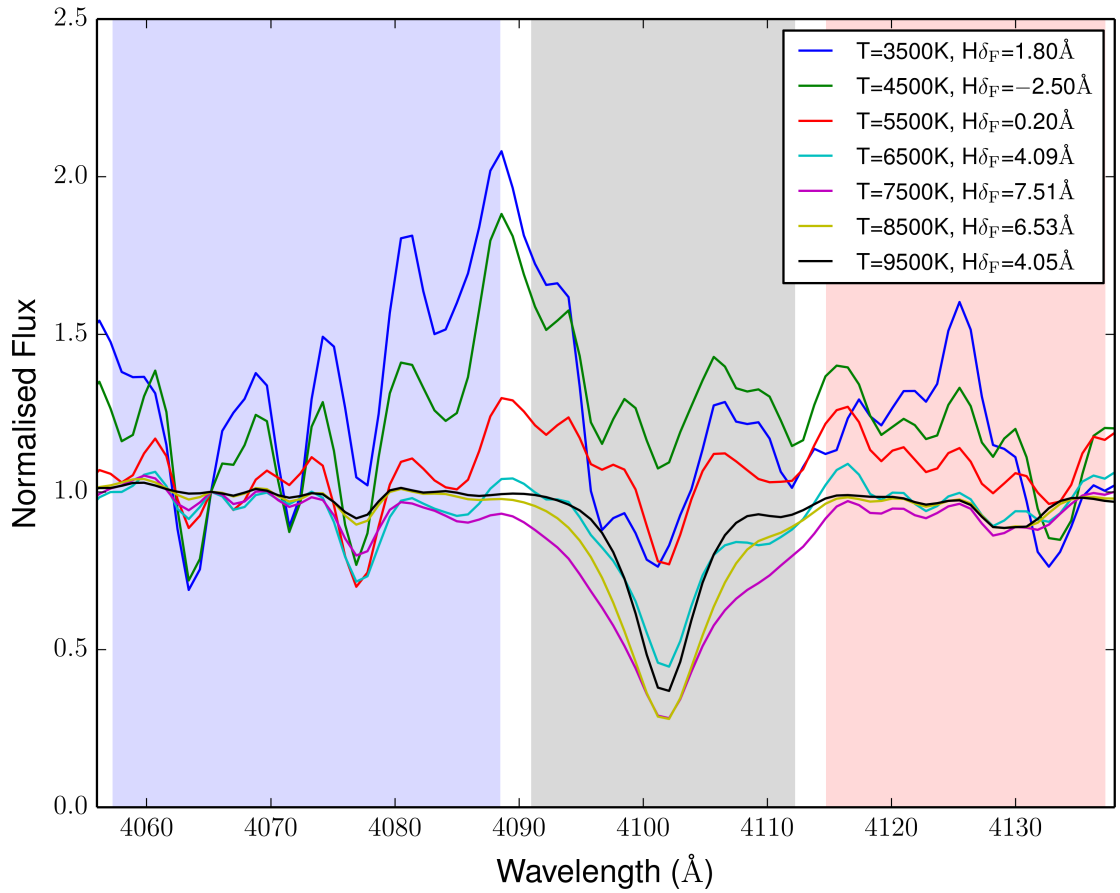


Figure 3.11: Effective temperature spectral sequence from the MILES resolution theoretical library in the $H\delta_F$ Lick index region. The blue, red and grey areas represent the blue continuum, red continuum and index band of the Lick definition respectively. Spectra are normalised to the flux at 4065.2\AA . The $T_{\text{eff}}=7500\text{K}$ model shows the strongest absorption feature.

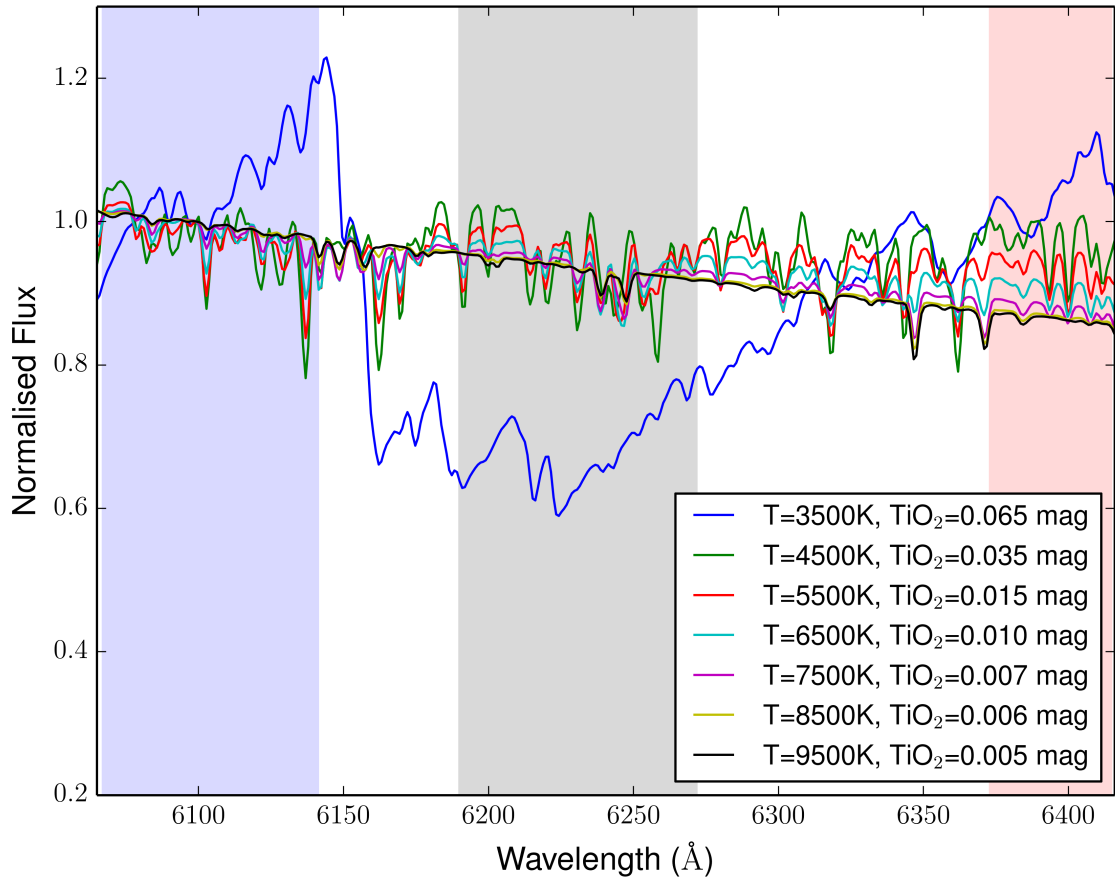


Figure 3.12: Effective temperature spectral sequence from the MILES resolution theoretical library in the TiO_2 Lick index region. The blue, red and grey areas represent the blue continuum, red continuum and index band of the Lick definition respectively. Spectra are normalised to the flux at 6099.2\AA . Lowest T_{eff} models show the strongest Lick absorption index, as expected. Note here that TiO lines were removed from the input to spectra with $T_{\text{eff}} > 6000\text{K}$, but the effect of including TiO at these temperatures is minimal (Figure 3.6).

CHAPTER 3

uncertainty in the characteristic energy of emission (natural broadening). This can be seen in more detail in Figures 3.14 and 3.15 where I plot the surface gravity sequence of our library, in the region of a well known sodium sensitive feature, that is also known to be sensitive to IMF slope (La Barbera et al. 2013), index Na_D and an IMF probe, TiO_2 . As expected, the Na_D index strength increases, as well as the line-width, with increasing surface gravity. This result highlights the use of Na_D for IMF variations in integrated light studies, with the strength of this index depending on dwarf to giant star ratios in stellar populations. It is important to note that Na_D is more strongly sensitive to Na abundance, but its use with IMF probes that are also sensitive to Na abundances to a lesser extent, such as Na8190, Na1.14 and Na2.21 (Conroy & van Dokkum 2012; La Barbera et al. 2013), helps to separate abundance and IMF effects in stellar population modelling (La Barbera et al. 2017). As expected, there is almost no surface gravity dependence seen in Figure 3.15, with TiO_2 , because as shown in section 3.4.1, this index is a IMF probe through its sensitivity to effective temperature. In Figure 3.16, I investigate known gravity sensitive indices in the infrared. I plot in the region of Ca1, Ca2 and Ca3 that are defined in (Cenarro et al., 2001a). Here we see an increasing index strength with decreasing surface gravity, apart from $\log g=5.0$, which shows a slight increase, although the cores of the lines are shallowest in the $\log g=5.0$ spectrum. This increase may be caused by our microturbulence equation (3.5), in which v_{turb} decreases from $\log g=0$ to 4 and then begins to increase when $\log g$ reaches 5, as well as differences in the side band predictions of the $\log g=5.0$ spectrum. On the other-hand, most of the work done previously on this feature has not measured CaT for stars with $\log g=5.0$, so the expected behaviour is not well defined at such high values of surface gravity and the effect may be real. The index behaviour of the models agrees with the observations of (Diaz et al., 1989) (and references therein) for $\log g \sim 0$ to 4.0, that showed the CaT absorption feature strength increasing with

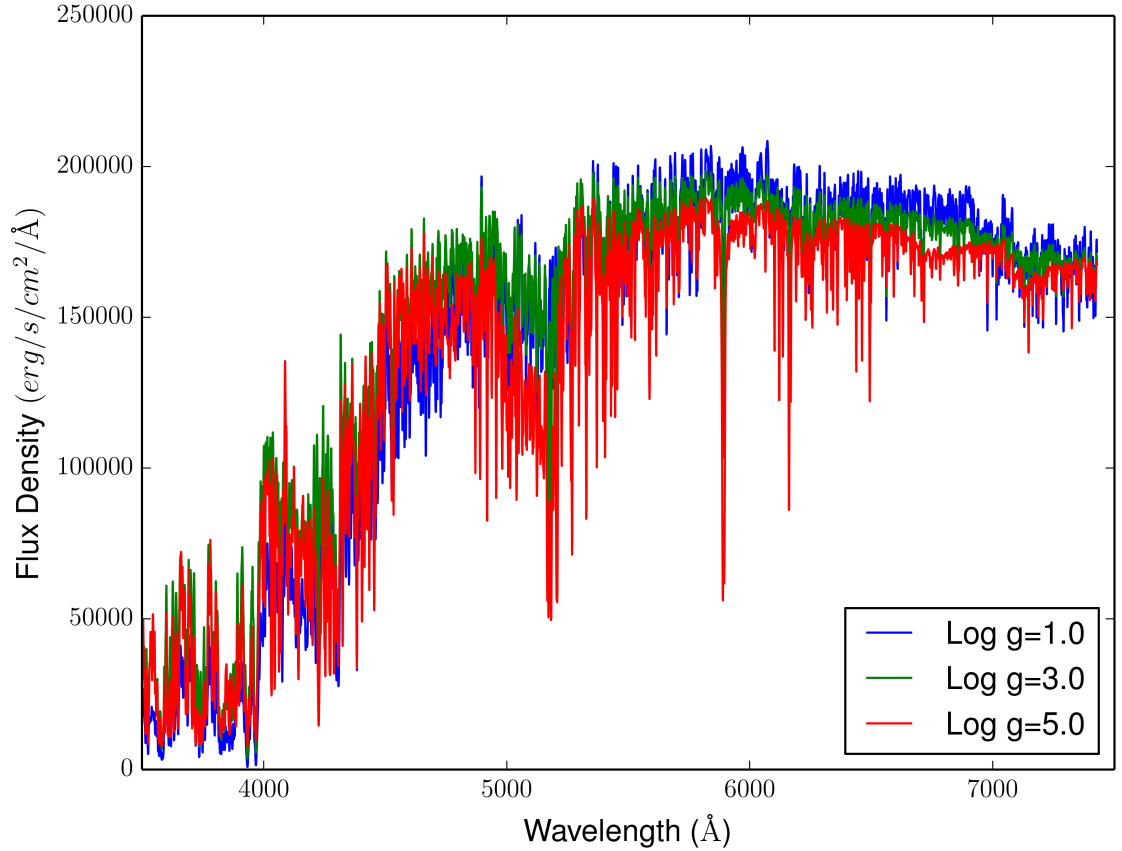


Figure 3.13: Spectral sequence of surface gravity from the MILES resolution and wavelength theoretical library. Stars have parameters $T_{\text{eff}}=4500\text{K}$ and $[M/H]=[C/M]=[\alpha/M]=0$.

decreasing surface gravity, particularly for stars at solar metallicity and above. This observation has been used in integrated light studies to investigate the changes in the IMF of early-type galaxies (e.g. Cenarro et al. 2003; Conroy & van Dokkum 2012; La Barbera et al. 2013)

3.4.3 [M/H]

Through $[Fe/H]$ measurements of MILES stars, we will be interpolating in our grid to match the star in fundamental stellar parameters and changing abundance ratios

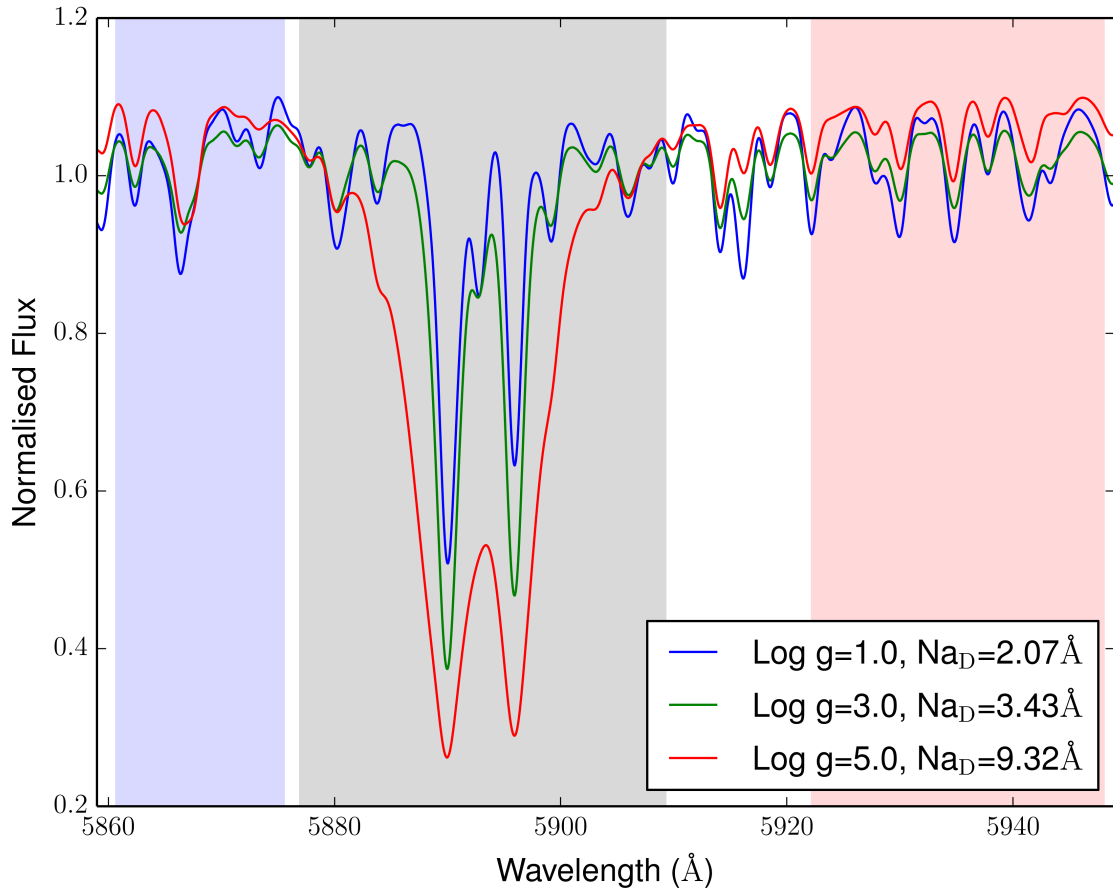


Figure 3.14: Spectral sequence of surface gravity from the library in the Na_D Lick index region. The Lick index values, measured using LECTOR, are also presented. The blue, red and grey areas represent the blue continuum, red continuum and index band of the Lick definition, respectively. Spectra are blurred to the FWHM of 1.36 \AA . The stars have parameters $T_{\text{eff}}=4500\text{K}$ and $[\text{M}/\text{H}]=[\text{C}/\text{M}]=[\alpha/\text{M}]=0$.

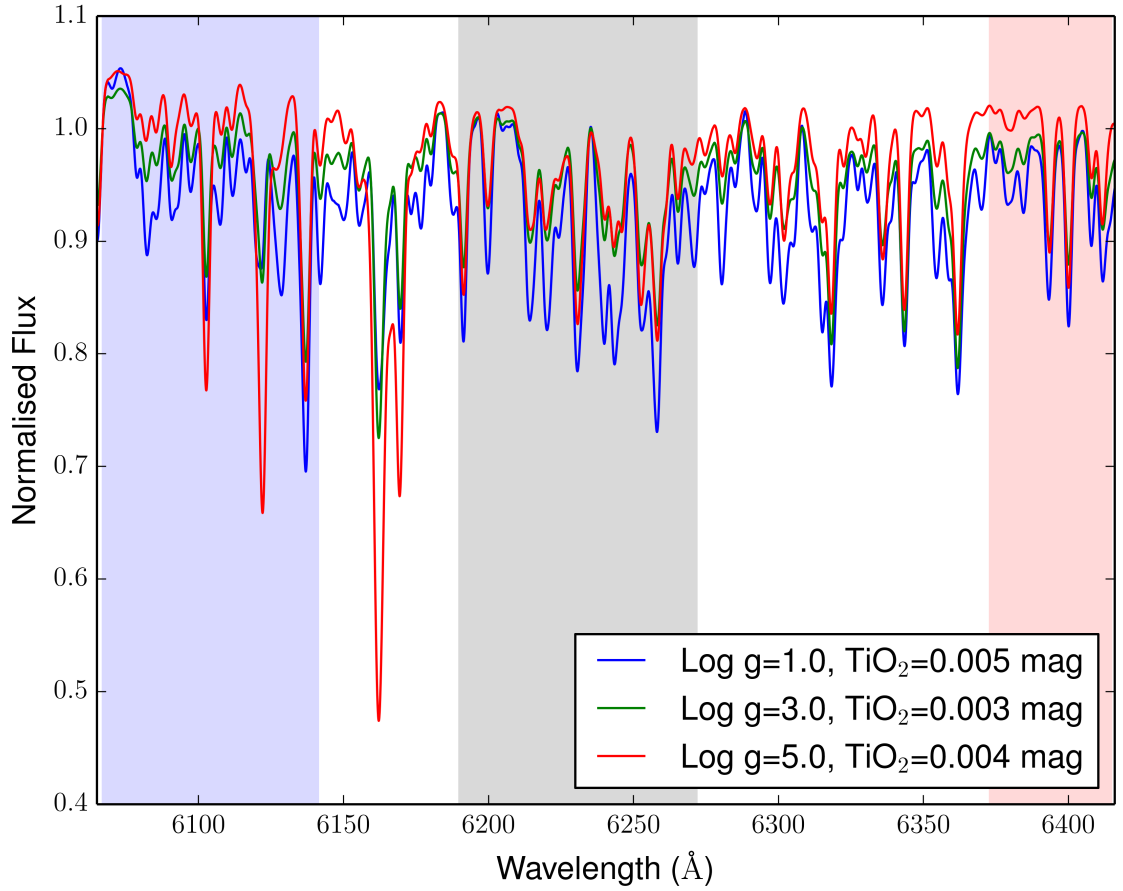


Figure 3.15: Spectral sequence of surface gravity from the MILES resolution theoretical library in the TiO₂ Lick index region. The index values, are also presented. The blue, red and grey areas represent the blue continuum, red continuum and index band of the Lick definition, respectively. The stars have parameters $T_{\text{eff}}=4500\text{K}$ and $[M/H]=[C/M]=[\alpha/M]=0$.

CHAPTER 3

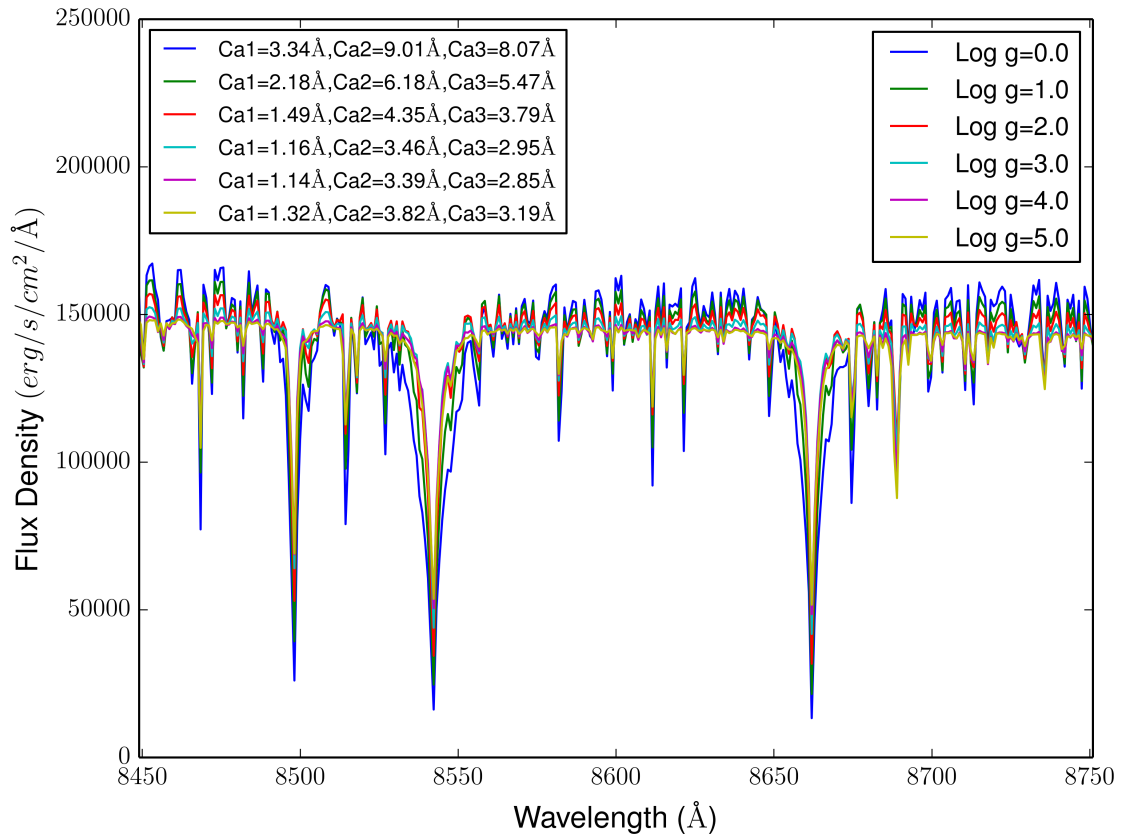


Figure 3.16: Spectral sequence of surface gravity from the high resolution library in the CaT region. The index, defined in (Cenarro et al., 2001a), values are also presented. The stars have parameters $T_{\text{eff}}=4500\text{K}$ and $[M/H]=[C/M]=[\alpha/M]=0$.

CHAPTER 3

to create semi-empirical stars that are non-Milky Way like in chemistry. I investigate metallicity dependencies on our grid by plotting the parameter range of metallicity computed. In Figure 3.17, I vary $[M/H]$ for a $T_{\text{eff}}=4000\text{K}$, $[C/M]=[α/M]=0$ giant star spectrum for the full MILES wavelength range. As expected, increasing metallicity reduces global continuum contributions due to increased absorption throughout the spectral range shown, due to the increase presence of molecular bands (e.g. TiO). I plot the sequence in a strong metal-sensitive Lick index region, Fe5270, in Figure 3.18. Not only the absorption feature, but side continua are effected by overall metallicity changes, seen in the $[M/H]=0.5$ spectrum offset. Also in Figure 3.18, I show Lick index strength variations with metallicity. The quantitative behaviour of the library agrees with previous works, with the Fe5270 index value increasing with increasing metallicity.

Besides the optical regime, I have created spectra that extend into the UV where observations and modelling of stellar populations in early-type galaxies found a UV-upturn, thought to be caused by extreme horizontal branch stars (e.g. Code & Welch 1979; Dorman et al. 1995; Hernández-Pérez & Bruzual 2014; Vazdekis et al. 2016). The UV has a plethora of features, which may be exploited to probe abundance patterns. For example, Fanelli et al. (1990); Fanelli et al. (1992), outlined a large amount of spectral features, with sensitivity to both iron-peak and α -capture elements. Other authors have also defined Lick-like indices (e.g. Chavez et al. 2007; Maraston & Strömbäck 2011; Serven et al. 2011). I investigate the effect of metallicity on the UV wavelength regime in Figure 3.19, where I plot regions of iron-sensitive indices Fe2332 and Fe2402 defined in Fanelli et al. (1990). In both indices, there is an increase in index strength from $[M/H]=-2.5$ to $[M/H]=-0.5$ and then a decrease from $[M/H]=0.0$ to $[M/H]=0.5$. In Figure 3.20, I plot another UV region. An index that is a blend of Al and Fe lines and therefore is expected to increase with metallicity, BL1853 (Fanelli et al. 1990; Fanelli et al. 1992; Maraston et al. 2009), is

CHAPTER 3

Table 3.1: 1930 and BL1853 (Fanelli et al. 1990) spectral indices definitions, presented in Figure 3.20.

Index	Blue Passband	Index Passband	Red Passband
1930	1915-1925Å	1928-1942Å	1945-1950Å
BL1853	1803-1823Å	1838-1868Å	1885-1915Å

present as well as a large feature at ≈ 1930 Å. To investigate this, I define a Lick-style index in the region around the main absorption feature. The definition is presented in Table 3.1, with the BL1853 index. For BL1853, Maraston et al. (2009) reported an increase in SSP index strength with decreasing temperature below spectral type A0 and (Vazdekis et al., 2016) reported a sensitivity to increased metallicity on a SSP level at ages older than ≈ 1 Gyr (their Figure 18). I report an opposite behaviour with our theoretical spectra, with BL1853 decreasing with increasing metallicity. This could be caused by limited linelists in this regime, with the models created mainly for use in the optical and infrared (García Pérez et al. 2016; Allende Prieto et al. 2018). For 1930, I find an increase in index strength for increasing metallicity between $[M/H]=-2.5$ to -1.0 , and then a decrease from $[M/H]=-0.5$ to 0.5 . This feature appears to the present in the SSP models in (Vazdekis et al., 2016), with a similar behaviour present, e.g. an increase in feature strength for increasing metallicities at the lowest metallicity and then a decrease in strength for increasing metallicity at super solar values (their Figures 15, 16 and 17).

3.4.4 $[\alpha/M]$

Because we plan to use predictions of how α variations affect MILES spectra, it is important that the grid can reproduce the expected effect of this group. To check this, I plot a sequence of $[\alpha/M]$ in Figures 3.21, 3.22 and 3.23 for a 4000K, $[M/H]=[C/M]=0$ giant ($\log g=2.0$) star to isolate the effects of α abundances. In

CHAPTER 3

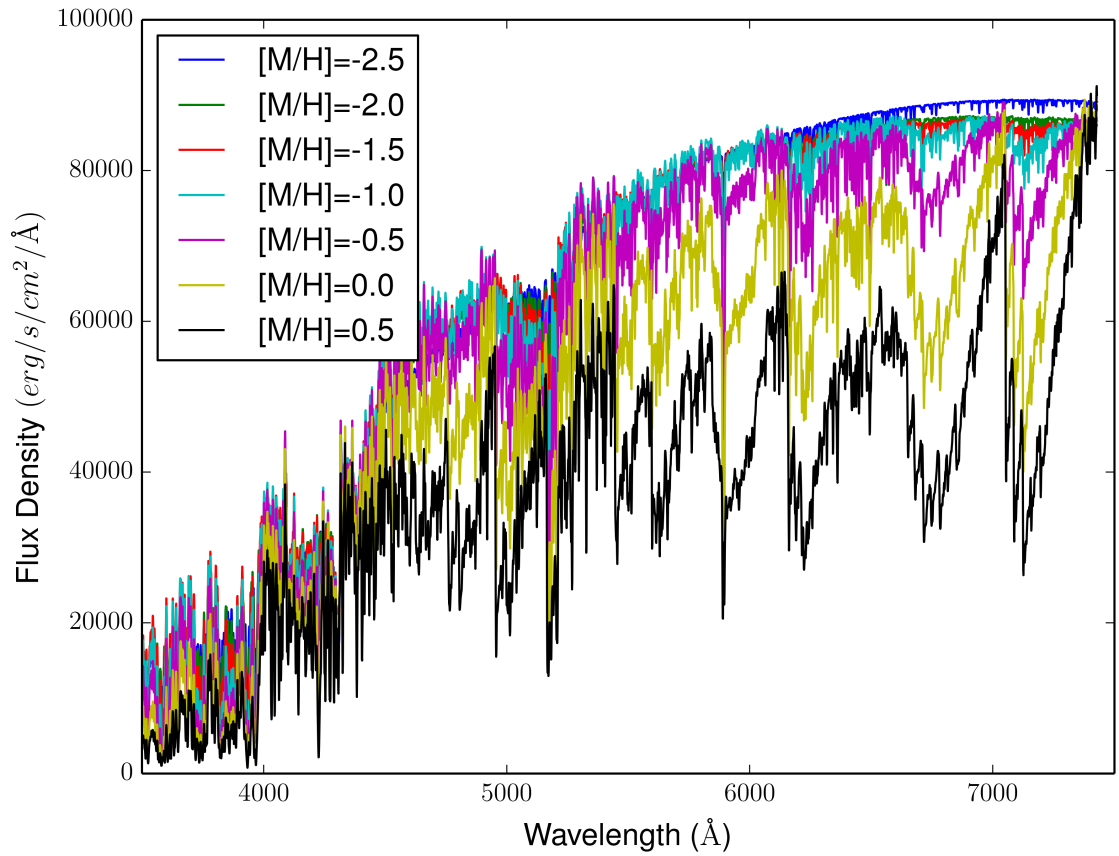


Figure 3.17: Spectral sequence of metallicity on the MILES resolution and wavelength range library. Stars have parameters $T_{\text{eff}}=4000\text{K}$, $\log g=2.0$ and $[\text{C}/\text{M}]=[\alpha/\text{M}]=0$.

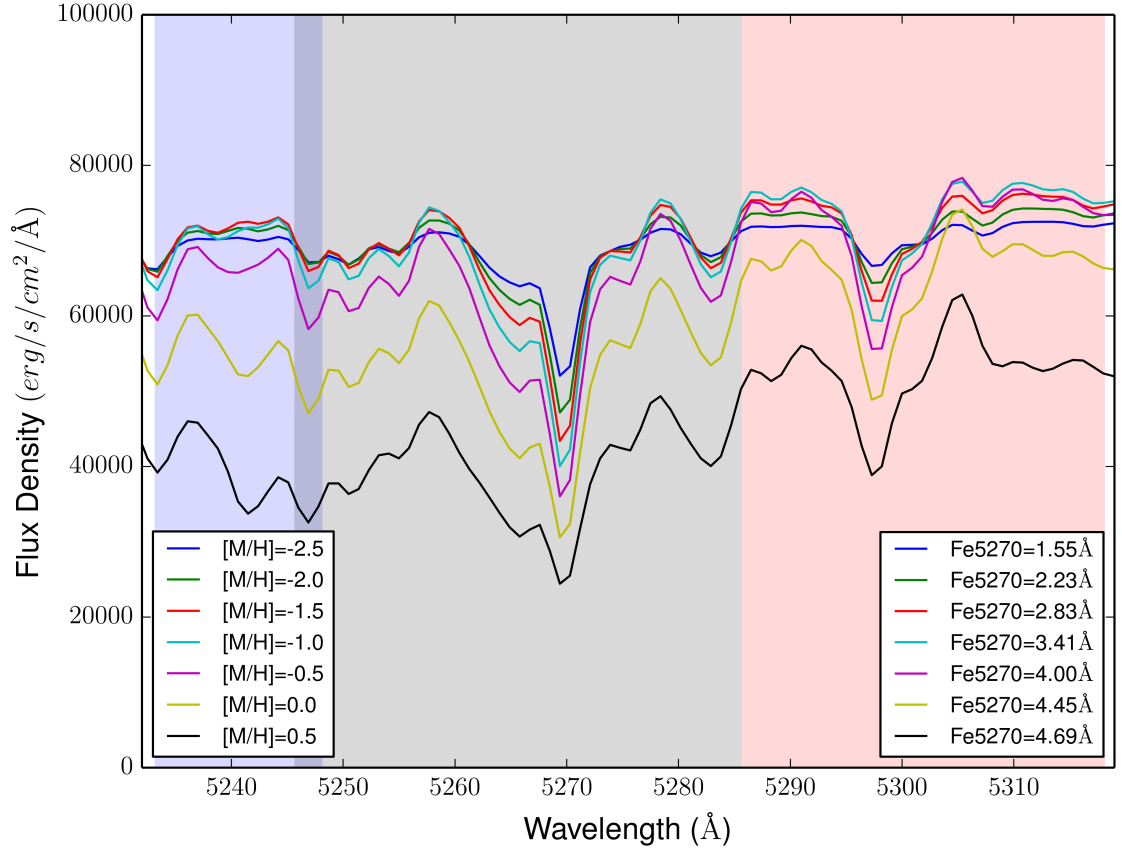


Figure 3.18: Spectral sequence of metallicity from the MILES resolution library in the Fe5270 index region. The Lick index values are also shown. The blue, red and grey areas represent the blue continuum, red continuum and index band of the Lick definition, respectively. The stars have parameters $T_{\text{eff}}=4000\text{K}$, $\log g=2.0$ and $[\text{C}/\text{M}]=[\alpha/\text{M}]=0$.

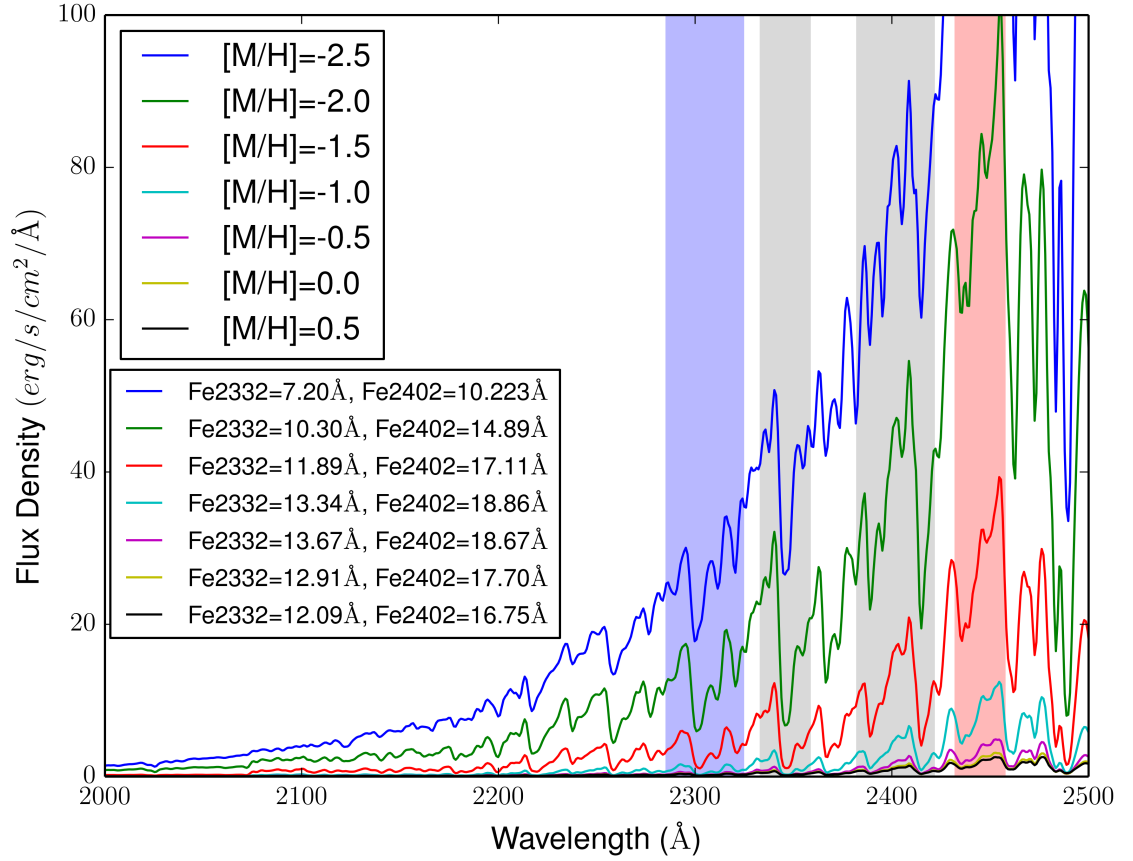


Figure 3.19: Spectral sequence of metallicity from the MILES resolution theoretical library in part of the UV regime. The blue, red and grey areas represent the blue continuum, red continuum and index band of two iron-sensitive UV indices (defined in Fanelli et al. 1990) respectively. Index values are also shown. The stars have parameters $T_{\text{eff}}=4000\text{K}$, $\log g=2.0$ and $[C/M]=[α/M]=0$.

CHAPTER 3

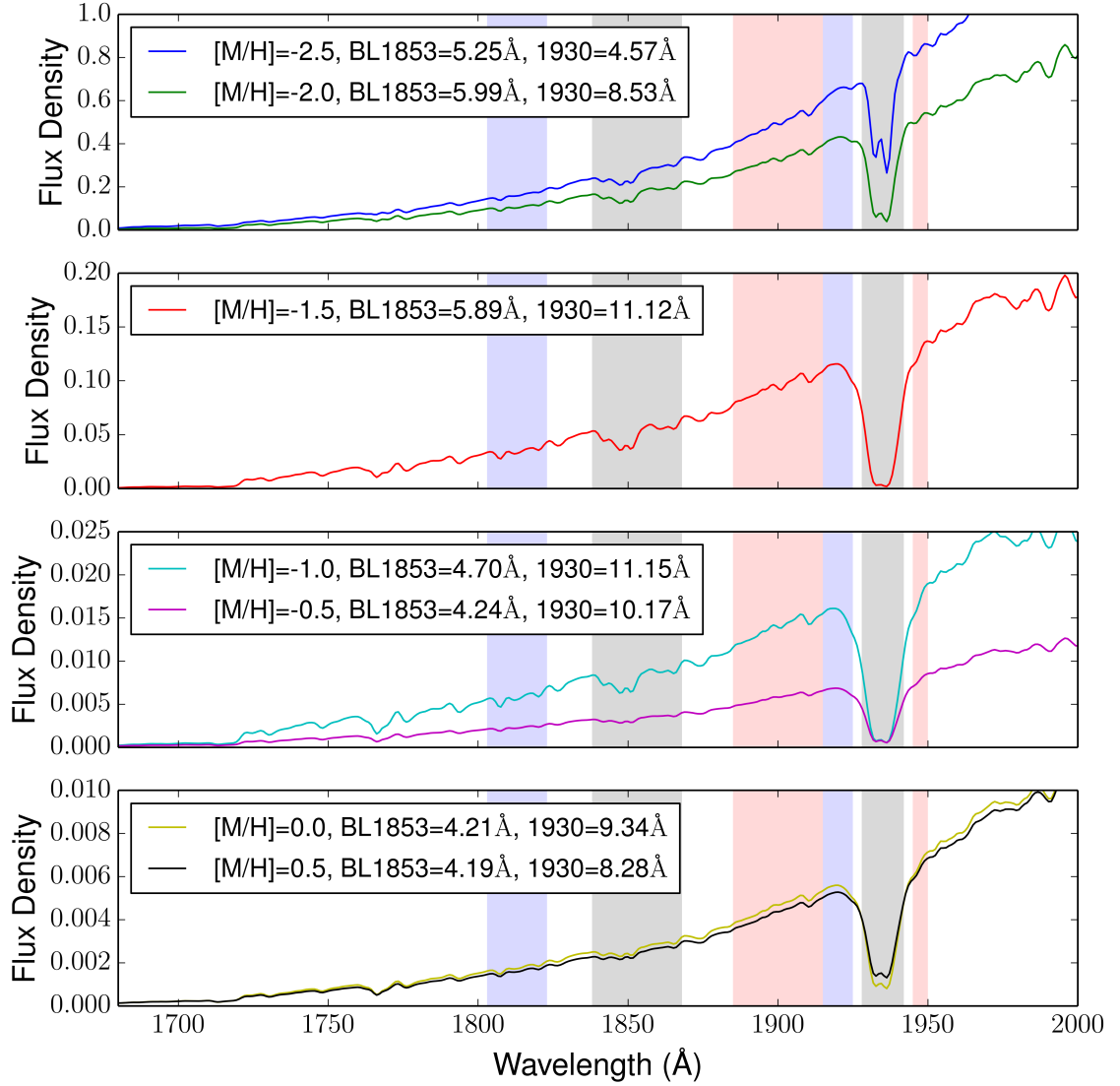


Figure 3.20: Spectral sequence of metallicity from the MILES resolution theoretical library in the UV regime. The blue, red and grey areas represent the blue continuum, red continuum and index band of two UV indices (defined in Table 3.1 and Fanelli et al. 1990). Index values are also shown. Note the changing scale on the vertical axes. Flux Density is in units of $\text{erg/s/cm}^2/\text{\AA}$. The stars have parameters $T_{\text{eff}}=4000\text{K}$, $\log g=2.0$ and $[C/M]=[α/M]=0$.

CHAPTER 3

Figure 3.21 I plot the full MILES wavelength range of models to check global effects of $[\alpha/M]$ changes. The effect of increasing $[\alpha/M]$ appears to change continuum contributions in redder wavelengths, caused by the large TiO bands (e.g. Figure 1.1 of Sparke & Gallagher 2007 and references in Figure 3.6) To highlight changes to absorption, I plot in the region of a strong $[\alpha/M]$ -sensitive Lick index, Mg_b , in Figure 3.22 with index values. The index behaviour is as expected, with Mg_b increasing with increasing α abundance. I also investigate the effect of $[\alpha/M]$ changes to different wavelength regimes in Figure 3.23. I plot a sequence of $[\alpha/M]$ in the calcium triplet region in our high resolution library. Although this regime is known to be very sensitive to surface gravity (see Figure 3.16), the indices should also be sensitive to α abundances because we include calcium in the α -capture group. For positive $[\alpha/M]$ abundances, the behaviour is as expected with index strength increasing with abundance. Interestingly, we see a slight increase in index strength with an $[\alpha/M]$ change from 0 to -0.25.

3.4.5 [C/M]

Another element varied in the grid was carbon. The carbon to oxygen balance is well known to have large effects on stellar atmospheric structure, and carbon stars are known to be present in other spectral libraries, such as the X-shooter Spectral Library (Gonneau et al. 2016). To investigate changes to spectra due to carbon variations, I plot a sequence of $[C/M]$ abundances from the grid for a 5000K, $[M/H]=[C/M]=0$ giant star. In Figure 3.24 I plot the full MILES wavelength range and highlight that an increase from $[C/Fe]=0$ results in a continuum contribution reduction at bluer wavelengths, where C, N and O abundances are known to have particularly strong effects with features such as CN_1 , CN_2 and G4300 present, all of which are sensitive to carbon, nitrogen and oxygen abundances (Worthey 1994; Tripicco & Bell 1995; Trager et al. 1998; Korn et al. 2005). Also in Figure 3.24

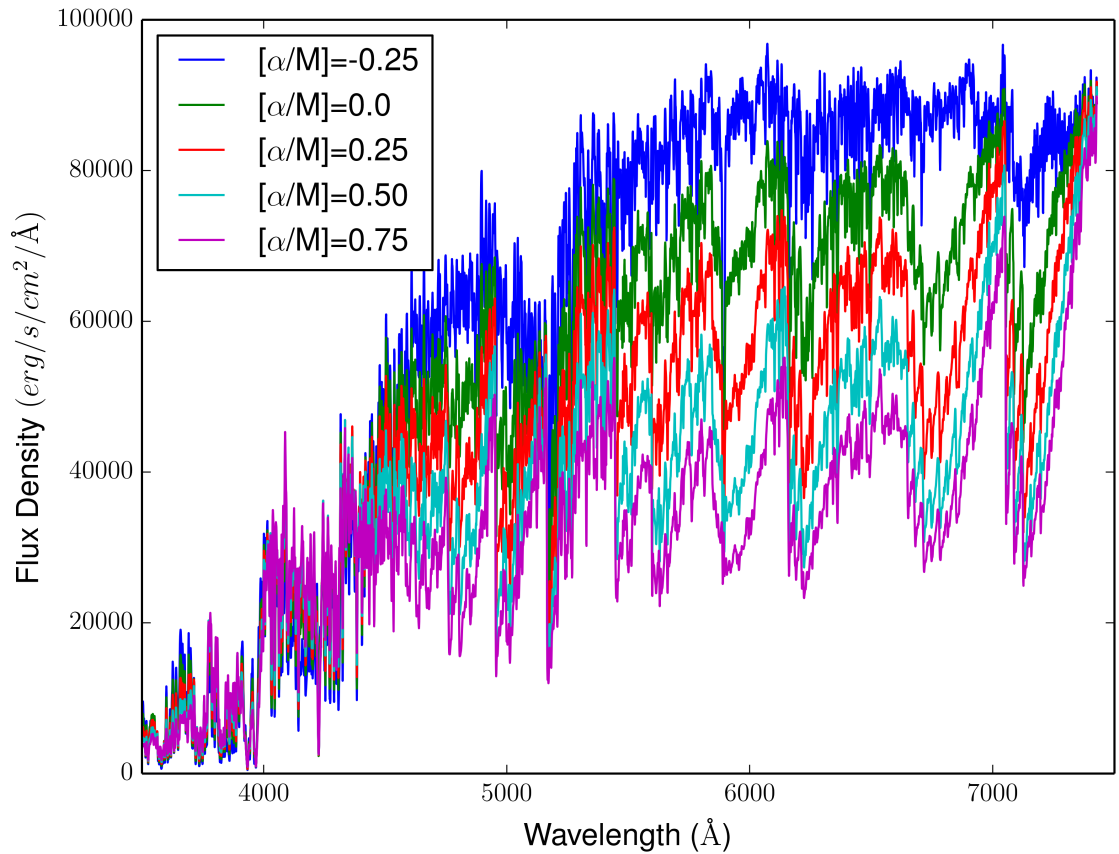


Figure 3.21: Spectral sequence of $[\alpha/M]$ for the MILES resolution and wavelength range theoretical library. Stars have parameters $T_{\text{eff}}=4000\text{K}$, $\log g=2.0$ and $[M/H]=[C/M]=0$.

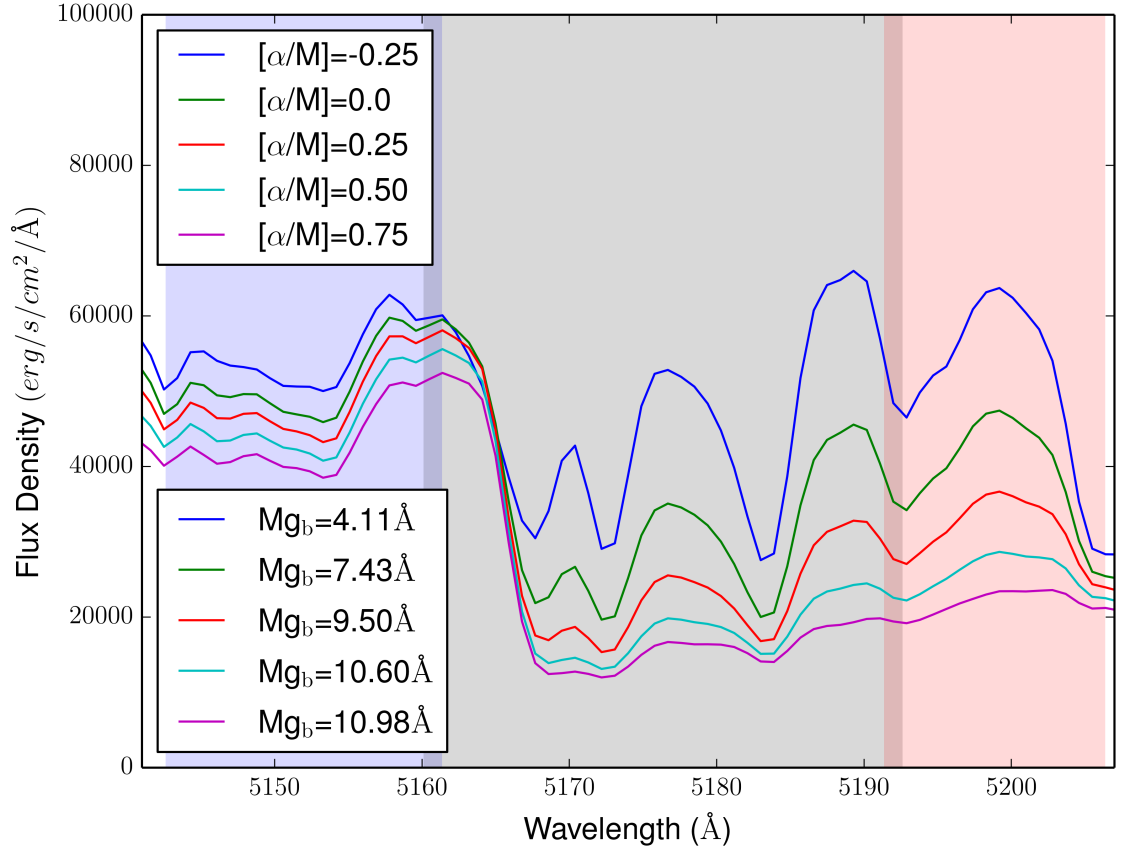


Figure 3.22: Spectral sequence of $[\alpha/M]$ variations in the MILES resolution theoretical library around the Mg_b index region. The blue, red and grey areas represent the blue continuum, red continuum and index band of the Lick definition, respectively. Index values are also shown. Stars have parameters $T_{\text{eff}}=4000\text{K}$, $\log g=2.0$ and $[M/H]=[C/M]=0$.

CHAPTER 3

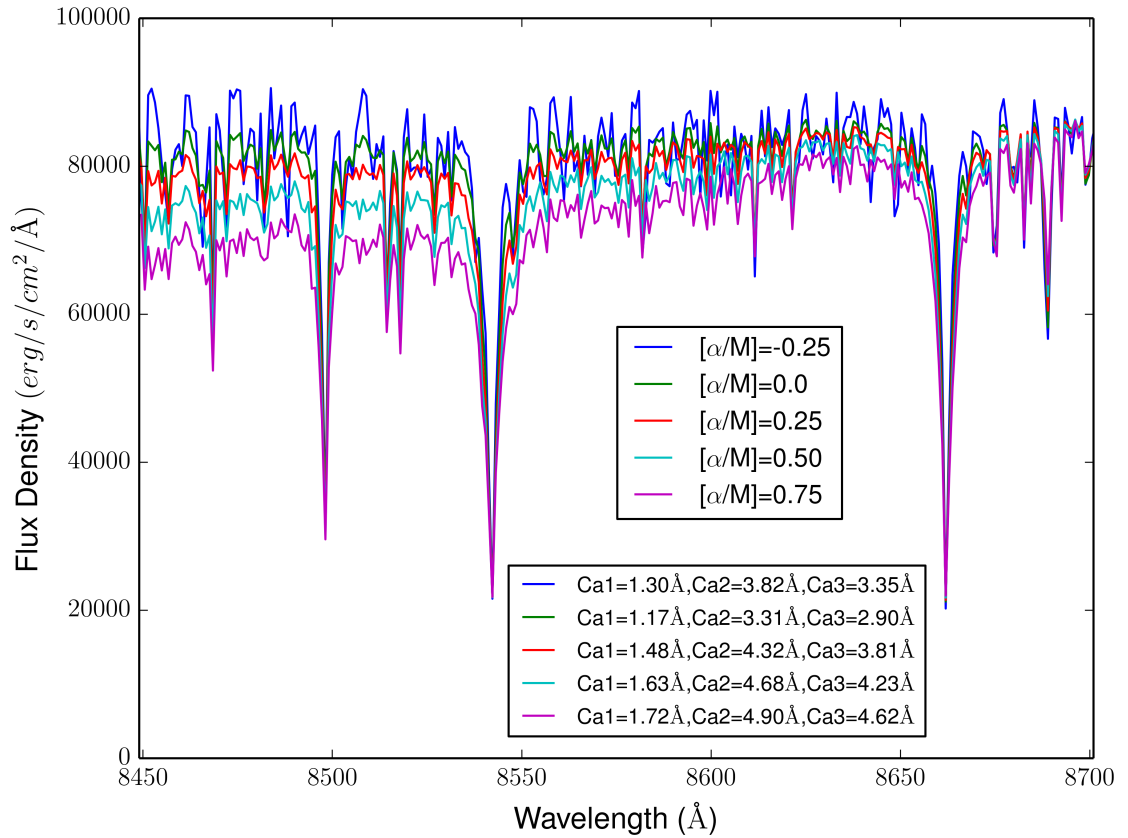


Figure 3.23: Spectral sequence of $[\alpha/M]$ variations for high resolution theoretical library in the CaT region (Cenarro et al. 2001a). Index values are also shown. Stars have parameters $T_{\text{eff}}=4000\text{K}$, $\log g=2.0$ and $[M/H]=[C/M]=0$.

CHAPTER 3

(bottom panel), I plot the spectral ratios of $[C/M]=-0.25$ and $[C/M]=0.0$, as well as $[C/M]=0.25$ and $[C/M]=0.0$, to highlight the main wavelength regions that carbon influences. As shown, carbon is particularly prevalent in the blue, with large molecular bands present. One such molecular feature, CNO3862, is defined in Serven et al. (2005) (see Table 1 and Figure 2 of that work). I also plot the same sequence in a region of a molecular carbon sensitive index, C_24668 , in Figure 3.25 along with corresponding index strengths. As shown, an increase in $[C/M]$ abundance increases the strength of absorption features in this region. Interestingly, there seems to be a smaller effect with a reduction in $[C/M]$, shown by the similarity in solar and $[C/M]=-0.25$ spectra in Figure 3.25, although there are clear differences in index strengths in both increases and decreases of carbon abundance. In Figure 3.26, I plot the effects of carbon abundances in our MILES resolution library for UV wavelengths. We highlight the large feature at $\approx 1930\text{\AA}$ that was also present in Figure 3.20, that seems to be independent of carbon abundance. I also plot a known nitrogen-sensitive index BL1719, defined in Fanelli et al. (1990), on Figure 3.26. Due to the interactions between C, N and O in stellar atmospheres, we find a carbon dependence on the BL1719 index, through changing side-band fluxes mostly, with index strength increasing with increasing carbon abundance from $[C/M]=-0.25$ to 0.0. We find a smaller change in BL1719 index strength from $[C/M]=0.0$ to 0.25. Finally, in Figure 3.27, I plot another UV index, NH3375, proposed by Serven et al. (2011) to be a mainly nitrogen, titanium and nickel-sensitive index. I find a slight carbon dependence on this index, with decreasing index strength with increasing carbon abundance. Like with B1719, this dependence may arise due to the interplay of C, N and O in stellar spectra.

CHAPTER 3

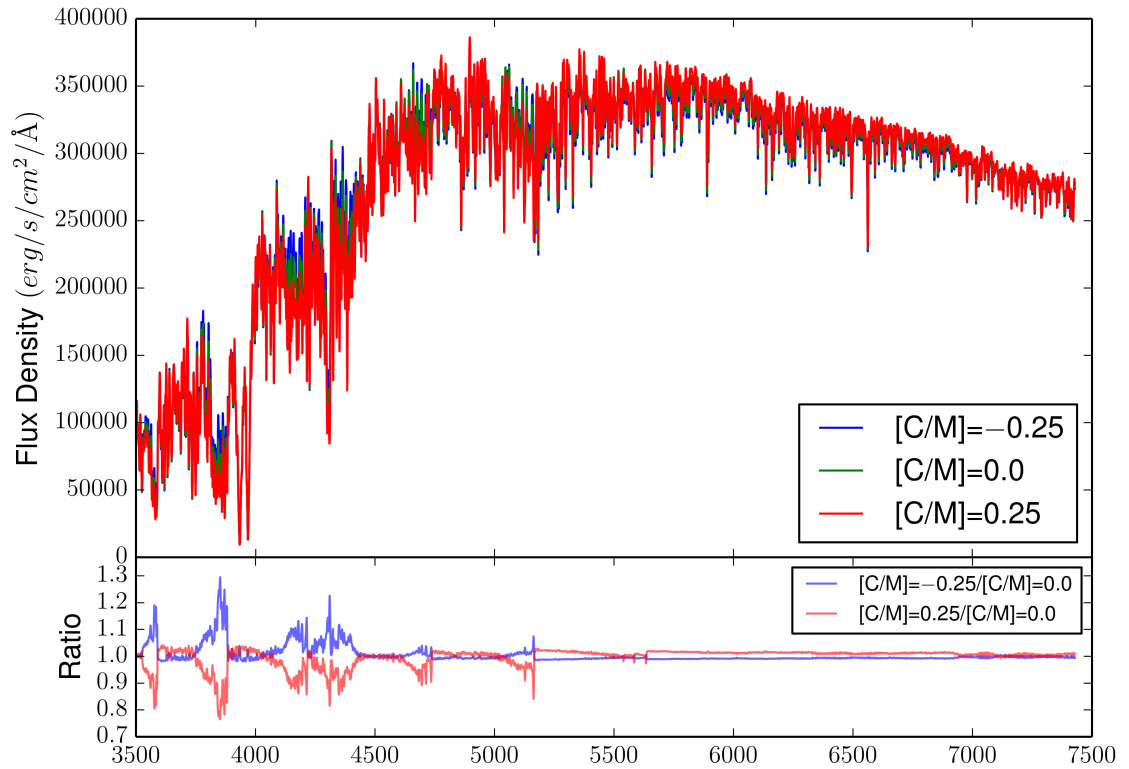


Figure 3.24: Top panel: Spectral sequence of $[\text{C}/\text{M}]$ variations for MILES resolution and wavelength theoretical library. Stars have parameters $T_{\text{eff}}=5000\text{K}$, $\log g=2.0$ and $[\text{M}/\text{H}]=[\alpha/\text{M}]=0$. Bottom panel: Spectral ratios of $[\text{C}/\text{M}]=-0.25$ and $[\text{C}/\text{M}]=0.0$ (red line), as well as $[\text{C}/\text{M}]=0.25$ and $[\text{C}/\text{M}]=0.0$ (blue line).

CHAPTER 3

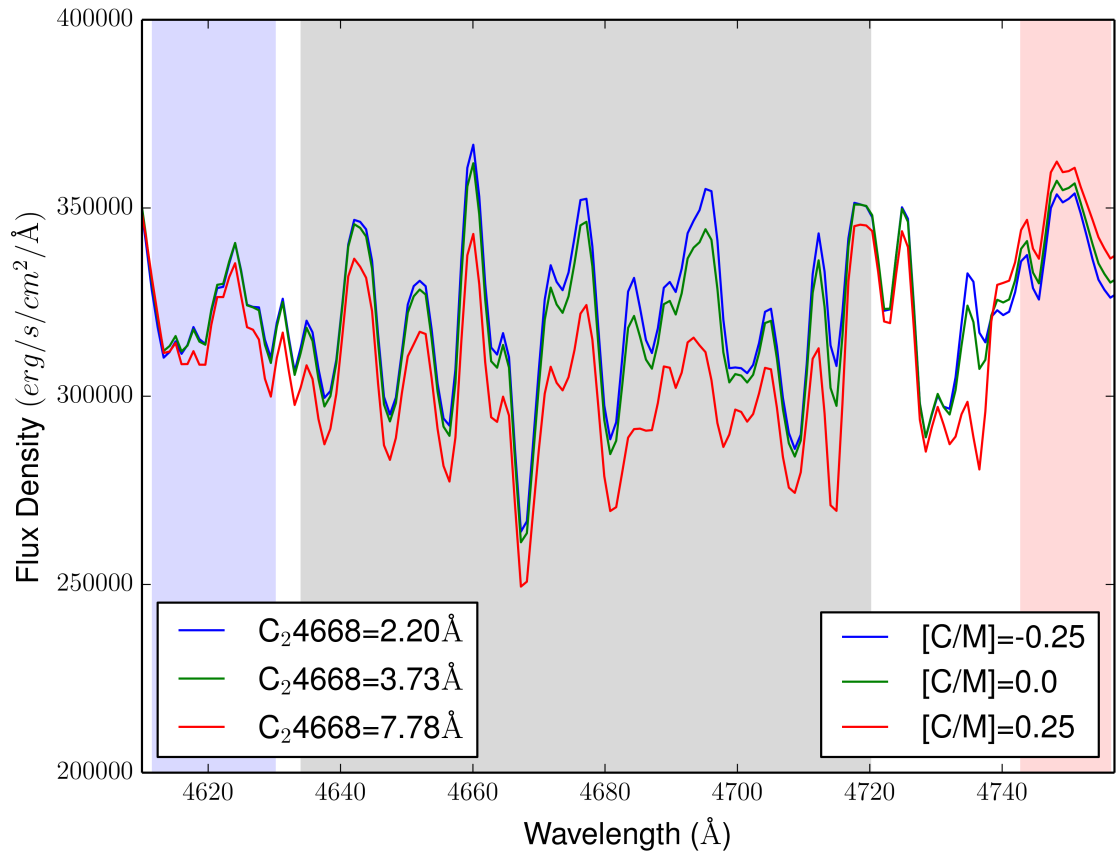


Figure 3.25: Spectral sequence of $[C/M]$ variations for the MILES resolution and wavelength theoretical library, in the carbon-sensitive index C_24668 region. Index strengths are also shown. The blue, red and grey areas represent the blue continuum, red continuum and index band of the Lick definition, respectively. Stars have parameters $T_{\text{eff}}=5000\text{K}$, $\log g=2.0$ and $[M/H]=[α/M]=0$.

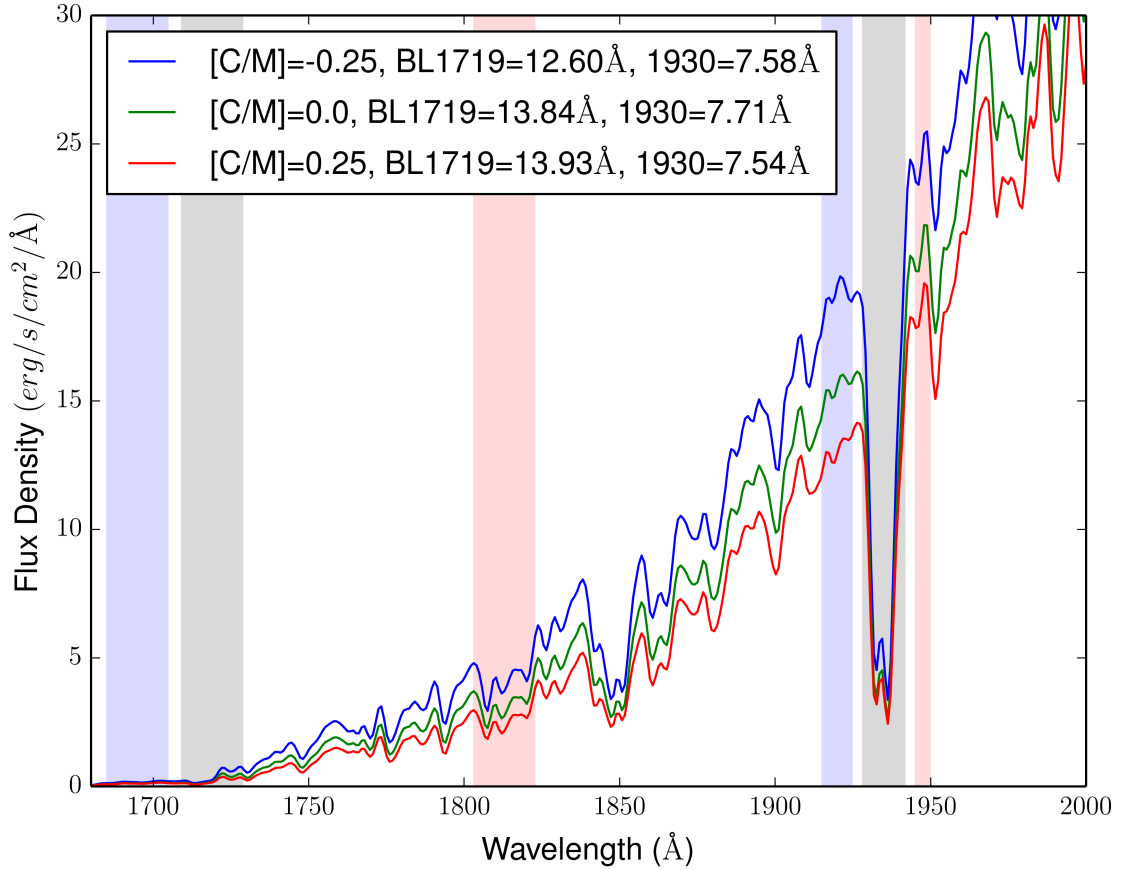


Figure 3.26: Spectral sequence of $[C/M]$ variations for the MILES resolution theoretical library, in UV wavelength regime. Stars have parameters $T_{\text{eff}}=5000\text{K}$, $\log g=2.0$ and $[M/H]=[α/M]=0$. The blue, red and grey areas represent the blue continuum, red continuum and index band of the BL1719 index (Fanelli et al. 1990) and the index we define in Table 3.1. Index values are also shown.

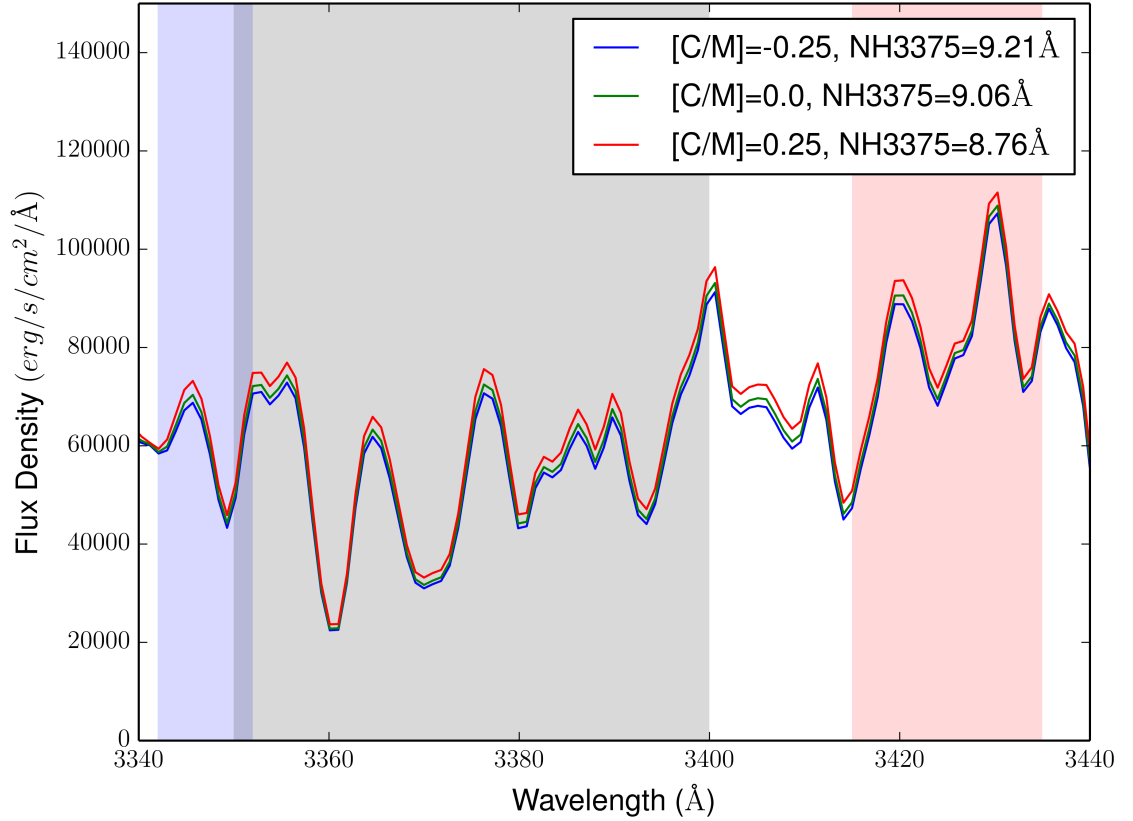


Figure 3.27: Spectral sequence of $[\text{C}/\text{M}]$ variations for the MILES resolution theoretical library, in UV wavelength regime. Stars have parameters $T_{\text{eff}}=5000\text{K}$, $\log g=2.0$ and $[\text{M}/\text{H}]=[\alpha/\text{M}]=0$. The blue, red and grey areas represent the blue continuum, red continuum and index band of the NH3375 index (Serven et al. (2011)). Index values are also shown.

3.5 Summary

In this Chapter we presented a new high resolution ($\delta\lambda = 0.05\text{\AA}$), theoretical spectral library that will be useful for stellar population analysis. The grid spans a large range of stellar parameters, metallicities and α and carbon abundances. The first section described the methods of spectra computation, the microturbulence relation adopted, the elements varied in the grid and outlined the atomic and molecular line lists used. The second section presented the steps taken to process raw spectra to both the high resolution and lower MILES resolution libraries. The lower resolution library will be used in differential corrections presented in Chapter 4. The final section in this chapter tested behaviours of the theoretical library, in both high and low resolution, through spectral plots and index measurements, for full wavelength range of the models. Sequences of stellar parameters and abundances were plotted to test general trends of the library as well as focusing on well-known parameter-sensitive Lick indices. We found the theoretical library qualitatively and quantitatively captures the effects of changes to stellar parameters and abundances correctly, with index strengths and spectra changing in the same way as observations of individual stars and SSPs as well as other published libraries (Coelho 2014; Allende Prieto et al. 2018; Conroy & van Dokkum 2012, see Chapter 2). It is intended to make both high and low resolution theoretical libraries publicly available through the UCLan online database. In Chapter 4 we move to a library application, namely the differential correction to MILES stars to generate semi-empirical stars.

Chapter 4

Semi-Empirical Stellar Library

4.1 Introduction

This Chapter describes the generation of a new semi-empirical stellar library, by applying predictions from theoretical stellar spectra of how variation in atmospheric abundance patterns change empirical MILES stellar spectra. Through these differential corrections, we expand the abundance pattern ($[\alpha/\text{Fe}]$) range of stellar population models that can be built with the current MILES stellar library. The full process can be split into the following steps:

1. Generate a grid of theoretical stellar spectra. The library varies effective temperature, surface gravity, metallicity and abundance pattern (see Chapter 3).
2. Interpolate in the model grid to generate theoretical MILES stars. The interpolation generates spectra that exactly match MILES stars in the four measured atmospheric parameters of effective temperature, surface gravity, metallicity ($[\text{Fe}/\text{H}]$) and α abundance ($[\text{Mg}/\text{Fe}]$). These are referred to as MILES theoretical base stars (M_{TB}).
3. Perform other interpolations in the model grid to generate theoretical MILES stars that have different abundance patterns. This interpolation matches the

CHAPTER 4

MILES stars in effective temperature, surface gravity and metallicity, but with different α abundances. These are referred to as MILES theoretical enhanced (or deficient) stars ($M_{T(\alpha=x)}$), where x gives the $[\alpha/\text{Fe}]$ abundance. For this work, $x = -0.20, 0.0, 0.20, 0.40, 0.60$.

4. Differential Corrections, for each star, are then computed through :

$$\text{Differential Correction (DC)} = \frac{M_{T(\alpha=x)}}{M_{TB}} \quad (4.1)$$

and are applied to empirical MILES stars to create semi-empirical MILES (sMILES) stars:

$$\text{sMILES} = \text{Differential Correction} \times \text{MILES empirical star} \quad (4.2)$$

This produces families of semi-empirical star spectra with the same stellar parameters (T_{eff} , $\log g$ and $[\text{Fe}/\text{H}]$) as the existing empirical MILES stars but with different abundance patterns ($[\text{Mg}/\text{Fe}]$).

5. Finally, generate SSP spectra with different abundance patterns using the semi-empirical stars.

The semi-empirical stars will be on a regular grid in abundance pattern, illustrated in Figure 4.1, and on an irregular grid in T_{eff} , $\log g$ and $[\text{Fe}/\text{H}]$. This methodology builds upon the work of La Barbera et al. (2017), implementing both the accuracy of empirical spectra with the differential abundance pattern predictions of theoretical spectra. Using only the differential predictions of theoretical spectra has been shown to reproduce observations of abundance pattern effects more accurately than fully theoretical spectra, particularly for wavelengths below Mg_b (Chapter 2). The current chapter is split as follows. Section 4.2 describes the choice of MILES star parameters used. Section 4.3 describes interpolation in the theoretical grid (Steps 2 and 3) and Section 4.4 describes the differential corrections performed to produce semi-empirical stars (Step 4). Section 4.5 describes the computation of SSPs from the semi-empirical stars (Step 5).

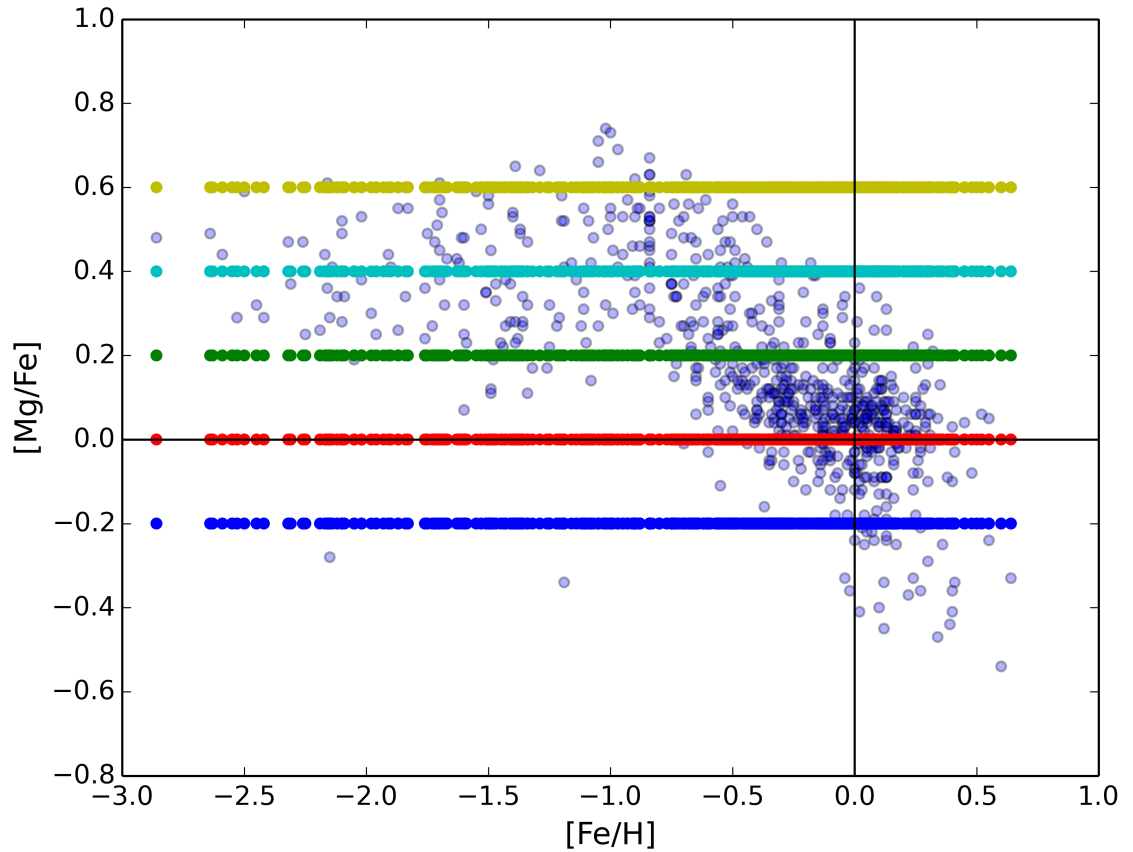


Figure 4.1: Illustration of the semi-empirical MILES (sMILES) stellar library aimed for in this work, in the $[Mg/Fe]$ vs $[Fe/H]$ plane. The coloured points that lie in horizontal lines represent the possible families of semi-empirical MILES stars and light blue points represent existing empirical MILES stars.

4.2 MILES Star Parameters

The choice of MILES parameters is particularly important in this work, because this will determine the coverage in stellar parameter space of the semi-empirical library and the accuracy of representation of the empirical and resultant semi-empirical (sMILES) stars. The two most widely used works for the MILES stellar parameters are those of Cenarro et al. (2007) and Prugniel & Sharma (Prugniel et al. 2011; Sharma et al. 2016). With both works possessing limitations and benefits, as explained in their respective sections, a semi-empirical library was made for each set of parameters.

4.2.1 Cenarro

From a bibliographic compilation, Cenarro et al. (2007) produced a high-quality standard reference of atmospheric parameters for the full library of 985 MILES stars. The process involved calibrations and corrections of systematic differences between different sources to produce an averaged source of final atmospheric parameters from the literature, corrected to a common reference system. The final result is a homogeneous system of atmospheric parameters generated by considering field and cluster stars separately, with estimated typical errors of $\approx 100\text{K}$, 0.2 dex and 0.1 dex for T_{eff} , $\log g$ and $[\text{Fe}/\text{H}]$ respectively. For $[\text{Mg}/\text{Fe}]$, measurements from Milone et al. (2011) for 752 stars were used, with approximate estimates of the remaining stars (at $[\text{Mg}/\text{Fe}]$ of 0, 0.2 or 0.4), using a relation from Bensby et al. (2014) (their Figure 15). This relation is estimated from a study of dwarf stars in the Milky Way disk. A subsample of the 985 MILES stars were found to not be representative of their tagged stellar parameters. Stars were identified as problematic by computing a spectrum with the given stellar parameters using the interpolator described in Vazdekis et al. (2010) with the target star removed from the sample. These were stars that were low quality, erroneous spectra that may have been contaminated, had a pointing error,

CHAPTER 4

be a spectroscopic binary, had large uncertainties in stellar parameters, incorrect extinction estimates, continuum shape problems, may be a carbon star or have segments that correspond to a wrong source. They were accounted for by either removing them from the library entirely or reducing the S/N weighting in the SSP calculation (Vazdekis et al., 2010). 75 of this subsample remained in the calculation, with decreased S/N weighting, because they improved coverage in regions of sparsely populated parameter space. This resulted in a final library of 925 stars. The semi-empirical library produced using these parameters is the one used in the final SSP generation in Section 4.5. The enhanced and deficient $[\alpha/\text{Fe}]$ in the semi-empirical stars ranged from -0.20 to 0.60 in steps of 0.20, to avoid grid edge effects in the interpolation of theoretical star spectra (see Section 4.3). This is a larger range, with a greater number of grid points, than previously computed by Vazdekis et al. (2015), that generated SSPs with $[\alpha/\text{Fe}]$ abundances of 0 and 0.4. A new step, compared to Vazdekis et al. (2015) models, is the inclusion of an $[\alpha/\text{Fe}]$ -deficient family of sMILES stars and therefore SSPs.

4.2.2 Prugniel & Sharma

MILES stellar parameters were determined by comparing MILES spectra to templates from the empirical library ELODIE (Prugniel et al. 2007). Interpolation in this library, using the ULySS code (Koleva et al. 2009), allowed for the determination of the wavelength-dependent line spread function (LSF) and atmospheric parameters (T_{eff} , $\log g$ and $[\text{Fe}/\text{H}]$) of the MILES stars (Prugniel et al. 2011). For cluster stars, $[\text{Fe}/\text{H}]$ values from Cenarro et al. (2007) were adopted. The result of Prugniel et al. (2011) was parameters with precisions of 60K, 0.13 and 0.05 dex in T_{eff} , $\log g$ and $[\text{Fe}/\text{H}]$ respectively, for FGK stars, mean errors of 38K, 0.26 and 0.12 dex for M stars and 3.5%, 0.17 and 0.13 dex errors for OBA stars. Figure 5 of Prugniel et al. (2011) compares their results to Cenarro et al. (2007). Typical differences

CHAPTER 4

of ± 150 K and ± 1500 K were for effective temperatures between 3000-4000K and 10000-30000K respectively. The smallest effective temperatures differences between Prugniel et al. (2011) and Cenarro et al. (2007) occur in between the two ranges stated previously, around the solar temperature at ~ 5700 K. For surface gravity, typical differences were found to be ≈ 0.5 dex. For $[\text{Fe}/\text{H}] < -1$, differences between Cenarro et al. (2007) and Prugniel et al. (2011) were typically found to be $\approx \pm 0.25$ dex, with larger differences ($\approx \pm 0.5$ dex) found for $[\text{Fe}/\text{H}]$ values > -1 . Sharma et al. (2016) addressed issues with Prugniel et al. (2011), namely issues with the determination of the coolest star ($T_{\text{eff}} \approx 4500$ K) parameters. This later work focused on the 332, lowest T_{eff} (≤ 4800 K) stars in the MILES library, addressing systematic effects found and took into account an updated literature compilation, improving the interpolator. There were 331 common stars in both data sets, and this overlap region between 4500 and 4800K had to be accounted for in a full set of parameters. The solution for this parameter set was as follows:

- If the star is in the Prugniel set only : use the Prugniel parameters and the associated errors (Prugniel et al. 2011).
- If $T_{\text{eff}} < 4500$ K in the Sharma set : use the Sharma parameters and the associated errors (Sharma et al. 2016).
- If $T_{\text{eff}} \geq 4500$ K in Sharma : use an averaged value of Sharma and Prugniel parameters with the largest of the two errors. The resulting 110 star parameters are presented in Table C.1. in the appendices, with the remaining parameters presented in Prugniel et al. (2011) for $T_{\text{eff}} > 4800$ K and in Sharma et al. (2016) for $T_{\text{eff}} < 4500$ K.

In Table 11 of Sharma et al. (2016), several errors were found with 11 MILES stars that included misidentification, pointing errors, light contamination, partly wrong sources or poor fits from the interpolation. The same problematic stars described

CHAPTER 4

in Section 4.2.1 were also removed from the final sample of stars, leaving 920 stars from which to compute semi-empirical spectra. $[\text{Mg}/\text{Fe}]$ values for the 752 stars in Milone et al. (2011) were used, with the remaining stars assumed to have $[\text{Mg}/\text{Fe}]$ values from the Bensby et al. (2014) Milky Way relation. The enhanced and deficient $[\alpha/\text{Fe}]$ values in semi-empirical stars ranged from -0.20 to 0.60 in steps of 0.20, to avoid grid edge effects in the interpolation (see Section 4.3). In Figures 4.2 and 4.3, I show the differences in T_{eff} , $\log g$ and $[\text{Fe}/\text{H}]$ values between Prugniel & Sharma (P & S) and Cenarro parameters, for the 925 stars used in the semi-empirical library and SSP calculations in Sections 4.4 and 4.5. The RMS scatter between the two is also given in each case. It is shown that the RMS scatter in $\log g$ and $[\text{Fe}/\text{H}]$ is on the order of the observational uncertainties of Cenarro, however there is a large scatter between the T_{eff} values in Figure 4.2, mainly caused by large differences at the very highest temperatures, which have the larger errors of ≈ 3.5 and ≈ 5 %, in Prugniel et al. (2011) and Cenarro et al. (2007), respectively. These very high T_{eff} ($>10000\text{K}$) stars are only used empirically in the SSP calculations and should not have a large effect on the abundance pattern information that this work focuses on. It can be seen in Figure 4.3 (top panel), that repeating the RMS scatter analysis on stars only in the parameter range used in the sMILES work ($<10000\text{K}$), that the RMS is significantly reduced, to 200K.

4.2.3 Final Parameter Choice

As highlighted in Sections 4.2.1 and 4.2.2, both sets of parameters have their benefits and limitations. In summary, the Prugniel & Sharma parameter set has the advantage of being derived in a homogeneous fashion, from a well tested and characterised library of templates, improved methodologies for lower temperatures and good understanding of the biases involved. However, the work is limited by the use of interpolation and full spectrum fitting, particularly at the lowest temperatures

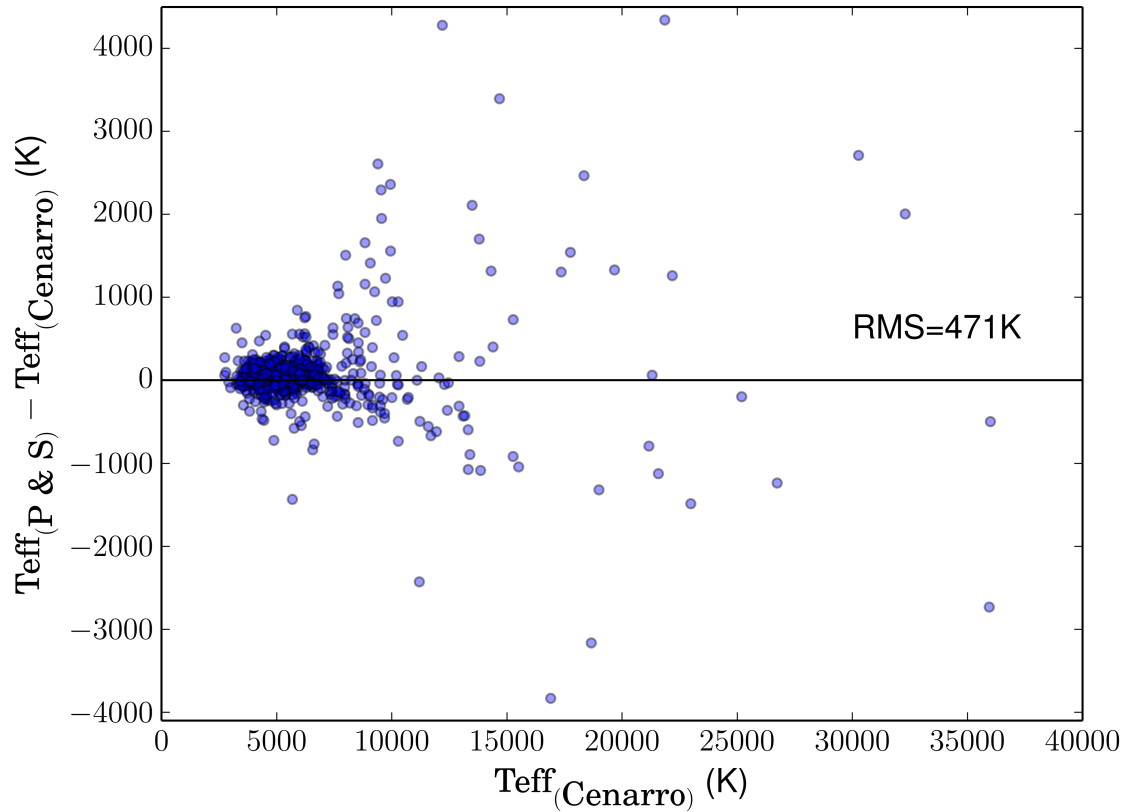


Figure 4.2: Comparison of MILES star T_{eff} values between Prugniel & Sharma and Cenarro parameter sets. Differences between the sets are plotted versus the Cenarro values. This comparison was done for the 925 stars described in Section 4.2.1. The RMS scatter between the two parameter sets is given. The 1:1 agreement line is plotted in black.

CHAPTER 4

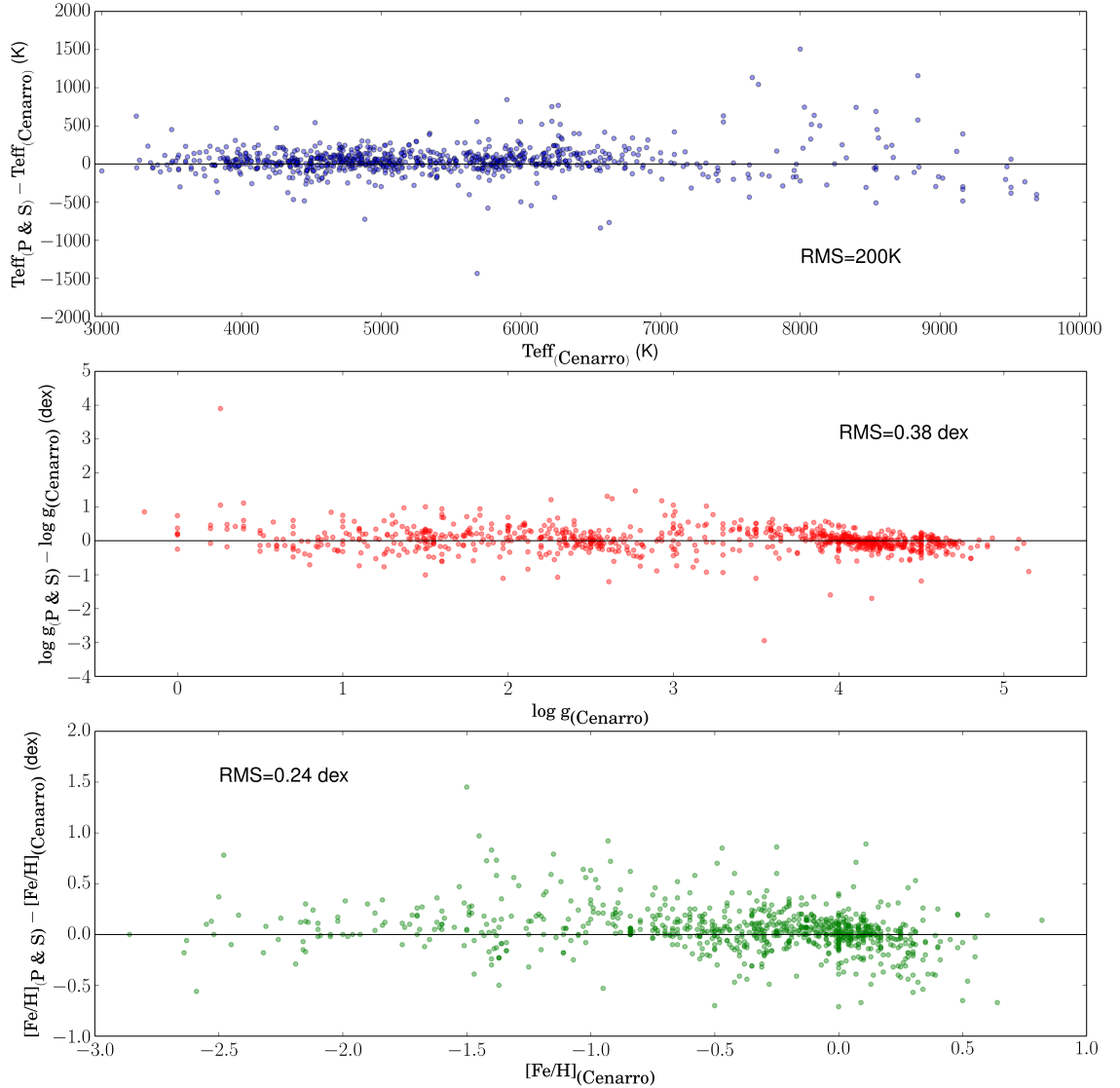


Figure 4.3: Top panel: Comparison of MILES star T_{eff} values between Prugniel & Sharma and Cenarro parameter sets, in the parameter range of the theoretical grid described in Chapter 3. The RMS scatter between the two parameter is shown to be significantly reduced compared to the full range in Figure 4.2. Middle panel: Comparison of MILES star $\log g$ values between Prugniel & Sharma and Cenarro parameter sets. The two extreme outliers ($\log g_{\text{Cenarro}}=0.26$, $\log g_{\text{P \& S}}=4.16$ and $\log g_{\text{Cenarro}}=3.55$, $\log g_{\text{P \& S}}=0.60$) are MILES stars m0568 and m0247. Bottom panel: Comparison of MILES star $[\text{Fe}/\text{H}]$ values between Prugniel & Sharma and Cenarro parameter sets. These comparisons were done for the 925 stars described in Section 4.2.1 and the RMS scatter is given in each case. Differences between the sets are plotted versus the Cenarro values. The black lines in each plot represent the 1:1 agreement line.

CHAPTER 4

where not many good star templates are available. Because we plan to use the Vazdekis et al. (2015) SSP methodology and existing code, a final choice was made to use the Cenarro et al. (2007) parameters, as was done previously in that work. A reason for using the Cenarro et al. (2007) parameters comes with the good agreement that the parameters show with the colour-temperature-metallicity scaling of Alonso et al. (1996) and Alonso et al. (1999), described in Section 5.1.4. The SSP methodology is therefore internally consistent with the Cenarro et al. (2007) parameters and with the $[\text{Mg}/\text{Fe}]$ measures from Milone et al. (2011). In future work, there will be the possibility to use $[\alpha/\text{Fe}]$ measurements currently being made for MILES stars (Garcia-Perez et al. submitted), rather than relying on the $[\text{Mg}/\text{Fe}]$ proxy, as we are limited to at the moment. That work is using abundance pattern analysis similar to that of APOGEE, using theoretical stellar templates and FERRE to obtain measures of T_{eff} , $\log g$, $[\text{Fe}/\text{H}]$ and $[\alpha/\text{Fe}]$, and is currently ongoing with the aim of publication this year (Garcia-Perez et al. submitted).

4.3 Interpolation of Theoretical Stellar Spectra

With MILES star parameters determined, the next step was to interpolate in the model grid to generate theoretical spectra that match MILES stars. This was done for both parameter sets, but because we use the Cenarro et al. (2007) set for the SSP computation in Section 4.5, I only describe the process for this set. The same process was used for the Prugniel & Sharma set.

The interpolation was performed using the quadratic Bézier function within FERRE, apart from in a few cases discussed later. A quadratic Bézier function is a parametric curve that is defined by three points in parameter space (e.g. in our case, the wavelength, flux density, T_{eff} , $\log g$, $[\text{M}/\text{H}]$, $[\alpha\text{M}]$ and $[\text{C}/\text{M}]$). The 925 star parameters were split into three groups depending on their parameters, such that they fell in the parameter range of one of the three MILES resolution and wavelength

CHAPTER 4

range grids described in Chapter 3. Any stars that fell outside, or on the upper and lower grid edges, of the theoretical grids were used only empirically in the SSP calculation. The results of these cuts meant 587, 169 and 45 stars were computed in the 3500-6000K, 6000-8000K and 8000-10000K grid, respectively. Python routines were used to read a MILES parameter file and create the input files, based on which of the three grids the star resided, used by the FERRE interpolation routines.

The first group of interpolations resulted in the MILES Theoretical Base stars, that will be the denominator in the differential correction (equation 4.1). These base stars were generated by interpolating to the MILES parameters of T_{eff} , $\log g$, $[\text{Fe}/\text{H}]$ and $[\text{Mg}/\text{Fe}]$, with $[\text{C}/\text{Fe}]=0.0$. Problems were found for 11 low T_{eff} stars, for which spectra were produced with negative flux values at wavelengths below 6000Å. These stars were :

- m0669 - $T_{\text{eff}}=3640\text{K}$, $\log g=0.70$, $[\text{Fe}/\text{H}]=0.00$, $[\text{Mg}/\text{Fe}]=0.22$
- m0704 - $T_{\text{eff}}=3550\text{K}$, $\log g=0.60$, $[\text{Fe}/\text{H}]=0.00$, $[\text{Mg}/\text{Fe}]=0.00$
- m0871 - $T_{\text{eff}}=3730\text{K}$, $\log g=0.90$, $[\text{Fe}/\text{H}]=0.27$, $[\text{Mg}/\text{Fe}]=0.27$
- m0099 - $T_{\text{eff}}=3560\text{K}$, $\log g=0.60$, $[\text{Fe}/\text{H}]=0.00$, $[\text{Mg}/\text{Fe}]=0.00$
- m0234 - $T_{\text{eff}}=3600\text{K}$, $\log g=0.70$, $[\text{Fe}/\text{H}]=-0.30$, $[\text{Mg}/\text{Fe}]=0.00$
- m0614 - $T_{\text{eff}}=3640\text{K}$, $\log g=0.70$, $[\text{Fe}/\text{H}]=-0.10$, $[\text{Mg}/\text{Fe}]=0.22$
- m0481 - $T_{\text{eff}}=3661\text{K}$, $\log g=1.55$, $[\text{Fe}/\text{H}]=0.30$, $[\text{Mg}/\text{Fe}]=0.00$
- m0271 - $T_{\text{eff}}=3530\text{K}$, $\log g=0.70$, $[\text{Fe}/\text{H}]=0.00$, $[\text{Mg}/\text{Fe}]=0.00$
- m0397 - $T_{\text{eff}}=3700\text{K}$, $\log g=1.22$, $[\text{Fe}/\text{H}]=-0.23$, $[\text{Mg}/\text{Fe}]=0.22$
- m0535 - $T_{\text{eff}}=3600\text{K}$, $\log g=0.70$, $[\text{Fe}/\text{H}]=0.00$, $[\text{Mg}/\text{Fe}]=0.00$
- m0053 - $T_{\text{eff}}=3600\text{K}$, $\log g=1.10$, $[\text{Fe}/\text{H}]=0.02$, $[\text{Mg}/\text{Fe}]=-0.09$

CHAPTER 4

The nearest computed grid points were checked for errors, however the problem with these stars was found to be with the quadratic interpolation near the grid edges. The erroneous stars were recomputed using a linear interpolation within FERRE, with an example of the correction shown in Figure 4.4, for m0669. For this example, it can be seen that negative fluxes are found for the quadratic interpolation around 5000\AA , which is corrected using a linear interpolation. Also plotted Figure 4.4 is the corresponding MILES empirical star (black line). The linear interpolation also lies closer to the observed spectrum than the resulting quadratic interpolation. Several other checks between linear and quadratic interpolations were made for the 11 problematic stars and the linear interpolation was found to be closer to the observed spectrum in all cases. Comparisons between linear and quadratic interpolations were also made for various locations within the grid at different effective temperatures and were found to be similar in all other locations. The next set of interpolations were made to produce the MILES enhanced (or deficient) star set, used in the numerator of equation (4.1). Stars were computed with quadratic Bézier interpolations, of the T_{eff} , $\log g$ and $[\text{Fe}/\text{H}]$ values of the existing MILES stars, but with $[\alpha/\text{M}]$ values of -0.20, 0.0, 0.20, 0.40 and 0.60. This choice of $[\alpha/\text{M}]$ steps reduced problems with interpolation at the theoretical grid edges, found previously. The 11 problem stars in the base family were computed also using linear interpolations for their α enhancements. The result was six families of theoretical MILES stars - one with all the existing MILES parameters and five with the same fundamental parameters but different $[\alpha/\text{Fe}]$ abundances, at MILES resolution and wavelength range. The resulting spectra were stored in a FERRE file format with a spectrum per line, resulting in 6 files for each of the three theoretical grids. The next stage of the process was to differentially correct MILES stars, described in Section 4.4.

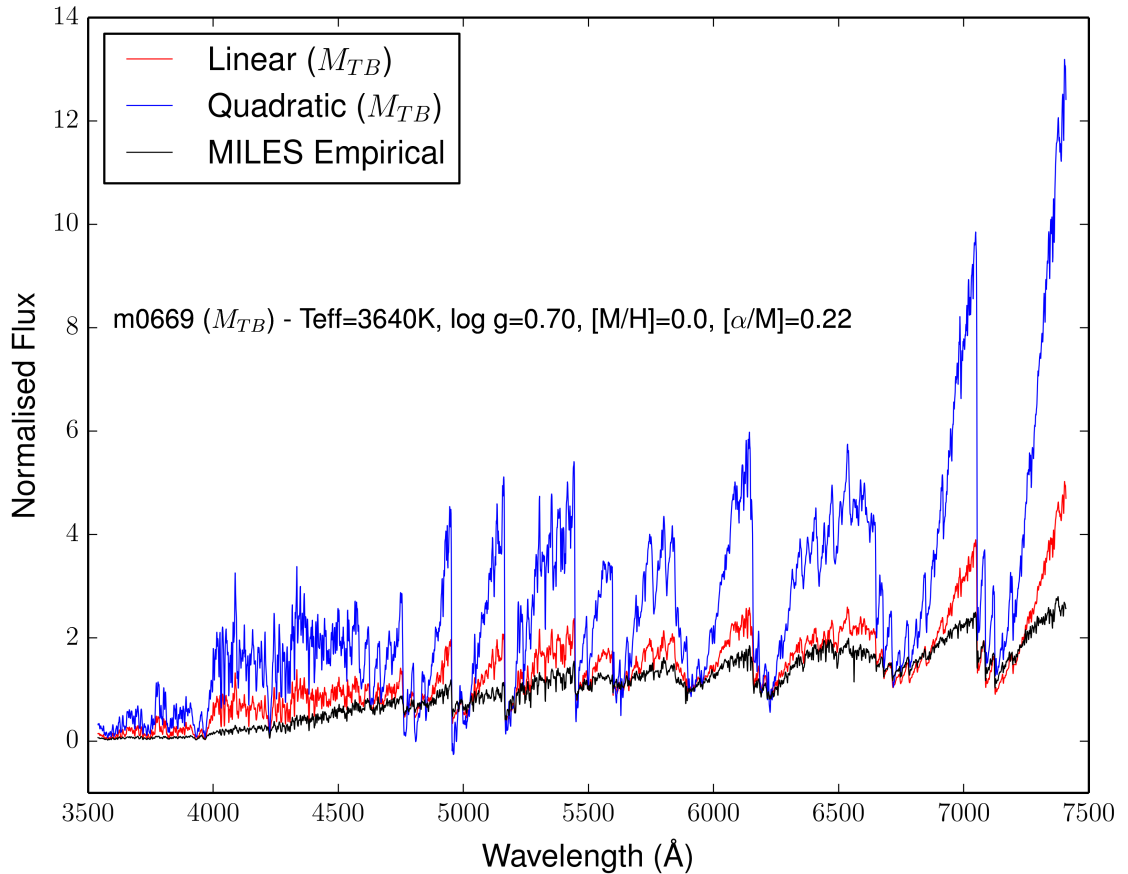


Figure 4.4: Comparison between the resulting spectra of a linear and quadratic Bézier interpolation in FERRE, near grid edges, compared to the corresponding empirical spectrum. Spectra are normalised to the flux at 5500.7\AA . The quadratic interpolation produces negative fluxes at $\approx 5000\text{\AA}$. A linear interpolation fixes this problem and also produces a closer match to the corresponding empirical spectrum for m0669 (black line).

4.4 Differential Correction to MILES Spectra

With theoretical spectra computed with the MILES parameters using FERRE interpolations, the next step was to calculate and apply the differential correction to MILES stars, to generate sMILES stars. Python codes were created to perform both the calculation and application, on files designed for use in FERRE, with a spectrum per line. Also using python codes, the empirical MILES spectra were set up in FERRE files, with stars in the same order as in the theoretical interpolated spectra. More python routines then performed the division of flux of the enhanced (or deficient) and base spectra, described in equation (4.1) for each wavelength point, where α gives the $[\alpha/\text{Fe}]$ abundance of the sMILES star that will be produced if the differential correction is applied to the empirical MILES star. Two example sequences of the differential corrections are shown for MILES stars m0067 ($T_{\text{eff}}=5264\text{K}$, $\log g=4.36$, $[\text{Fe}/\text{H}]=-0.50$, $[\text{Mg}/\text{Fe}]=0.40$) and m0923 ($T_{\text{eff}}=4367\text{K}$, $\log g=1.27$, $[\text{Fe}/\text{H}]=-1.34$, $[\text{Mg}/\text{Fe}]=0.30$) in Figures 4.5 and 4.6 respectively. As shown, the differential correction is smallest for abundance patterns closest to the measured value of the empirical star. The largest differential corrections are found for wavelengths below $\approx 4500\text{\AA}$. Another noticeable feature in the corrections is also present around the Mg_b index, which again increases as the $[\alpha/\text{Fe}]$ abundances differ from the measured abundance of the empirical star.

The differential correction was then applied to the corresponding empirical star flux value (equation 4.2). The result was five files, with sMILES spectra in a line-by-line format for the five α enhancement steps, for the three T_{eff} grids. Python routines were then used to convert FERRE format files into individual files for each sMILES spectrum, for use in the SSP software described in Section 4.5. The result was 801 spectra per five α steps, with a wavelength coverage of $3540.5\text{\AA} - 7409.6\text{\AA}$ in steps of 0.9\AA . The sMILES spectra were finally normalised to the total V-band flux using a routine provided by Vazdekis (priv comm.) for use in the SSP calculation,

CHAPTER 4

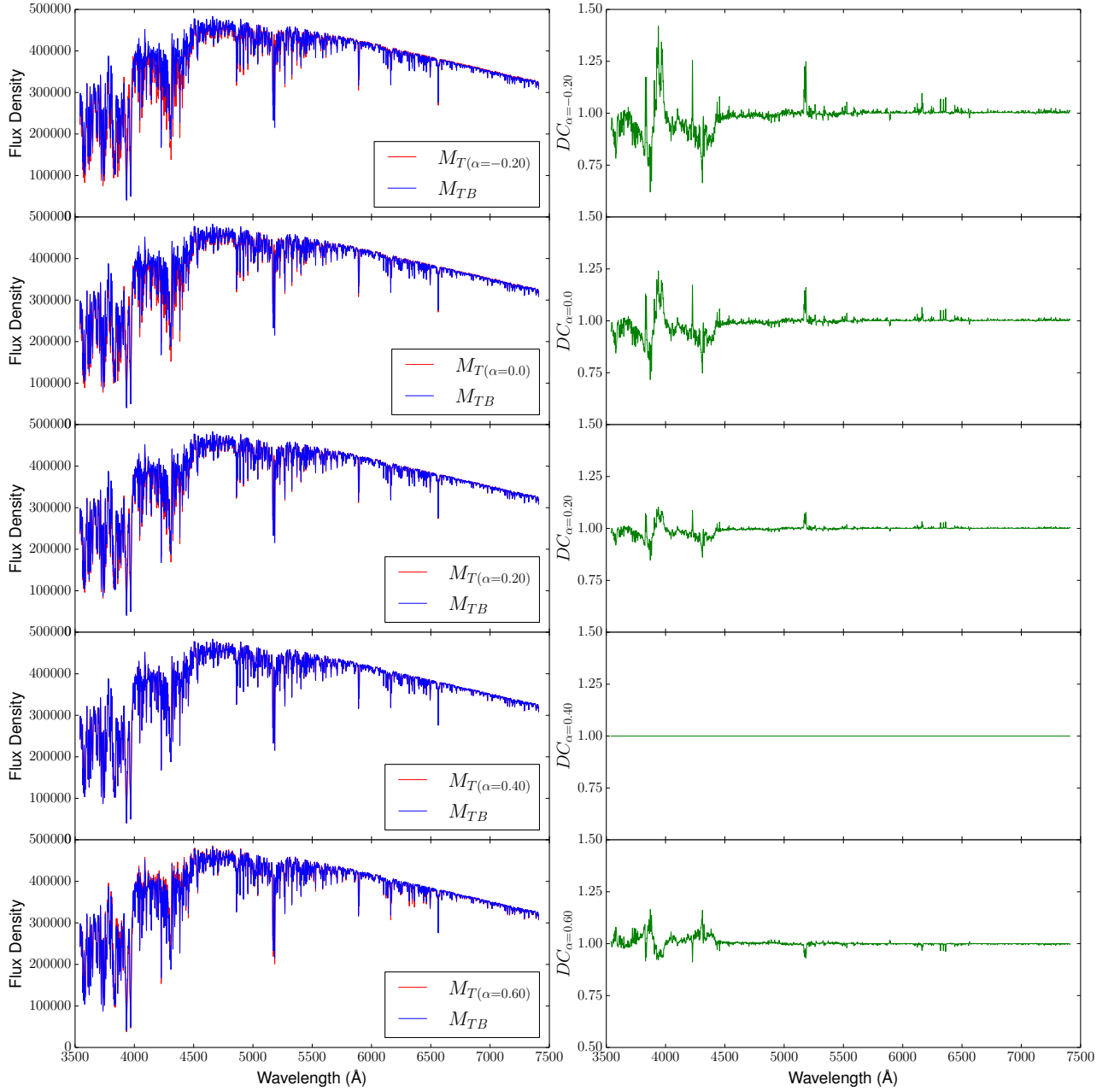


Figure 4.5: Example differential corrections for MILES star m0067. The left panel compares the resulting spectra of the theoretical enhanced (or deficient) ($M_{T(\alpha=x)}$) and theoretical base M_{TB} stars. Flux Density is in units of $\text{erg/s/cm}^2/\text{\AA}$. The right panel shows the resulting differential correction ($DC_{(\alpha=x)}$), derived from equation 4.1, for each of the $[\alpha/Fe]$ abundances. Note that for this star, the differential correction for $[\alpha/Fe]=0.40$ is 1, because the empirical MILES star is already at $[Mg/Fe]=0.40$.

CHAPTER 4

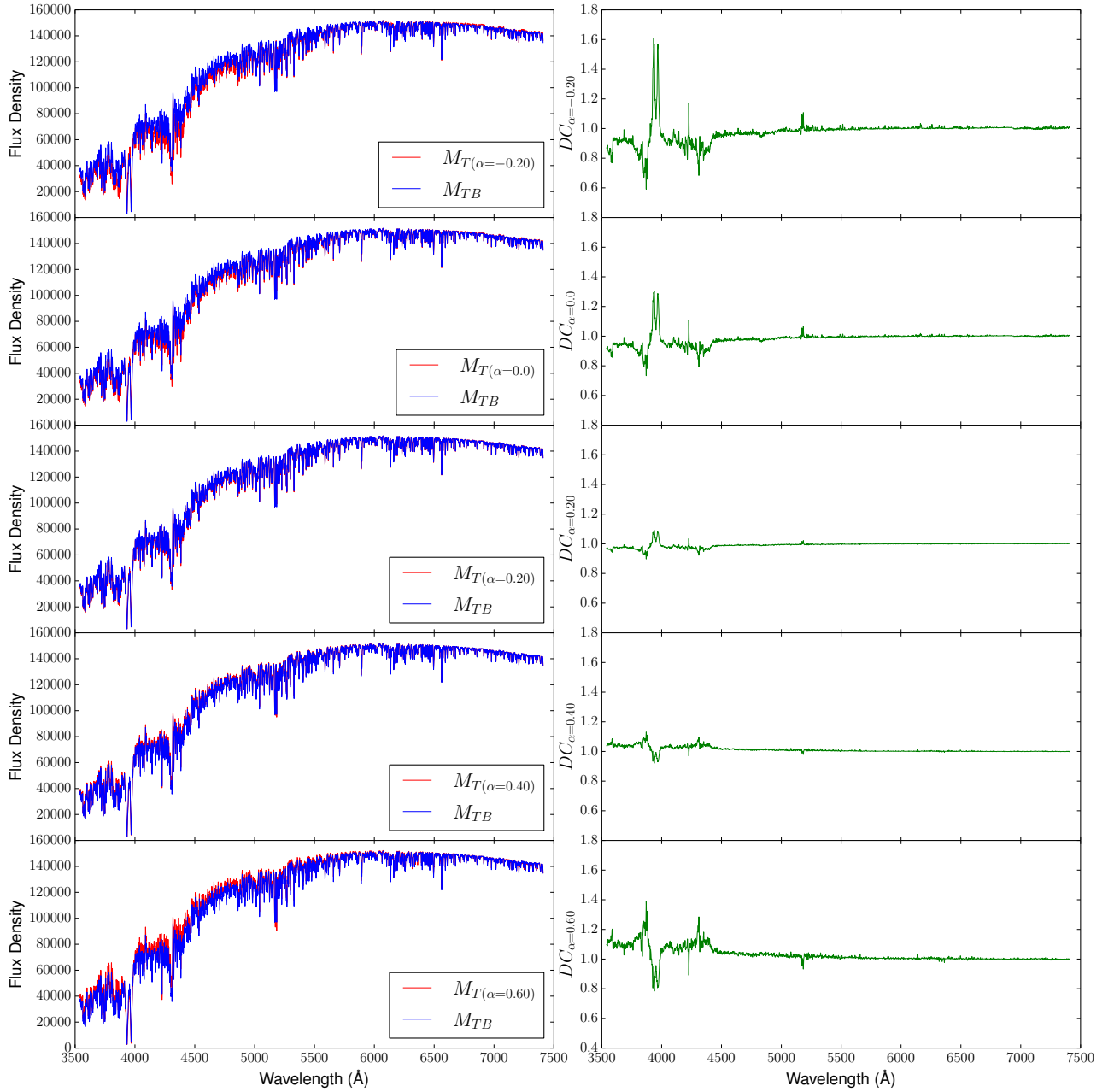


Figure 4.6: Example of Differential corrections for MILES star m0923. This empirical MILES star has an $[Mg/Fe]$ value of 0.3. The left panel compares the resulting spectra of the theoretical enhanced (or deficient) ($M_{T(\alpha=x)}$) and theoretical base M_{TB} stars. Flux Density is in units of $\text{erg/s/cm}^2/\text{\AA}$. The right panel shows the resulting differential correction ($DC_{(\alpha=x)}$), derived from equation 4.1, for each of the $[\alpha/Fe]$ abundances.

CHAPTER 4

described in Section 4.5.1. The routine follows the method presented in Falcón-Barroso et al. (2011), which adopted the V filter response from Buser & Kurucz (1978) and originates from Fukugita et al. (1995). This method calculates the V-band flux of each star, relative to the Vega V band magnitude and zero point (see equation 1 of Falcón-Barroso et al. 2011). The V band magnitude of Vega was taken to be 0.03 mag to be consistent with the Alonso et al. (1995) work, that is used in the SSP calculation for converting theoretical isochrone parameters, described in section 4.5.1. Example sequences for MILES star m0067 are shown in Figures 4.7 and 4.8 for the α -sensitive Mg_b and Ca4227 index regions, respectively. These sequences show the qualitative behaviour expected, with the strongest features present in the largest $[\alpha/\text{Fe}]$ abundance (0.60) sMILES spectra, in agreement with the $[\alpha/\text{M}]$ abundance sequences of theoretical spectra in Chapter 3. In Figure 4.8, the absorption features at ≈ 4237 and 4250\AA are known FeI lines (see the Kurucz website¹ for details of these lines).

In Figures 4.9-4.13 I show plots summarising final, full sMILES libraries for $[\alpha/\text{Fe}] = -0.20, 0.0, 0.20, 0.40$ and 0.60 respectively, with the flux normalised to the flux at 5500.7\AA for each spectrum. Recomputing the erroneous spectra with a linear interpolation, listed in Section 4.3, removed large negative outliers in these plots. These figures highlight the lack of unphysical outliers for the full 801 sub-sample used in the SSP calculations. Most noticeable in these figures are the increasing strength of the TiO bands, with increasing $[\alpha/\text{Fe}]$ abundance, which are prominent in the coolest MILES stars.

To summarise the final library, we plot the final sMILES stars in the $[\alpha/\text{Fe}]$ vs $[\text{Fe}/\text{H}]$ plane, similar to Figure 4.1, in Figure 4.14 to show the final coverage in these parameters, including the 925 empirical MILES stars used in the SSP calculations. Note the reduced range of $[\text{Fe}/\text{H}]$ of sMILES stars, compared to Figure 4.1, caused

¹<http://kurucz.harvard.edu/>

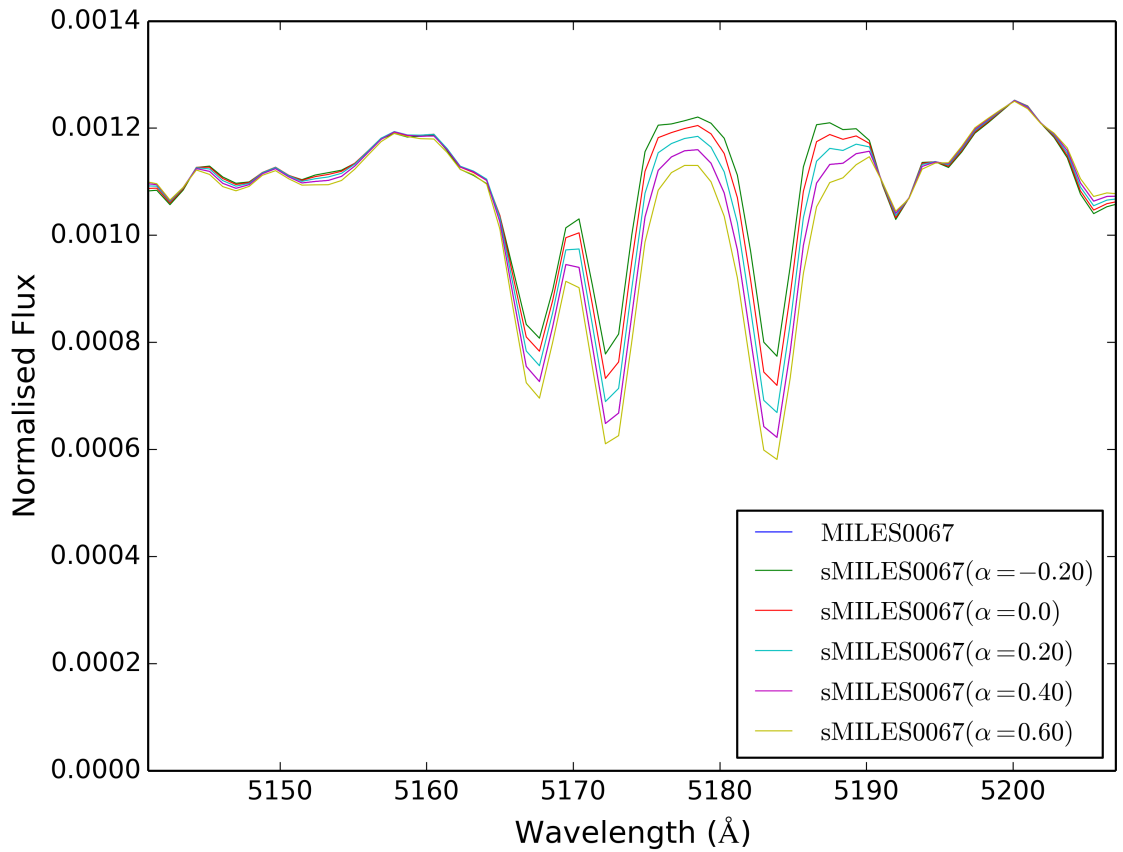


Figure 4.7: Example of a sequence of sMILES stars, with the corresponding MILES star, for the wavelength range around the α -sensitive Mg_b index. For this case, the MILES star is equivalent to the sMILES star at ($\alpha=0.40$), because the empirical MILES star is at $[\text{Mg}/\text{Fe}]=0.40$. The α label here represents the $[\alpha/\text{Fe}]$ abundance that the MILES star has been corrected to. The sequence is qualitatively correct, with increasing feature strength for increasing α abundance.

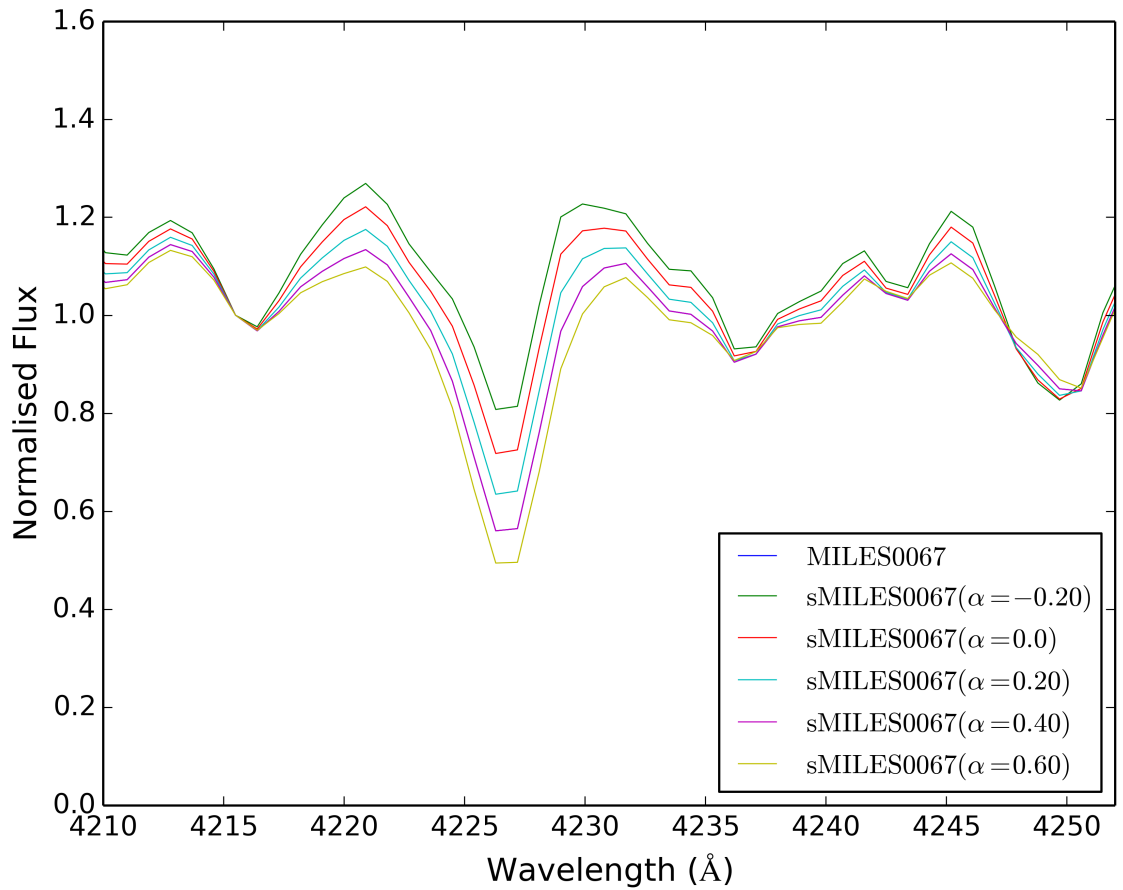


Figure 4.8: Example of a sequence of sMILES stars, with the corresponding MILES star, for the wavelength range around the α -sensitive Ca4227 index. In this case, the MILES star is equivalent to the sMILES star at ($\alpha=0.40$), because the empirical MILES star is at $[\text{Mg}/\text{Fe}]=0.40$. Colours and labelling are as in Figure 4.7. Spectra are normalised to the flux at 4215.5Å.

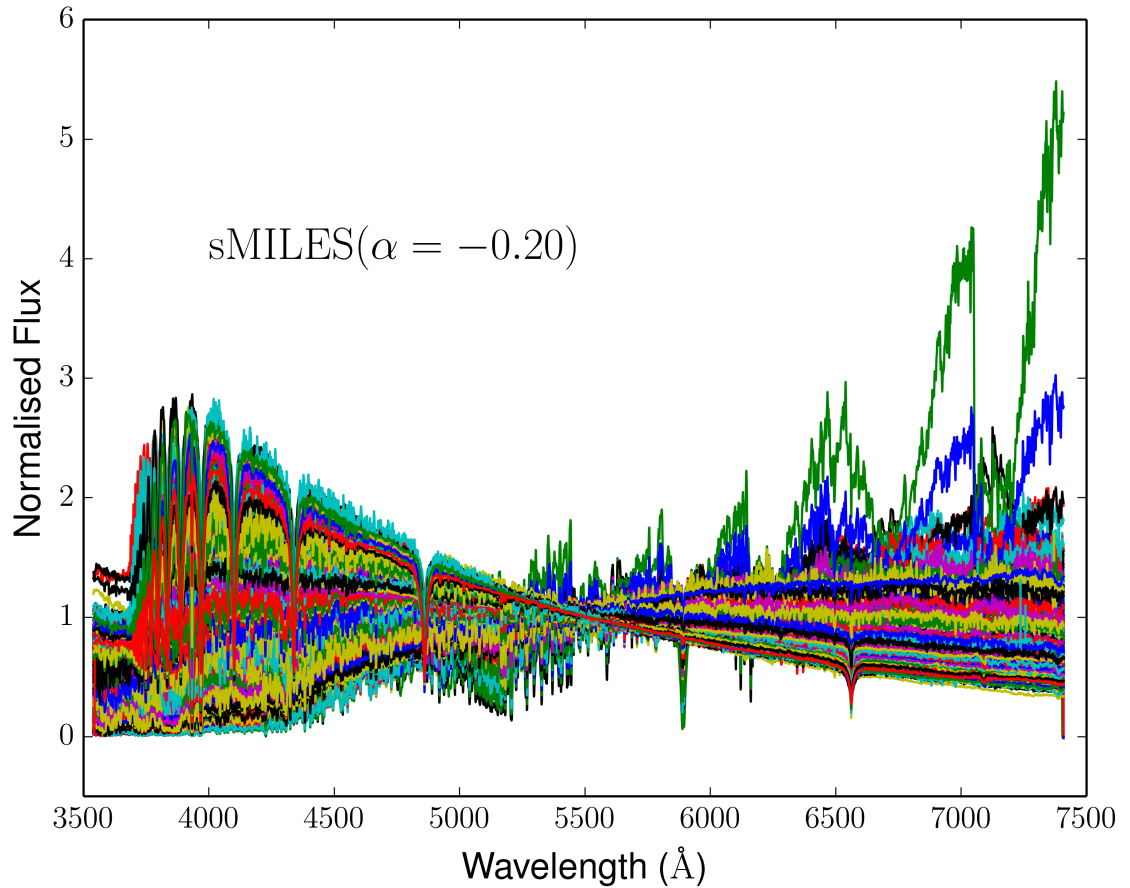


Figure 4.9: $[\alpha/\text{Fe}]=-0.20$ sMILES library for MILES wavelength range. Fluxes are normalised to flux at 5500.7\AA , for each spectrum. The 801 stars that were in the range of our theoretical grid, and therefore the stars that were differentially corrected, are plotted. The remaining 124 stars that had parameters outside the range of our grid were used only empirically in the SSP calculation. All 801 spectra are overplotted and have a randomly chosen colour.

CHAPTER 4

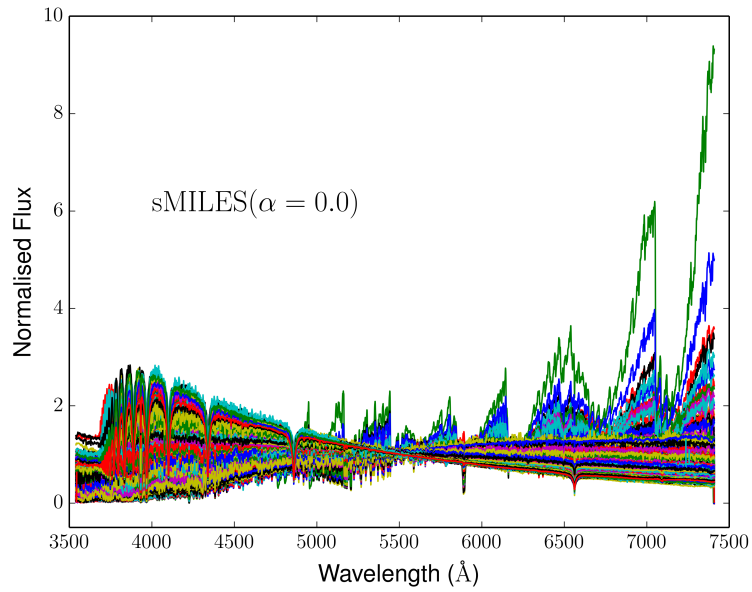


Figure 4.10: $[\alpha/\text{Fe}]=0.0$ sMILES library for the MILES wavelength range. Fluxes are normalised to flux at 5500.7\AA , for each spectrum. Colours and labelling as in Figure 4.9.

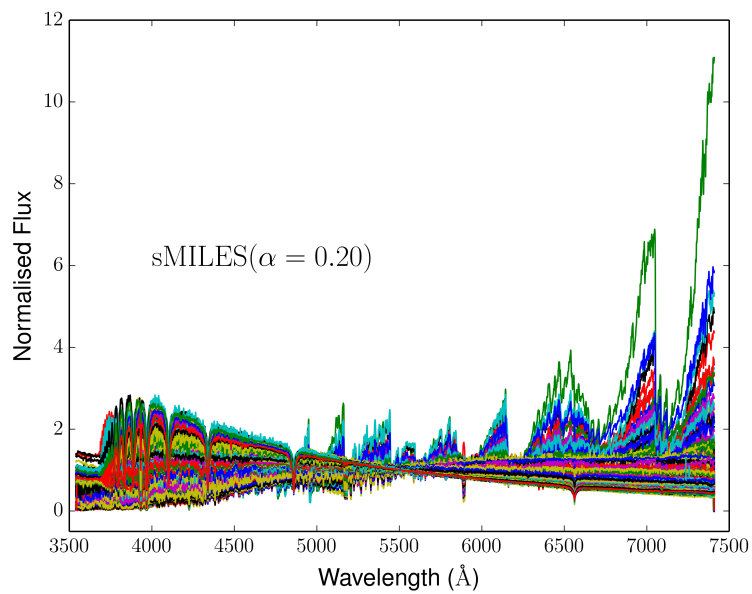


Figure 4.11: $[\alpha/\text{Fe}]=0.20$ sMILES library for the MILES wavelength range. Fluxes are normalised to flux at 5500.7\AA , for each spectrum. Colours and labelling as in Figure 4.9.

CHAPTER 4

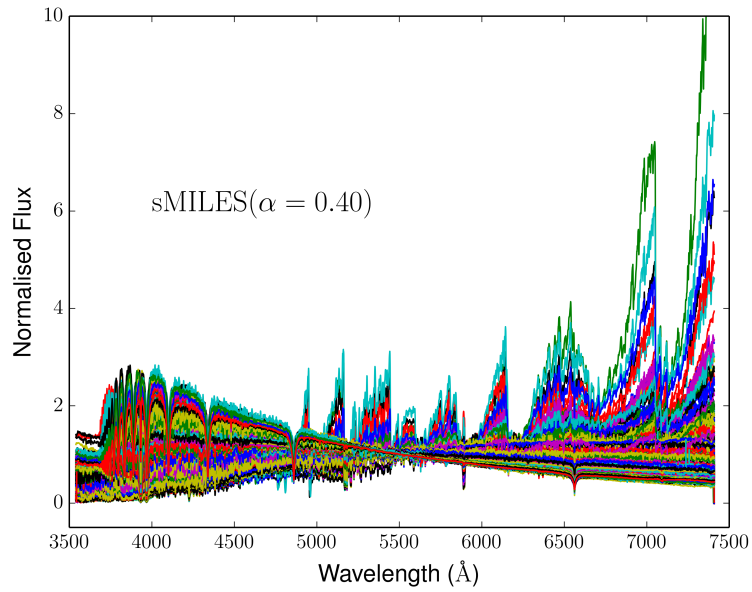


Figure 4.12: $[\alpha/\text{Fe}]=0.40$ sMILES library for the MILES wavelength range. Fluxes are normalised to flux at 5500.7\AA , for each spectrum. Colours and labelling as in Figure 4.9.

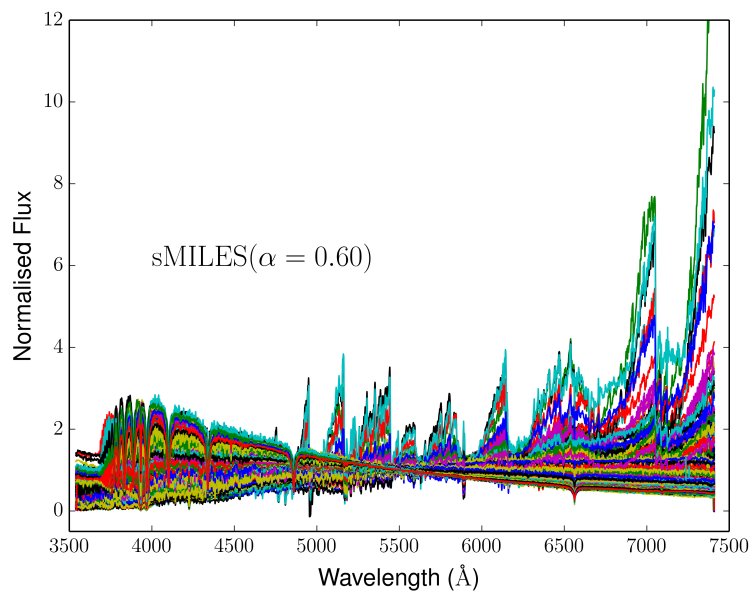


Figure 4.13: $[\alpha/\text{Fe}]=0.60$ sMILES library for the MILES wavelength range. Fluxes are normalised to flux at 5500.7\AA for each spectrum. Colours and labelling as in Figure 4.9.

by the limits of the theoretical grid, computed in Chapter 3. The remaining 124 stars that could not be differentially corrected, are used empirically in the SSP calculations (see Section 4.5). Each horizontal coloured line represents a family of 801 sMILES stars at a given $[\alpha/\text{Fe}]$. The next section describes the methods of SSP computation.

4.5 SSP Generation

With sMILES stars generated, the next stage of the process was to incorporate them into new SSPs, building on the previous methods of La Barbera et al. (2017). Using semi-empirical stars, SSPs will be built with varying $[\alpha/\text{Fe}]$ abundances, for a range of ages and metallicities. This section is split as follows. The first section will detail the SSP calculations which includes a description of parameter conversions, such as metallicity, that allow for the translation of the stellar library component into locations on pre-computed isochrones.

4.5.1 SSP calculation

For the calculation of SSP spectra, we follow the general methodology of Vazdekis et al. (2015), using the families of sMILES stars and the empirical MILES stars to compute SSP spectra of varying $[\alpha/\text{Fe}]$ abundances. The difference in methodology between sMILES SSPs here and those of Vazdekis et al. (2015) is that the differential corrections are performed on individual MILES star spectra, rather than on MILES empirical SSP spectra. I first discuss the individual components of the SSP and then describe the calculation.

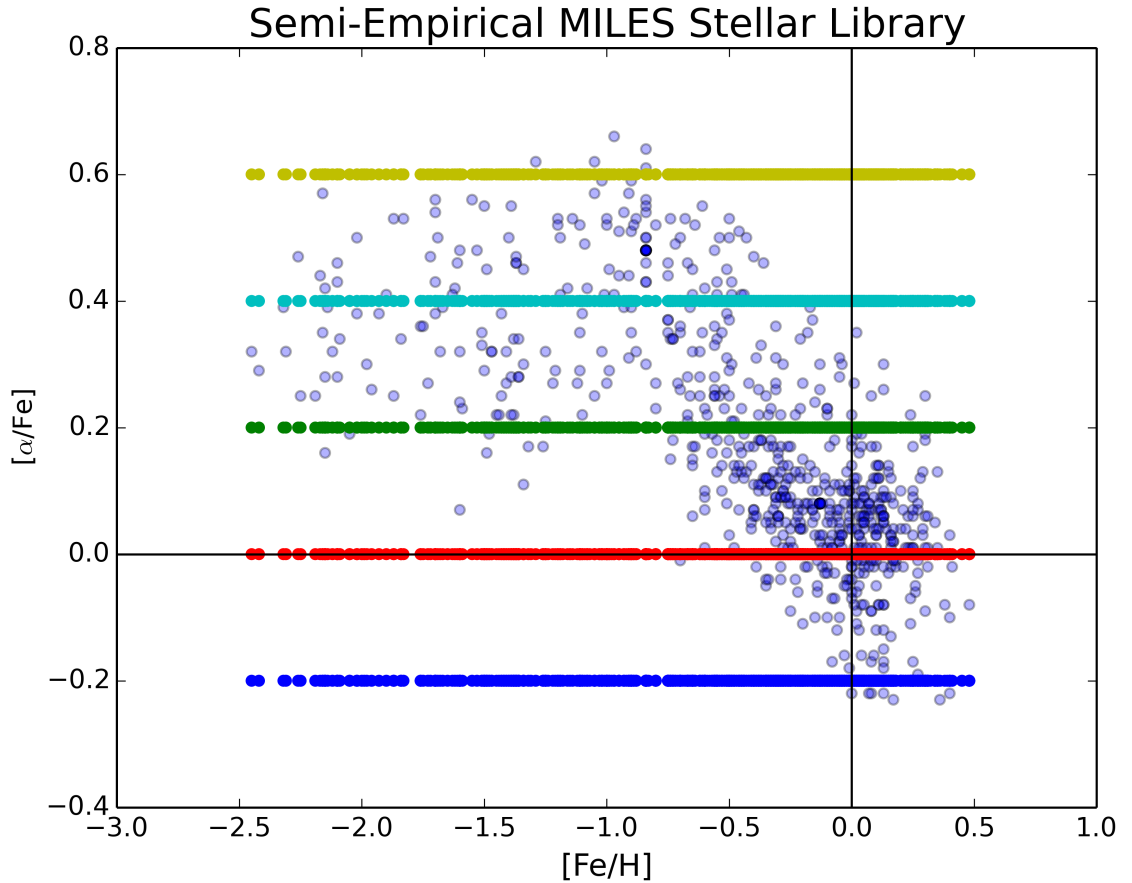


Figure 4.14: Final semi-empirical MILES (sMILES) stellar library in the $[\alpha/\text{Fe}]$ vs $[\text{Fe}/\text{H}]$ plane. The coloured points that lie in horizontal lines represent the families of 801 semi-empirical MILES stars and light blue points represent the same 801 empirical MILES stars. T_{eff} , $\log g$ and $[\text{Fe}/\text{H}]$ values were taken from Cenarro et al. (2007). $[\text{Mg}/\text{Fe}]$ values are from Milone et al. (2011) for 752 stars, with the remaining stars tagged with an $[\text{Mg}/\text{Fe}]$ value taken from a Milky Way relation derived from the work of Bensby et al. (2014).

CHAPTER 4

IMF

Although several IMF parameterisations can be adopted within the Vazdekis et al. (2015) SSP code, because of the more recent applications of published models has been the investigation of IMF variations within early-type galaxies (e.g. La Barbera et al. 2016; La Barbera et al. 2017), we compute models with only two IMF variations, namely the universal and revised Kroupa IMFs (Kroupa 2001). These IMFs are described as multipart power-laws, given by:

$$\xi(m) \propto m^{-\alpha_i}, \quad (4.3)$$

where $\xi(m)dm$ is the number of individual stars in the interval m to $m+dm$. The multipart power law of the universal Kroupa IMF is given by:

$$\begin{aligned} \alpha_0 &= 0.3, & 0.01 \leq m/M_\odot < 0.08 \\ \alpha_1 &= 1.3, & 0.08 \leq m/M_\odot < 0.50 \\ \alpha_2 &= 2.3, & 0.50 \leq m/M_\odot < 1.00 \\ \alpha_3 &= 2.3, & 1.00 \leq m/M_\odot \end{aligned} \quad (4.4)$$

The difference between the universal and revised Kroupa IMF is that α_1 and α_2 change to 1.8 and 2.7 in the revised version, respectively. In the SSP calculations, the lower and upper mass cutoffs are set at 0.1^2 and $100 M_\odot$, respectively. We fix the IMF because we focus on an abundance pattern application in Chapter 5, rather than an investigation of IMF variations.

Isochrones

We use two sets of theoretical isochrone in the SSP calculation. For the $[\alpha/\text{Fe}]=0.20$, 0.0 and 0.20 SSPs we adopt the scaled-solar isochrones from Pietrinferni et al. (2004) and for the $[\alpha/\text{Fe}]=0.40$ and 0.60 SSPs we use the α -enhanced isochrones from Pietrinferni et al. (2006). The α -enhanced isochrones are computed at $[\alpha/\text{Fe}]=0.40$.

²Note that this means that α_0 from equation 4.4 is not used in the SSP calculations.

CHAPTER 4

Both sets of isochrones are computed for 53 different ages in the range 0.03-14Gyr, with step sizes given in Table 4.1. The total metallicities, defined on the Grevesse & Noels (1993) solar abundance scale, were computed for 10 steps in metallicity in the range $Z=0.0003, 0.0006, 0.0010, 0.0020, 0.0040, 0.0080, 0.0100, 0.0198, 0.0240, 0.0300$, for total metal mass fraction. On this scale, the solar metallicity at birth is given as $Z_{\odot}=0.0198$. The BaSTI models isochrones also include a consistent prescription for the atomic diffusion of helium and metals in the solar metallicity models, in order to match the helioseismological constraints of the depth of the convective envelope, the present helium abundance of the solar envelope and current (Z/X) ratio. These isochrones have been constrained by various observations, such as eclipsing binaries, cluster colour-magnitude diagrams and unresolved stellar populations (Pietrinferni et al. 2004; Percival et al. 2009). We use the isochrones that include convective overshooting with a mass loss rate given by $\eta = 0.4$. η is the free parameter in the Reimers law (Reimers 1975), describing the mass loss of a star depending on its luminosity, surface gravity and radius. The value of 0.4 is a commonly used value as this value provides good matches to observations of horizontal branch colours in globular clusters. The thermally pulsing asymptotic giant branch is included in the isochrones, through models described in Marigo et al. (1996) based on methods from Iben & Truran (1978). The details of these techniques and isochrones used here are described in more detail in Vazdekis et al. (2015) and Pietrinferni et al. (2004, 2006, 2009, 2013).

Stellar Spectral Library

The stellar libraries used in the SSP calculations are the sMILES library, and the empirical MILES library. As discussed in Sections 4.2 and 4.3, the semi-empirical

CHAPTER 4

Table 4.1: Age steps of computed sMILES SSPs. The first, second and third columns represent the range in age, the step size in that range and the number of steps, respectively.

Age Range (Gyr)	Step Size (Gyr)	Number of Steps
0.03-0.1	0.01	8
0.1-0.5	0.05	8
0.5-1.00	0.1	5
1.00-4.00	0.25	12
4.00-14.00	0.5	20

MILES library was created through differential corrections to empirical MILES spectra. This differential correction was calculated through equation 4.1, through interpolated theoretical stellar spectra described in Chapter 3. These corrections are then applied to MILES stars through equation 4.2. The final result was a family of 801 semi-empirical MILES spectra for 5 $[\alpha/\text{Fe}]$ abundances of -0.2, 0.0, 0.2, 0.4 and 0.6. The 124 stars that could not be differentially corrected, due to their stellar parameters falling outside of the theoretical stellar grid, were used empirically in each sMILES SSP. The stellar parameters and $[\text{Mg}/\text{Fe}]$ abundances used were those of Cenarro et al. (2007) and Milone et al. (2011), described in Section 4.2.3. The empirical spectra typically have good signal-to-noise that is above 100 and were carefully flux calibrated (Falc3n-Barroso et al. 2011).

Calculation

A key part of the computation of an SSP is the relation between the theoretical isochrone and stellar library components. Translation between the different parameter planes of the isochrone and stellar library is important, because the resultant spectrum is computed through integrations, with the summations of star contributions at different locations on the isochrone. Therefore, a relation between the

CHAPTER 4

observed stellar parameters and theoretical isochrone parameters is required. Theoretical isochrones are computed with T_{eff} , $\log g$, $[M/H]$ whereas stellar spectra are computed on T_{eff} , $\log g$ and $[Fe/H]^3$ and it is important to know the differences between these. The total metallicity in isochrone parameters ($[M/H]_{\text{SSP}}$) is defined by:

$$[M/H]_{\text{SSP}} = \log_{10}(Z/X)_{*} - \log_{10}(Z/X)_{\odot}, \quad (4.5)$$

where Z and X are defined as mass fractions of metals and hydrogen, respectively. The spectroscopic metallicity ($[Fe/H]$), usually defined for stellar spectra is the scaled-metallicity we define in Chapter 2 (Section 2.2.3). For the case of scaled-solar abundances, the total metallicity and $[Fe/H]$ are equivalent, however, in the case where $[\alpha/Fe]$ abundance ratios are non-solar a conversion is needed, which requires a relation between the two metallicities, similar to that done in equation 4 of Vazdekis et al. (2015). To do this for the theoretical models used for differential corrections, a calculation of the total metallicity for various $[Fe/H]$ and $[Mg/Fe]$ values was made. This calculation was done for the Asplund et al. (2005) solar abundances⁴ for a range of $[Fe/H]$ from -2.5 to 0.5, in steps of 0.05 dex, and a range of $[Mg/Fe]$ from -0.25 to 0.75 in steps of 0.05 dex (i.e. the range of our theoretical models in Chapter 3). This was performed with an idl routine provided by Allende Prieto (priv comm.) A fit to the results, using python routine, ‘curvefit’, of the form:

$$[M/H]_{\text{SSP}} = [Fe/H] + a[\alpha/Fe] + b[\alpha/Fe]^2, \quad (4.6)$$

provided an empirical relation between the isochrone $[M/H]_{\text{SSP}}$ and stellar $[Fe/H]$ for use in the SSP calculation. The coefficients a and b were found to be 0.66154 ± 0.00128

³Note that in Chapter 3, we computed theoretical spectra with a different $[M/H]$ that is defined the same as $[Fe/H]$ here. I differentiate between the $[M/H]$ isochrone and stellar definitions, by defining the isochrone symbol as $[M/H]_{\text{SSP}}$.

⁴Note here that there is an inconsistency between the solar abundances in the isochrones and those used in our theoretical stellar spectra.

CHAPTER 4

and 0.20465 ± 0.00218 , respectively. In Figure 4.15, I plot the comparison of results between the calculation and fit for a range of $[\text{Fe}/\text{H}]$ and varying $[\alpha/\text{Fe}]$ abundances. For the full range of our models, the fit is good. To convert the theoretical isochrone parameters into observables (e.g. colours and fluxes), we use relations between fundamental stellar parameters (T_{eff} , $\log g$ and $[\text{Fe}/\text{H}]$) and colours from empirical photometric libraries, rather than using only predictions of theoretical atmosphere calculations, as is done with other SSP methods. The main empirical relations used are those of Alonso et al. (1996) and Alonso et al. (1999) that are empirical, metallicity-dependent relations for dwarfs and giants. Note that these relations do still have a slight dependence on theoretical atmospheres. Bolometric corrections, that are also metal-dependent, from Alonso et al. (1995) and Alonso et al. (1999) are used.

The computation of the SSP is performed through methods described in detail in Vazdekis et al. (2010). I will summarise this information below. The method involves integration of stellar spectra along isochrones, with the adopted IMF providing the number of stars per mass bin. The SSPs are computed for fixed total metallicities for various $[\alpha/\text{Fe}]$ through:

$$S_{\lambda}(t, [\text{M}/\text{H}]_{\text{SSP}}, [\alpha/\text{Fe}], \Phi, I_{\alpha}) = \int_{m_l}^{m_t} S_{\lambda V}(m, t, [\text{Fe}/\text{H}], [\alpha/\text{Fe}]) \times F_V(m, t, [\text{Fe}/\text{H}], [\alpha/\text{Fe}]) \times N_{\Phi}(m, t) dm, \quad (4.7)$$

where $S_{\lambda}(t, [\text{M}/\text{H}]_{\text{SSP}}, [\alpha/\text{Fe}], \Phi, I_{\alpha})$, gives the SSP spectrum at time t , with total metallicity $[\text{M}/\text{H}]_{\text{SSP}}$ (defined in equation 4.5), $[\alpha/\text{Fe}]$ abundance, with a specific IMF (Φ) and isochrone with an $[\alpha/\text{Fe}]$ abundance I_{α} (either 0.0 or 0.4 dex). The units of the resulting SSP spectra are $\frac{L_{\lambda}}{L_{\odot}} \text{\AA}^{-1} \text{M}_{\odot}^{-1}$, where $L_{\odot} = 3.826 \times 10^{33} \text{ erg s}^{-1}$ (Vazdekis et al. 2015). $S_{\lambda V}(m, t, [\text{Fe}/\text{H}], [\alpha/\text{Fe}])$ gives the star spectrum (in units of \AA^{-1}), normalised by the V-band flux for each sMILES star, for a given star mass, spectroscopic metallicity ($[\text{Fe}/\text{H}]$) and $[\alpha/\text{Fe}]$ abundance which is alive at time t . The $[\alpha/\text{Fe}]$ abundances here are the values discussed in previous sections

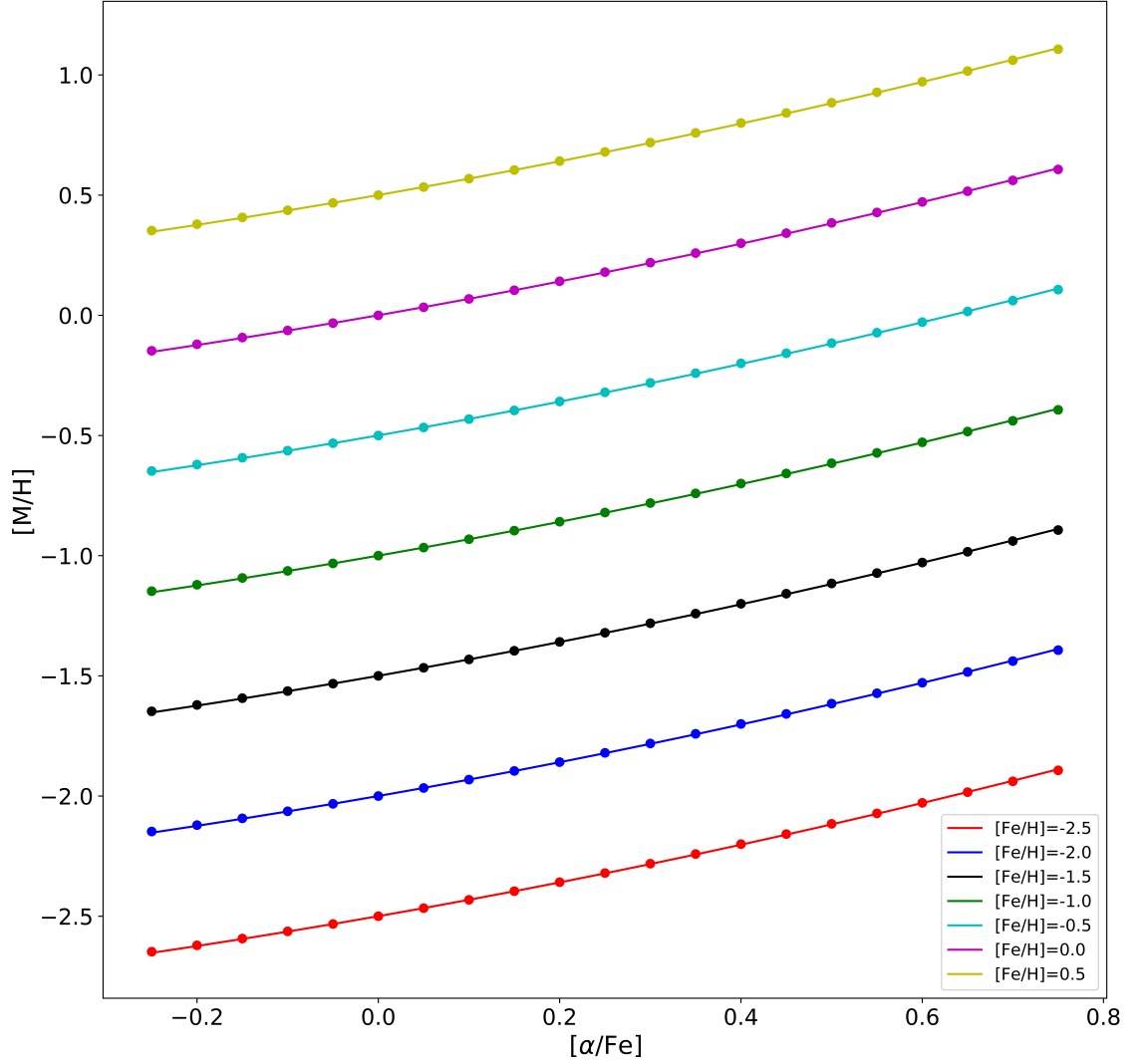


Figure 4.15: Total metallicity ($[M/H]_{SSP}$) as a function of $[\alpha/Fe]$ for the range of metallicities ($[Fe/H]$) in our models. The coloured points represent the results from the full calculation and the solid lines represent the fitted relation, given in equation 4.6. For the full range of $[Fe/H]$ and $[\alpha/Fe]$ in our models, the calculations are fit well by the relation.

CHAPTER 4

(4.5.1), which are made up of 801 sMILES stars with the abundance pattern achieved through differential corrections and remaining 124 empirical MILES stars that have the parameters and abundances of Cenarro et al. (2007) and Milone et al. (2011). $F_V(m, t, [\text{Fe}/\text{H}], [\alpha/\text{Fe}])$ is the total flux of the star in the V-band, in units of erg s^{-1} . F_V values are predicted by the empirical relations from Alonso et al. (1996) and Alonso et al. (1999), for the atmospheric parameters of the star. The adopted total initial SSP mass is $1M_\odot$. The product of $S_{\lambda V}$ and F_V is a monochromatic luminosity that when integrated with respect to mass is a total luminosity, in agreement with the units of the left-hand side of equation 4.7. The V-band normalisation is used so that the absolute magnitudes can be found from the calculated SSPs and will be fully consistent with absolute V-band magnitudes found from the photometric libraries used in the isochrone parameter conversions. In other words, photometric and spectroscopic predictions of the SSPs will be consistent. $N_\Phi(m, t)$ is the number fraction of stars in a mass interval $(m + dm)$ (Vazdekis et al. 2015). m_l and m_t represent the lowest and highest mass stars alive at time t , which is given by the isochrone.

To obtain stellar spectra that match the required T_{eff} , $\log g$ and $[\text{Fe}/\text{H}]$ for locations on the isochrone, given in equation 4.7, the 3D interpolator described fully in Vazdekis et al. (2003, 2010) was used. This interpolator follows a local interpolation scheme in which the routine locates stars in the stellar library within a cube around the required location. The size of the cube is increased in the three dimensions if no stars are found, by splitting the cube into eight smaller cubes at the vertices of the original cube. The size of the smallest cubes are obtained by taking the typical uncertainties in the parameters, given in Cenarro et al. (2001b). Stars in the cubes are combined with their parameters and signal-to-noise considered. Stars that have parameters closer to the required point and higher signal-to-noise are weighted more, through a Gaussian function in each dimension. These combined

CHAPTER 4

spectra in the smaller cubes are then used to obtain the final spectrum, through a series of linear equations. Unphysical solutions, such as negatively weighted stars, that may be found in sparsely populated regions of parameter space are avoided by using the previous weighting system used for the individual cubes in the previous step. We note here that because we have computed families of 801 sMILES stars that all have the same $[\alpha/\text{Fe}]$ abundance and treat the remaining 124 empirical stars as if they had the same abundance, we do not require the extended version of the interpolator that also includes the $[\text{Mg}/\text{Fe}]$ dimension.

For the final result, we computed two libraries of SSPs: one with the universal and one with the revised Kroupa IMF, for the range of isochrone ages and total metallicities, described in Section 4.5, for the five sMILES families. This was 53 steps in age from 0.03-14Gyr and 10 steps in metallicity (Z) from 0.0003-0.030, resulting in 2650 SSPs per IMF.

In summary, this chapter has described the methods of generating a new semi-empirical MILES stellar library. Computed through differential corrections to empirical MILES stars, we have created 5 families of 801 stars for $[\alpha/\text{Fe}] = -0.2, 0.0, 0.2, 0.4$ and 0.6 . I first described the choices of MILES parameters used, discussing both the Cenarro et al. (2007) and Prugniel & Sharma (Prugniel et al. 2011; Sharma et al. 2016) sets of parameters. I then discussed the methods of interpolation used to create theoretical MILES stars, with a set of stars that matched the parameters of empirical MILES stars exactly and then sets of different $[\alpha/\text{Fe}]$ abundances, using the $[\text{Mg}/\text{Fe}]$ measurements as a proxy for all the α elements. Next, I outlined the method of differential corrections, through equations 4.1 and 4.2, and show two examples of the series of differential corrections computed. Finally, I described the SSP calculation, using sMILES stars to build a new library of semi-empirical SSPs with different $[\alpha/\text{Fe}]$ abundances. This outlined all aspects of the calculation such as

CHAPTER 4

isochrones and IMF adopted. This resulted in two libraries of 2650 semi-empirical SSPs, with one calculated with the universal Kroupa IMF and the other with the revised Kroupa IMF. Chapter 5 of this thesis will focus firstly on testing these new SSPs, through comparisons to previous works in both spectral and index analyses, and then will show an example of the application of the SSPs to galaxy studies.

Chapter 5

Semi-Empirical SSPs : Testing and Application

With semi-empirical SSP models generated, using a newly computed library of sMILES stellar spectra, the next stage of this project is the initial testing and application of these models. This Chapter is split into two sections. The first section will focus on testing SSPs, with an analysis of indices and spectra. The second section will show an example application of the new SSPs to a sample of external galaxies.

5.1 Testing SSPs

The testing of SSPs will focus on sequences of spectra, similar to those produced in Chapter 3, with certain parameters fixed. I begin with sequences of individual parameters (age, metallicity, then $[\alpha/\text{Fe}]$) for a few examples in parameter space, with checks of Lick index line-strengths. I compare the results of the sMILES models to those of Vazdekis et al. (2015), because the two sets of models are based on the same methods and codes presented in these models, so differences between them should originate from the treatment of the differential correction and theoretical

CHAPTER 5

stellar models used, rather than differences in SSP calculation. Vazdekis et al. models differentially correct on the SSP level, rather than star level like that of sMILES SSPs.

Another recent set of published models is that of Conroy et al. 2018, mentioned briefly in Chapter 1 (Section 1.2). These models are an update of the Conroy & van Dokkum (2012) models, in that SSPs are calculated for a larger range of metallicities ($[\text{Fe}/\text{H}]^1$) than previously. These models differ from the sMILES SSPs presented here in a few aspects. Firstly, like the work of Vazdekis et al. (2015), Conroy et al. (2018) perform differential corrections on an SSP-level, through calculations of fully theoretical SSPs, using Kurucz model atmospheres and stellar spectra (Kurucz 1979b; Kurucz & Avrett 1981; Kurucz 1993), that are then applied to empirical SSPs calculated using MILES and extended IRTF (Villaume et al. 2017b) libraries. The theoretical stellar spectra used in Conroy et al. (2018) are computed with a larger number of molecules included in the line lists than in the models computed in Chapter 3, with the inclusion of FeH, H₂O, MgO, AlO, NaH, VO, SiH, CrH and CaH. Secondly, the differential corrections are computed differently, in that the Conroy et al. (2018) SSPs calculate the responses of individual elements and then combine them, through multiplications, to obtain arbitrary abundance patterns. Conroy et al. (2018) calculate SSP responses for 18 elements, for $[\text{X}/\text{H}]=-0.3$ and 0.3 apart from C, which is computed at $[\text{C}/\text{H}]=0.15$ to avoid the generation of carbon stars. sMILES models compute the stellar responses for total $[\alpha/\text{Fe}]$ changes, with fully consistent model atmospheres and spectral synthesis calculations, and use the responses to differentially correct empirical MILES stars that are used in the SSP calculations. The range of $[\alpha/\text{Fe}]$ for sMILES SSPs is -0.2 to 0.6 in steps of 0.2 dex for a large range of total metallicities. Thirdly, the adopted isochrones in the calculations are different, with Conroy et al. (2018), using MIST scaled-solar isochrones

¹As Conroy et al. (2018) models are computed with scaled-solar isochrones, $[\text{M}/\text{H}]_{\text{SSP}}=[\text{Fe}/\text{H}]$.

CHAPTER 5

for all models (Choi et al. 2016; Dotter 2016), although α -enhanced isochrone calculations are currently in progress. The isochrone and stellar model solar abundance scales are fully consistent in Conroy et al. (2018), with both components using Asplund et al. (2009). sMILES SSPs are calculated with scaled-solar isochrones for $[\alpha/\text{Fe}]=-0.2, 0$ and 0.2 SSPs and α -enhanced (0.4) isochrones for $[\alpha/\text{Fe}]=0.4$ and 0.6 , from BaSTI (Pietrinferni et al. 2004; Pietrinferni et al. 2006). sMILES SSPs calculations are inconsistent in solar abundance scales, in that the stellar models are computed assuming Asplund et al. (2005) abundances whereas BaSTI isochrones are calculated with Grevesse & Noels (1993) abundances. With these numerous differences in mind, initial sMILES model predictions are compared to the models of Vazdekis et al. (2015) for simplicity.

5.1.1 Age

In Figure 5.1, I show a sequence of sMILES SSP spectra for varying age, with fixed solar metallicity and α abundance ($[\text{M}/\text{H}]_{\text{SSP}}=0.06$, $[\alpha/\text{Fe}]=0.0$) and a universal Kroupa IMF. This figure shows two commonly used age-sensitive Lick indices, $\text{H}\beta$ and $\text{H}\beta_o$. Spectra are normalised to their flux at 4834.7\AA and 4825.7\AA for the $\text{H}\beta$ and $\text{H}\beta_o$ plots, respectively. As shown, both indices behave in a sense similar to previous work (Vazdekis et al. 2015), in that the strength of these features decrease with increasing SSP age. $\text{H}\beta_o$ is a stronger feature than $\text{H}\beta$, with larger indices present for all ages. Interestingly, the sMILES SSPs show approximately the same decrease with age for these features, compared to the models of Vazdekis et al. (2015). For the same parameters, Vazdekis et al. models change from 2.96 to 1.73\AA in $\text{H}\beta$ with ages of 2 Gyr to 14 Gyr, whereas the sMILES models change from 2.93 to 1.67\AA . For $\text{H}\beta_o$, sMILES models change from 4.11 to 2.92\AA with 2 Gyr to 14 Gyr, whereas Vazdekis et al. models change from 4.13 to 2.97\AA . The similarity in index strength and strength change with age presented gives confidence in the sMILES

CHAPTER 5

models for age estimates in stellar population studies in this part of parameter space. This is to be expected because around $[\alpha/\text{Fe}]=0.0$ and $[\text{M}/\text{H}]_{\text{SSP}}=0.06$, the SSP predictions are constructed mainly from empirical stars, for both sMILES and Vazdekis et al. models.

I test a region of parameter space, in which differential corrections are required to construct SSPs. In Figure 5.2, I plot sMILES and Vazdekis et al. SSP predictions of $\text{H}\beta$ and $\text{H}\beta_o$ changes with age, for solar metallicity and $[\alpha/\text{Fe}]=0.4$ models. The $[\alpha/\text{Fe}]$ -enhancement requires differential corrections, which are performed on individual MILES stars in sMILES models and on an SSP-level in Vazdekis et al. models. As shown, the sMILES models predict stronger index strengths, at all ages for both $\text{H}\beta$ and $\text{H}\beta_o$. Despite this offset, the change of index strength with age is similar in both models. For $\text{H}\beta$, sMILES models predict a change of index strength from 3.01 to 1.90 Å for a change in age from 2 to 14 Gyr, whereas Vazdekis et al. models predict a change of index strength from 2.87 to 1.75 for the same change in age. For $\text{H}\beta_o$, sMILES models predict a change of index strength from 4.12 to 2.99 Å and Vazdekis et al. models predict a change of index strength from 3.87 to 2.65, for the same change in age. Therefore, sMILES and Vazdekis et al. models have similar predictions of the effect of age on SSPs, in this region of parameter space.

5.1.2 Metallicity

In Figure 5.3, I show a sequence of sMILES SSPs for varying metallicity, with a fixed age (10 Gyr), α abundance ($[\alpha/\text{Fe}]=0.0$) and universal Kroupa IMF. I show two of the more commonly used, metallicity-sensitive Lick indices, particularly in the $[\text{MgFe}]$ and $[\text{MgFe}]'$ definitions I investigate in Section 5.1.4. SSPs are plotted in the wavelength range of Fe5270 and Fe5335, with their index strengths shown. Spectra are normalised to their flux at 5240.6 Å and 5310.8 Å for the Fe5270 and Fe5335 plots, respectively. Again, the sequence is as expected with an increase

CHAPTER 5

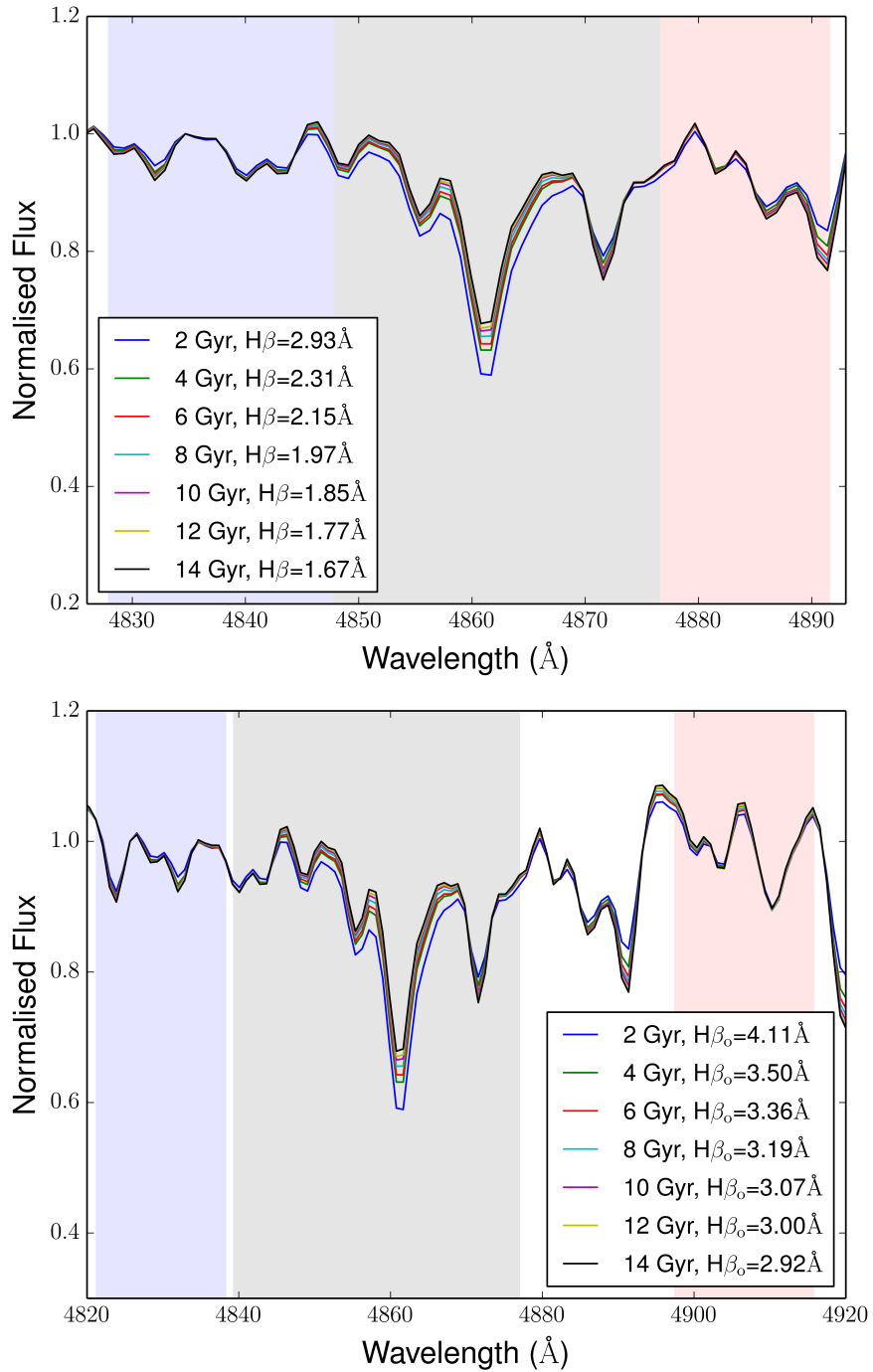


Figure 5.1: sMILES SSP age sequence for two age-sensitive features (Top panel: $H\beta$ with flux normalised at 4834.7\AA , Bottom panel: $H\beta_o$ with flux normalised at 4825.7\AA) for solar metallicity and $[\alpha/\text{Fe}]$ abundance. $H\beta$ and $H\beta_o$ line strength indices are also plotted, showing the age-sensitivity of these features, with decreasing strength for increasing age. The blue pseudo-continuum, feature and red pseudo-continuum bands definitions (Trager et al. 1998; Cervantes & Vazdekis 2009) are plotted in blue, grey and red respectively.

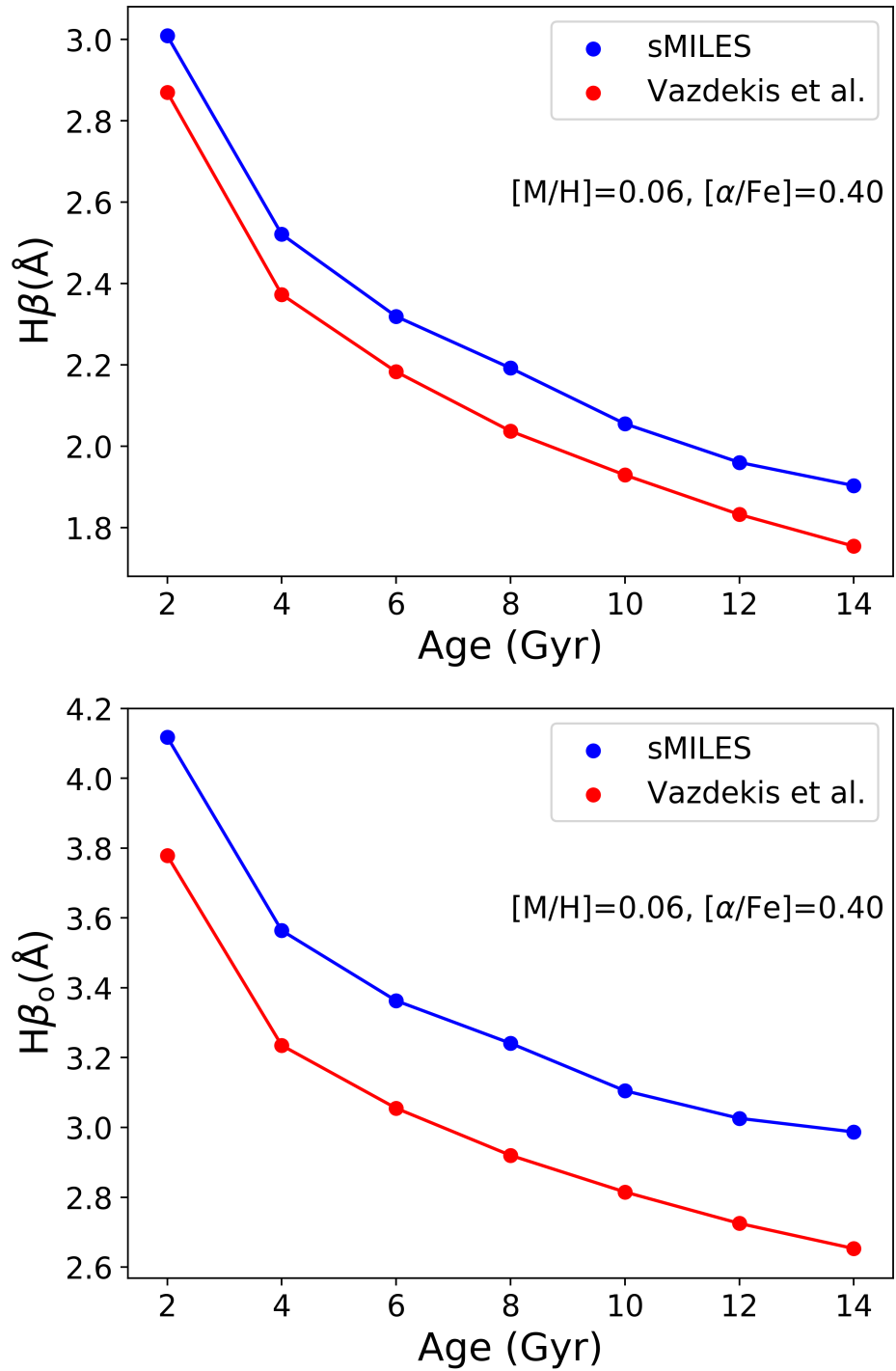


Figure 5.2: sMILES and Vazdekis et al. SSP predictions of $H\beta$ (Top panel) and $H\beta_0$ (Bottom panel) Lick index variations with age. The SSPs are solar metallicity, with $[\alpha/\text{Fe}]$ -enhanced abundances.

CHAPTER 5

in index strength for increasing metallicity. Similar behaviours between models is found in terms of the change of index strength with metallicity. In Fe5270, sMILES models show a change from 0.80 to 3.91Å with $[M/H]_{\text{SSP}}=-1.79$ to $[M/H]_{\text{SSP}}=+0.26$, and Vazdekis et al. models change from 0.88 to 3.88Å. For Fe5335, Vazdekis et al. models change from 0.92 to 3.89Å for a change of metallicity from $[M/H]_{\text{SSP}}=-1.79$ to 0.26, whereas sMILES models change from 0.87 to 3.93Å. For 10 Gyr old, solar α abundance SSPs, the two model sets agree well. This demonstrates the similarity of the two differential correction methods in this region of parameter space.

As in Section 5.1.1, I also test in a region where differential corrections were required to construct SSPs. In $[\alpha/\text{Fe}]=0.4$ SSPs, sMILES models and Vazdekis et al. models use differential corrections to produce predictions. Any differences in predictions should arise from differences in the underlying stellar spectral models used to perform this correction, and/or from the differential correction method. In Figure 5.4, I plot sMILES and Vazdekis et al. SSP predictions of Fe5270 and Fe5335 index changes with total metallicity, for 10 Gyr old and $[\alpha/\text{Fe}]=0.4$ populations. For the full metallicity range of sMILES models, the predictions of sMILES and Vazdekis et al. SSPs are very similar, with very good agreement in the lowest metallicity bins and small differences in the highest metallicity bins. The agreement in the lowest metallicity bins may originate from the differential correction, due to $[\alpha/\text{Fe}]$ variations, being small at low overall metal abundances. Therefore both sets of models, that are constructed using differential corrections, are similar in this low metallicity regime. For the highest metallicities ($[M/H]=0.06$ and $[M/H]=0.26$) sMILES models predict slightly larger index strengths than the Vazdekis et al. models, with differences of $\sim 0.2-0.3$ Å. Further differences between the two sets of models are explored in Section 5.1.4.

In Figure 5.5, I demonstrate the well-known age-metallicity degeneracy of SSPs (Worthey 1994), using sMILES models. In the top panel of this figure, I plot a

CHAPTER 5

sequence of ages of sMILES SSPs from 4 Gyr to 14 Gyr for a fixed metallicity and universal Kroupa IMF. In the bottom panel I plot a sequence of sMILES SSPs from $[M/H]_{\text{SSP}}=-1.79$ to $+0.26$ for a fixed age (10 Gyr) and universal Kroupa IMF. The effect of ageing a stellar population can be mimicked by increasing the metallicity of the population at a fixed age, demonstrated by the similarity in the sequences, particularly for older populations, where the 10, 12 and 14 Gyr spectra look very much the same as the 10 Gyr, $[M/H]_{\text{SSP}}=0.06$ and 0.26 spectra. The use of a combination of spectral indices that are more sensitive to age (e.g. $H\beta$) or metallicity (e.g. Fe5270) can be used to break this degeneracy.

5.1.3 $[\alpha/\text{Fe}]$

In Figure 5.6, I show a sequence of sMILES SSPs for varying α abundance with fixed solar metallicity, 10 Gyr age and universal Kroupa IMF. In this figure I focus on two α -sensitive Lick indices of Ca4227 and Mg_b , the latter of which is used in the total metallicity-sensitive indices $[\text{MgFe}]$ and $[\text{MgFe}]'$. Spectra are normalised to their flux at 4211.9\AA and 5150.6\AA in the Ca4227 and Mg_b plots, respectively. The sense of the change is as expected from first order, in that there is a general increase of index strength for increasing α abundance. The new sMILES SSP models cover a wider range of $[\alpha/\text{Fe}]$ (-0.2 to 0.6) than the Vazdekis et al. models (0 to 0.4), therefore comparisons can only be made for the $[\alpha/\text{Fe}]=0.0$ and 0.4 SSPs. The change of Ca4227 index strength for sMILES models is 1.79 to 2.53\AA for a change of $[\alpha/\text{Fe}]=0.0$ to 0.4 . Vazdekis et al. models show a similar change in Ca4227 from 1.83 to 2.43\AA for the same change in $[\alpha/\text{Fe}]$. Similar changes in Mg_b are also found for both models, with sMILES changing from change from 3.79 to 4.54\AA and Vazdekis et al. models changing from 3.77 to 4.61\AA . This verifies the similarity in differential correction on SSPs compared to corrections individual stars, and both Coelho and CAP stellar spectra model predictions of Mg_b variations with changes

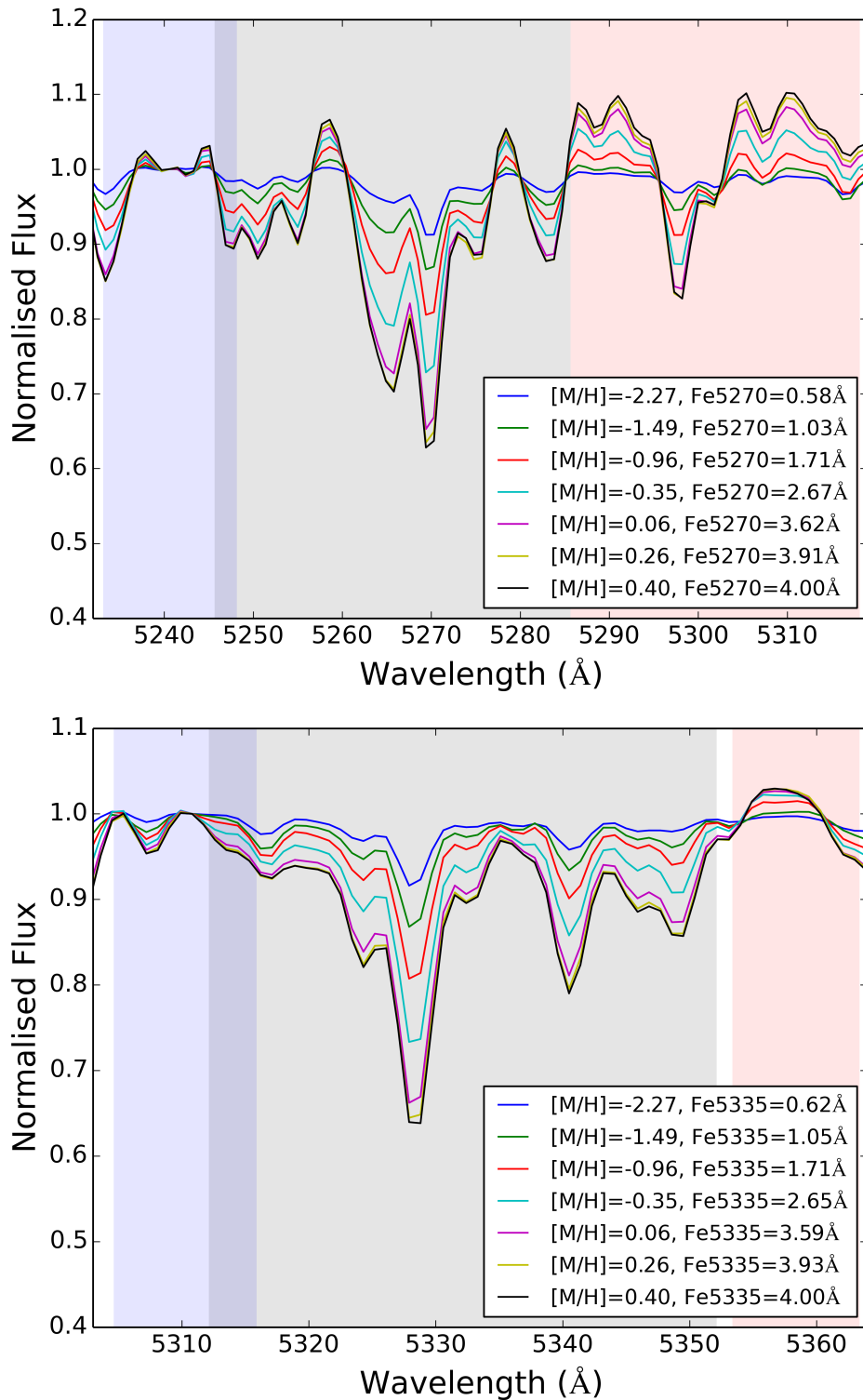


Figure 5.3: sMILES SSP spectral sequences for two metal-sensitive features (Top panel: Fe5270 with flux normalised at 5240.6Å, Bottom panel: Fe5335 with flux normalised at 5310.8Å) for a fixed age (10 Gyr) and solar $[\alpha/\text{Fe}]$ abundance pattern. The blue pseudo-continuum, feature and red pseudo-continuum bands definitions (Trager et al. 1998) are plotted in blue, grey and red respectively.

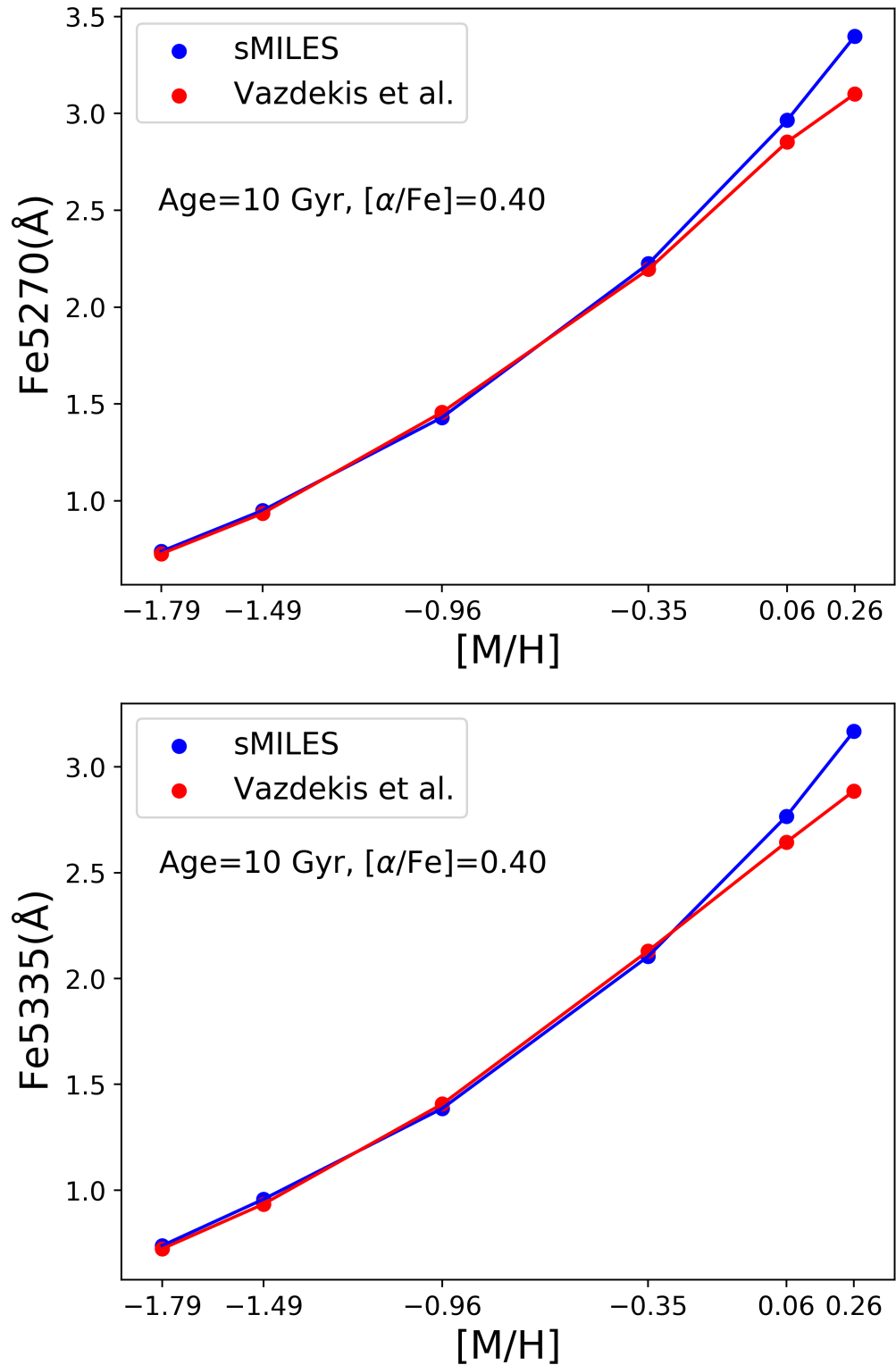


Figure 5.4: sMILES and Vazdekis et al. SSP predictions of Fe5270 (Top panel) and Fe5335 (Bottom panel) Lick index variations with $[M/H]$. The SSPs are 10 Gyr old, with $[\alpha/Fe]$ -enhanced abundances.

CHAPTER 5

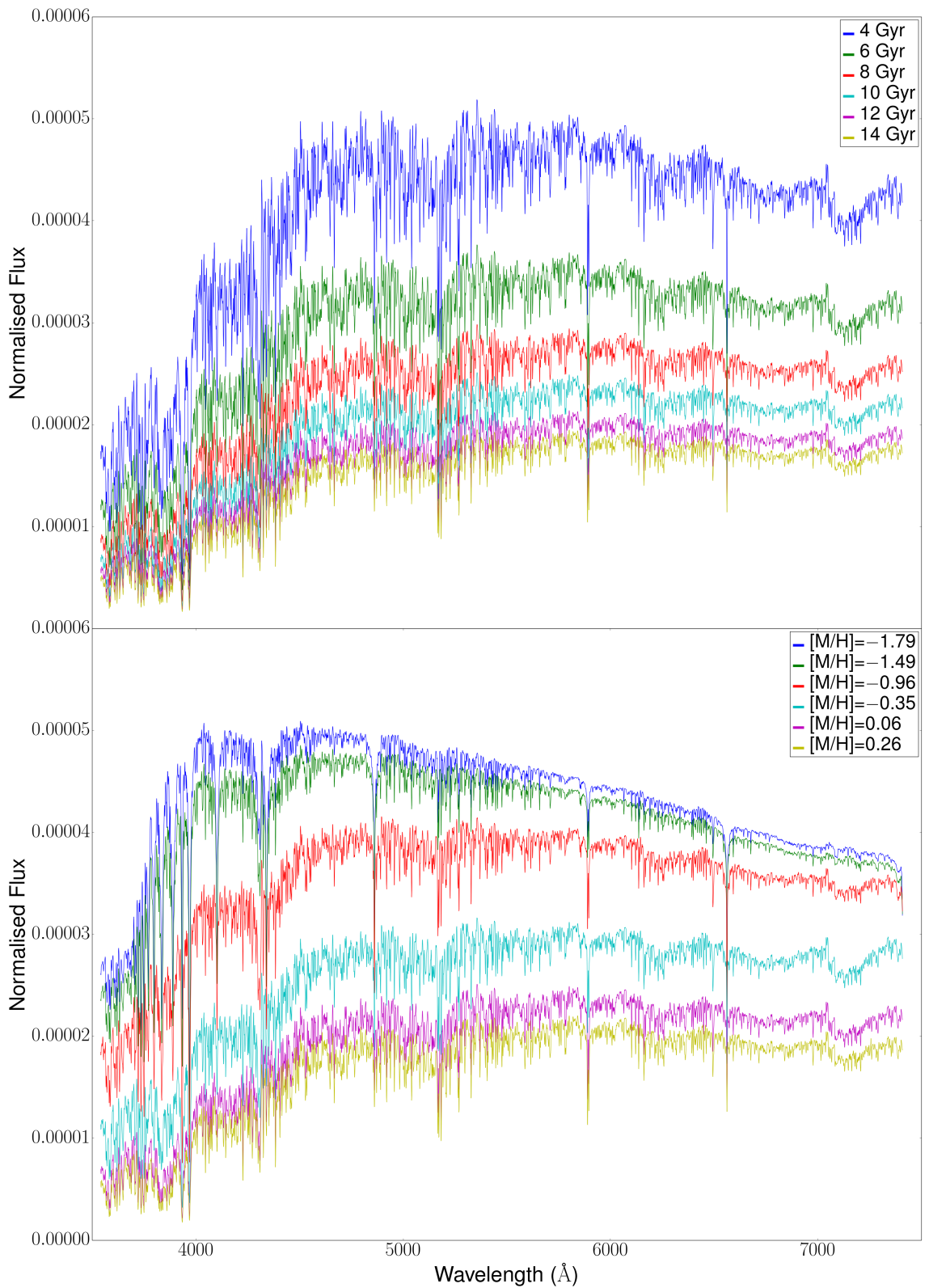


Figure 5.5: Top panel: sMILES SSP sequence of age for fixed metallicity ($[M/H]_{\text{SSP}}=0.06$) and universal Kroupa IMF in the full MILES wavelength range. Bottom panel: sMILES SSP sequence of metallicity for a fixed age (10 Gyr) and universal Kroupa IMF.

CHAPTER 5

in $[\alpha/\text{Fe}]$ (Figures 2.3 and 2.8). Other metallicity and age regimes are investigated in Section 5.2.

5.1.4 $[\text{MgFe}]$ and $[\text{MgFe}]'$

Two important index combinations used in the study of integrated stellar populations are the total metallicity-sensitive indices of $[\text{MgFe}]$ and $[\text{MgFe}]'$. These indices, defined in González (1993) and Thomas et al. (2003b) respectively, are given by:

$$[\text{MgFe}] = \sqrt{(\text{Mg}_b \times \langle \text{Fe} \rangle)} \quad (5.1)$$

$$\langle \text{Fe} \rangle = 0.5 \times (\text{Fe}5270 + \text{Fe}5335) \quad (5.2)$$

$$[\text{MgFe}]' = \sqrt{\text{Mg}_b \times (0.72 \times \text{Fe}5270 + 0.28 \times \text{Fe}5335)} \quad (5.3)$$

To test the accuracy of sMILES models, I compare their indices to those previously calculated with Vazdekis et al. (2015). Both indices were found to be almost insensitive to $[\alpha/\text{Fe}]$ abundance in Vazdekis et al. (2015) (their Figure 14) and Thomas et al. (2003b) (their Figure 7 for an old, solar metallicity model) SSP models. Both of these models took a semi-empirical approach to account for $[\alpha/\text{Fe}]$ variations, with Vazdekis et al. performing differential corrections through ratios of theoretical spectra, whereas Thomas et al. (2003b) modified Lick indices through response functions. I compare sMILES models to those of Vazdekis et al. models. I first test the sMILES models using only the two $[\alpha/\text{Fe}]$ points computed in Vazdekis et al. and then I test for the full range of α abundances computed in this project. In Figures 5.7 and 5.8 I show the differences in $[\text{MgFe}]$ and $[\text{MgFe}]'$ indices between sMILES and Vazdekis et al. models for three ages and various metallicities. Calculated here are the gradients (e.g. how much the index changes with changing $[\alpha/\text{Fe}]$), of the line between the $[\alpha/\text{Fe}]=0$ and 0.4 points in units of $\text{\AA} \text{ dex}^{-1}$. To maintain the total metallicity of sMILES SSP models, when varying $[\alpha/\text{Fe}]$, we use equations discussed in Chapter 4 (4.5 and 4.6) to calculate the amount that the other elements (defined

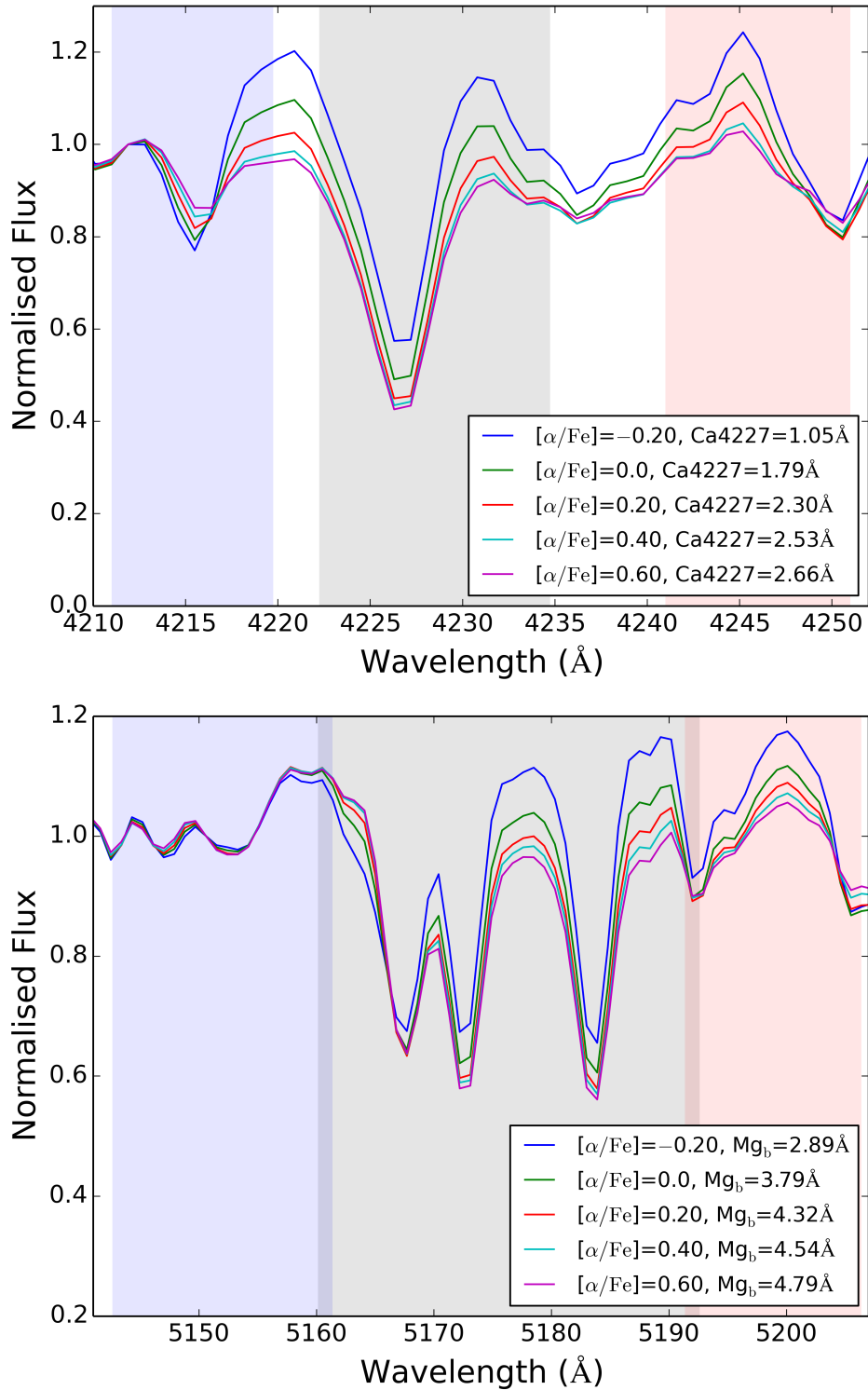


Figure 5.6: sMILES SSP spectral sequences for two α -sensitive features (Top panel: Ca4227 with flux normalised at 4211.9Å, Bottom panel: Mg_b with flux normalised at 5150.6Å for a fixed age (10 Gyr) and solar metallicity. The blue pseudo-continuum, feature and red pseudo-continuum bands definitions (Trager et al. 1998) are plotted in blue, grey and red respectively

CHAPTER 5

by $[\text{Fe}/\text{H}]$), that does not include the α -capture elements, must be reduced by so that $[\text{M}/\text{H}]_{\text{SSP}}$ remains constant. For example, for fixed $[\text{M}/\text{H}]_{\text{SSP}}=0.26$, if $[\alpha/\text{Fe}]=0.0$, then $[\text{Fe}/\text{H}]=0.26$. However, for fixed $[\text{M}/\text{H}]_{\text{SSP}}=0.26$, if $[\alpha/\text{Fe}]=0.4$ then $[\text{Fe}/\text{H}]$ must $=-0.0374$ to maintain total metallicity. This reduction can be seen in Table 5.1, where an increase in $[\alpha/\text{Fe}]$ abundance, at fixed total metallicity results in an increase in Mg_b index and decreases in Fe5270 and Fe5335 indices.

For 7.5 and 14 Gyr SSPs, both models generally agree in $[\text{MgFe}]$ and $[\text{MgFe}]'$ values and change of values with metallicity and α abundances, with very similar gradients found. However, differences are found with the younger 2 Gyr SSP models, with sMILES models predicting a much larger change in both $[\text{MgFe}]$ and $[\text{MgFe}]'$ with increasing $[\alpha/\text{Fe}]$, particularly for the highest metallicity bins. For $[\text{M}/\text{H}]_{\text{SSP}}=0.26$, sMILES models predict gradients of 1.01 and 1.07 $\text{\AA} \text{ dex}^{-1}$ for $[\text{MgFe}]$ and $[\text{MgFe}]'$ changes compared to 0.114 and 0.158 $\text{\AA} \text{ dex}^{-1}$ of Vazdekis et al. models. This difference is caused by the combination of larger Mg_b line strength changes and smaller Fe5270 and Fe5335 line strength changes with an increase of $[\alpha/\text{Fe}]$ for sMILES models, compared to Vazdekis et al. models (see Table 5.1). For Mg_b , Vazdekis et al. models predict a change from 2.85 to 3.71 \AA for a change of 0.4 dex in $[\alpha/\text{Fe}]$, compared to a sMILES model prediction from 2.62 to 3.76 \AA . The opposite behaviour is true for Fe5270 and Fe5335, in which sMILES models predict changes from 3.03 to 2.85 \AA and 3.10 to 2.73 \AA for Fe5270 and Fe5335 respectively, whereas Vazdekis et al. models predict changes of 3.04 to 2.47 \AA and 3.12 to 2.40 \AA . These differences may be a reflection of differences in the predictions of underlying stellar spectral models or different degrees of inconsistency between total metallicity treatment, derived for the stars compared to isochrones.

In conclusion, the sMILES SSP predictions of $[\text{MgFe}]$ and $[\text{MgFe}]'$ changes with $[\alpha/\text{Fe}]$ agree well with Vazdekis et al. models, for intermediate and old SSP ages in a wide range of total metallicities. Differences exist at the youngest age tested (2

CHAPTER 5

Gyr), with sMILES models predicting a larger change in $[\text{MgFe}]$ and $[\text{MgFe}]'$ indices with changing $[\alpha/\text{Fe}]$, compared to Vazdekis et al. models. These differences are largest at the highest metallicities tested. Further work to understand the origin of these differences is required, as well as comparisons to observations to determine the true sensitivity of $[\text{MgFe}]$ and $[\text{MgFe}]'$ indices to abundance pattern. Observations at the star level should help this issue. If $[\text{MgFe}]$ and $[\text{MgFe}]'$ is measured as a function of $[\text{Fe}/\text{H}]$ and $[\alpha/\text{Fe}]$ for a large number of Milky Way stars, this would help define a correlation that in principle the SSP models should also follow. In regards to the type of stars required, AGB, main-sequence and RGB stars all have significant contributions to the total SSP light at 2 Gyr, however at the wavelength regime of $[\text{MgFe}]$ and $[\text{MgFe}]'$, main-sequence stars are the dominate source. Due to the chemical history of the Milky Way, trends would only be available in the age, metallicity and $[\alpha/\text{Fe}]$ regimes where stars currently reside (e.g. young, metal-rich with \sim solar $[\alpha/\text{Fe}]$ or old, metal-poor with high $[\alpha/\text{Fe}]$). Observations of stars in other nearby systems (like those highlighted in Figure 1.2), would allow for $[\text{MgFe}]$ and $[\text{MgFe}]'$ trends to be obtained in other metallicity and abundance pattern regimes. I note, however, that sMILES and Vazdekis et al. SSP models deviate the most in young, high metallicity and high $[\alpha/\text{Fe}]$ stellar populations, which may not represent any real systems in the universe. Through comparisons of $[\text{MgFe}]$ and $[\text{MgFe}]'$, it was also found that a choice of using an α enhanced isochrone for intermediate $[\alpha/\text{Fe}]$ SSP (+0.2) models produced a smaller sensitivity of $[\text{MgFe}]$ and $[\text{MgFe}]'$ to $[\alpha/\text{Fe}]$ changes, particularly for older SSP ages.

There is an important caveat of this work, regarding $[\text{MgFe}]$ and $[\text{MgFe}]'$. The assumption of is that both of these indices are sensitive to the total metallicity of the stellar populations. It is first worth noting that all spectral indices will be sensitive to the total metallicity. Secondly, because $[\text{MgFe}]$ and $[\text{MgFe}]'$ are computed through Mg and Fe lines they are mainly sensitive to $[\alpha/\text{Fe}]$ and $[\text{Fe}/\text{H}]$. These sensitivities

CHAPTER 5

will provide a reasonable tracer of the total metallicity, with oxygen and iron being the third and fifth most abundant elements in the universe. However, they will not provide a complete or accurate measure of the total metallicity mainly because of the lack of sensitivity to the fourth most abundant element, carbon. Future work to include a sensitivity to carbon will improve the total metallicity index definition.

CHAPTER 5

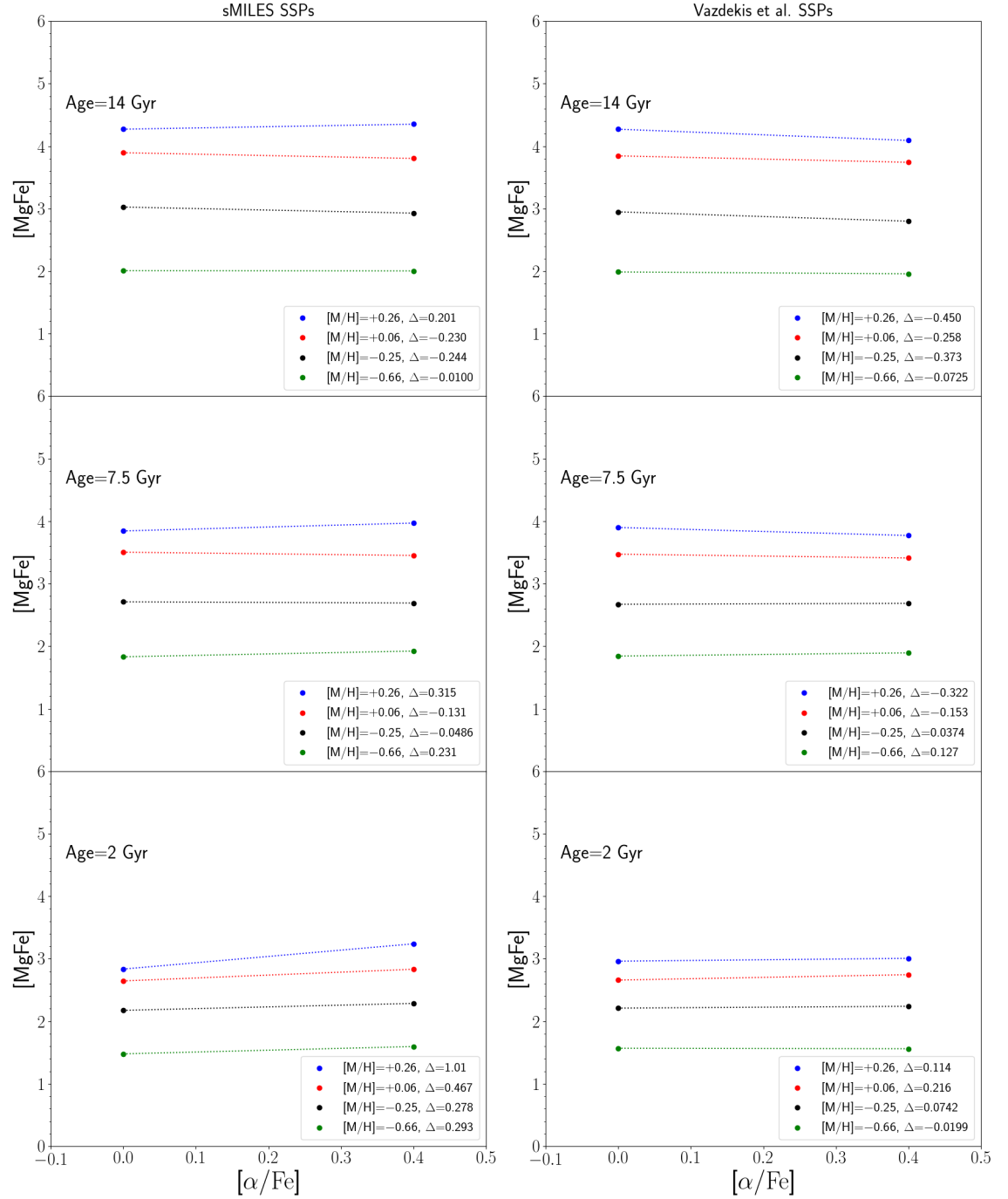


Figure 5.7: Difference in $[MgFe]$ between sMILES and Vazdekis et al. SSP models for 3 ages and 4 metallicity bins. The left and right panels show the $[MgFe]$ values of sMILES and Vazdekis et al. SSP models, respectively. The gradient of the line between $[MgFe]$ values of $[\alpha]=0.0$ and 0.4 models is given, in units of \AA dex^{-1} .

CHAPTER 5

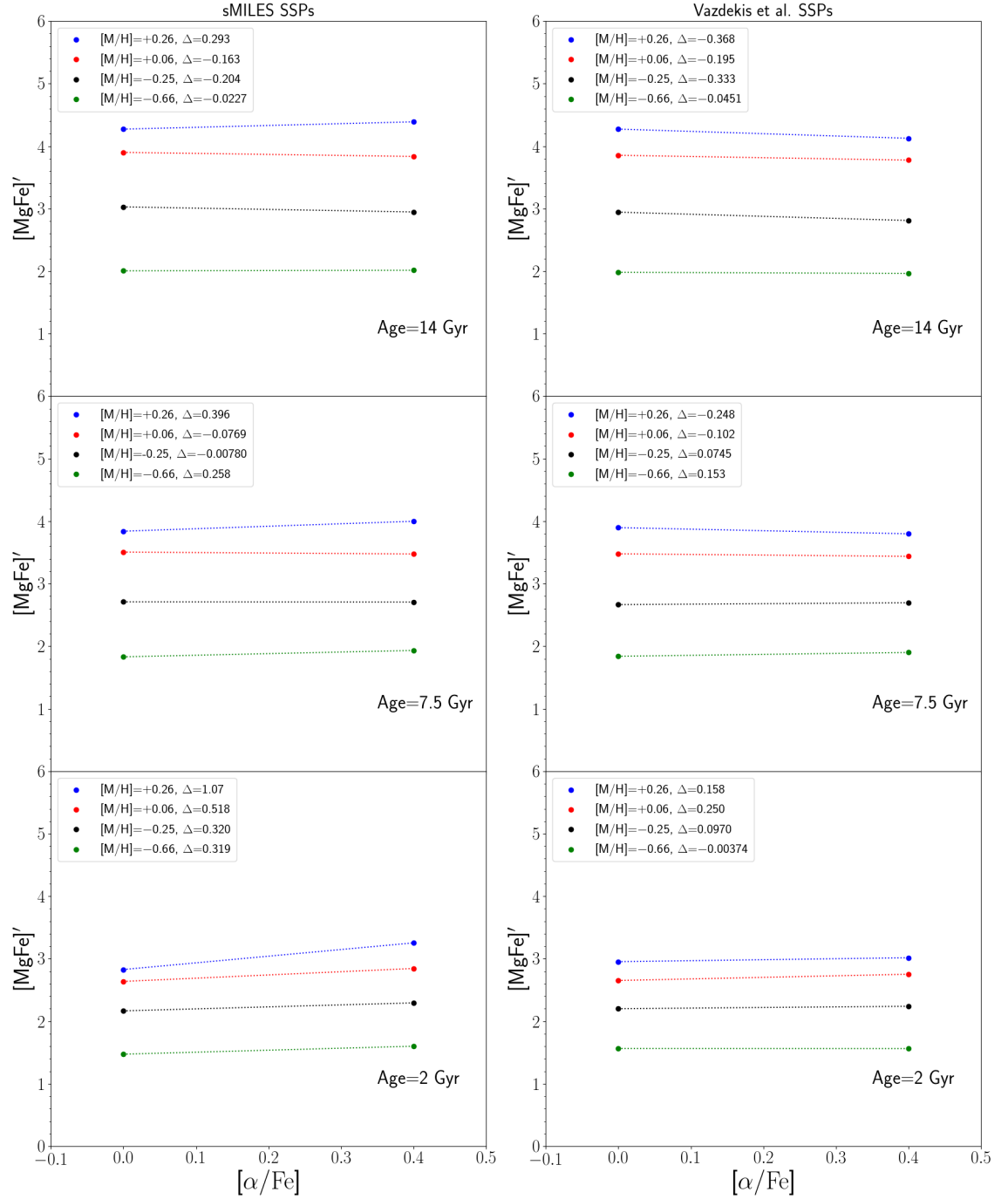


Figure 5.8: Difference in $[\text{MgFe}]'$ between sMILES and Vazdekis et al. SSP models for 3 ages and 4 metallicity bins. The left and right panels show the $[\text{MgFe}]'$ values of sMILES and Vazdekis et al. SSP models, respectively. The gradient of the line between $[\text{MgFe}]'$ values of $[\alpha]=0.0$ and 0.4 models is given, in units of $\text{\AA} \text{ dex}^{-1}$.

Table 5.1: Differences between sMILES and Vazdekis et al. SSP predictions for changes in Mg_b , Fe5270 and Fe5330 indices for a change in $[\alpha/Fe]$ of 0.4 dex. Units of Mg_b , Fe5270 and Fe5330 are given in Å. The bold rows of Δ sMILES and Δ Vazdekis represent the sMILES and Vazdekis et al. model predictions of changes in index for a change of $[\alpha/Fe]$ from 0.0 to 0.4, respectively.

SSP Model	Age (Gyr)	$[M/H]_{SSP}$	$[\alpha/Fe]$	Mg_b	Fe5720	Fe5335
sMILES ($\alpha=0.0$)	2	0.26	0.0	2.62	3.03	3.10
sMILES ($\alpha=0.40$)	2	0.26	0.40	3.76	2.85	2.73
ΔsMILES=sMILES ($\alpha=0.40$) - sMILES ($\alpha=0.0$)	2	0.26		1.14	-0.18	-0.37
Vazdekis et al. ($\alpha=0.0$)	2	0.26	0.0	2.85	3.04	3.12
Vazdekis et al. ($\alpha=0.4$)	2	0.26	0.40	3.71	2.47	2.40
ΔVazdekis=Vazdekis et al. ($\alpha=0.4$) - Vazdekis et al. ($\alpha=0.0$)	2	0.26		0.86	-0.57	-0.72

CHAPTER 5

A choice in the SSP calculations, described in Chapter 4, was the treatment of $[\alpha/\text{Fe}]=0.2$ models, given that the isochrones available were only calculated at $\alpha=0$ and 0.4. In Figure 5.9, I investigate the effect of the choice of isochrone on these models. I plot the $[\text{MgFe}]$ and $[\text{MgFe}]'$ values for the full range of $[\alpha/\text{Fe}]$ SSP models for the same age and metallicity bins as in Figures 5.7 and 5.8. The closed and open symbols in each panel shows the difference in results for models that included the scaled-solar or $\alpha=0.4$ isochrones for $[\alpha/\text{Fe}]=0.2$ SSPs, respectively. Also plotted are the differences (δ) of the maximum and minimum values of $[\text{MgFe}]$ and $[\text{MgFe}]'$ (δ) from the range of α abundance for each metallicity and age. As shown, the effect of using the $\alpha=0.4$ isochrone for the $[\alpha/\text{Fe}]=0.2$ SSP is to reduce the range of $[\text{MgFe}]$ and $[\text{MgFe}]'$ for varying α -abundances at different metallicities. This is particularly strong at 14 Gyr and $[\text{M}/\text{H}]_{\text{SSP}}=0.26$ where the difference between the maximum and minimum value of $[\text{MgFe}]$ is reduced from 0.421 to 0.326Å and the difference in $[\text{MgFe}]'$ is reduced from 0.452 to 0.354Å. This effect is much smaller at younger ages of SSP.

Due to the larger range of $[\alpha/\text{Fe}]$ computed in Figure 5.9, compared to Vazdekis et al. SSPs, sMILES models can be used to further investigate the $[\alpha/\text{Fe}]$ dependence on $[\text{MgFe}]$ and $[\text{MgFe}]'$. From Vazdekis et al. (2015) and Thomas et al. (2003b) model predictions, the expectation is that $[\text{MgFe}]$ and $[\text{MgFe}]'$ should be almost independent of $[\alpha/\text{Fe}]$. For the highest metallicity bins in 7.5 and 14 Gyr old populations, sMILES models predict a non-linear dependence of $[\text{MgFe}]$ and $[\text{MgFe}]'$ to $[\alpha/\text{Fe}]$ variations. sMILES models predict an increase of line strength for increasing $[\alpha/\text{Fe}]$ variations, until a peak at $[\alpha/\text{Fe}]=0.2$, followed by a decrease in line strength for increasing $[\alpha/\text{Fe}]$. This behaviour flattens to an almost linear dependence or to no dependence at the lowest metallicity bins as well as the youngest ages.

CHAPTER 5

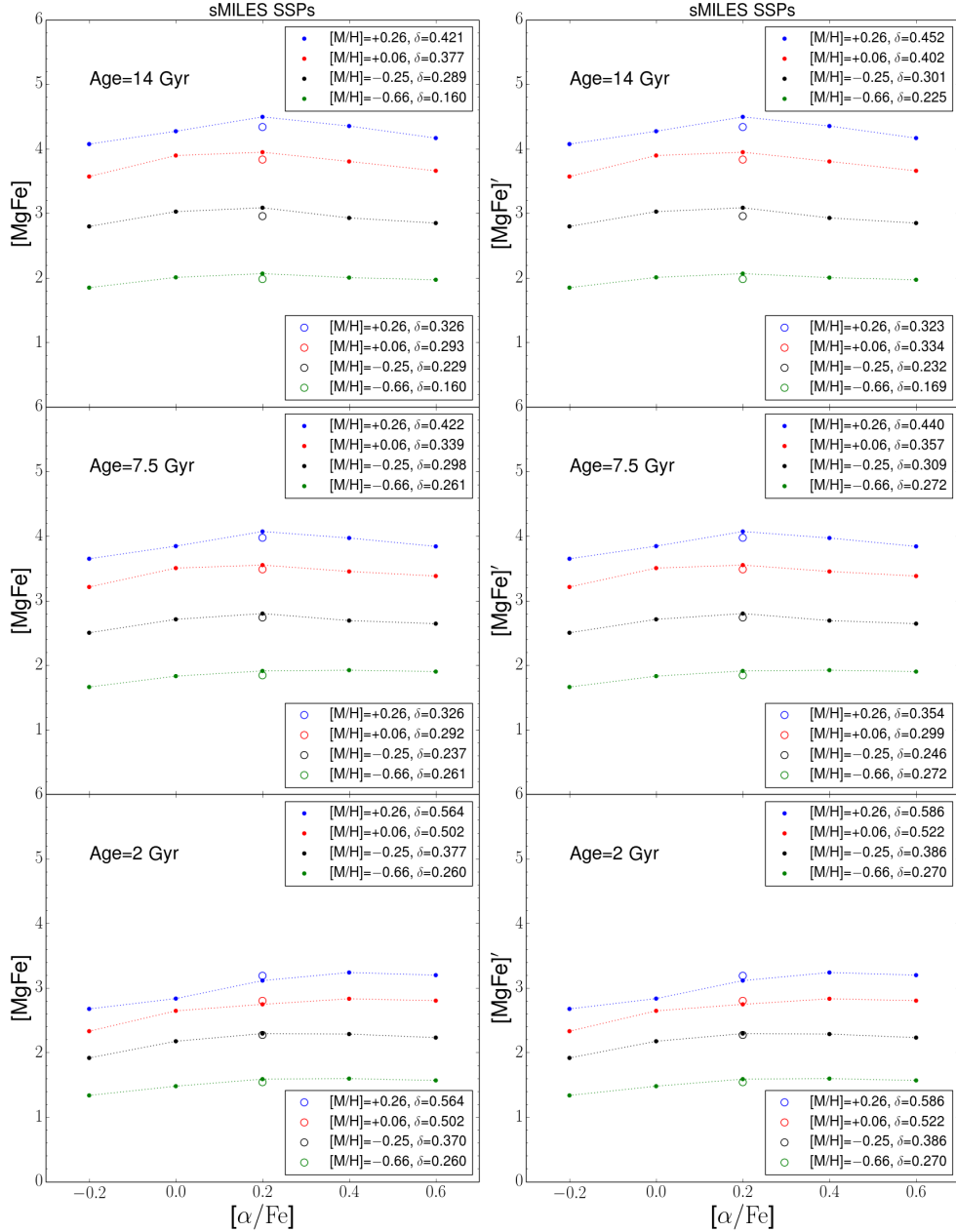


Figure 5.9: Difference in $[\text{MgFe}]$ and $[\text{MgFe}]'$ values between sMILES SSP models that compute the $[\alpha/\text{Fe}]=0.2$ model with a scaled-solar isochrone or α -enhanced ($[\alpha/\text{Fe}]=0.4$) isochrone, for 3 age and 4 metallicity bins. Left and right panels show the $[\text{MgFe}]$ and $[\text{MgFe}]'$ value differences, respectively. Closed symbols represent sMILES SSPs models that have $[\alpha/\text{Fe}]=-0.2, 0.0$ and 0.2 computed with scaled-solar isochrones, and $[\alpha/\text{Fe}]=0.4$ and 0.6 computed with α -enhanced ($[\alpha/\text{Fe}]=0.4$) isochrones. Open symbols represent $[\alpha/\text{Fe}]=0.2$ models computed with the α -enhanced isochrone. The difference between the maximum and minimum values of $[\text{MgFe}]$ and $[\text{MgFe}]'$ (δ) for the range of α in the metallicity and age bin is given in units of \AA .

5.2 Application

I now focus on an application of the new sMILES SSP models to external galaxies. I study the effect of abundance pattern on a set of galaxy data presented in Ferreras et al. (2019). This work is an investigation of the growth of massive ($M > 10^{11}M_{\odot}$) galaxies through mergers, by studying close pairs of galaxies that are thought to be possible progenitors of such events. These data of massive galaxies were obtained from the Sloan Digital Sky Survey (SDSS) DR14 (Abolfathi et al. 2018). Dynamically close pairs of galaxies were searched for in these data, using the criteria defined in Ferreras et al. (2017). A close pair was defined to be a system separated by a projected distance within 100 kpc and with a velocity difference, derived from redshift differences, of less than 700km/s. The redshift range of the sample was restricted to $z=0.07-0.014$. These systems consist of two galaxies, the more massive of which is referred to as the primary and the less massive as the satellite. Spectra are then stacked, using the procedure described in Ferreras et al. (2017), based on the velocity dispersion of the satellite and the mass ratio between primary and secondary.

The most accepted model for the formation and evolution of massive galaxies is a two-step process (Lackner et al. 2012; Oser et al. 2012). Early stages consists of gas collapse and resultant efficient star formation that creates the centre (in-situ), followed by an ex-situ phase with the outer regions built up by merging events, in which stars that formed in other galaxies are accreted.

Observations support this model, with old, metal-rich and $[\alpha/\text{Fe}]$ -enhanced stellar populations found in the cores of massive galaxies (e.g. Thomas et al. 2005; Conroy et al. 2014) that is indicative of an efficient, short burst of star formation at early times. Stellar population properties as a function of galaxy radius would shed further light on the interplay of in-situ and ex-situ processes. In early-type galaxies, for example, observations suggest strong decreases of metallicity for increasing radius with almost no changes in age (La Barbera et al. 2012; Greene et al. 2015). The

CHAPTER 5

fact that old, $[\alpha/\text{Fe}]$ -enhanced stellar populations are observed in the outer regions of these galaxies (Greene et al. 2013) would suggest that accreted systems are low metallicity and that the merging event occurred at early times.

If one could observe a merging event occurring, or observe the stellar populations of galaxies that would eventually merge, this would assess the concept of two-step galaxy formation. If the stellar population properties of the system are known, it would be possible to predict the radial gradients of stellar population properties of the resulting system after the merger.

Ferreras et al. (2014) obtained photometry of close pairs, in distance and velocity, of galaxies that were dynamically bound and therefore had the potential to merge. This was using the Survey for High- z Absorption Red and Dead Survey (SHARDS) (Pérez-González et al. 2013), that consists of medium-band photometry. The data covered the wavelength range 5000-9500 Å with 24 medium band filters. This medium-band photometry can be equated to low resolution optical spectra. They found that the ages of satellite² galaxies followed the same mass-age trend as galaxies in the field, and therefore the observations of shallow age gradients of early-type galaxies would not be consistent with large contributions of growth originating from minor-mergers, in which there is a large difference in mass between satellite and primary. Instead, they found that most of the growth of massive galaxies is from mergers with mass ratios $\mu \gtrsim 0.3$, where μ is defined as:

$$\mu = M_{\text{sat}}/M_{\text{pri}}, \quad (5.4)$$

with M_{sat} and M_{pri} representing the satellite and primary galaxy masses, respectively. These type of mergers would introduce older ages to the outer regions of galaxies, and would therefore be consistent with the observations of a lack of age gradient within early-type galaxies.

²I emphasise here that the term satellite throughout these works refers to the lower mass galaxy of the system.

CHAPTER 5

Ferreras et al. (2017) then built upon this work, using stacked optical spectra from the Galaxy Mass and Assembly (GAMA) survey, to more closely investigate the stellar population properties of both satellite and primary galaxies in close pairs. It was found that at the same mass, satellites galaxies connected to more massive galaxies tend to be older, particularly at lower masses of satellite ($\approx 10^{10}M_{\odot}$) where the age differences obtained from SSP-fitting can be between 1-2 Gyr. In other words, the older (and therefore more massive) the primary, the older the satellite, compared to a satellite with the same mass connected to a lower mass primary. This trend is in agreement with the observations of little to no age gradients in early-type galaxies (La Barbera et al. 2011; La Barbera et al. 2012).

Ferreras et al. (2019) investigate this further, using the same stacking method on higher signal-to-noise SDSS optical spectra, with the aim of studying both age and metallicity trends with satellite and primary galaxy mass ratio. In summary, they produce stacked spectra of satellite galaxies in four bins of satellite velocity dispersion such that:

$$\sigma_1 = 100 - 130\text{km/s}$$

$$\sigma_2 = 130 - 160\text{km/s}$$

$$\sigma_3 = 160 - 190\text{km/s}$$

$$\sigma_4 = 190 - 220\text{km/s}$$

$$\sigma_5 = 220 - 250\text{km/s}$$

For each dispersion bin, spectra are stacked for three bins of satellite-to-primary

CHAPTER 5

mass ratio such that:

$$\log \mu = \log(M_{\text{sat}}/M_{\text{pri}})$$

$$\log \mu_1 = (-0.278, 0.000)$$

$$\log \mu_2 = (-0.490, -0.278)$$

$$\log \mu_3 = (-0.800, -0.490)$$

Therefore, μ_1 represents a system in which the satellite has a similar mass to the primary, whereas μ_3 is a system in which the satellite has much lower mass than the primary.

Here, I demonstrate an example application of sMILES SSP models, considering these high signal-to-noise SDSS spectra (Ferrerias. priv. comm). With different ages of SSP models that vary both total metallicity and $[\alpha/\text{Fe}]$ abundance, I show that sMILES SSPs could be used to investigate abundance pattern trends between satellite and primary galaxy masses, as well as with velocity dispersion. The inclusion of $[\alpha/\text{Fe}]$ stellar population measurements would be useful in the context of galaxy formation, because in principle one could rule out or highlight potential accretion progenitors based on the observations of $[\alpha/\text{Fe}]$ -enhanced stellar populations in the outer-most regions of massive galaxies. Based on SSP-estimates of age and metallicity presented in Ferreras et al. (2019) that used MIUSCAT (Vazdekis et al. 2012) model estimates, I create sMILES models for steps in $[\alpha/\text{Fe}]$ through interpolations in the sMILES SSP grid (Chapter 4). These interpolations are performed using FERRE and the results are compared to the stacked SDSS data. All sMILES SSP models in this section are computed assuming a universal Kroupa IMF. The age and metallicity estimates are presented in Table 2. For σ_3 , the metallicity estimates were calculated via a linear interpolation between the assumed MIUSCAT estimates for σ_1 and σ_5 . The data provided were all blurred to 250 km/s (Ferrerias, priv comm.) and then rebinned from logarithmic to linear sampling, taking the maximum linear

CHAPTER 5

bin size ($\delta\lambda = 1.612\text{\AA}$), using IRAF. For comparison, the models were blurred to 250 km/s using python routines (Jesús Falcón-Barroso, priv comm.) and rebinned to the same linear sampling as the data, using IRAF.

In Figure 5.10, I plot the stacked SDSS spectra for μ_1 satellite-to-primary mass ratio and σ_1 , σ_3 and σ_5 velocity bins, in the wavelength region of Mg_b and Fe5270, with Lick index measurements given. Also plotted, are the equivalent age and metallicity sMILES SSPs, for a number of $[\alpha/\text{Fe}]$ abundances. As shown by comparison between the top, middle and bottom panels of this Figure, there is a sequence of increasing index strength with velocity dispersion, which can be explained with mass-metallicity relation³ as well as σ - $[\alpha/\text{Fe}]$ relation, in which the most massive galaxies tend to be the most α -enhanced (e.g. Conroy et al. 2014). For sMILES SSPs, there is a reasonable agreement with the data for Mg_b , in that the closest fitting models in this index tend to be α -enhanced, with the amount of $[\alpha/\text{Fe}]$ enhancement of the closest fit increasing with σ . This demonstrates that the sMILES SSP models would be able to distinguish between α -enhancements in stellar populations of satellite galaxies in these type of systems. Also shown is a good agreement with iron-sensitive features for sMILES models compared to the data in Figure 5.10, apart from σ_1 . In σ_1 , sMILES models overpredict feature strengths of Fe5270, which may originate from differences in total metallicity predictions of sMILES and MIUSCAT models or may suggest a true difference in metallicity of the data. In summary, this investigation suggests that for the metallicity and age estimates from MIUSCAT, sMILES models would be able to fit Mg_b and Fe5270 simultaneously. Figure 5.10 also shows that for systems of similar mass primary and satellite galaxies, stellar populations in the satellite galaxy appear to be $[\alpha/\text{Fe}]$ enhanced, compared to solar abundances, at all velocity dispersions tested. There are some issues present in the Mg_b region of Figure 5.10. In particular, the depth ratio of the two strongest lines in

³It is worth noting here that some of the index differences could also be explained by increasing stellar population age of stellar populations with increasing galaxy σ .

CHAPTER 5

the models does not match the observations. This could be explained by a problem with the blurring of the observations compared with the models, with different software used for the stacks and SSP models. There could be also an issue with the σ weighting per galaxy within a stack, causing an additional blurring from the stated 250km/s of the observations. This problem is seen more clearly in the observations (black lines) in Figure 5.11, with the lowest σ bin appearing more blurred than the highest σ bin. A difference in metallicity and age predictions between MIUSCAT and sMILES models may also explain differences in the depth ratio between the SSP predictions and observations, because these Mg lines are sensitive to the $[\alpha/\text{Fe}]$ of the underlying stellar population. Further work, suggested later in this chapter and also in Chapter 6, would be needed to fully assess these issues.

Figure 5.11 plots the same sequence as Figure 5.10, but for the μ_3 satellite-to-primary mass ratio, in which there is a greater difference in satellite and primary mass. Between velocity bins, there is a trend with σ similar to Figure 5.10, with increases in Mg_b and Fe5270 for increasing σ . In terms of Mg_b index strength, sMILES models are again able to distinguish between different $[\alpha/\text{Fe}]$ abundances at fixed total metallicity. The extent of α enhancement for the closest fitting sMILES model is smaller for μ_3 compared to μ_1 at the lowest mass (σ_1), with μ_3 lying close to $[\alpha/\text{Fe}]=0.0$ and μ_1 lying closer to $[\alpha/\text{Fe}]=0.35$. This suggests that at the lowest σ , the more likely progenitors of merging, would originate from satellites with similar masses to the primary, in order to match the $[\alpha/\text{Fe}]$ -enhanced populations observed in the outer regions of galaxies. Similar trends exist for iron-sensitive features, like that in Figure 5.10, such that Fe5270 is matched well for σ_3 and σ_5 , but are slightly over predicted at σ_1 the closest fitting sMILES models in Mg_b . Figure 5.11 does show a slight trend of $[\alpha/\text{Fe}]$ with velocity dispersion, with the lowest velocity dispersion systems consisting of stellar populations with almost solar $[\alpha/\text{Fe}]$, whereas

CHAPTER 5

Table 5.2: MIUSCAT SSP-equivalent ages and metallicities of stacked satellite galaxy spectra for various velocity dispersion and mass ratio bins (Ferrerias et al. 2019). The first two columns give the σ and mass bin, respectively. The metallicities of σ_1 and σ_5 were estimated from the probability maps of MIUSCAT fits. The metallicities of σ_3 galaxies were estimated through linear interpolations between σ_1 and σ_5 estimates.

σ (km/s)	$\log \mu = \log(M_{\text{sat}}/M_{\text{pri}})$	Age (Gyr)	$[M/H]_{\text{SSP}}$
σ_1	μ_1	$1.67^{+0.19}_{-0.18}$	0.06
σ_1	μ_3	$2.19^{+0.20}_{-0.33}$	0.10
σ_3	μ_1	$2.81^{0.35}_{0.31}$	0.16
σ_3	μ_3	$3.41^{+0.78}_{-0.40}$	0.18
σ_5	μ_1	$4.68^{+0.97}_{-0.41}$	0.26
σ_5	μ_3	$3.89^{+1.14}_{-0.44}$	0.26

the highest velocity dispersion systems possess populations with the greatest $[\alpha/\text{Fe}]$ -enhancement.

More detailed spectral analysis, including the assessment of errors and fitting of indices or spectra, of the satellite compared to the primary galaxy would be required to draw out any further conclusions of this initial comparison. Nevertheless, this basic study has highlighted the possibility of investigating satellite galaxy abundance pattern, using sMILES SSPs.

5.3 Summary

This chapter has tested and then demonstrated a possible application of newly generated sMILES SSPs. The first half of the chapter compared sequences of sMILES SSPs in age, metallicity and $[\alpha/\text{Fe}]$ abundance to previously computed Vazdekis

CHAPTER 5

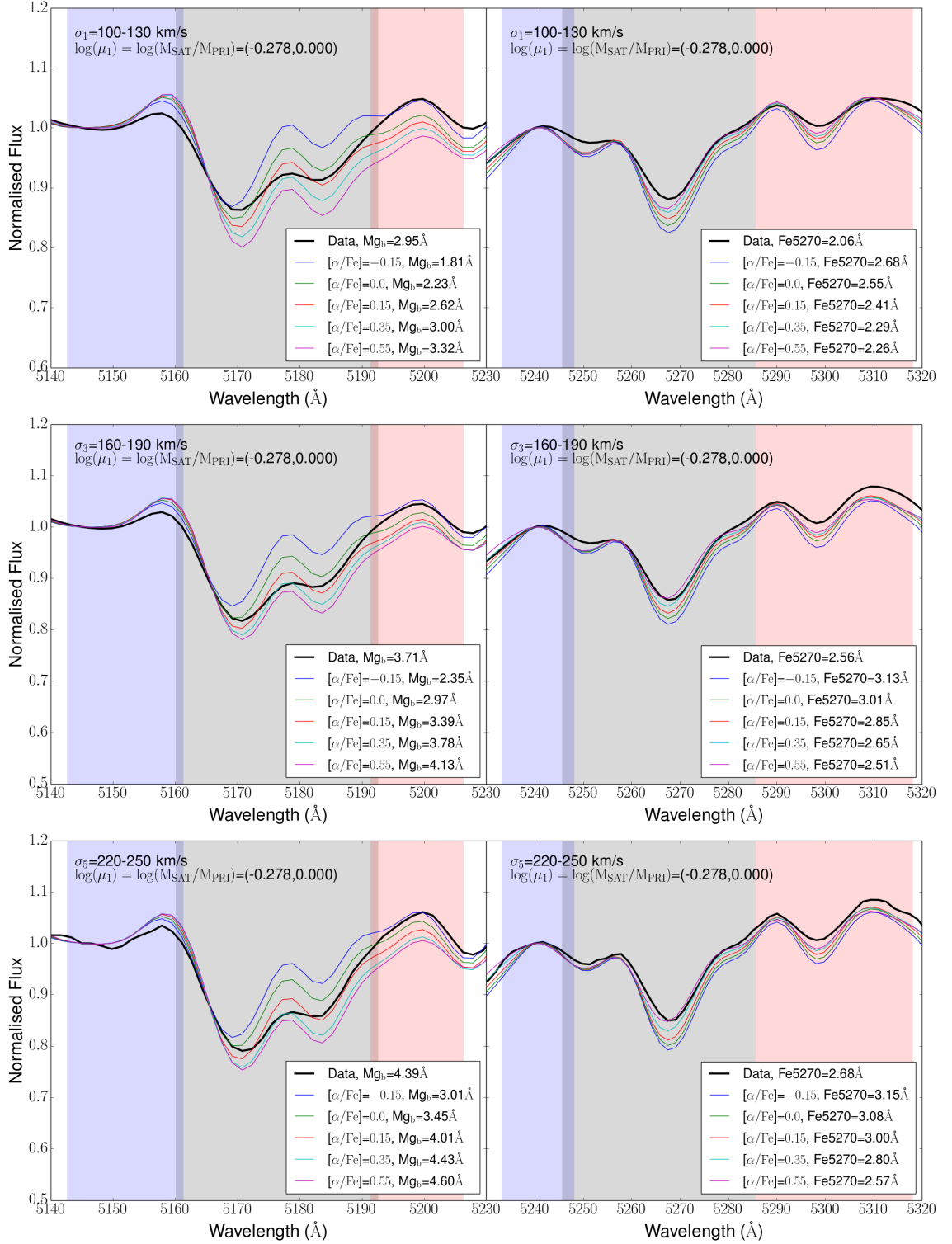


Figure 5.10: Stacked SDSS spectra of satellite galaxies for μ_1 mass ratio and various σ bins (black lines) and sMILES SSPs for various $[\alpha/\text{Fe}]$ abundances (coloured lines), plotted in the wavelength region of Mg_b (left panel) and Fe5270 (right panel). The blue pseudo-continuum, feature and red pseudo-continuum bands definitions (Trager et al., 1998) are plotted in blue, grey and red respectively. All spectra are blurred to 250km/s and binned to $\delta\lambda = 1.612\text{\AA}$. In the Mg_b and Fe5270 regions, spectra are normalised to the flux at $\lambda=5144.98\text{\AA}$ and $\lambda=5240.88\text{\AA}$, respectively.

CHAPTER 5

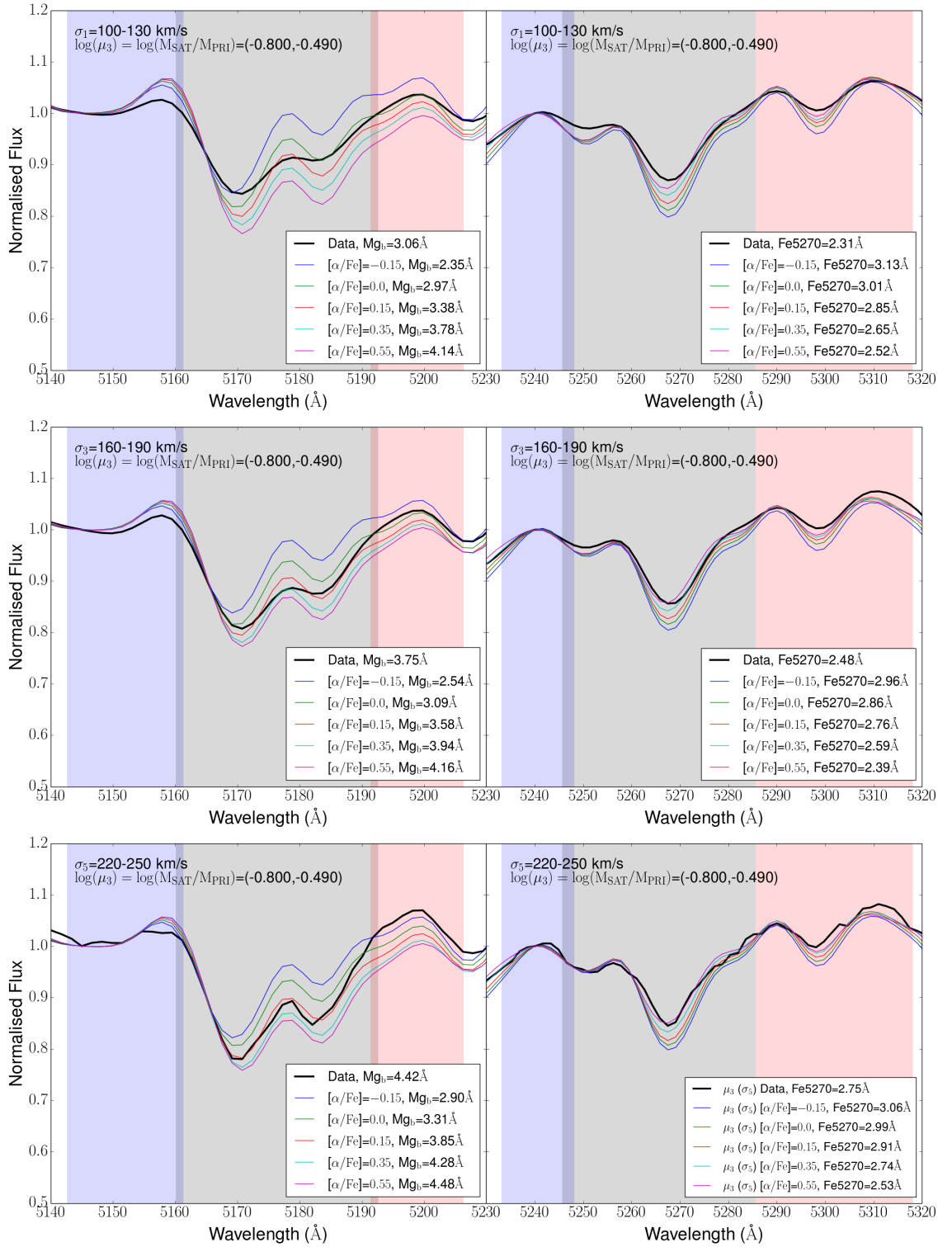


Figure 5.11: Stacked SDSS spectra of satellite galaxies for μ_3 mass ratio and various σ bins (black lines) and sMILES SSPs for various $[\alpha/\text{Fe}]$ abundances (coloured lines), plotted in the wavelength region of Mg_b (left panel) and Fe5270 (right panel). The blue pseudo-continuum, feature and red pseudo-continuum bands definitions (Trager et al., 1998) are plotted in blue, grey and red respectively. All spectra are blurred to 250km/s and binned to $\delta\lambda = 1.612\text{\AA}$. In the Mg_b and Fe5270 regions, spectra are normalised to the flux at $\lambda=5144.98\text{\AA}$ and $\lambda=5240.88\text{\AA}$, respectively.

CHAPTER 5

et al. (2015) SSPs, that are different in both the underlying theoretical stellar spectral models and differential correction method, but the same in isochrones used and general SSP calculation method. Reasonable results were found for predictions of $H\beta$ and $H\beta_o$ line-strengths with changes in age in $[\alpha/\text{Fe}]=0$ populations. For $[\alpha/\text{Fe}]=0.4$ SSPs, sMILES models predict greater $H\beta$ and $H\beta_o$ line-strengths than the Vazdekis et al. models at all ages, although predictions of the change of index strength with age are similar in both. Similarities in predictions of iron-sensitive feature changes with metallicity were found between sMILES and Vazdekis SSPs, for old, $[\alpha/\text{Fe}]=0$ populations. For old, $[\alpha/\text{Fe}]=0.4$ populations, sMILES and Vazdekis SSPs predict very similar changes in metallicity for Fe52570 and Fe5335, apart from at the highest metallicity bins where sMILES models predict slightly larger line strengths. sMILES and Vazdekis models predict similar changes of α -sensitive indices with changes in $[\alpha/\text{Fe}]$ abundance, for old, solar metallicity populations. Differences in total metallicity indicators $[\text{MgFe}]$ and $[\text{MgFe}]'$, that were previously found to be almost insensitive to $[\alpha/\text{Fe}]$ changes, were found between SSP models for younger, metal-rich populations. For 2 Gyr, $[\text{M}/\text{H}]_{\text{SSP}}=0.26$ populations, sMILES models predict large sensitivities to $[\alpha/\text{Fe}]$ abundances compared to Vazdekis et al. models, that show almost no sensitivity. For intermediate and old ages, sMILES and Vazdekis et al. model predictions of $[\text{MgFe}]$ and $[\text{MgFe}]'$ agree well, for a range of metallicities. The adopted isochrone in the SSP calculation was then tested, comparing $[\text{MgFe}]$ and $[\text{MgFe}]'$ sensitivities when using a scaled-solar isochrone compared to an $\alpha=0.4$ isochrone for $[\alpha/\text{Fe}]=0.2$ SSP models. Using an α -enhanced isochrone for $[\alpha/\text{Fe}]=0.2$ SSPs reduced the sensitivity of $[\text{MgFe}]$ and $[\text{MgFe}]'$ to $[\alpha/\text{Fe}]$ changes, compared to using a scaled-solar isochrone for the oldest and most metal-rich populations. With a larger range of $[\alpha/\text{Fe}]$ variations computed than done previously, a better investigation of the dependence of $[\text{MgFe}]$ and $[\text{MgFe}]'$ line-strengths with $[\alpha/\text{Fe}]$ variations is possible. Qualitatively, for the highest metallicity bins in old

CHAPTER 5

and intermediate age, sMILES models predict a non-linear dependence of $[\text{MgFe}]$ and $[\text{MgFe}]'$ to $[\alpha/\text{Fe}]$ variations with a peak in index strength at $[\alpha/\text{Fe}]=0.2$. This behaviour flattens to linear or no dependence at the lowest metallicity and youngest age bins.

The next part of this chapter focused on a potential application of sMILES SSPs, which involved a demonstration that abundance pattern effects may be investigated for a set of stacked galaxy spectra from Ferreras et al. (2019). That work is aimed at testing models of the formation and evolution of massive galaxies, through studies of sets of close pairs of galaxies that are expected to merge and produce the most massive early-type galaxy populations observed. By investigating the stellar populations properties of age, metallicity and α -abundance in both satellite and primary galaxies, possible progenitors of merging and therefore contributors to the outer regions of massive galaxies can be identified or ruled-out based on current observations of galaxies. Using age and metallicity estimates from another set of SSPs, I was able to demonstrate that sMILES SSP models would be able to distinguish between α variations of stellar populations in stacked satellite galaxy spectra for different σ and satellite-to-primary mass ratios, which would be used to help differentiate between possible merger progenitors based on the observations of $[\alpha/\text{Fe}]$ enhanced stellar populations in early-type galaxies. Differences between iron-sensitive indices of the data and sMILES models were found in the lowest σ bin, that may originate from either differences in metallicity predictions of MIUSCAT and sMILES SSPs or metallicity of the satellite galaxies data itself. For systems in which the satellite and primary galaxy are similar in mass, the stellar populations in the satellite appear to be $[\alpha/\text{Fe}]$ enhanced at all velocity dispersions. For systems with a satellite that is much less massive than the primary, there appears to be a trend of increasing satellite stellar population $[\alpha/\text{Fe}]$ with velocity dispersion. The smallest velocity dispersion systems appear to have stellar populations with close to solar $[\alpha/\text{Fe}]$ and

CHAPTER 5

the largest velocity dispersion systems seem to have the greatest $[\alpha/\text{Fe}]$ -enhancement in their stellar populations.

The last chapter in this thesis will summarise the main results and products that the work in this thesis has produced, as well as identifying possible avenues for future work.

Chapter 6

Conclusions & Future Work

6.1 Conclusions

This thesis has focused on addressing a well known limitation of SSPs built from purely empirical stellar spectra. The fact that the majority of empirical stellar spectra have been obtained from locations around the solar neighbourhood marks them with an abundance pattern that is indicative of the Milky Way’s formation history. Large parts of parameter space, particularly in abundance pattern, is therefore not covered or covered very sparsely. If one wants to model systems that have gone through a different star formation history, theoretical stellar spectra must be used in SSP modelling to predict the abundance pattern effects of these systems. This thesis describes the process of using the differential predictions of theoretical stellar spectra for the changes of spectra due to abundance pattern variations to correct empirical stars to different $[\alpha/\text{Fe}]$ values. These so-called ‘semi-empirical’ stars are then used to create a new library of semi-empirical SSPs with different $[\alpha/\text{Fe}]$ abundances at different total metallicities.

Chapter 2 of this thesis tested three state-of-the-art libraries of theoretical stellar spectra through comparisons to MILES observations in an absolute and differential sense. The aim of that chapter was to highlight current strengths and weakness of

CHAPTER 6

commonly used models, particularly in the context of stellar population modelling. Through analyses of both Lick indices and full spectra, we found that, generally, models have similar predictions of abundance pattern changes with differences between models often smaller than the differences between models and observations. There are Lick indices, such as iron-sensitive and sodium-sensitive indices, in which the models predict the abundance pattern effects well. However, all the models that we tested have problems modelling the effect of abundance patterns on Balmer features, particularly for the cool stars, which may impact the age measurements of SSP models. A highlight of this work was the identification of a corruption with the Coelho (2014) set of models, which had a corrupted C_2 line list. This corruption was corrected for during the course of this project. The most important result of this work was to confirm a result that was previously known, that in general the absolute differences between models and observations was worse than the differential predictions, particularly for bluer wavelengths below Mg_b . Using one set of cool giant models to investigate this result, we found that the differential predictions of some Hydrogen features were scattered about the observations by a factor of ~ 2 less than the absolute predictions. This result motivates using theoretical stellar spectra in a differential sense in the modelling of stellar populations, in that the differential approach produces less or similar scatter about the observations than the absolute predictions.

Chapter 3 of this thesis presented the generation and testing of a new high resolution theoretical stellar spectral library, based on the methodology presented in Allende Prieto et al. (2018). The choice of creating a new library, rather than using an existing one, was mainly driven by the control of parameter coverage in effective temperature, surface gravity, metallicity ($[M/H]$), $[\alpha/M]$ and $[C/M]$, such that a large proportion of the existing empirical MILES stellar library was covered. The result of this chapter was a new, high resolution theoretical stellar spectral

CHAPTER 6

library, which can be split in temperature into three sub-grids, with the fundamental parameter coverage described in Chapter 3 (Section 3.2.2). These models were generated with consistent abundances in both their model atmosphere and spectral synthesis components. All three grids have a metallicity coverage from -2.5 to 0.5 in steps of 0.5 dex, an $[\alpha/M]$ coverage of -0.25 to 0.75 in steps of 0.25 dex and a $[C/M]=-0.25$ to 0.25 in steps of 0.25 dex. All theoretical spectra have wavelength coverage of 1680-9000Å, with a linear sampling of $\delta\lambda=0.05\text{Å}$. To reduce computation time, the TiO line list was removed for spectra with effective temperature greater than 6000K, which is shown to have minimal effect (Figure 3.6). The chapter described the computation of the raw theoretical spectra and then the processing, to create a high resolution, full wavelength library and a library at MILES wavelength coverage and resolution (FWHM=2.5Å). The next section of the chapter was testing of the spectra, through spectral sequences across the full wavelength of the models and index analyses at both high and MILES resolution. I find that the theoretical library captures the effect of changing stellar parameters and abundances correctly in a qualitative and quantitative way, through comparisons to results of previous libraries of stars and SSPs. The intention is to make the high and MILES resolution libraries publicly available through the online database at UCLan.

Chapter 4 described the semi-empirical stellar library and following semi-empirical SSP calculations. Using the theoretical spectra in Chapter 3, I perform differential corrections to MILES stars to create a library of semi-empirical MILES stellar spectra from which to build SSPs with. The early parts of the chapter outlined the methodology used to perform the differential corrections and create semi-empirical stars. I describe the choice of parameters used for the MILES stars, considering both Cenarro et al. (2007) and Prugniel & Sharma (Prugniel et al. 2011; Sharma et al. 2016). Differences between these parameters were presented. Both sets of parameters were used to create two libraries of semi-empirical stars, one with Cenarro

CHAPTER 6

et al. (2007) and one with Prugniel & Sharma sets of parameters. In the SSP calculation, the Cenarro et al. (2007) parameters were used to be internally consistent with the SSP methodology used. $[\text{Mg}/\text{Fe}]$ values for 752 stars came from Milone et al. (2011) with the remaining stars in the library estimated from the Bensby et al. (2014) trends. The interpolation within the theoretical grid, performed to create the ‘MILES Theoretical Base’ and ‘MILES Theoretical Enhanced or Deficient’ sets of stars, using a software package FERRE was described in detail. The differential correction process was then described. Examples of the computed differential corrections and then sequences of the generated semi-empirical stars were presented. The final semi-empirical MILES library is presented in Figure 4.14. The result was a new semi-empirical stellar spectral library with variable $[\alpha/\text{Fe}]$ abundance. The library consists of 5 families of 801 semi-empirical spectra for $[\alpha/\text{Fe}]$ abundances from -0.2 to 0.6, in steps of 0.2 dex, for the $[\text{Fe}/\text{H}]$ range of the current empirical MILES library, with either Cenarro et al. or Prugniel & Sharma parameters. Finally, the SSP calculations were described, outlining the general methodology, including how SSPs were calculated at total metallicities, rather than the spectroscopic metallicity ($[\text{M}/\text{H}]$) used in the theoretical stellar spectra calculations (Chapter 3). The isochrones and adopted IMFs were described, as well as the input stellar spectral libraries. The result was a library of semi-empirical SSPs with 10 steps in total metallicity ranging of 0.0003 to 0.030 and 53 steps in ages from 0.03 to 14 Gyr, with universal or revised Kroupa IMFs. For each metallicity and age step, 5 $[\alpha/\text{Fe}]$ steps from -0.2 to 0.6, in 0.2 dex steps was computed, to make a total of 2650 SSPs per IMF. The new negative $[\alpha/\text{Fe}]$ step as well as the larger and finer range of $[\alpha/\text{Fe}]$ presents an improvement from the previous work in Vazdekis et al. (2015), in which only two steps in $[\alpha/\text{Fe}]$ of 0.0 and 0.4 were computed using a differential correction on the SSP-level from Coelho model predictions.

The work in Chapter 5 of this thesis was to test the new SSPs and present an

CHAPTER 6

example application of them in the context of external galaxy data. The SSP results were compared to Vazdekis et al. (2015) SSPs, that were different in the theoretical stellar spectra and differential correction method, but the same in general SSP calculation. Through sequences of SSPs in age, metallicity and $[\alpha/\text{Fe}]$, I found that sMILES SSPs predicted similar changes in $\text{H}\beta$ and $\text{H}\beta_o$ line-strengths with age at solar metallicity and $[\alpha/\text{Fe}]$, similar changes in iron-sensitive features with metallicity for old, $[\alpha/\text{Fe}]=0$ populations and similar predictions of α -sensitive indices for a change in $[\alpha/\text{Fe}]$ from 0 to 0.4 at solar metallicity and old ages to those of Vazdekis et al. models. Some differences between models were found in total metallicity indicators $[\text{MgFe}]$ and $[\text{MgFe}]'$ were found for the youngest, most metal-rich populations. For 2 Gyr, $[\text{M}/\text{H}]=0.26$ populations, sMILES models predict a large sensitivity of $[\text{MgFe}]$ and $[\text{MgFe}]'$ to $[\alpha/\text{Fe}]$ abundance, compared to Vazdekis et al. models that showed almost no change. The choice of adopted isochrone for $[\alpha/\text{Fe}]=0.20$ populations was tested for sMILES models, with α -enhanced isochrones reducing the $[\alpha/\text{Fe}]$ dependence of $[\text{MgFe}]$ and $[\text{MgFe}]'$ for the oldest, most metal-rich populations.

The second half of this chapter investigated a potential application of sMILES SSPs for a set of stacked galaxy spectra from Ferreras et al. (2019). These data were a set of stacked SDSS spectra of satellite galaxies in close pairs. I demonstrated that sMILES SSPs would be able to distinguish different $[\alpha/\text{Fe}]$ abundances of stacked satellite galaxies for different velocity dispersions as well as satellite-to-primary mass ratio. The $[\alpha/\text{Fe}]$ measurement of these data would be used to determine potential merger progenitors based on current observations of $[\alpha/\text{Fe}]$ enhanced stellar populations in early-type galaxies. For systems in which the satellite and primary galaxy are similar in mass, the stellar populations in the satellite appear to be $[\alpha/\text{Fe}]$ enhanced at all velocity dispersions. For systems with a satellite that is much less massive than the primary, there may be a trend of increasing satellite stellar population $[\alpha/\text{Fe}]$ with velocity dispersion.

CHAPTER 6

In summary, the new high resolution theoretical stellar library, new sMILES stellar library and new sMILES SSP models can be seen as an expansion and improvement on the well-known and used Vazdekis et al. (2015) models. The sMILES SSPs present a greater range of $[\alpha/\text{Fe}]$, increasing the maximum $[\alpha/\text{Fe}]$ range from 0.4 to 0.6 and increasing the number of intermediate abundance models. A new SSP is also the $[\alpha/\text{Fe}]=-0.2$, which is a largely unexplored region of parameter space, which external systems such as dwarf spheroidals are known to occupy. I now present some possible projects for future work.

6.2 Future Work

I split the potential avenues of future work into specific Chapter below.

- **Chapter 2** - Further work in the testing of theoretical stellar spectral models would be to test the effect of non-LTE and 3D geometry effects. This is largely known to have an impact at the coolest and hottest temperatures, particularly for the higher order Balmer features. All the models tested in this chapter omitted both of these effects. Another main limitation of this chapter was that we did not investigate if the Prugniel & Sharma MILES star parameters would change the outcomes of the testing. Also, if more abundance ratios besides $[\text{Mg}/\text{Fe}]$, are measured for MILES stars, the effect of C, N and O on the outcomes of this work may be investigated. These elements are not changed from scaled-solar in the models and derived response functions we test in this chapter. Some work is currently underway to measure a total $[\alpha/\text{Fe}]$ value for MILES stars, which could be compared to changing individual α -elements separately through response functions. Because carbon is varied in theoretical grid I generate in Chapter 3, a future application of the library may involve obtaining $[\text{C}/\text{Fe}]$ estimates for MILES stars.

CHAPTER 6

- **Chapter 3** - Extension of the parameter range covered by the theoretical grid I generate in Chapter 3 would be useful, particularly in effective temperature. Inclusion of cool models (e.g. from MARCS model atmospheres), as well as higher temperature models (greater than 10000K in ATLAS9) would allow for a greater number of empirical MILES stars to be included in the sMILES library, that currently fall outside of the parameter range. Because sodium is an element used in IMF diagnostics in stellar population modelling, the obvious extension to the theoretical grid would be to include variations in this element. As already described in La Barbera et al. (2017), because the expected effect of sodium on atmospheric structure is minimal, it could be varied in the spectral synthesis component only. To match the UV-extended E-MILES stellar population models, it would be useful to increase the maximum wavelength of the theoretical models to 50000Å. These two additions (sodium variations and increased wavelength range) would significantly increase computation times and would therefore require greater computing resources. The inclusion of sodium and increased wavelength range would then include for sMILES SSPs to predict all of the Na indices used in the IMF investigations of La Barbera et al. (2017). More rigorous testing of the theoretical models, through quantitative analyses would be important, using previous model libraries (e.g. Conroy & van Dokkum (2012); Allende Prieto et al. (2018); Coelho (2014)) and star observations, particularly for understanding some of the differences found between sMILES SSP models and Vazdekis et al. (2015) models. This would result in a quantitative analysis of how each stellar parameter (effective temperature, surface gravity, metallicity and $[\alpha/\text{Fe}]$) is predicted to affect spectra and Lick indices across the full parameter space and wavelength range of the models generated. The inclusion of Wing-Ford bands (FeH) in the molecular line lists would improve the sMILES SSPs for greater use in the investigation

CHAPTER 6

of IMF variations.

- **Chapter 4** - Testing of the semi-empirical stars, through comparisons of spectra and indices to observations, would confirm the accuracy of sMILES stars in capturing abundance pattern effects. Although most of the current spectral observations of stars come from the Milky Way galaxy, such as GAIA-ESO, and therefore have only a small range of abundance patterns, some observations of particular star types in external systems have been made, such as the Fornax dwarf and the LMC. Even using the abundance variation present in the Milky Way would be useful in determining how well sMILES stars predict small changes in $[\alpha/\text{Fe}]$ abundances, from surveys such as Gaia-ESO. A new and important dimension of the theoretical grid I generate in Chapter 3 is $[\text{C}/\text{M}]$. If carbon measures can be made for the MILES stars, then sMILES stars can be created with $[\text{C}/\text{Fe}]$ variations and therefore sMILES SSP models could be computed with carbon variations. With stellar spectral models in this thesis computed with fully consistent model atmosphere and radiative transfer variations of carbon, this is a potential future application. The issue of assuming $[\text{C}/\text{Fe}]=0$ in MILES stars is an important caveat of the procedure followed in this thesis. I assume that α abundances are the dominant source of variation in spectra and spectral indices. It can be seen in the response tables presented in Appendix A that both carbon and nitrogen also have a large impact on spectra, particularly in the blue. A more complete procedure would include differential corrections due to variations in carbon, nitrogen and α abundances together. This would be possible in future, if N abundances (as well as C) in MILES stars were measured or estimated and models were computed with fully consistent nitrogen variations. Incorporation of total $[\alpha/\text{Fe}]$ measurements of MILES stars into the differential corrections would increase

CHAPTER 6

the accuracy of the corrections - currently I tag $[\text{Mg}/\text{Fe}]$ as $[\alpha/\text{Fe}]$ in the models. The inclusion of newer isochrones, particularly for an α -deficient SSP would improve the consistency of the models.

- **Chapter 5** - Further testing of sMILES SSPs would be needed before publication of these models. The globular cluster catalogue of Schiavon et al. (2005), would be a good starting sample to test the abundance pattern predictions of the models in comparison to well-used models (e.g. Vazdekis et al. 2015; Conroy et al. 2018). A more detailed analysis is needed to understand $[\text{Mg}/\text{Fe}]$ and $[\text{Mg}/\text{Fe}]'$ sensitivities to $[\alpha/\text{Fe}]$, particularly the differences found between sMILES and Vazdekis at young, metal rich population models. The origin of this difference must be in the theoretical stellar models used, or solar abundance scale inconsistencies, because the SSP calculation is otherwise identical. A quantitative analysis to obtain a relation between $[\text{Mg}/\text{Fe}]$ (or $[\text{Mg}/\text{Fe}]'$) and $[\alpha/\text{Fe}]$, as predicted by sMILES models for a wide range of $[\alpha/\text{Fe}]$ variations, at different total metallicities would be of interest to the community as whole. Finally, in Chapter 5 I demonstrate a potential application of sMILES SSPs to determine $[\alpha/\text{Fe}]$ abundances for SDSS stacked spectra of satellite galaxies from Ferreras et al. (2019). A detailed analysis, involving either fitting of indices or full spectra would allow for a more robust identification of potential merger systems and would be a potential publication for future. Several packages for the fitting of full spectra (e.g. pPXF; Cappellari 2017, ULySS; Koleva et al. 2009 or FIREFLY; Wilkinson et al. 2017) or indices (e.g. rmodel Cardiel et al. 2003) using a library of SSP templates are publicly available.

Bibliography

- Abolfathi, B., Aguado, D. S., Aguilar, G., et al. 2018, *ApJS*, 235, 42
- Allard, F., Hauschildt, P. H., & Schwenke, D. 2000, *ApJ*, 540, 1005
- Allende Prieto, C., Beers, T. C., Wilhelm, R., et al. 2006, *ApJ*, 636, 804
- Allende Prieto, C., Fernández-Alvar, E., Schlesinger, K. J., et al. 2014, *A&A*, 568, A7
- Allende Prieto, C., Koesterke, L., Hubeny, I., et al. 2018, *A&A*, 618, A25
- Alonso, A., Arribas, S., & Martínez-Roger, C. 1995, *A&A*, 297, 197
- Alonso, A., Arribas, S., & Martínez-Roger, C. 1996, *A&A*, 313, 873
- Alonso, A., Arribas, S., & Martínez-Roger, C. 1999, *A&AS*, 140, 261
- Alves-Brito, A., Meléndez, J., Asplund, M., Ramírez, I., & Yong, D. 2010, *A&A*, 513, A35
- Amarsi, A. M., Nordlander, T., Barklem, P. S., et al. 2018, *A&A*, 615, A139
- Asplund, M. 2005, *ARA&A*, 43, 481
- Asplund, M., Grevesse, N., & Sauval, A. J. 2005, in *Astronomical Society of the Pacific Conference Series*, Vol. 336, *Cosmic Abundances as Records of Stellar Evolution and Nucleosynthesis*, ed. T. G. Barnes, III & F. N. Bash, 25

- Asplund, M., Grevesse, N., Sauval, A. J., & Scott, P. 2009, *ARA&A*, 47, 481
- Balcells, M. & Peletier, R. F. 1994, *AJ*, 107, 135
- Bastian, N., Covey, K. R., & Meyer, M. R. 2010, *ARA&A*, 48, 339
- Bell, R. A., Paltoglou, G., & Tripicco, M. J. 1994, *MNRAS*, 268, 771
- Bembenek, Z., Kepa, R., & Rytel, M. 1997, *JMS*, 183, 1
- Bender, R., Burstein, D., & Faber, S. M. 1993, *ApJ*, 411, 153
- Bensby, T., Feltzing, S., & Lundström, I. 2004, *A&A*, 415, 155
- Bensby, T., Feltzing, S., & Oey, M. S. 2014, *A&A*, 562, A71
- Bensby, T., Yee, J. C., Feltzing, S., et al. 2013, *A&A*, 549, A147
- Bertone, E., Buzzoni, A., Chávez, M., & Rodríguez-Merino, L. H. 2008, *A&A*, 485, 823
- Blanton, M. R., Bershady, M. A., Abolfathi, B., et al. 2017, *AJ*, 154, 28
- Bohlin, R. C., Mészáros, S., Fleming, S. W., et al. 2017, *AJ*, 153, 234
- Brooke, J. S. A., Bernath, P. F., Schmidt, T. W., & Bacskay, G. B. 2013, *J. Quant. Spec. Radiat. Transf.*, 124, 11
- Brooke, J. S. A., Ram, R. S., Western, C. M., et al. 2014, *ApJS*, 210, 23
- Bruntt, H., Basu, S., Smalley, B., et al. 2012, *MNRAS*, 423, 122
- Bruzual, A. G. 1983, *ApJ*, 273, 105
- Bruzual, G. & Charlot, S. 2003, *MNRAS*, 344, 1000
- Burstein, D., Faber, S. M., Gaskell, C. M., & Krumm, N. 1984, *ApJ*, 287, 586

- Buser, R. & Kurucz, R. L. 1978, *A&A*, 70, 555
- Şen, Ş., Peletier, R. F., Boselli, A., et al. 2018, *MNRAS*, 475, 3453
- Cappellari, M. 2017, *MNRAS*, 466, 798
- Cappellari, M., McDermid, R. M., Alatalo, K., et al. 2012, *Nature*, 484, 485
- Cardiel, N., Gorgas, J., Sánchez-Blázquez, P., et al. 2003, *A&A*, 409, 511
- Carter, D., Visvanathan, N., & Pickles, A. J. 1986, *ApJ*, 311, 637
- Castelli, F. 2005a, *Memorie della Societa Astronomica Italiana Supplementi*, 8, 25
- Castelli, F. 2005b, *Memorie della Societa Astronomica Italiana Supplementi*, 8, 34
- Cenarro, A. J., Cardiel, N., Gorgas, J., et al. 2001a, *MNRAS*, 326, 959
- Cenarro, A. J., Gorgas, J., Cardiel, N., et al. 2001b, *MNRAS*, 326, 981
- Cenarro, A. J., Gorgas, J., Vazdekis, A., Cardiel, N., & Peletier, R. F. 2003, *MNRAS*, 339, L12
- Cenarro, A. J., Peletier, R. F., Sánchez-Blázquez, P., et al. 2007, *MNRAS*, 374, 664
- Cervantes, J. L. & Vazdekis, A. 2009, *MNRAS*, 392, 691
- Chabrier, G. 2003, *ApJ*, 586, L133
- Chavez, M., Bertone, E., Buzzoni, A., et al. 2007, *ApJ*, 657, 1046
- Choi, J., Conroy, C., Moustakas, J., et al. 2014, *ApJ*, 792, 95
- Choi, J., Dotter, A., Conroy, C., et al. 2016, *ApJ*, 823, 102
- Code, A. D. & Welch, G. A. 1979, *ApJ*, 228, 95

- Coelho, P., Barbuy, B., Meléndez, J., Schiavon, R. P., & Castilho, B. V. 2005, *A&A*, 443, 735
- Coelho, P., Bruzual, G., Charlot, S., et al. 2007, *MNRAS*, 382, 498
- Coelho, P. R. T. 2014, *MNRAS*, 440, 1027
- Colin, R. & Bernath, P. F. 2010, *JMS*, 263, 120
- Concas, A., Pozzetti, L., Moresco, M., & Cimatti, A. 2017, *MNRAS*, 468, 1747
- Conroy, C. 2013, *ARA&A*, 51, 393
- Conroy, C., Graves, G. J., & van Dokkum, P. G. 2014, *ApJ*, 780, 33
- Conroy, C. & van Dokkum, P. 2012, *ApJ*, 747, 69
- Conroy, C., Villaume, A., van Dokkum, P. G., & Lind, K. 2018, *ApJ*, 854, 139
- da Silva, R., Milone, A. C., & Reddy, B. E. 2011, *A&A*, 526, A71
- da Silveira, C. R., Barbuy, B., Friaça, A. C. S., et al. 2018, *A&A*, 614, A149
- Delgado Mena, E., Israelian, G., González Hernández, J. I., et al. 2010, *ApJ*, 725, 2349
- Diaz, A. I., Terlevich, E., & Terlevich, R. 1989, *MNRAS*, 239, 325
- Dorman, B., O'Connell, R. W., & Rood, R. T. 1995, *ApJ*, 442, 105
- Dotter, A. 2016, *ApJS*, 222, 8
- Dutra-Ferreira, L., Pasquini, L., Smiljanic, R., Porto de Mello, G. F., & Steffen, M. 2016, *A&A*, 585, A75
- Edvardsson, B., Andersen, J., Gustafsson, B., et al. 1993, *A&A*, 275, 101
- Eggen, O. J., Lynden-Bell, D., & Sandage, A. R. 1962, *ApJ*, 136, 748

- Erwin, P., Saglia, R. P., Fabricius, M., et al. 2015, *MNRAS*, 446, 4039
- Faber, S. M. 1972, *A&A*, 20, 361
- Faber, S. M. & French, H. B. 1980, *ApJ*, 235, 405
- Faber, S. M., Friel, E. D., Burstein, D., & Gaskell, C. M. 1985, *ApJS*, 57, 711
- Falcón-Barroso, J., Peletier, R. F., & Balcells, M. 2002, *MNRAS*, 335, 741
- Falcón-Barroso, J., Sánchez-Blázquez, P., Vazdekis, A., et al. 2011, *A&A*, 532, A95
- Fanelli, M. N., O’Connell, R. W., Burstein, D., & Wu, C.-C. 1990, *ApJ*, 364, 272
- Fanelli, M. N., O’Connell, R. W., Burstein, D., & Wu, C.-C. 1992, *ApJS*, 82, 197
- Ferreras, I., Hopkins, A. M., Gunawardhana, M. L. P., et al. 2017, *MNRAS*, 468, 607
- Ferreras, I., Hopkins, A. M., Lagos, C., et al. 2019, *MNRAS*, 487, 435
- Ferreras, I. & Silk, J. 2002, *MNRAS*, 336, 1181
- Ferreras, I., Trujillo, I., Mármod-Queraltó, E., et al. 2014, *MNRAS*, 444, 906
- Fisher, D. B. & Drory, N. 2008, in *Astronomical Society of the Pacific Conference Series*, Vol. 396, *Formation and Evolution of Galaxy Disks*, ed. J. G. Funes & E. M. Corsini, 309
- Fisher, D. B. & Drory, N. 2016, in *Astrophysics and Space Science Library*, Vol. 418, *Galactic Bulges*, ed. E. Laurikainen, R. Peletier, & D. Gadotti, 41
- Fontanot, F., La Barbera, F., De Lucia, G., Pasquali, A., & Vazdekis, A. 2018, *MNRAS*, 479, 5678
- Friça, A. C. S. & Barbuy, B. 2017, *A&A*, 598, A121

- Fukugita, M., Shimasaku, K., & Ichikawa, T. 1995, *PASP*, 107, 945
- Fulbright, J. P., McWilliam, A., & Rich, R. M. 2007, *ApJ*, 661, 1152
- Gadotti, D. A. 2009, *MNRAS*, 393, 1531
- Ganda, K., Peletier, R. F., McDermid, R. M., et al. 2007, *MNRAS*, 380, 506
- García Pérez, A. E., Allende Prieto, C., Holtzman, J. A., et al. 2016, *AJ*, 151, 144
- García Pérez, A. E., Ness, M., Robin, A. C., et al. 2018, *ApJ*, 852, 91
- Gilmore, G., Randich, S., Asplund, M., et al. 2012, *The Messenger*, 147, 25
- Gonneau, A., Lançon, A., Trager, S. C., et al. 2016, *A&A*, 589, A36
- González, J. J. 1993, PhD thesis, Thesis (PH.D.)—UNIVERSITY OF CALIFORNIA, SANTA CRUZ, 1993. Source: Dissertation Abstracts International, Volume: 54-05, Section: B, page: 2551.
- Gonzalez, O. A., Zoccali, M., Vasquez, S., et al. 2015, *A&A*, 584, A46
- Graves, G. J., Faber, S. M., & Schiavon, R. P. 2009, *ApJ*, 693, 486
- Gray, R. O., Graham, P. W., & Hoyt, S. R. 2001, *AJ*, 121, 2159
- Greene, J. E., Janish, R., Ma, C.-P., et al. 2015, *ApJ*, 807, 11
- Greene, J. E., Murphy, J. D., Graves, G. J., et al. 2013, *ApJ*, 776, 64
- Grevesse, N. & Noels, A. 1993, in *Origin and Evolution of the Elements*, ed. N. Prantzos, E. Vangioni-Flam, & M. Casse, 15–25
- Grevesse, N. & Sauval, A. J. 1998, *Space Sci. Rev.*, 85, 161
- Gustafsson, B., Edvardsson, B., Eriksson, K., et al. 2008, *A&A*, 486, 951

- Hardy, E. 1990, in European Southern Observatory Conference and Workshop Proceedings, Vol. 35, 209
- Hayden, M. R., Bovy, J., Holtzman, J. A., et al. 2015, *ApJ*, 808, 132
- Hernández-Pérez, F. & Bruzual, G. 2014, *MNRAS*, 444, 2571
- Holtzman, J. A., Shetrone, M., Johnson, J. A., et al. 2015, *AJ*, 150, 148
- Husser, T.-O., Wende-von Berg, S., Dreizler, S., et al. 2013, *A&A*, 553, A6
- Iben, Jr., I. & Truran, J. W. 1978, *ApJ*, 220, 980
- Jablonka, P., Gorgas, J., & Goudfrooij, P. 2007, *A&A*, 474, 763
- Jablonka, P., Martin, P., & Arimoto, N. 1996, *AJ*, 112, 1415
- Johansson, J., Thomas, D., & Maraston, C. 2012, *MNRAS*, 421, 1908
- Johnson, C. I., Rich, R. M., Kobayashi, C., Kunder, A., & Koch, A. 2014, *AJ*, 148, 67
- Jorgensen, U. G., Larsson, M., Iwamae, A., & Yu, B. 1996, *A&A*, 315, 204
- Kepa, R., Para, A., Rytel, M., & Zachwieja, M. 1996, *JMS*, 178, 189
- Kirkpatrick, J. D., Henry, T. J., & McCarthy, Jr., D. W. 1991, *ApJS*, 77, 417
- Knowles, A. T., Sansom, A. E., Coelho, P. R. T., et al. 2019, *MNRAS*, 486, 1814
- Koesterke, L. 2009, in American Institute of Physics Conference Series, Vol. 1171, American Institute of Physics Conference Series, ed. I. Hubeny, J. M. Stone, K. MacGregor, & K. Werner, 73–84
- Koleva, M., Prugniel, P., Bouchard, A., & Wu, Y. 2009, *A&A*, 501, 1269
- Kormendy, J. & Kennicutt, Jr., R. C. 2004, *ARA&A*, 42, 603

- Korn, A. J., Maraston, C., & Thomas, D. 2005, *A&A*, 438, 685
- Kroupa, P. 2001, *MNRAS*, 322, 231
- Kroupa, P., Tout, C. A., & Gilmore, G. 1993, *MNRAS*, 262, 545
- Kurucz, R. 1993, ATLAS9 Stellar Atmosphere Programs and 2 km/s grid. Kurucz CD-ROM No. 13. Cambridge, Mass.: Smithsonian Astrophysical Observatory, 1993., 13
- Kurucz, R. L. 1979a, *ApJS*, 40, 1
- Kurucz, R. L. 1979b, *ApJS*, 40, 1
- Kurucz, R. L. 1996, in IAU Symposium, Vol. 176, Stellar Surface Structure, ed. K. G. Strassmeier & J. L. Linsky, 523
- Kurucz, R. L. 2005, *Memorie della Societa Astronomica Italiana Supplementi*, 8, 14
- Kurucz, R. L. & Avrett, E. H. 1981, SAO Special Report, 391
- La Barbera, F., Ferreras, I., de Carvalho, R. R., et al. 2012, *MNRAS*, 426, 2300
- La Barbera, F., Ferreras, I., de Carvalho, R. R., et al. 2011, *ApJ*, 740, L41
- La Barbera, F., Ferreras, I., Vazdekis, A., et al. 2013, *MNRAS*, 433, 3017
- La Barbera, F., Vazdekis, A., Ferreras, I., et al. 2017, *MNRAS*, 464, 3597
- La Barbera, F., Vazdekis, A., Ferreras, I., et al. 2016, *MNRAS*, 457, 1468
- Lackner, C. N., Cen, R., Ostriker, J. P., & Joung, M. R. 2012, *MNRAS*, 425, 641
- Lecureur, A., Hill, V., Zoccali, M., et al. 2007, *A&A*, 465, 799
- Lee, H.-c., Worthey, G., Dotter, A., et al. 2009, *ApJ*, 694, 902

- Lee, S.-K., Ferguson, H. C., Somerville, R. S., Wiklind, T., & Giavalisco, M. 2010, *ApJ*, 725, 1644
- Leitherer, C., Ortiz Otálvaro, P. A., Bresolin, F., et al. 2010, *ApJS*, 189, 309
- Letarte, B., Hill, V., & Tolstoy, E. 2007, in EAS Publications Series, Vol. 24, EAS Publications Series, ed. E. Emsellem, H. Wozniak, G. Massacrier, J.-F. Gonzalez, J. Devriendt, & N. Champavert, 33–38
- Letarte, B., Hill, V., Tolstoy, E., et al. 2010, *A&A*, 523, A17
- Lyubenova, M., Martín-Navarro, I., van de Ven, G., et al. 2016, *MNRAS*, 463, 3220
- MacArthur, L. A., González, J. J., & Courteau, S. 2009, *MNRAS*, 395, 28
- Majewski, S. R. 2012, in American Astronomical Society Meeting Abstracts, Vol. 219, American Astronomical Society Meeting Abstracts #219, 205.06
- Mannucci, F. 2008, Chinese Journal of Astronomy and Astrophysics Supplement, 8, 143
- Maoz, D., Sharon, K., & Gal-Yam, A. 2010, *ApJ*, 722, 1879
- Maraston, C. 2005, *MNRAS*, 362, 799
- Maraston, C., Nieves Colmenárez, L., Bender, R., & Thomas, D. 2009, *A&A*, 493, 425
- Maraston, C., Pforr, J., Renzini, A., et al. 2010, *MNRAS*, 407, 830
- Maraston, C. & Strömbäck, G. 2011, *MNRAS*, 418, 2785
- Marigo, P., Bressan, A., & Chiosi, C. 1996, *A&A*, 313, 545
- Martinez-Valpuesta, I. & Gerhard, O. 2013, *ApJ*, 766, L3

- Martins, L. P. & Coelho, P. 2007, *MNRAS*, 381, 1329
- McDermid, R. M., Alatalo, K., Blitz, L., et al. 2015, *MNRAS*, 448, 3484
- McWilliam, A. 2016, *PASA*, 33, e040
- McWilliam, A. & Smecker-Hane, T. A. 2005, in Astronomical Society of the Pacific Conference Series, Vol. 336, Cosmic Abundances as Records of Stellar Evolution and Nucleosynthesis, ed. T. G. Barnes, III & F. N. Bash, 221
- Meléndez, J., Asplund, M., Alves-Brito, A., et al. 2008, *A&A*, 484, L21
- Mentz, J. J., La Barbera, F., Peletier, R. F., et al. 2016, *MNRAS*, 463, 2819
- Mészáros, S., Allende Prieto, C., Edvardsson, B., et al. 2012, *AJ*, 144, 120
- Mihos, J. C. & Hernquist, L. 1994, *ApJ*, 427, 112
- Milone, A. D. C., Sansom, A. E., & Sánchez-Blázquez, P. 2011, *MNRAS*, 414, 1227
- Montalbán, J., Nendwich, J., Heiter, U., et al. 2007, in IAU Symposium, Vol. 239, Convection in Astrophysics, ed. F. Kupka, I. Roxburgh, & K. L. Chan, 166–168
- Moorthy, B. K. & Holtzman, J. A. 2006, *MNRAS*, 371, 583
- Morelli, L., Parmiggiani, M., Corsini, E. M., et al. 2016, *MNRAS*, 463, 4396
- Morelli, L., Pompei, E., Pizzella, A., et al. 2008, *MNRAS*, 389, 341
- Munari, U., Sordo, R., Castelli, F., & Zwitter, T. 2005, *A&A*, 442, 1127
- Niemczura, E., Murphy, S. J., Smalley, B., et al. 2015, *MNRAS*, 450, 2764
- O’Connell, R. W. 1976, *ApJ*, 206, 370
- Onodera, M., Carollo, C. M., Renzini, A., et al. 2015, *ApJ*, 808, 161
- Oser, L., Naab, T., Ostriker, J. P., & Johansson, P. H. 2012, *ApJ*, 744, 63

- Pagel, B. E. J. 2009, *Nucleosynthesis and Chemical Evolution of Galaxies*, 182 & 200
- Parikh, T., Thomas, D., Maraston, C., et al. 2018, *MNRAS*, 477, 3954
- Parikh, T., Thomas, D., Maraston, C., et al. 2019, *MNRAS*, 483, 3420
- Peletier, R. F. 1989, PhD thesis, , University of Groningen, The Netherlands, (1989)
- Peletier, R. F. & Balcells, M. 1996, *AJ*, 111, 2238
- Peletier, R. F., Falcón-Barroso, J., Bacon, R., et al. 2007, *MNRAS*, 379, 445
- Percival, S. M., Salaris, M., Cassisi, S., & Pietrinferni, A. 2009, *ApJ*, 690, 427
- Pérez, I. & Sánchez-Blázquez, P. 2011, *A&A*, 529, A64
- Pérez-González, P. G., Cava, A., Barro, G., et al. 2013, *ApJ*, 762, 46
- Pietrinferni, A., Cassisi, S., Salaris, M., & Castelli, F. 2004, *ApJ*, 612, 168
- Pietrinferni, A., Cassisi, S., Salaris, M., & Castelli, F. 2006, *ApJ*, 642, 797
- Pietrinferni, A., Cassisi, S., Salaris, M., & Hidalgo, S. 2013, *A&A*, 558, A46
- Pietrinferni, A., Cassisi, S., Salaris, M., Percival, S., & Ferguson, J. W. 2009, *ApJ*, 697, 275
- Plez, B. 1998, *A&A*, 337, 495
- Poggianti, B. M. & Barbaro, G. 1997, *A&A*, 325, 1025
- Pompéia, L., Hill, V., Spite, M., et al. 2008, *A&A*, 480, 379
- Prochaska, L. C., Rose, J. A., & Schiavon, R. P. 2005, *AJ*, 130, 2666
- Proctor, R. N. & Sansom, A. E. 2002, *MNRAS*, 333, 517

- Prugniel, P., Koleva, M., Ocvirk, P., Le Borgne, D., & Soubiran, C. 2007, in IAU Symposium, Vol. 241, Stellar Populations as Building Blocks of Galaxies, ed. A. Vazdekis & R. Peletier, 68–72
- Prugniel, P., Vauglin, I., & Koleva, M. 2011, *A&A*, 531, A165
- Ramírez, I., Allende Prieto, C., & Lambert, D. L. 2013, *ApJ*, 764, 78
- Recio-Blanco, A., Rojas-Arriagada, A., de Laverny, P., et al. 2017, *A&A*, 602, L14
- Reimers, D. 1975, *Memoires of the Societe Royale des Sciences de Liege*, 8, 369
- Rose, J. A. 1984, *AJ*, 89, 1238
- Salaris, M. & Cassisi, S. 2005, *Evolution of Stars and Stellar Populations*, 400
- Salpeter, E. E. 1955, *ApJ*, 121, 161
- Sánchez-Blázquez, P. 2016, in *Astrophysics and Space Science Library*, Vol. 418, Galactic Bulges, ed. E. Laurikainen, R. Peletier, & D. Gadotti, 127
- Sánchez-Blázquez, P., Ocvirk, P., Gibson, B. K., Pérez, I., & Peletier, R. F. 2011, *MNRAS*, 415, 709
- Sánchez-Blázquez, P., Peletier, R. F., Jiménez-Vicente, J., et al. 2006, *MNRAS*, 371, 703
- Sansom, A. E., Milone, A. d. C., Vazdekis, A., & Sánchez-Blázquez, P. 2013, *MNRAS*, 435, 952
- Sansom, A. E. & Northeast, M. S. 2008, *MNRAS*, 387, 331
- Sbordone, L., Bonifacio, P., Buonanno, R., et al. 2007, *A&A*, 465, 815
- Sbordone, L., Bonifacio, P., Castelli, F., & Kurucz, R. L. 2004, *Memorie della Societa Astronomica Italiana Supplementi*, 5, 93

- Scannapieco, C. & Tissera, P. B. 2003, *MNRAS*, 338, 880
- Schiavon, R. P. 2007, *ApJS*, 171, 146
- Schiavon, R. P., Rose, J. A., Courteau, S., & MacArthur, L. A. 2005, *ApJS*, 160, 163
- Schmidt, M. 1959, *ApJ*, 129, 243
- Searle, L., Sargent, W. L. W., & Bagnuolo, W. G. 1973, *ApJ*, 179, 427
- Serven, J., Worthey, G., & Briley, M. M. 2005, *ApJ*, 627, 754
- Serven, J., Worthey, G., Toloba, E., & Sánchez-Blázquez, P. 2011, *AJ*, 141, 184
- Sesto, L. A., Faifer, F. R., Smith Castelli, A. V., Forte, J. C., & Escudero, C. G. 2018, *MNRAS*, 479, 478
- Sharma, K., Prugniel, P., & Singh, H. P. 2016, *A&A*, 585, A64
- Sheth, K., Vogel, S. N., Regan, M. W., Thornley, M. D., & Teuben, P. J. 2005, *ApJ*, 632, 217
- Shetrone, M., Venn, K. A., Tolstoy, E., et al. 2003, *AJ*, 125, 684
- Short, C. I., Young, M. E., & Layden, N. 2015, *ApJ*, 810, 76
- Smith, L. J., Norris, R. P. F., & Crowther, P. A. 2002, *MNRAS*, 337, 1309
- Smith, R. J. 2014, *MNRAS*, 443, L69
- Smith, R. J., Lucey, J. R., & Conroy, C. 2015, *MNRAS*, 449, 3441
- Sparke, L. S. & Gallagher, III, J. S. 2007, *Galaxies in the Universe: An Introduction* (Cambridge University Press)
- Spinrad, H. & Taylor, B. J. 1971, *ApJS*, 22, 445

- Struve, O. & Elvey, C. T. 1934, *ApJ*, 79, 409
- Sullivan, M., Le Borgne, D., Pritchett, C. J., et al. 2006, *ApJ*, 648, 868
- Swan, W. 1875, Transactions of the Royal Society of Edinburgh, 21, 411
- Thomas, D., Johansson, J., & Maraston, C. 2011, *MNRAS*, 412, 2199
- Thomas, D., Maraston, C., & Bender, R. 2003a, *MNRAS*, 343, 279
- Thomas, D., Maraston, C., & Bender, R. 2003b, *MNRAS*, 339, 897
- Thomas, D., Maraston, C., Bender, R., & Mendes de Oliveira, C. 2005, *ApJ*, 621, 673
- Thygesen, A. O., Frandsen, S., Bruntt, H., et al. 2012, *A&A*, 543, A160
- Tinsley, B. M. 1968, *ApJ*, 151, 547
- Tinsley, B. M. 1978, *ApJ*, 222, 14
- Tinsley, B. M. 1980, *Fund. Cosmic Phys.*, 5, 287
- Tinsley, B. M. & Gunn, J. E. 1976, *ApJ*, 203, 52
- Trager, S. C., Dalcanton, J. J., & Weiner, B. J. 1999, in The Formation of Galactic Bulges, ed. C. M. Carollo, H. C. Ferguson, & R. F. G. Wyse, 42
- Trager, S. C., Faber, S. M., Worthey, G., & González, J. J. 2000a, *AJ*, 120, 165
- Trager, S. C., Faber, S. M., Worthey, G., & González, J. J. 2000b, *AJ*, 119, 1645
- Trager, S. C., Worthey, G., Faber, S. M., Burstein, D., & González, J. J. 1998, *ApJS*, 116, 1
- Treu, T., Auger, M. W., Koopmans, L. V. E., et al. 2010, *ApJ*, 709, 1195
- Tripicco, M. J. & Bell, R. A. 1995, *AJ*, 110, 3035

- Valdes, F., Gupta, R., Rose, J. A., Singh, H. P., & Bell, D. J. 2004, *ApJS*, 152, 251
- van Dokkum, P. G. & Conroy, C. 2010, *Nature*, 468, 940
- van Paradijs, J. 1972, *Nature Physical Science*, 238, 37
- Vazdekis, A. 2011, LECTOR: Line-strengths in One-dimensional ASCII Spectra, Astrophysics Source Code Library
- Vazdekis, A. & Arimoto, N. 1999, *ApJ*, 525, 144
- Vazdekis, A., Cenarro, A. J., Gorgas, J., Cardiel, N., & Peletier, R. F. 2003, *MNRAS*, 340, 1317
- Vazdekis, A., Coelho, P., Cassisi, S., et al. 2015, *MNRAS*, 449, 1177
- Vazdekis, A., Koleva, M., Ricciardelli, E., Röck, B., & Falcón-Barroso, J. 2016, *MNRAS*, 463, 3409
- Vazdekis, A., Peletier, R. F., Beckman, J. E., & Casuso, E. 1997, *ApJS*, 111, 203
- Vazdekis, A., Ricciardelli, E., Cenarro, A. J., et al. 2012, *MNRAS*, 424, 157
- Vazdekis, A., Sánchez-Blázquez, P., Falcón-Barroso, J., et al. 2010, *MNRAS*, 404, 1639
- Venn, K. A., Irwin, M., Shetrone, M. D., et al. 2004, *AJ*, 128, 1177
- Villaume, A., Brodie, J., Conroy, C., Romanowsky, A. J., & van Dokkum, P. 2017a, *ApJ*, 850, L14
- Villaume, A., Conroy, C., Johnson, B., et al. 2017b, *ApJS*, 230, 23
- Walcher, C. J., Coelho, P., Gallazzi, A., & Charlot, S. 2009, *MNRAS*, 398, L44
- White, S. D. M. 1980, *MNRAS*, 191, 1P

- Whitford, A. E. 1977, *ApJ*, 211, 527
- Wilkinson, D. M., Maraston, C., Goddard, D., Thomas, D., & Parikh, T. 2017, *MNRAS*, 472, 4297
- Worthey, G. 1994, *ApJS*, 95, 107
- Worthey, G., Faber, S. M., & Gonzalez, J. J. 1992, *ApJ*, 398, 69
- Worthey, G. & Ottaviani, D. L. 1997, *ApJS*, 111, 377
- Zachwieja, M. 1995, *JMS*, 170, 285
- Zachwieja, M. 1997, *JMS*, 182, 18
- Zamora, O., García-Hernández, D. A., Allende Prieto, C., et al. 2015, *AJ*, 149, 181
- Zoccali, M., Lecureur, A., Barbuy, B., et al. 2006, *A&A*, 457, L1

Appendix A

Response Function Tables

I show the derived response function tables from Chapter 2. This is for the Conroy, Coelho and CAP models respectively, for Cool Dwarf, Cool Giant and Turn-off star types. The tables are publicly available on the UCLan database at <https://doi.org/10.17030/uclan.data.00000175>.

Table A.1: Conroy Cool Dwarf Response Function. Column 1 is the Lick index name, Column 2 is the units of the index, Column 3 is the model base star index strength and Columns 4-12 are the variation of the index strength (in units of mag or Å) when the element at the top of the column is increased by 0.3 dex (0.15 dex for C). The last column shows the variation of the index strength when there is an overall metallicity increase of 0.3 dex.

Index	Units	I ₀	C	N	Mg	Fe	Ca	Na	Si	Cr	Ti	[M/H]
H δ A	Å	-10.483	-0.603	-0.071	0.888	-4.021	0.688	0.189	1.580	0.160	-0.367	-0.754
H δ F	Å	-1.726	-0.046	-0.013	0.141	-1.638	0.448	0.009	1.295	-0.073	-0.319	-0.471
CN ₁	mag	0.160	0.056	0.039	-0.022	-0.014	-0.017	-0.006	0.069	-0.021	0.001	0.014
CN ₂	mag	0.342	0.058	0.038	-0.042	-0.026	-0.024	-0.011	0.115	-0.021	0.000	0.015
Ca4227	Å	6.548	-0.314	-0.099	0.053	-0.114	0.882	-0.004	-0.235	-0.072	-0.036	0.479
G4300	Å	7.876	1.097	0.040	-0.056	-0.843	0.210	-0.068	-0.248	-0.018	0.509	-0.191
H γ A	Å	-13.117	-0.300	-0.069	0.769	-1.005	-0.011	0.192	-0.075	0.392	-0.527	-0.306
H γ F	Å	-5.055	-0.413	-0.023	0.265	-0.172	-0.143	0.094	-0.174	0.257	-0.046	0.007
Fe4383	Å	10.127	-0.058	0.002	-0.749	1.877	-0.428	-0.108	-0.014	0.014	-0.040	0.641
Ca4455	Å	3.973	-0.060	-0.003	-0.101	-0.146	0.266	-0.026	-0.136	0.157	0.105	0.467
Fe4531	Å	6.929	0.048	0.014	-0.556	0.259	-0.256	-0.079	0.080	0.247	0.981	0.652
C ₂ 4668	Å	-0.105	0.892	0.008	-0.652	0.143	0.128	0.027	-0.192	-0.345	0.268	-0.054
H β	Å	-0.781	-0.100	0.007	-0.494	0.304	-0.021	0.046	0.046	-0.080	0.057	-0.116
Fe5015	Å	10.973	0.061	0.034	-1.122	1.138	-0.007	0.009	-0.089	0.049	1.310	1.424
Mg ₁	mag	0.424	0.008	0.001	0.090	-0.033	-0.018	-0.014	-0.009	-0.005	-0.007	0.023
Mg ₂	mag	0.592	0.008	0.002	0.082	-0.028	-0.014	-0.013	-0.007	-0.006	0.002	0.033
Mg _b	Å	4.622	0.128	0.027	0.821	-0.369	0.057	-0.045	0.007	-0.401	-0.098	0.104
Fe5270	Å	5.805	0.036	0.015	-0.500	0.765	0.222	-0.079	-0.025	-0.012	0.104	0.408
Fe5335	Å	6.349	0.019	0.011	-0.489	1.058	-0.089	-0.109	-0.037	0.337	0.029	0.767
Fe5406	Å	4.448	0.021	0.010	-0.385	0.697	-0.096	-0.076	-0.049	0.243	0.022	0.439
Fe5709	Å	1.502	0.003	0.000	-0.093	0.231	-0.003	-0.092	-0.001	0.068	0.080	0.230
Fe5782	Å	1.255	0.007	0.001	-0.003	-0.012	-0.017	-0.011	-0.004	0.361	-0.031	0.305
Na _D	Å	7.142	0.053	0.019	-0.374	-0.139	-0.171	1.894	-0.080	0.018	-0.126	1.077
TiO ₁	mag	0.013	-0.001	0.000	-0.001	0.000	-0.001	0.000	0.000	0.001	0.005	0.006
TiO ₂	mag	0.026	-0.001	0.000	-0.002	0.005	-0.007	0.000	0.000	0.000	0.005	0.010

Table A.2: Conroy Cool Giant Response Function. Column 1 is the Lick index name, Column 2 is the units of the index, Column 3 is the model base star index strength and Columns 4-12 are the variation of the index strength (in units of mag or Å) when the element at the top of the column is increased by 0.3 dex (0.15 dex for C). The last column shows the variation of the index strength when there is an overall metallicity increase of 0.3 dex.

Index	Units	I ₀	C	N	Mg	Fe	Ca	Na	Si	Cr	Ti	[M/H]
H δ A	Å	-11.954	-0.494	0.180	0.320	-3.895	0.104	0.021	1.584	0.119	-0.394	-1.770
H δ F	Å	-3.788	-0.141	-0.013	-0.012	-1.746	0.076	-0.009	1.170	-0.111	-0.321	-1.334
CN ₁	mag	0.356	0.105	0.087	-0.037	-0.031	-0.009	-0.005	0.042	-0.015	-0.001	0.035
CN ₂	mag	0.476	0.106	0.088	-0.050	-0.045	-0.012	-0.006	0.080	-0.016	-0.003	0.032
Ca4227	Å	5.205	-0.288	-0.171	0.025	0.051	1.825	0.021	0.082	-0.045	-0.122	1.440
G4300	Å	9.197	0.752	0.088	-0.073	-0.614	0.126	-0.060	-0.113	-0.193	0.259	-0.351
H γ A	Å	-12.170	0.435	-0.175	0.339	-1.022	-0.068	0.117	-0.342	-0.065	-0.221	-0.708
H γ F	Å	-4.486	-0.250	-0.054	0.134	-0.246	-0.074	0.062	-0.166	-0.092	0.041	-0.380
Fe4383	Å	8.905	-0.513	-0.103	-0.417	1.620	-0.117	-0.013	0.086	0.070	0.080	0.640
Ca4455	Å	3.503	-0.081	-0.038	0.004	-0.127	0.135	0.001	-0.085	0.215	0.086	0.396
Fe4531	Å	6.237	0.068	0.076	-0.260	0.310	-0.177	-0.006	0.105	0.170	0.584	0.814
C ₂ 4668	Å	3.591	3.518	0.030	-0.766	-0.424	-0.010	-0.106	-0.367	-0.340	0.159	0.903
H β	Å	0.218	-0.136	0.012	-0.171	0.313	0.007	0.007	0.052	-0.056	0.043	0.091
Fe5015	Å	13.008	-0.140	-0.003	-0.624	1.659	0.051	0.023	-0.067	0.069	0.713	2.018
Mg ₁	mag	0.238	0.032	-0.001	0.061	-0.027	-0.006	-0.004	-0.007	-0.003	-0.005	0.035
Mg ₂	mag	0.378	0.017	0.002	0.087	-0.025	-0.005	-0.004	-0.006	-0.003	0.002	0.062
Mg _b	Å	3.996	0.144	0.026	1.277	-0.240	-0.005	-0.062	-0.038	-0.286	0.006	0.867
Fe5270	Å	4.991	0.040	0.036	-0.311	0.606	0.078	-0.022	-0.027	-0.071	0.131	0.428
Fe5335	Å	6.052	-0.040	-0.020	-0.249	0.846	-0.025	-0.024	0.001	0.195	0.064	0.952
Fe5406	Å	3.911	0.001	0.008	-0.190	0.465	-0.027	-0.018	-0.037	0.140	0.028	0.493
Fe5709	Å	2.234	-0.022	-0.021	-0.035	0.213	0.017	-0.024	-0.008	0.054	0.075	0.322
Fe5782	Å	1.710	-0.001	-0.006	0.028	0.014	-0.002	-0.001	0.032	0.285	-0.036	0.367
Na _D	Å	3.240	0.062	0.058	-0.151	-0.028	-0.063	1.256	-0.059	0.030	-0.067	0.992
TiO ₁	mag	0.021	0.000	0.000	-0.001	0.001	-0.001	0.000	0.000	0.001	0.005	0.008
TiO ₂	mag	0.057	0.002	0.003	-0.002	0.005	-0.002	0.000	0.000	0.001	0.005	0.015

Table A.3: Conroy Turn-off Response Function. Column 1 is the Lick index name, Column 2 is the units of the index, Column 3 is the model base star index strength and Columns 4-12 are the variation of the index strength (in units of mag or Å) when the element at the top of the column is increased by 0.3 dex (0.15 dex for C). The last column shows the variation of the index strength when there is an overall metallicity increase of 0.3 dex.

Index	Units	I ₀	C	N	Mg	Fe	Ca	Na	Si	Cr	Ti	[M/H]
HδA	Å	1.250	-0.133	-0.049	0.173	-0.537	0.113	0.009	0.150	0.079	-0.095	-0.540
HδF	Å	2.029	-0.023	-0.009	0.092	-0.241	0.118	0.004	0.086	-0.009	-0.063	-0.189
CN ₁	mag	-0.079	-0.004	0.008	0.002	0.004	-0.002	0.000	0.000	-0.003	0.002	0.004
CN ₂	mag	-0.022	-0.004	0.009	0.003	0.003	-0.001	0.000	0.001	-0.002	0.003	0.006
Ca4227	Å	0.894	-0.059	-0.061	0.018	0.108	0.251	-0.002	0.015	-0.051	0.002	0.178
G4300	Å	5.507	0.550	-0.025	-0.315	-0.337	0.048	-0.031	-0.220	-0.095	0.137	0.404
HγA	Å	-1.625	-0.512	0.028	0.442	0.241	0.020	0.021	0.260	0.037	-0.190	-0.364
HγF	Å	1.290	-0.308	0.015	0.214	0.249	-0.015	0.014	0.133	0.013	0.008	-0.047
Fe4383	Å	3.244	0.161	-0.015	-0.108	0.326	-0.040	0.024	-0.061	0.091	0.100	0.711
Ca4455	Å	1.347	-0.013	-0.004	-0.018	-0.059	0.063	0.000	-0.015	0.063	0.048	0.296
Fe4531	Å	3.098	-0.004	-0.004	-0.026	0.131	-0.006	0.005	0.009	0.100	0.233	0.509
C ₂ 4668	Å	1.178	0.227	-0.004	0.011	-0.012	0.008	0.015	-0.122	-0.115	0.132	0.248
Hβ	Å	3.547	-0.020	0.003	0.032	0.098	0.007	0.001	0.040	-0.030	0.081	0.253
Fe5015	Å	6.048	-0.169	-0.016	0.279	1.036	0.065	0.050	-0.035	-0.010	0.314	1.561
Mg ₁	mag	-0.004	-0.001	0.000	0.002	-0.004	0.000	0.000	0.000	-0.001	0.001	-0.003
Mg ₂	mag	0.060	-0.001	0.000	0.018	-0.005	0.000	0.000	-0.001	-0.002	0.002	0.009
Mg _b	Å	1.076	-0.029	-0.005	0.649	-0.076	0.010	-0.023	-0.024	-0.076	-0.043	0.211
Fe5270	Å	1.686	-0.010	-0.005	-0.061	0.345	0.091	0.000	0.035	0.042	0.061	0.494
Fe5335	Å	2.292	0.000	-0.006	0.016	0.462	0.009	0.000	0.059	0.063	0.020	0.654
Fe5406	Å	0.877	-0.026	-0.003	0.009	0.193	-0.004	0.001	-0.008	0.052	0.004	0.202
Fe5709	Å	0.663	0.000	-0.002	0.014	0.134	0.006	-0.027	-0.015	0.031	0.008	0.204
Fe5782	Å	0.399	0.020	-0.001	0.051	0.023	-0.001	0.001	0.029	0.144	-0.009	0.274
NaD	Å	0.607	-0.003	-0.002	-0.027	-0.015	-0.016	0.276	-0.057	0.008	-0.021	0.142
TiO ₁	mag	0.005	0.000	0.000	0.000	0.000	0.000	0.000	0.000	0.000	0.000	0.000
TiO ₂	mag	0.009	0.000	0.000	0.000	0.000	0.000	0.003	0.000	0.000	0.001	0.004

Table A.4: Coelho Cool Dwarf Response Function. Column 1 is the Lick index name, Column 2 is the units of the index, Column 3 is the model base star index strength and Columns 4-8 are the variation of the index strength (in units of mag or Å) when the element at the top of the column is increased by 0.3 dex. The last column shows the variation of the index strength when there is an overall metallicity increase of 0.3 dex.

Index	Units	I ₀	C	N	O	Mg	Ca	[M/H]
Hδ _A	Å	-12.008	-3.181	-0.55	0.487	1.334	0.504	-1.708
Hδ _F	Å	-2.145	-0.648	-0.126	-0.033	0.23	0.338	-0.525
CN ₁	mag	0.084	0.124	0.029	-0.027	-0.015	-0.015	0.017
CN ₂	mag	0.214	0.128	0.029	-0.033	-0.03	-0.021	0.029
Ca4227	Å	6.281	-0.743	-0.083	0.179	-0.129	1.112	0.73
G4300	Å	9.214	3.207	0.035	-1.143	-0.377	0.195	0.126
Hγ _A	Å	-16.126	-0.385	-0.046	0.582	1.367	-0.072	-1.347
Hγ _F	Å	-5.885	-2.081	-0.018	0.672	0.546	-0.077	-0.187
Fe4383	Å	10.131	-0.694	0.01	0.229	-0.895	-0.703	1.074
Ca4455	Å	2.897	-0.029	0.005	0.003	-0.116	0.156	0.329
Fe4531	Å	5.972	-0.018	-0.012	-0.013	-0.623	-0.4	0.578
C ₂ 4668	Å	2.016	4.006	0.011	-0.308	-0.208	0.079	0.384
Hβ	Å	-0.21	-0.135	0.004	0.024	-0.176	-0.03	-0.048
Fe5015	Å	6.925	-0.208	0.01	0.022	-1.118	0.017	1.19
Mg ₁	mag	0.291	0.047	0.001	-0.003	0.065	-0.011	0.028
Mg ₂	mag	0.588	0.033	0.002	-0.002	0.1	-0.012	0.056
Mg _b	Å	6.965	0.246	0.031	-0.021	1.263	0.005	0.432
Fe5270	Å	5.701	0.006	0.012	0.004	-0.402	0.133	0.546
Fe5335	Å	5.633	-0.092	0.005	0.01	-0.461	-0.064	0.726
Fe5406	Å	3.686	-0.043	0.004	0.004	-0.311	-0.066	0.449
Fe5709	Å	1.387	-0.016	0.000	-0.002	-0.033	0.007	0.289
Fe5782	Å	1.143	-0.015	0.000	0.000	-0.016	-0.048	0.266
Na _D	Å	7.854	-0.046	0.021	0.009	-0.431	-0.132	1.302
TiO ₁	mag	0.001	0.001	0.000	0.000	0.000	-0.002	-0.001
TiO ₂	mag	0.021	0.001	0.000	0.000	-0.001	-0.006	0.003

Table A.5: Coelho Cool Giant Response Function. Column 1 is the Lick index name, Column 2 is the units of the index, Column 3 is the model base star index strength and Columns 4-8 are the variation of the index strength (in units of mag or Å) when the element at the top of the column is increased by 0.3 dex. The last column shows the variation of the index strength when there is an overall metallicity increase of 0.3 dex.

Index	Units	I ₀	C	N	O	Mg	Ca	[M/H]
Hδ _A	Å	-13.165	-4.409	-1.412	1.505	0.969	-0.082	-3.116
Hδ _F	Å	-3.434	-1.239	-0.432	0.343	0.151	0.052	-1.381
CN ₁	mag	0.222	0.212	0.075	-0.068	-0.034	-0.01	0.041
CN ₂	mag	0.327	0.218	0.078	-0.072	-0.043	-0.015	0.047
Ca4227	Å	4.936	-0.242	-0.176	0.156	0.016	1.676	1.292
G4300	Å	10.365	1.859	0.095	-0.871	-0.170	0.125	0.1
Hγ _A	Å	-14.825	1.235	-0.109	0.159	0.445	-0.139	-1.905
Hγ _F	Å	-5.885	-1.096	-0.04	0.497	0.305	-0.043	-0.525
Fe4383	Å	9.616	-0.461	0.008	0.065	-0.489	-0.259	1.45
Ca4455	Å	2.903	-0.034	0.007	-0.015	-0.058	0.131	0.289
Fe4531	Å	5.745	-0.18	-0.07	-0.016	-0.258	-0.253	0.662
C ₂ 4668	Å	5.051	10.266	0.044	-1.2	-0.553	0.003	1.552
Hβ	Å	-0.018	-0.187	0.014	0.083	-0.074	-0.012	-0.07
Fe5015	Å	7.72	-0.708	-0.011	0.163	-0.707	0.046	1.223
Mg ₁	mag	0.222	0.12	0.001	-0.022	0.038	-0.004	0.041
Mg ₂	mag	0.398	0.04	0.002	-0.01	0.079	-0.005	0.075
Mg _b	Å	4.139	-0.533	0.016	0.101	1.477	-0.031	0.854
Fe5270	Å	5.031	0.071	0.036	-0.052	-0.23	0.063	0.601
Fe5335	Å	4.749	-0.198	-0.022	-0.014	-0.187	-0.01	0.713
Fe5406	Å	3.244	-0.091	0.006	-0.014	-0.146	-0.013	0.471
Fe5709	Å	2.136	-0.107	-0.014	-0.003	-0.031	0.02	0.35
Fe5782	Å	1.683	-0.051	-0.004	-0.018	0.011	-0.017	0.343
NaD	Å	4.318	0.237	0.064	-0.088	-0.165	-0.043	1.166
TiO ₁	mag	0.009	0.000	0.000	0.004	-0.001	-0.001	0.006
TiO ₂	mag	0.053	0.004	0.001	0.006	-0.003	-0.003	0.014

Table A.6: Coelho Turn-off Response Function. Column 1 is the Lick index name, Column 2 is the units of the index, Column 3 is the model base star index strength and Columns 4-8 are the variation of the index strength (in units of mag or Å) when the element at the top of the column is increased by 0.3 dex. The last column shows the variation of the index strength when there is an overall metallicity increase of 0.3 dex.

Index	Units	I ₀	C	N	O	Mg	Ca	[M/H]
Hδ _A	Å	2.492	-0.070	-0.033	0.010	0.154	0.048	-0.171
Hδ _F	Å	2.844	0.010	-0.004	0.005	0.083	0.075	0.062
CN ₁	mag	-0.086	-0.006	0.004	0.000	0.002	-0.002	-0.004
CN ₂	mag	-0.031	-0.007	0.004	0.000	0.003	-0.002	-0.001
Ca4227	Å	0.774	-0.097	-0.031	0.002	0.012	0.239	0.200
G4300	Å	5.497	1.311	-0.030	-0.037	-0.293	0.054	0.697
Hγ _A	Å	-1.000	-0.900	0.036	0.033	0.367	-0.008	-0.578
Hγ _F	Å	1.809	-0.604	0.018	0.018	0.194	0.000	-0.112
Fe4383	Å	1.955	-0.033	-0.011	-0.014	-0.044	-0.088	0.477
Ca4455	Å	0.879	-0.012	-0.002	-0.001	-0.031	0.051	0.212
Fe4531	Å	2.951	-0.005	-0.009	-0.002	-0.039	-0.058	0.502
C ₂ 4668	Å	0.931	0.609	-0.006	-0.008	0.073	0.024	0.747
Hβ	Å	3.768	-0.001	0.005	0.003	0.025	0.003	0.258
Fe5015	Å	4.520	-0.009	-0.011	0.013	0.001	0.052	1.030
Mg ₁	mag	0.009	0.011	0.000	-0.001	0.000	-0.001	0.008
Mg ₂	mag	0.076	0.006	0.000	0.000	0.019	0.001	0.022
Mg _b	Å	1.431	-0.046	-0.007	0.000	0.655	0.014	0.299
Fe5270	Å	1.983	-0.020	-0.006	0.000	-0.003	0.081	0.533
Fe5270	Å	1.983	-0.020	-0.006	0.000	-0.003	0.081	0.533
Fe5335	Å	1.749	-0.030	-0.006	0.006	0.007	0.005	0.415
Fe5406	Å	0.855	-0.033	-0.003	0.000	0.009	0.002	0.201
Fe5709	Å	0.635	-0.008	-0.002	0.000	0.029	0.006	0.263
Fe5782	Å	0.336	-0.005	-0.002	-0.001	0.037	-0.010	0.192
NaD	Å	0.924	-0.008	-0.003	0.000	-0.020	-0.019	0.251
TiO ₁	mag	0.002	0.000	0.000	0.000	0.000	0.000	0.000
TiO ₂	mag	0.008	0.000	0.000	0.000	0.000	-0.001	0.002

Table A.7: CAP Cool Dwarf Response Function. Column 1 is the Lick index name, Column 2 is the units of the index, Column 3 is the model base star index strength and Columns 4-13 are the variation of the index strength (in units of mag or Å) when the element at the top of the column is increased by 0.3 dex. The last column shows the variation of the index strength when there is an overall metallicity increase of 0.3 dex.

Index	Units	I ₀	C	N	O	Mg	Fe	Ca	Na	Si	Cr	Ti	[M/H]
Hδ _A	Å	-10.167	-2.360	-0.164	0.544	1.490	-2.796	0.353	0.120	1.837	0.144	-0.305	-0.843
Hδ _F	Å	-1.048	-0.636	-0.072	-0.020	0.178	-1.356	0.271	0.008	1.460	0.016	-0.210	-0.298
CN ₁	mag	0.127	0.313	0.050	-0.051	-0.024	-0.017	-0.014	-0.004	0.054	-0.020	0.004	0.023
CN ₂	mag	0.275	0.316	0.050	-0.057	-0.039	-0.027	-0.017	-0.005	0.091	-0.019	0.005	0.033
Ca4227	Å	5.927	-1.582	-0.162	0.325	-0.105	-0.203	1.071	0.029	-0.264	-0.074	-0.016	0.572
G4300	Å	8.077	3.447	-0.001	-1.052	-0.901	-1.107	0.095	-0.129	-0.539	-0.077	0.399	-0.204
Hγ _A	Å	-13.805	0.644	-0.012	0.344	1.508	-0.979	-0.167	0.160	0.232	0.449	-0.462	-0.761
Hγ _F	Å	-5.077	-1.064	-0.002	0.361	0.518	-0.290	-0.097	0.063	-0.043	0.383	-0.084	-0.083
Fe4383	Å	10.171	-0.632	-0.028	-0.004	-1.150	1.921	-0.607	-0.085	-0.276	-0.112	-0.078	0.625
Ca4455	Å	2.556	-0.268	-0.010	0.053	-0.087	-0.184	0.185	0.001	-0.174	0.105	0.024	0.238
Fe4531	Å	5.496	0.114	-0.017	-0.049	-0.505	0.239	0.031	0.011	-0.094	0.146	0.863	0.588
C ₂ 4668	Å	1.406	5.415	-0.002	0.156	-0.659	0.203	0.037	-0.074	-0.252	-0.356	0.487	0.414
Hβ	Å	0.147	-0.427	0.000	0.170	-0.508	-0.111	-0.057	-0.021	-0.049	-0.114	0.108	0.019
Fe5015	Å	7.817	-0.453	-0.009	0.151	-1.268	0.317	-0.001	0.015	-0.227	0.057	1.198	1.078
Mg ₁	mag	0.228	0.054	-0.001	-0.006	0.084	-0.021	-0.003	-0.002	-0.008	-0.004	-0.004	0.030
Mg ₂	mag	0.518	0.035	-0.001	0.005	0.065	-0.042	-0.006	-0.006	-0.019	-0.005	0.005	0.051
Mg _b	Å	7.213	0.200	-0.002	0.155	0.161	-0.775	-0.078	-0.149	-0.277	-0.559	-0.009	0.372
Fe5270	Å	5.389	0.036	0.002	-0.041	-0.553	0.691	0.206	-0.047	-0.066	-0.027	0.019	0.504
Fe5335	Å	5.742	-0.078	-0.007	-0.067	-0.604	0.677	-0.058	-0.057	-0.059	0.362	-0.005	0.674
Fe5406	Å	3.658	-0.007	-0.002	0.001	-0.364	0.528	-0.039	-0.031	-0.079	0.192	0.039	0.430
Fe5709	Å	1.273	-0.071	-0.006	-0.001	-0.101	0.119	-0.001	-0.111	-0.027	0.051	0.077	0.227
Fe5782	Å	0.958	-0.003	-0.002	-0.040	-0.042	-0.053	-0.034	-0.009	-0.020	0.296	-0.064	0.166
Na _D	Å	7.041	-0.008	-0.001	-0.058	-0.296	-0.233	-0.023	1.971	-0.132	0.006	-0.040	1.083
TiO ₁	mag	0.006	-0.004	0.000	0.014	0.001	0.001	-0.001	0.001	0.001	0.000	0.009	0.011
TiO ₂	mag	0.027	-0.005	0.000	0.020	-0.001	0.002	-0.005	0.000	0.000	0.000	0.011	0.020

Table A.8: CAP Cool Giant Response Function. Column 1 is the Lick index name, Column 2 is the units of the index, Column 3 is the model base star index strength and Columns 4-13 are the variation of the index strength (in units of mag or Å) when the element at the top of the column is increased by 0.3 dex. The last column shows the variation of the index strength when there is an overall metallicity increase of 0.3 dex.

Index	Units	I ₀	C	N	O	Mg	Fe	Ca	Na	Si	Cr	Ti	[M/H]
HδA	Å	-10.125	-2.337	0.007	0.865	0.966	-2.010	-0.085	-0.003	1.768	0.151	-0.321	-1.433
HδF	Å	-1.922	-1.071	-0.156	0.225	0.074	-1.025	0.031	-0.017	1.267	-0.014	-0.254	-0.794
CN ₁	mag	0.341	0.510	0.089	-0.108	-0.053	-0.057	-0.010	-0.005	0.022	-0.016	0.002	0.040
CN ₂	mag	0.461	0.517	0.089	-0.110	-0.059	-0.064	-0.012	-0.004	0.049	-0.014	0.002	0.046
Ca4227	Å	4.111	-0.866	-0.172	0.386	0.439	0.266	1.897	0.091	-0.010	-0.040	-0.023	1.430
G4300	Å	9.106	2.860	-0.006	-0.798	-0.716	-0.907	0.075	-0.101	-0.502	-0.169	0.266	-0.167
HγA	Å	-12.092	2.490	-0.062	-0.064	0.557	-1.071	-0.201	0.077	-0.088	-0.012	-0.364	-1.313
HγF	Å	-4.456	-0.842	-0.012	0.165	0.202	-0.327	-0.078	0.031	-0.072	0.043	-0.051	-0.517
Fe4383	Å	9.085	-2.952	-0.132	0.015	-0.579	1.754	-0.212	-0.001	-0.155	-0.066	0.023	0.751
Ca4455	Å	2.189	-0.268	-0.032	0.079	0.044	-0.120	0.137	0.010	-0.088	0.139	0.069	0.228
Fe4531	Å	5.154	0.032	-0.061	-0.039	-0.238	0.258	0.020	0.018	-0.061	0.003	0.504	0.594
C ₂ 4668	Å	3.923	12.574	-0.016	-0.165	-0.822	-0.252	-0.002	-0.099	-0.456	-0.377	0.666	1.453
Hβ	Å	0.449	-0.457	-0.001	0.336	-0.290	-0.071	-0.024	-0.009	-0.060	-0.093	0.187	0.117
Fe5015	Å	8.163	-1.656	-0.057	0.649	-0.710	0.426	0.040	0.032	-0.201	0.113	0.806	1.316
Mg ₁	mag	0.163	0.153	-0.002	-0.019	0.053	-0.009	-0.001	-0.001	-0.008	-0.002	-0.005	0.031
Mg ₂	mag	0.336	0.048	-0.002	0.039	0.081	-0.012	0.002	0.001	-0.014	-0.003	0.023	0.084
Mg _b	Å	4.555	-0.753	-0.005	1.106	1.187	-0.225	0.041	-0.022	-0.221	-0.427	0.527	1.244
Fe5270	Å	4.442	0.231	0.022	-0.069	-0.288	0.557	0.075	-0.013	-0.077	-0.058	0.053	0.537
Fe5335	Å	4.961	-0.327	-0.045	-0.081	-0.276	0.496	-0.005	-0.011	-0.063	0.194	-0.026	0.666
Fe5406	Å	3.104	0.036	-0.002	0.019	-0.149	0.402	0.003	-0.001	-0.077	0.108	0.046	0.478
Fe5709	Å	1.819	-0.338	-0.042	0.034	-0.077	0.051	0.017	-0.024	-0.042	0.042	0.089	0.278
Fe5782	Å	1.315	-0.033	-0.012	-0.081	-0.011	-0.052	-0.006	0.000	-0.019	0.225	-0.083	0.207
NaD	Å	3.566	0.400	0.047	0.055	0.014	-0.011	0.017	1.238	-0.088	0.020	0.058	1.018
TiO ₁	mag	0.021	-0.012	0.000	0.037	0.002	0.002	0.001	0.001	-0.001	0.001	0.019	0.024
TiO ₂	mag	0.069	0.001	0.002	0.063	0.002	0.002	0.001	0.002	-0.001	0.000	0.031	0.045

Table A.9: CAP Turn-off Response Function. Column 1 is the Lick index name, Column 2 is the units of the index, Column 3 is the model base star index strength and Columns 4-13 are the variation of the index strength (in units of mag or Å) when the element at the top of the column is increased by 0.3 dex. The last column shows the variation of the index strength when there is an overall metallicity increase of 0.3 dex.

Index	Units	I ₀	C	N	O	Mg	Fe	Ca	Na	Si	Cr	Ti	[M/H]
H δ _A	Å	2.354	-0.230	-0.044	0.023	-0.117	-0.722	-0.004	-0.009	-0.105	0.013	-0.088	-0.396
H δ _F	Å	2.739	-0.043	-0.013	0.016	-0.084	-0.402	0.035	-0.004	-0.066	-0.008	-0.047	-0.134
CN ₁	mag	-0.092	-0.003	0.007	0.000	0.003	0.006	-0.001	0.000	0.002	-0.001	0.002	0.001
CN ₂	mag	-0.037	-0.006	0.007	0.000	0.003	0.004	-0.002	0.000	0.002	-0.001	0.002	0.003
Ca4227	Å	0.646	-0.147	-0.045	0.001	0.031	0.106	0.256	-0.006	0.024	-0.053	0.001	0.138
G4300	Å	4.630	1.163	0.000	-0.023	-0.041	-0.057	0.076	-0.023	-0.028	-0.055	0.134	0.610
H γ _A	Å	-0.243	-0.879	0.001	0.036	-0.066	-0.474	-0.058	0.005	-0.130	-0.017	-0.164	-0.606
H γ _F	Å	2.086	-0.538	0.002	0.023	-0.067	-0.216	-0.032	-0.002	-0.083	-0.014	-0.022	-0.185
Fe4383	Å	2.052	0.215	-0.002	-0.014	0.052	0.543	-0.076	0.018	0.030	0.044	0.049	0.481
Ca4455	Å	0.773	-0.019	0.000	0.000	-0.011	-0.081	0.049	0.001	-0.034	0.052	0.033	0.146
Fe4531	Å	2.480	0.001	0.000	0.000	-0.010	0.106	0.013	0.005	-0.022	0.092	0.217	0.411
C ₂ 4668	Å	0.481	0.394	0.000	-0.004	0.081	0.303	0.040	0.007	-0.080	-0.090	0.144	0.502
H β	Å	3.864	-0.034	0.001	0.013	-0.099	-0.182	-0.014	-0.004	-0.070	-0.044	0.072	0.157
Fe5015	Å	4.277	0.000	-0.001	0.002	0.050	0.490	0.053	0.030	-0.004	-0.002	0.250	1.006
Mg ₁	mag	0.011	0.004	0.000	0.000	0.001	0.002	0.000	0.000	0.000	-0.002	0.000	0.008
Mg ₂	mag	0.073	0.002	0.000	0.000	0.023	0.005	0.001	0.000	0.000	-0.001	0.001	0.020
Mg _b	Å	1.668	-0.031	0.000	0.000	0.787	0.098	0.023	-0.014	0.009	-0.091	-0.016	0.391
Fe5270	Å	1.793	-0.019	0.000	0.000	0.031	0.324	0.082	0.001	0.107	0.023	0.043	0.475
Fe5335	Å	1.909	-0.017	0.000	0.005	0.041	0.315	0.005	0.002	0.140	0.052	0.025	0.493
Fe5406	Å	0.851	-0.021	0.000	0.001	0.022	0.207	0.003	0.001	0.024	0.026	-0.002	0.198
Fe5709	Å	0.543	-0.006	0.000	0.000	0.039	0.119	0.006	-0.022	0.016	0.020	0.011	0.214
Fe5782	Å	0.254	-0.002	0.000	0.000	0.042	-0.003	-0.005	0.001	0.012	0.123	-0.008	0.134
Na _D	Å	0.712	-0.007	0.001	0.000	0.014	0.022	-0.023	0.270	-0.007	0.004	-0.006	0.184
TiO ₁	mag	0.002	0.000	0.000	0.000	0.000	0.000	0.000	0.000	0.000	0.000	0.000	0.000
TiO ₂	mag	0.008	-0.001	0.000	0.000	0.000	0.001	-0.001	0.000	0.000	0.000	0.000	0.001

Appendix B

Models vs MILES Lick Indices

In Figures B1, B2 and B3 I plot MILES empirical star Lick Indices versus the absolute predictions of Lick indices for the same stars generated through interpolations of the theoretical stellar library presented in Chapter 3, for effective temperature, surface gravity, $[\text{Fe}/\text{H}]$ and $[\text{Mg}/\text{Fe}]$. This is for the 801 stars that fell inside the range of the theoretical grid with Cenarro et al. (2007) parameters, discussed in Chapter 4. The $[\text{Mg}/\text{Fe}]$ estimates come from the Milone et al. (2011) work and Bensby et al. (2014) galactic relation.

Although different behaviours are seen in the four parameters, the main driver of these differences is the temperature that is then seen indirectly in the other parameters. In general, the models and observations start to deviate at the lowest temperatures (\approx below 5000K), with particularly large differences seen in the hydrogen features. This may be due to a lack of non-LTE effects in the models, which is known to have a significant effect on hydrogen indices and the bluest wavelengths (e.g. Asplund 2005, Short et al. 2015). This effect is reflected in the analysis in Chapter 2 (Figures 2.1 and 2.6) where cool star models tend to overpredict the effect of abundance pattern in these regions of the spectra. The main differences in the log g plots are seen at both low and high surface gravity. However, this is due to temperature decreasing as log g decreases and temperature also increasing as log g

increases. Effects of the parameter coverage of MILES also shows up in these plots for both $[\text{Fe}/\text{H}]$ and $[\text{Mg}/\text{Fe}]$, where most of the cooler stars in the library tend to lie at solar $[\text{Fe}/\text{H}]$ and abundance pattern.

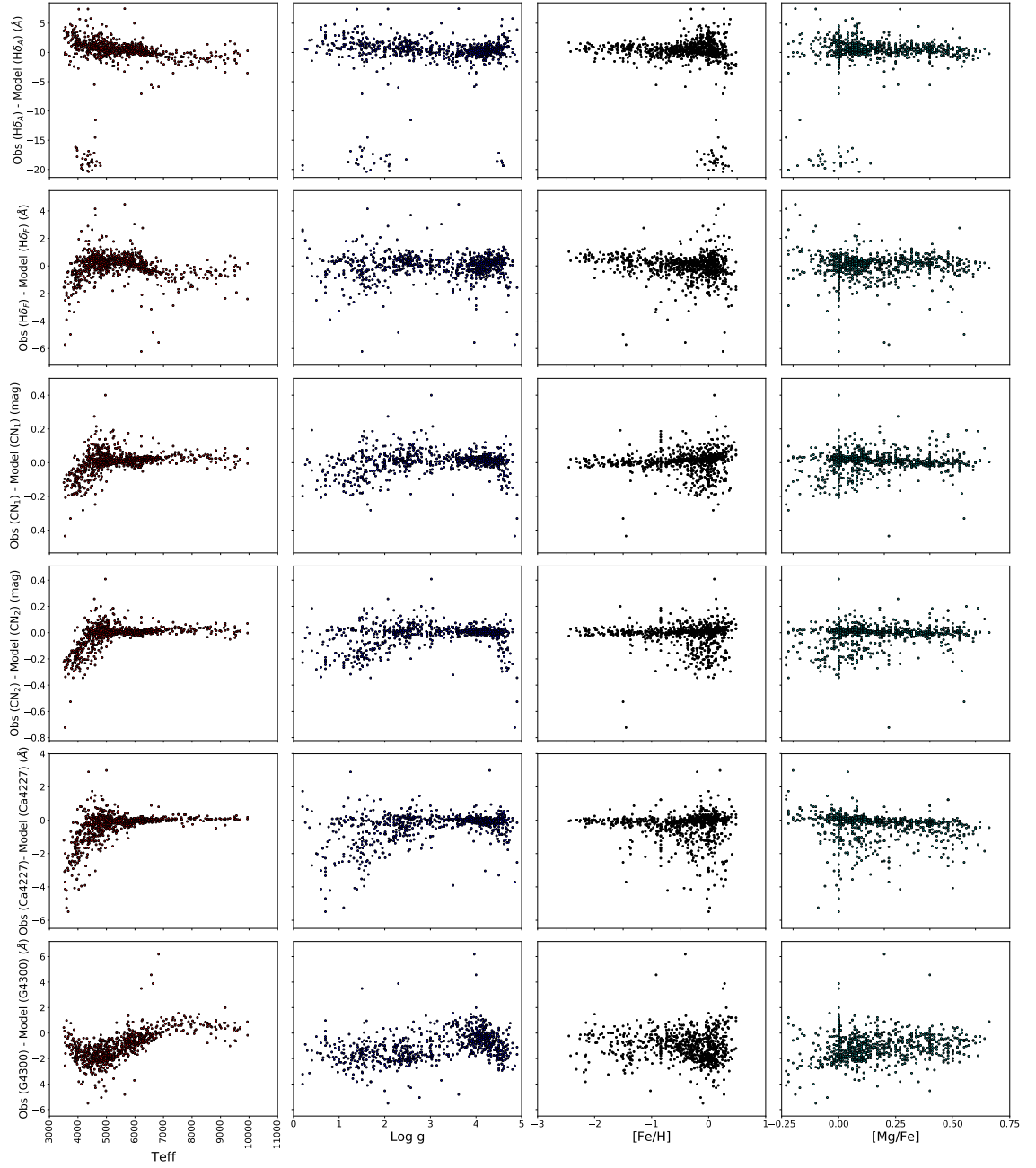


Figure B.1: Difference in MILES Lick Indices versus equivalent model predictions as a function of effective temperature, surface gravity, $[\text{Fe}/\text{H}]$ and $[\text{Mg}/\text{Fe}]$.

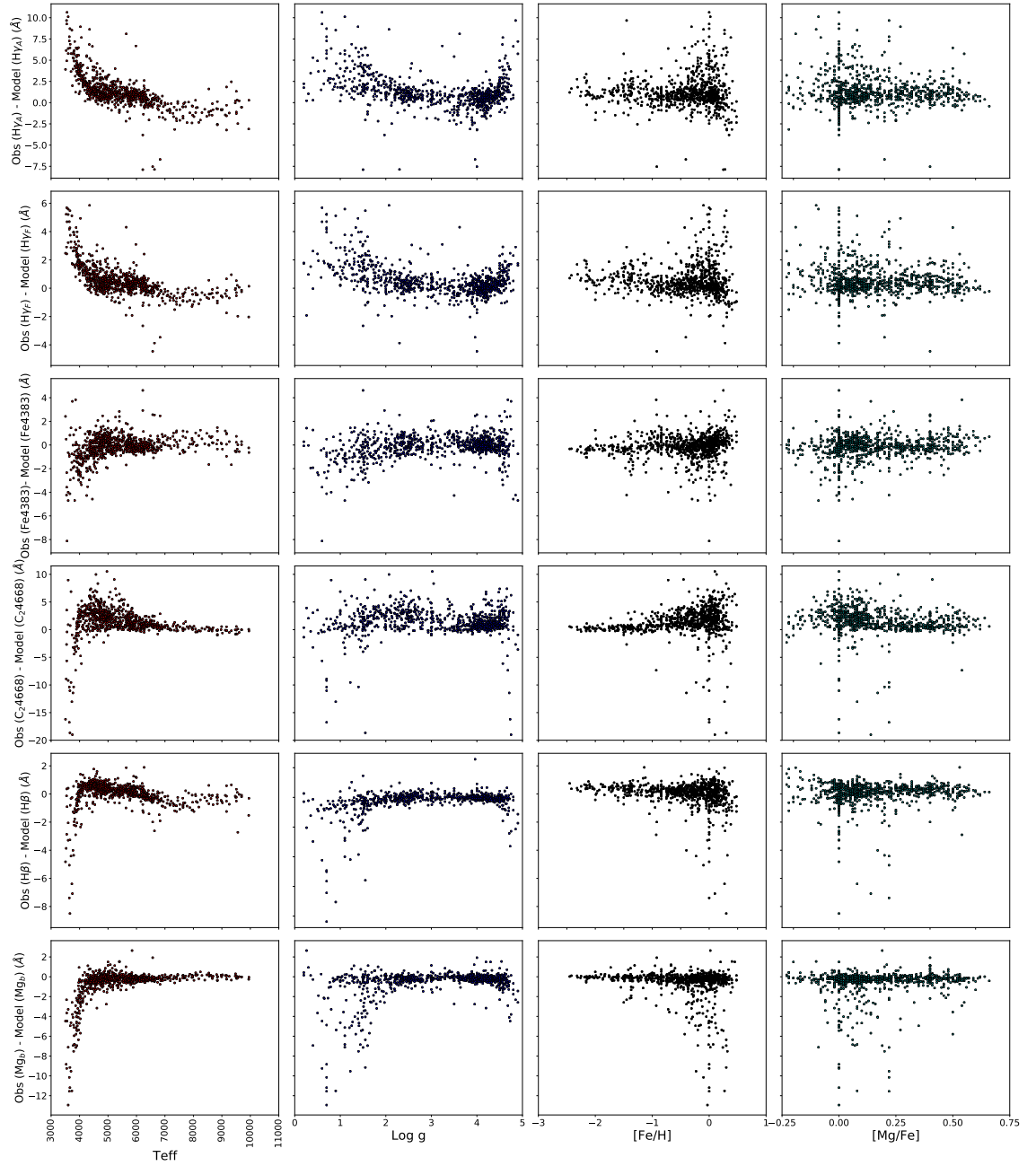


Figure B.2: Difference in MILES Lick Indices versus equivalent model predictions as a function of effective temperature, surface gravity, $[\text{Fe}/\text{H}]$ and $[\text{Mg}/\text{Fe}]$.

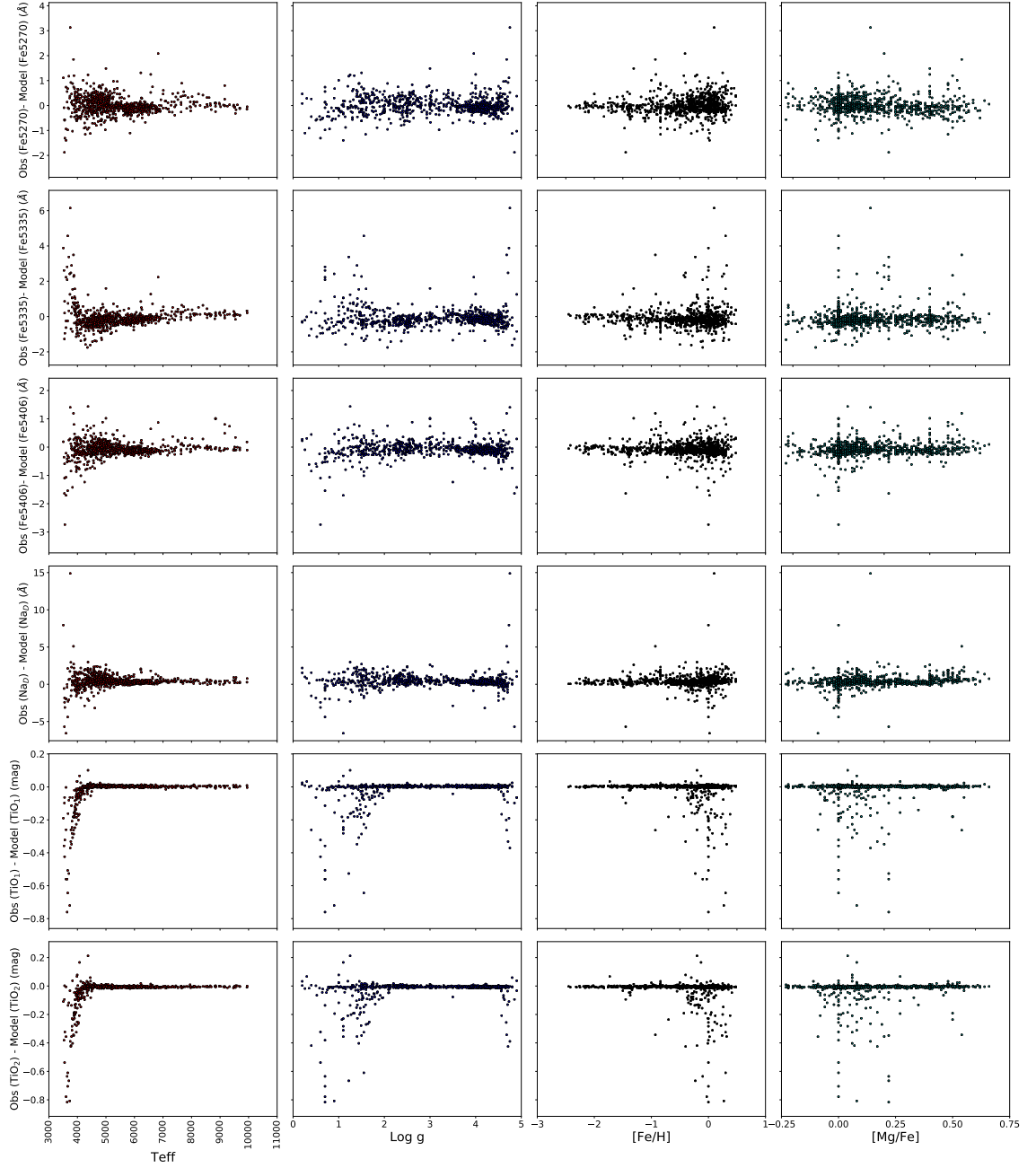


Figure B.3: Difference in MILES Lick Indices versus equivalent model predictions as a function of effective temperature, surface gravity, $[\text{Fe}/\text{H}]$ and $[\text{Mg}/\text{Fe}]$.

Appendix C

Prugniel & Sharma MILES

Parameters

I present the parameters of MILES stars, discussed in Chapter 4 (section 4.2.2). These are for the Sharma et al. (2016) stars and overlap region between Prugniel et al. (2011) and Sharma et al. (2016) parameter sets. The stars are in numerical MILES ID order for the Sharma et al. (2016) parameters up to 985. After this, starting from 5, the stars are in numerical MILES ID order for the overlap region between Prugniel et al. (2011) and Sharma et al. (2016).

Table C.1: MILES star parameters from Sharma et al. (2016) and then the overlap region between Prugniel et al. (2011) and Sharma et al. (2016), for which we take the average parameter and larger of the two errors to be conservative.

MILES	$T_{\text{eff}}(\text{K})$	Error	$\log g$	Error	[Fe/H]	Error
2	4117	49	0.68	0.15	0.14	0.07
12	3563	93	4.85	0.22	-0.57	0.09
19	4364	98	0.68	0.24	-1.83	0.09
24	4019	35	1.13	0.07	0.01	0.16
32	3934	77	1.67	0.14	-0.13	0.11
36	3933	23	1.79	0.12	0.18	0.04
38	3917	24	1.64	0.14	-0.71	0.06
45	4401	93	2.55	0.26	0	0.11
48	4451	27	2.25	0.16	0.09	0.06

Table C.1 – continued

MILES	T _{eff} (K)	Error	log g	Error	[Fe/H]	Error
53	3619	96	0.36	0.25	-0.35	0.1
55	4327	23	1.82	0.13	-0.68	0.07
59	4041	70	1.89	0.21	-0.5	0.08
65	4154	161	1.85	0.39	-0.24	0.18
80	4023	74	1.61	0.22	-0.27	0.08
99	3258	54	0.65	0.15	-0.15	0.06
103	3199	65	0.78	0.2	-0.05	0.07
114	4363	126	2.26	0.38	0.07	0.16
116	4419	79	2.67	0.2	0.07	0.07
117	4376	26	4.5	0.25	0.13	0.23
130	4306	83	2.05	0.28	-0.66	0.12
135	4418	107	4.57	0.27	-0.09	0.12
139	4497	39	1.11	0.17	-1.79	0.07
156	4034	40	1.69	0.16	-0.35	0.06
157	3851	91	1.62	0.23	-0.13	0.09
161	4022	31	1.75	0.16	-0.5	0.06
164	3562	107	0.37	0.26	-0.09	0.11
165	4194	75	1.61	0.19	-0.35	0.07
167	4367	17	1.5	0.15	-0.02	0.15
177	3637	24	0.09	0.19	-0.53	0.16
181	4184	60	2	0.19	0.1	0.07
182	4378	84	4.58	0.14	-0.15	0.09
183	3579	59	4.72	0.17	-0.05	0.07
186	3775	69	0.22	0.12	0.14	0.07
189	4445	121	2.15	0.31	-0.52	0.12
197	3858	65	1.58	0.11	-0.61	0.09
199	3666	51	0.2	0.18	0.07	0.07
201	4264	57	1.81	0.11	-0.73	0.07
203	4044	65	1.77	0.12	-0.75	0.1
210	3719	105	0.62	0.22	-0.13	0.13
211	3707	127	0.17	0.3	0.18	0.16
219	4026	93	1.75	0.15	-0.51	0.08
220	4006	30	1.51	0.15	-0.32	0.06
223	4499	26	0.56	0.18	0.11	0.08
227	3938	30	1.79	0.14	0.04	0.07
228	4496	19	0.75	0.18	0.08	0.14
229	4464	52	2.01	0.19	-0.22	0.07
233	4168	55	1.82	0.17	0.17	0.07
234	3830	77	0.44	0.13	0.13	0.07
236	4009	121	1.77	0.2	-0.43	0.1
238	4313	39	1.72	0.26	-0.66	0.35
239	4071	159	0.66	0.4	0.08	0.16
245	4405	57	2.14	0.22	0.13	0.07
250	3904	47	0.48	0.08	0.12	0.06
264	3834	40	1.54	0.08	-0.02	0.12
268	4096	93	1.46	0.24	-0.04	0.1
269	3953	18	1.43	0.11	0.19	0.06
271	3568	108	0.55	0.26	0.06	0.14

Table C.1 – continued

MILES	T _{eff} (K)	Error	log g	Error	[Fe/H]	Error
275	3913	59	1.81	0.18	-0.36	0.08
276	4264	113	0.12	0.18	0.12	0.12
277	4149	89	1.71	0.21	-0.6	0.07
279	3515	84	0.19	0.23	-0.11	0.09
287	3986	21	1.73	0.14	-0.34	0.08
289	4265	24	1.98	0.19	-0.51	0.12
295	4068	47	1.49	0.17	-0.19	0.07
300	3921	31	1.46	0.14	-0.06	0.07
305	4495	92	2.13	0.24	0.1	0.09
321	4299	93	2.1	0.26	-0.16	0.11
332	4343	25	1.89	0.23	-0.89	0.13
333	3917	19	1.45	0.15	-0.37	0.07
339	3846	65	4.63	0.18	-0.17	0.07
343	3366	36	0.53	0.17	-0.1	0.07
347	4171	35	1.65	0.19	0.01	0.08
354	4472	64	0.99	0.15	-1.64	0.08
355	4168	85	1.4	0.18	0.15	0.07
356	4150	33	1.99	0.18	-0.47	0.07
357	4244	61	1.88	0.15	-0.2	0.07
358	4167	63	1.41	0.19	-0.85	0.08
366	4425	52	2.56	0.21	0.27	0.07
367	4345	15	0.66	0.11	-2.48	0.04
373	4017	43	4.67	0.21	-0.01	0.1
376	4417	56	0.91	0.19	-2.82	0.08
382	4381	35	1.79	0.12	-0.5	0.05
388	4106	88	4.64	0.22	-0.16	0.08
391	4112	51	1.77	0.17	-0.43	0.06
397	3849	21	1.26	0.11	-0.01	0.05
398	3454	75	4.78	0.2	-0.27	0.08
399	3628	92	4.87	0.22	-0.48	0.08
400	3471	19	0.8	0.13	0	0.06
404	4307	38	2.16	0.18	-0.19	0.06
413	3979	23	1.53	0.14	-0.37	0.05
418	4455	81	2.02	0.19	-0.4	0.07
420	4380	13	2.56	0.15	0.28	0.09
426	4431	21	4.55	0.12	0.06	0.06
427	4423	81	2.24	0.15	-0.07	0.09
447	4425	36	2.34	0.14	0.25	0.06
452	3908	148	4.67	0.39	0.02	0.16
455	4384	26	2.46	0.21	0.22	0.19
457	4269	132	1.47	0.36	-0.81	0.14
459	2902	24	0.21	0.12	-0.33	0.05
472	4417	57	3.31	0.19	0.15	0.08
477	4391	32	0.78	0.16	-1.86	0.06
478	4277	19	4.48	0.12	-0.14	0.05
481	3705	69	1.06	0.17	-0.1	0.06
483	4295	48	4.57	0.15	0.04	0.06
484	3740	135	0.89	0.34	-0.11	0.16

Table C.1 – continued

MILES	T _{eff} (K)	Error	log g	Error	[Fe/H]	Error
486	3543	99	0.85	0.23	-0.02	0.09
487	3594	72	1.05	0.18	-0.15	0.07
497	3408	119	0.66	0.32	-0.05	0.14
499	4384	56	2.56	0.19	0.27	0.07
501	4245	63	1.94	0.22	-0.7	0.1
505	4375	25	0.77	0.16	-1.86	0.07
508	2908	31	0.37	0.05	-0.33	0.07
526	4375	18	2.56	0.17	0.34	0.17
527	4093	109	1.74	0.28	-0.77	0.12
528	4287	73	2.19	0.28	0.09	0.1
530	4118	96	1.56	0.23	-0.1	0.08
531	3541	96	4.72	0.19	-0.14	0.12
533	4403	45	2.54	0.17	0.31	0.06
535	3797	43	1.3	0.17	-0.71	0.07
536	4006	52	1.76	0.18	-0.01	0.07
537	3965	48	4.59	0.18	-0.42	0.08
538	4400	117	1.04	0.29	-1.45	0.11
549	4176	60	1.85	0.18	-0.09	0.07
551	3929	50	1.1	0.12	0.06	0.07
554	4459	36	2.43	0.06	0.08	0.07
555	3793	65	1.13	0.18	-0.04	0.01
557	4044	56	1.74	0.18	-0.47	0.07
560	3898	27	1.25	0.04	-0.07	0.04
561	3930	43	1.44	0.18	0.12	0.07
590	3779	17	1.46	0.13	-0.15	0.05
591	3873	27	4.68	0.05	0.06	0.11
597	4114	23	2.16	0.04	0.19	0.09
600	4278	22	0.99	0.23	-1.2	0.17
603	3862	135	1.2	0.45	0.09	0.17
606	3915	28	1.64	0.15	-0.26	0.07
614	3570	58	0.91	0.18	0.03	0.07
615	3878	53	1.59	0.17	0.05	0.06
620	4227	55	2.2	0.11	-0.09	0.06
624	4206	50	1.58	0.16	0.02	0.06
625	4381	188	4.66	0.46	-0.28	0.19
630	4023	111	4.64	0.3	-0.01	0.12
640	3949	73	1.86	0.12	-0.14	0.11
642	4497	65	2.49	0.2	0.2	0.07
648	4486	44	2.45	0.07	-0.06	0.07
650	3963	83	1.51	0.26	0.07	0.09
651	3318	53	0.48	0.18	-0.04	0.08
657	4391	4	0.75	0.04	-2.32	0.02
667	4478	72	2.19	0.19	-0.05	0.07
669	3597	89	1.12	0.22	-0.16	0.08
674	3788	85	1.45	0.23	-0.08	0.09
677	4396	116	2.1	0.23	-0.49	0.16
680	4184	60	4.33	0.1	-0.01	0.07
682	4220	16	2.04	0.16	-0.1	0.08

Table C.1 – continued

MILES	T _{eff} (K)	Error	log g	Error	[Fe/H]	Error
685	3364	57	0.42	0.1	-0.06	0.07
690	3311	28	5.01	0.27	-0.34	0.13
691	3318	19	0.72	0.19	-0.14	0.13
697	4392	23	-0.25	0.23	-0.67	0.16
704	3484	73	0.47	0.18	-0.14	0.07
705	3316	80	0.36	0.2	0.06	0.09
717	4024	125	1.79	0.31	-0.66	0.14
719	4437	17	2.74	0.17	-0.02	0.15
727	3454	75	0.35	0.23	0.03	0.08
728	4428	160	2.71	0.51	0.03	0.21
731	3965	83	0.64	0.17	-1.63	0.12
736	4473	16	1.13	0.14	-1.71	0.05
755	4438	85	1.67	0.14	-0.75	0.08
758	4126	76	1.05	0.24	-0.07	0.07
760	3942	37	0.91	0.16	-0.02	0.07
781	3387	50	0.12	0.18	-0.25	0.06
782	3503	44	0.2	0.18	-0.07	0.07
784	3977	38	0.79	0.08	0.1	0.12
785	4225	56	4.59	0.11	0.02	0.07
788	4162	68	4.64	0.2	-0.31	0.07
804	4111	24	4.61	0.19	-0.11	0.12
814	4196	29	0.67	0.16	0.04	0.06
816	3022	59	0.74	0.08	-0.12	0.09
827	4286	74	0.65	0.17	0.11	0.1
830	4318	71	1.84	0.12	-0.42	0.11
833	3914	90	1.42	0.26	-0.14	0.1
838	2805	49	5.13	0.18	-0.04	0.07
845	4371	30	1.82	0.18	-0.61	0.07
850	4105	112	1.96	0.18	0.09	0.08
859	3796	73	1.46	0.21	0.19	0.08
871	3665	14	0.99	0.12	-0.04	0.06
873	3910	31	0.19	0.14	0.18	0.06
874	4296	19	1.9	0.13	-0.8	0.06
884	3259	33	4.82	0.2	-0.26	0.07
890	2894	163	5.04	0.28	0.09	0.14
897	4238	63	1.12	0.11	-1.32	0.07
915	4269	91	0.77	0.26	-1.6	0.11
916	4264	21	0.67	0.17	-1.6	0.08
917	4170	50	0.68	0.09	-1.6	0.09
918	4421	70	1.9	0.11	-0.31	0.07
919	4235	51	2.21	0.22	0	0.07
923	4442	72	1.02	0.18	-1.5	0.12
924	4306	105	0.74	0.29	-1.5	0.12
926	4174	19	0.51	0.14	-1.29	0.05
930	4251	25	0.9	0.15	-1.29	0.07
934	4266	21	1.35	0.22	-0.8	0.12
935	4114	22	0.43	0.14	-1.53	0.06
937	4226	85	0.38	0.21	-2.31	0.07

Table C.1 – continued

MILES	T _{eff} (K)	Error	log g	Error	[Fe/H]	Error
939	4499	47	1.44	0.16	0.03	0.06
940	3382	39	0.2	0.13	0.42	0.05
941	3193	47	1.12	0.08	0.42	0.06
942	3890	32	1.81	0.05	0.42	0.06
943	3904	26	1.95	0.14	0.42	0.06
944	4404	85	1.41	0.24	-0.78	0.09
951	4397	76	1.8	0.21	-0.78	0.08
954	4250	24	1.65	0.14	-0.78	0.05
958	4486	18	1.4	0.15	-0.78	0.16
967	4261	79	1.87	0.21	-0.22	0.09
968	3955	81	1.48	0.18	-0.78	0.11
969	4244	64	1.28	0.19	-0.78	0.07
971	4222	25	1.43	0.23	-0.78	0.16
973	4167	101	1.75	0.26	0.01	0.11
976	3815	22	1.16	0.17	0.01	0.07
977	4123	60	1.75	0.19	0.01	0.08
978	4057	68	1.69	0.11	0.01	0.08
981	4397	57	2.07	0.2	0.01	0.07
985	3746	139	1.22	0.37	0.01	0.15
5	4748	93	2.87	0.22	-0.29	0.09
9	4785	98	2.62	0.24	0.03	0.09
33	4614	93	2.335	0.26	-0.69	0.11
37	4857	96	2.44	0.25	-0.415	0.1
41	4535	70	2.24	0.21	-0.365	0.08
42	4653	161	1.275	0.39	-2.495	0.18
47	4534	82	2.545	0.21	0.095	0.08
51	4549	126	1.84	0.38	-0.77	0.16
52	4689	79	2.565	0.2	-0.005	0.07
57	4782	107	1.725	0.27	-1.635	0.12
70	4857	91	2.45	0.23	-0.225	0.09
87	4835	107	2.76	0.26	-0.67	0.11
98	4646	75	2.57	0.19	0.04	0.07
115	4734	84	4.7	0.14	-0.355	0.09
122	4810	121	2.46	0.31	-0.435	0.12
128	4812	65	4.62	0.11	-1	0.09
136	4973	65	4.625	0.12	-1.53	0.1
142	4583	127	1.235	0.3	-1.985	0.16
146	4939	93	4.665	0.15	0.195	0.08
168	4626	77	4.555	0.13	0.17	0.07
175	5223	121	4.43	0.2	0.085	0.1
178	4934	159	2.38	0.4	-0.61	0.16
184	4782	93	2.69	0.24	-0.605	0.1
187	4514	108	1.345	0.26	-1.385	0.14
190	4905	113	4.705	0.18	-0.005	0.12
194	4814	89	2.725	0.21	0.145	0.07
196	4683	84	2.45	0.23	-0.695	0.09
207	4699	92	2.45	0.24	-0.275	0.09
209	4619	93	2.01	0.26	-0.52	0.11

Table C.1 – continued

MILES	T _{eff} (K)	Error	log g	Error	[Fe/H]	Error
215	4542	65	2.465	0.18	-0.02	0.07
225	4756	85	3.16	0.18	0.2	0.07
244	4741	88	2.595	0.22	-0.315	0.08
253	4620	75	2.45	0.2	-0.37	0.08
254	4815	92	2.56	0.22	-0.11	0.08
270	4820	81	2.59	0.19	-0.045	0.07
278	4896	148	2.395	0.39	-0.695	0.16
281	4844	132	1.985	0.36	-1.585	0.14
302	4630	69	2.925	0.17	0.19	0.06
309	4582	135	1.385	0.34	-1.51	0.16
311	4828	99	2.85	0.23	-0.165	0.09
315	4705	72	2.53	0.18	-0.015	0.07
319	4760	119	1.825	0.32	-1.385	0.14
346	4767	109	2.565	0.28	-0.74	0.12
351	4926	96	2.58	0.23	0.21	0.08
360	4897	117	2.375	0.29	0.13	0.11
433	4794	188	2.76	0.46	-0.545	0.19
440	4740	111	2.445	0.3	-0.745	0.12
442	4654	73	4.665	0.13	-0.935	0.11
460	4587	72	2.355	0.19	0.01	0.07
476	4716	85	2.31	0.23	-0.475	0.09
489	4717	73	2.61	0.18	0.12	0.07
493	4609	80	1.31	0.2	-2.685	0.09
496	4721	125	1.565	0.31	-1.68	0.14
520	4646	85	4.645	0.14	-0.17	0.08
532	4504	56	4.59	0.11	-0.045	0.07
542	4983	71	4.735	0.12	-1.275	0.11
546	4571	90	2.31	0.26	-0.015	0.1
552	4868	112	4.52	0.18	0.25	0.08
580	4721	163	4.015	0.28	-0.155	0.14
583	4779	63	4.73	0.11	-0.27	0.07
588	4555	91	2.3	0.26	-0.29	0.11
593	4780	70	4.725	0.11	-0.27	0.07
601	4648	105	2.43	0.29	-0.65	0.12
616	4687	85	2.695	0.21	0.125	0.07
654	4608	79	1.75	0.21	-0.01	0.09
672	4762	101	2.36	0.26	-0.48	0.11
683	4955	139	2.29	0.37	-0.71	0.15
712	4635	68	2.325	0.18	-0.21	0.07
730	4840	108	2.56	0.26	-0.175	0.11
773	4738	96	2.48	0.25	-0.185	0.1
779	4737	108	2.595	0.28	-0.665	0.12
795	4583	81	2.545	0.21	0.145	0.08
803	4603	108	1.24	0.23	-1.865	0.12
807	4717	103	2.585	0.26	0.03	0.1
808	4775	113	2.585	0.29	-0.56	0.12
810	4672	78	2.655	0.19	0.18	0.08
812	4762	76	2.67	0.18	0.1	0.07

Table C.1 – continued

MILES	T_{eff} (K)	Error	log g	Error	[Fe/H]	Error
825	4881	178	2.295	0.48	-1.245	0.18
832	4655	97	2.685	0.25	-0.275	0.1
835	4509	71	4.5	0.15	0.14	0.07
844	4762	80	2.515	0.2	-0.01	0.07
847	4665	113	1.43	0.27	-2.025	0.14
851	4631	78	3.15	0.18	0.185	0.07
857	4728	76	2.44	0.19	-0.165	0.07
864	4737	67	4.6	0.11	0.05	0.06
867	4681	94	2.555	0.24	0.015	0.09
879	4757	131	2.61	0.32	0.065	0.12
880	4582	95	1.22	0.22	-2.05	0.12
881	4620	94	3.255	0.21	0.35	0.07
882	4673	91	2.37	0.24	-0.315	0.1
887	4770	98	3.205	0.21	0.105	0.08
893	4585	72	2.5	0.19	0.05	0.07
895	4814	92	2.28	0.24	-0.44	0.1
925	4614	127	1.29	0.39	-1.42	0
927	5916	624	2.91	1.99	-1.2	0
936	4785	163	1.605	0.48	-2.235	0
945	4736	202	2.32	0.81	-0.81	0
946	4539	79	1.58	0.29	-0.81	0
948	4793	201	2.525	0.79	-0.81	0
949	4794	302	2.285	1.13	-0.81	0
955	4643	158	2	0.62	-0.81	0
956	4490	139	1.67	0.52	-0.81	0
957	4677	161	1.67	0.56	-0.81	0
959	4552	137	2.065	0.56	-0.81	0
961	4775	204	2.075	0.79	-0.81	0
964	4677	141	1.68	0.48	-0.81	0
972	5068	69	2.41	0.22	-0.06	0
975	4510	76	2.23	0.28	-0.06	0
979	4531	61	2.115	0.21	-0.06	0
980	4834	86	2.455	0.29	-0.06	0
982	4622	84	2.395	0.29	-0.06	0